Technische Universität München

Fakultät für Elektrotechnik und Informationstechnik

Lehrstuhl für Elektrische Energiespeichertechnik

Aging of Lithium-Ion Batteries in Electric Vehicles

Dipl.-Ing. Univ. Peter Keil

Vollständiger Abdruck der von der Fakultät für Elektrotechnik und Informationstechnik der Technischen Universität München zur Erlangung des akademischen Grades eines

Doktor-Ingenieurs (Dr.-Ing.)

genehmigten Dissertation.

Vorsitzender:	Prof. Dr.-Ing. Ulrich Wagner
Prüfende der Dissertation:	1. Prof. Dr.-Ing. Andreas Jossen
	2. Prof. Dr.-Ing. Julia Kowal

Die Dissertation wurde am 19.04.2017 bei der Technischen Universität München eingereicht und durch die Fakultät für Elektrotechnik und Informationstechnik am 19.06.2017 angenommen.

Danksagung

Die vorliegende Dissertation entstand während meiner Tätigkeit als wissenschaftlicher Mitarbeiter am Lehrstuhl für Elektrische Energiespeichertechnik (EES) der Technischen Universität München.

An erster Stelle gilt mein Dank Herrn Professor Dr. Andreas Jossen für die Betreuung meiner Arbeit und die vielfältigen Forschungsthemen, mit denen ich mich am Lehrstuhl beschäftigen durfte. Es war für mich eine spannende und lehrreiche Zeit, als einer der ersten Doktoranden den 2010 neu gegründeten Lehrstuhl mitgestalten zu dürfen. Für das entgegengebrachte Vertrauen und die großen Freiheiten im Rahmen meiner Forschungstätigkeit möchte ich mich ganz herzlich bedanken. Mein besonderer Dank gilt auch Frau Professor Dr. Julia Kowal für die Übernahme des Koreferats und Herrn Professor Dr. Ulrich Wagner für die Leitung der mündlichen Prüfung.

Ich bedanke mich bei allen EES-Kollegen für die angenehme Atmosphäre und die gute Zusammenarbeit am Lehrstuhl. Allen Studenten, die mich bei meinen Forschungsthemen unterstützt haben, möchte ich ebenfalls danken. Mein ganz besonderer Dank gilt meinem langjährigen Bürokollegen Martin Brand und meinen Kollegen des Li.plus-Gründerteams: Vielen Dank für die schöne, erlebnisreiche und spannende Zeit, die wir gemeinsam am Lehrstuhl verbringen durften. Ein großes Dankeschön auch an das Kollegenteam, das die Feierlichkeiten am Prüfungstag organisiert und vorbereitet hat.

Abschließend möchte ich mich ganz herzlich bei meiner Familie und meiner Partnerin Sabine für ihre fortwährende Unterstützung bedanken.

Peter Keil

München, Juli 2017

Kurzfassung

Reichweite, Kosten und Lebensdauer sind zentrale Herausforderungen bei der Entwicklung von Lithium-Ionen-Batteriesystemen für Elektrofahrzeuge. Nur mit einer ausreichend langen Haltbarkeit der Antriebsbatterie lassen sich teure Batteriewechsel während der Fahrzeuglebensdauer vermeiden. Um dies zu erreichen, ist eine genaue Kenntnis des Alterungsverhaltens von Hochenergie-Lithium-Ionen-Batterien in Elektrofahrzeugen notwendig.

Bei der Nutzung eines Elektrofahrzeugs lassen sich typischerweise drei Betriebszustände unterscheiden: Inaktivitätsphasen, Laden und Fahrbetrieb. Zu jedem der drei Zustände präsentiert diese Arbeit umfassende experimentelle Alterungsuntersuchungen, die dominierende Alterungsmechanismen aufzeigen und die Sensitivitäten der Batteriealterung hinsichtlich verschiedener Einflussfaktoren, wie beispielsweise Ladezustand oder Temperatur, analysieren. In den Alterungsstudien werden kommerzielle Hochenergie-Rundzellen untersucht, die Graphit als Anodenmaterial und Lithium-Nickel-Kobalt-Aluminium-Oxid (NCA) als Kathodenmaterial beinhalten.

Für die Untersuchung der im Elektrofahrzeugbetrieb auftretenden kalendarischen Alterung und Zyklenalterung werden mehrere Diagnoseverfahren zur zerstörungsfreien Alterungsdetektion eingesetzt. Diese umfassen neben Kapazitäts- und Widerstandsmessungen auch die Auswertung der Spannungsableitung mittels Differential Voltage Analysis sowie eine neu entwickelte Coulometriemethode, das sog. Coulomb-Tracking. Ziel der Verfahren ist es, Alterungsvorgänge an einzelnen Elektroden zu identifizieren, ohne die Zellen öffnen und somit zerstören zu müssen. Mithilfe der eingesetzten Diagnoseverfahren lassen sich auch Mechanismen identifizieren, die zu einer Regeneration der Batteriezellen während längerer Ruhephasen führen.

Die Untersuchungen zur kalendarischen Alterung zeigen auf, welche Arten von Nebenreaktionen in der Zelle ablaufen und in welchem Umfang diese zu einem Verlust von zyklisierbarem Lithium, einer Degradation der Aktivmaterialien und zu einem Anstieg der Innenwiderstände führen. Für das Laden einer Elektrofahrzeugsbatterie werden klassische Ladeverfahren und Schnellladeverfahren untersucht. Es bestätigt sich, dass Lithium-Plating insbesondere beim Schnellladen einen dominanten Einfluss auf die Batteriealterung hat. Die Untersuchungen machen auch deutlich, welche Auswirkungen eine verringerte Zyklentiefe infolge einer reduzierten Ladespannung oder einer erhöhten Entladeschlussspannung auf die Zyklenlebensdauer hat. Die Alterungsstudie zum Fahrbetrieb basiert auf einem repräsentativen, dynamischen Belastungsprofil und fokussiert sich auf den Einfluss der Rekuperation auf die Batterielebensdauer. Es werden bis zu 200.000 km Fahrstrecke in der Alterungsstudie nachgebildet und der Einfluss des Ladezustands, der Temperatur und der Zyklentiefe umfassend untersucht. Zudem wird die dynamische Fahrbelastung mit einer Konstantstrombelastung vergleichen. Erstmals wird auch der schädigende Einfluss niedriger Batterietemperaturen getrennt für den Lade- und für den Entladevorgang gezeigt.

Basierend auf den Erkenntnissen der einzelnen Alterungsstudien werden Empfehlungen für einen lebensdaueroptimierten Betrieb von Lithium-Ionen-Batterien in Elektrofahrzeugen abgeleitet. Die Arbeit zeigt, dass bei moderaten Betriebstemperaturen bereits mit den heutigen Zelltypen die erforderlichen Batterielebensdauern erreicht werden können. Der Betrieb bei niedrigen Temperaturen von 10°C und darunter stellt jedoch noch eine Herausforderung dar, die durch verbesserte Zelltypen und Maßnahmen zur thermischen Konditionierung gelöst werden muss.

Abstract

Range, cost, and battery life are the central challenges for the development of lithium-ion battery systems for electric vehicles. A sufficiently long battery life is necessary to avoid costly battery replacements during the vehicle life. To achieve this, a profound knowledge of the aging behavior of high-energy lithium-ion batteries in electric vehicles is essential.

For the operation of an electric vehicle, three operating conditions can typically be distinguished: inactivity periods, charging, and driving operation. For each of the three operating conditions, this thesis presents extensive experimental aging studies, which reveal dominant aging mechanisms and analyze the sensitivity of battery aging to different influencing factors, such as state of charge (SoC) or temperature. The aging studies examine commercial high-energy cells of format 18650, which contain graphite as anode material and lithium nickel cobalt aluminum oxide (NCA) as cathode material.

To investigate the calendar and cycle aging of lithium-ion batteries used in electric vehicle applications, several analysis techniques for nondestructive aging diagnostics are applied. In addition to capacity and resistance measurements, the derivative of voltage curves is analyzed by Differential Voltage Analysis and a novel coulometry technique, named Coulomb Tracking, is introduced. The purpose of these methods is to identify aging reactions at the individual electrodes without opening and destroying the cells. They also enable to identify mechanisms behind recovery effects of the cells, which occur during longer idle periods.

The investigations on calendar aging disclose the types of side reactions occurring inside the cells and also the extent to which they lead to a loss of cyclable lithium, a degradation of the active materials, and an increase of internal resistances.

For charging an EV battery, standard charging protocols and fast-charging protocols are examined. The results confirm that lithium plating has a dominant impact on battery aging, particularly for fast charging. The study also presents the effects of a reduced cycle depth by either decreasing the charging voltage or decreasing the discharging voltage.

The aging study on driving operation bases on a representative, dynamic load profile and focuses on the impact of regenerative braking on battery aging. The study reproduces up to 200,000 km of driving to thoroughly examine the impact of SoC, temperature, and cycle depth. In addition to that, dynamic load profiles and constant-current discharging are compared. Furthermore, the detrimental impact of low battery temperatures is shown separately for charging and discharging.

Based on the findings of the different aging studies, recommendations for optimized operational strategies are derived which enable a long battery life. This thesis demonstrates that at moderate operating temperatures, the required battery life can already be achieved with the state-of-the-art battery types. However, operating at low temperatures of 10°C and below remains challenging. Improved types of lithium-ion cells and constructive means of thermal conditioning have to be developed to overcome the cycle life limitations at low temperatures.

Table of Contents

List of Abbreviations

Abbreviation	Description
AC	alternating current
BC	boost charging
CC	constant current
CCCV	constant current constant voltage
CCPC	constant current + pulsed charging
CID	current interrupt device
CV	constant voltage
DC	direct current
DVA	Differential Voltage Analysis
EFC	equivalent full cycles
EIS	Electrochemical Impedance Spectroscopy
EoL	end of life
EV	electric vehicle
FCEV	fuel-cell electric vehicle
GHG	greenhouse gas
HEV	hybrid electric vehicle
ICA	Incremental Capacity Analysis
LFP	lithium iron phosphate
MSCC	multistage constant current
NCA	lithium nickel cobalt aluminum oxide
NMC	lithium nickel manganese cobalt oxide
PC	pulse charging
RMS	root mean square
SC	supercharging
SEI	solid electrolyte interphase
SoC	state of charge
SPI	solid permeable interface
USABC	United States Advanced Battery Consortium
VC	vinylene carbonate

1 Introduction

Lowering emissions in the automotive passenger transportation sector is an integral part of the global attempt to reduce greenhouse gas (GHG) generation. With an electrification of the vehicles' powertrains, a reduction of fossil fuel consumption and GHG generation can be achieved. Figure 1 illustrates the amount of CO_2 generated per driven kilometer for different conventional and electric vehicles (EVs); it also illustrates electrification pathways, which provide the possibility to drive GHG emissions toward zero [1]. Hybrid electric vehicles (HEVs), in which an electric motor and a small battery assist the conventional combustion engine during acceleration and recover energy by regenerative braking, can reduce CO_2 emissions by approximately one third, compared to conventional gasoline or diesel vehicles. For even lower CO_2 emissions, a further electrification of the powertrain is necessary to reduce the consumption of fossil fuels. [1]

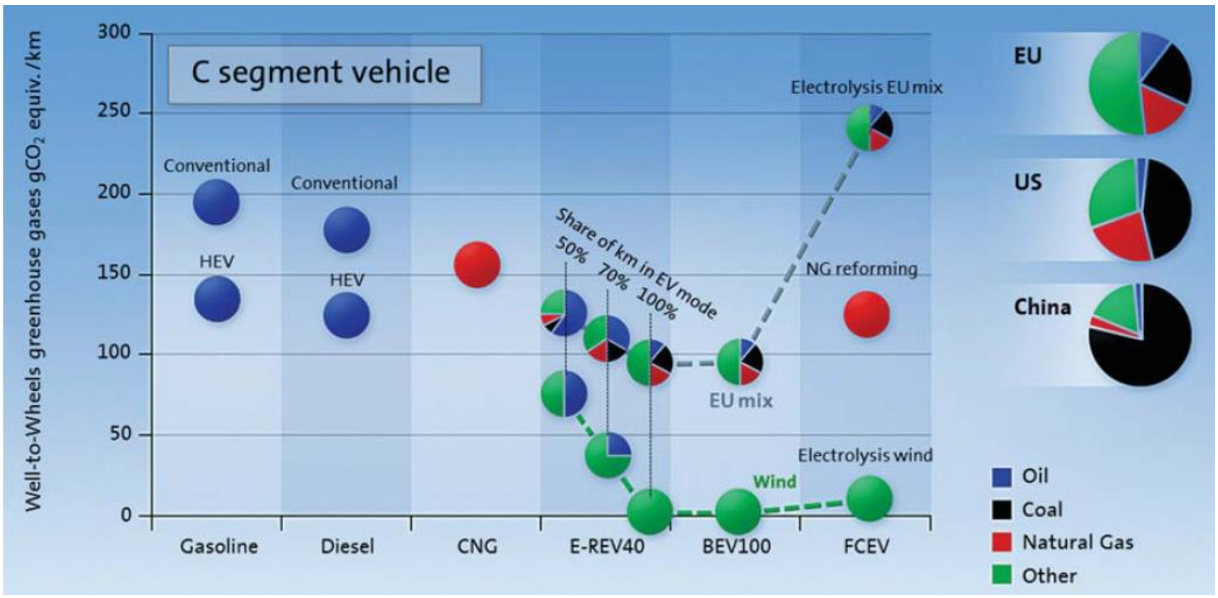

Figure 1. Well-to-wheels greenhouse gas emissions for various propulsion types and fuel sources for a compact passenger car. (Reproduced from Ref. [1] with permission from The Royal Society of Chemistry.)

Figure 1 compares two battery-based EVs: an extended-range EV (E-REV40), which contains a battery for an electric driving range of 64 km (40 miles) and an additional combustion engine to generate electricity for longer driving distances, as well as a pure battery EV (BEV100), where the battery provides a driving range of 160 km (100 miles). These two examples demonstrate that CO_2 emissions can be reduced with a higher share of kilometers in EV mode. However, overall well-to-wheels emissions depend largely on the energy sources used for electricity production. EVs can only reduce GHG emissions substantially when the share of energy produced by burning coal or other fossil fuels is low [2,3]. Fuel-cell electric vehicles (FCEVs) using hydrogen for energy storage are a viable alternative to battery-based EVs [1]. They can typically provide a higher driving range but suffer from lower efficiencies. With the current energy mix in the EU, FCEVs can produce higher CO_2 emissions than combustion engines due to the energy-demanding electrolysis process. Figure 1 also illustrates that by operating EVs with electricity from renewable sources only, their CO_2 emissions during operation can be reduced toward zero.

1.1 Motivation

Currently, pure battery EVs appear to be the most promising approach for the introduction of sustainable mobility. The performance of these EVs is largely determined by the traction battery. Lithium-ion batteries are typically used in EVs due to their high energy density and specific energy compared to other commercial battery technologies. Also, the cost of an EV depends strongly on the traction battery, as it is the most expensive component of the vehicle. Driving range and cost are the two major concerns of potential customers that have to be overcome to achieve a widespread adoption of EVs [4].

To obtain a sufficient driving range at reasonable cost, the first generations of EVs based on lithium-ion batteries are typically equipped with high-energy battery cells containing graphite as anode material and lithium nickel manganese cobalt oxide (NMC) or lithium nickel cobalt aluminum oxide (NCA) as cathode material [5]. However, high-energy batteries tend to age faster than high-power batteries, as charge-discharge cycling exerts higher stress on the thicker and less porous active materials typically used in this type of batteries [6]. Typically, not the entire nameplate capacity of the battery is utilized, as certain safety margins are defined toward the fully charged and fully discharged state of the battery. These margins are expected to prolong battery life and are often regarded as aging reserve to buffer capacity fade. When the battery life is shorter than the vehicle life, additional cost has to be considered upon purchase for a battery replacement. To prevent an excessive total cost of ownership, replacements of the EV traction battery have to be circumvented. This is also reflected in the development targets of the United States Advanced Battery Consortium (USABC) for commercial EV batteries in 2020: The USABC goals from 2014 for advanced EV batteries contain a battery life of 15 years and 1000 cycles [7].

As further advances in energy density of lithium-ion EV batteries appear to be limited [8], it is important to improve the utilization of available energy storage technologies. To achieve this, better knowledge of the aging behavior of lithium-ion EV batteries is essential. This will help to improve the design of future battery systems and to optimize operational strategies, which decreases degradation and prolongs battery life. With more experience in the real-world aging behavior of lithium-ion batteries in EVs, safety reserves can be reduced and a larger portion of the battery capacity can be utilized in the vehicle application, while still reaching the lifetime requirements of the battery. As such, the driving range increases without enlarging the battery, which always entails higher cost.

1.2 Purpose

Investigating the degradation of lithium-ion batteries in pure battery EVs is the focus of this thesis. Hence, the aging of high-energy lithium-ion battery cells is examined under representative operating conditions to gain an extensive knowledge of the predominant degradation mechanisms. As there are different basic operating scenarios for the traction battery of an EV, such as driving periods, charging periods, and nonoperating periods, these operating conditions have to be examined separately for a thorough understanding of the ongoing aging mechanisms. For each operating condition, various influencing factors, such as SoC, temperature, and amperage, affect

the degradation behavior. This leads to complex interdependencies and a substantial variety of load conditions that need to be examined and compared.

Since knowledge on lithium-ion battery aging under complex load conditions has not yet been available to such an extent that simulation models can predict the precise effects of varying individual operating parameters, experimental studies with representative load scenarios are the preferred way to obtain reliable and meaningful insights on battery aging under typical EV operating conditions. As the aging behavior of a lithium-ion battery system is mainly determined by the aging behavior of the individual cells, this thesis investigates battery aging by examining the degradation of single lithium-ion cells which are tested under a variety of different operating conditions. Additional aging effects originating from the system design, such as thermal gradients or inhomogeneous current distributions, are beyond the scope of this thesis, but can be deduced from the findings on cell level. Furthermore, no effects from electronics, such as the battery management system, onboard and offboard chargers, or power electronics from the electrified powertrain are examined. This thesis concentrates on the aging processes on cell level, which originate from electrochemical and mechanical processes inside the cells.

To examine a large variety of operating conditions, aging studies were conducted with commercial lithium-ion cells of the 18650 format. These small cylindrical cells are available from many renowned manufacturers with mature manufacturing processes. Furthermore, the small cell size eases the requirements on the test infrastructure, as the demand for the charging and discharging power is substantially lower than for prismatic hardcase cells or pouch cells, which typically have about ten times the capacity of the small 18650 cells. Using 18650 cells enables this thesis to examine a large number of test conditions for identical cells under comparable test conditions. The objective of this thesis is to examine a variety of test conditions far beyond datasheet measurements of the cell manufacturers and typical aging studies presented in the literature. The purpose of this thesis is to provide comprehensive insights into battery degradation under typical EV operating conditions and identify the main aging drivers.

For the degradation monitoring and aging analysis, noninvasive and nondestructive analysis techniques were employed. Several diagnostic techniques are presented in detail and further developed to provide a precise picture of the battery degradation processes. This thesis contains several approaches to determine the contributions of the individual cell components, without the need for opening the cells for inserting reference electrodes or performing post-mortem analyses.

The results of the experimental studies are discussed and compared with the current state of battery aging knowledge to confirm results from preceding studies and to present new findings on battery aging under EV operating conditions. Based on these results, strategies for reducing battery aging in EVs are deduced. The results will support the design and operation of future EV battery systems to maximize battery life and reduce overall cost.

1.3 Outline

Figure 2 illustrates the structure of this thesis, which examines the aging of lithium-ion batteries under EV operating conditions. The operating conditions of an EV battery can be categorized into three operating states: nonoperating, charging, and driving. In all three states, the aging behavior differs substantially. As such, three aging studies related to the different operating conditions of an EV battery are presented. To obtain maximum comparability of results, the studies were performed with the same type of lithium-ion cell. In total, more than 200 test conditions with numerous parameter variations of influencing factors, such as temperature, SoC, charging current, discharging current, and cycle depth, were examined. Checkup procedures under identical environmental conditions were used to analyze the degradation of the cells.

Chapters 2 to 3 provide the fundamentals for the three experimental aging studies, which follow in Chapters 4 to 6. Based on the findings of the aging studies, Chapter 7 presents strategies for reducing EV battery aging.

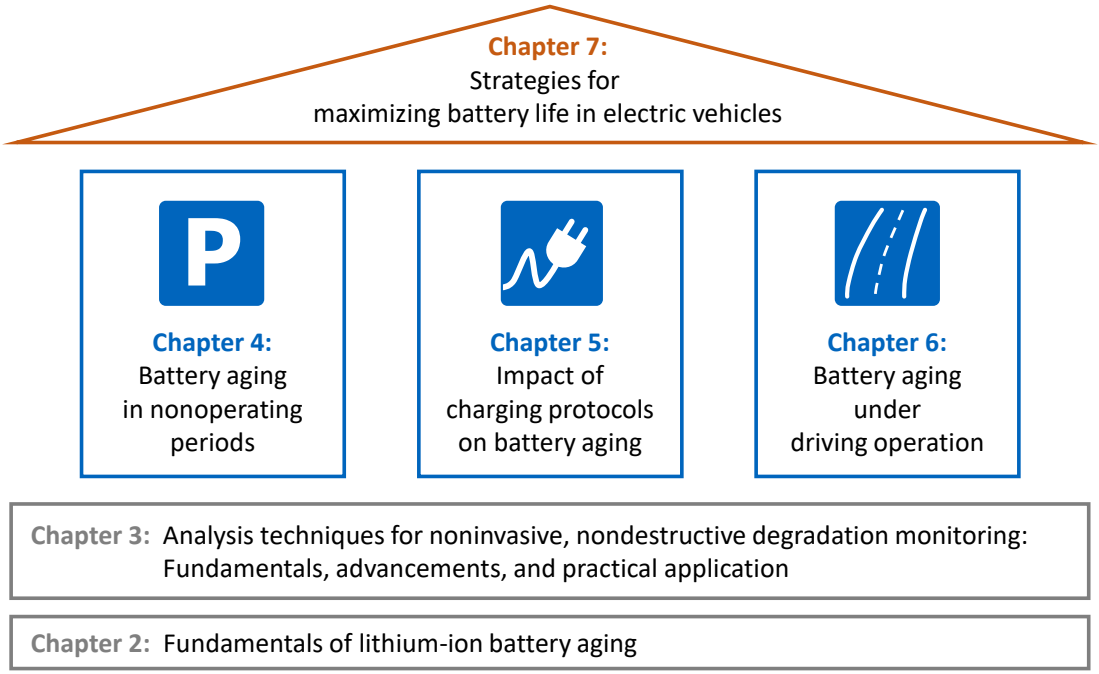

Figure 2. Structure of this thesis on the aging of lithium-ion batteries in electric vehicles

For the general analysis and interpretation of battery degradation, Chapter 2 presents the fundamentals of lithium-ion battery aging. Degradation mechanisms are introduced and discussed for the individual cell components. This overview focuses on graphite as the anode active material and NCA as the cathode active material, as these were the electrode materials of the lithium-ion cells examined in the experimental studies of this thesis.

Chapter 3 presents the lithium-ion cells examined and the analysis techniques for degradation monitoring that were applied in the three experimental aging studies. Based on the current state-of-the-art in battery testing, techniques for noninvasive and nondestructive aging diagnostics for lithium-ion batteries are introduced. Extensive analyses of measurement techniques and identification of individual aging contributions from both electrodes are provided for Electrochemical Impedance Spectroscopy (EIS) and Differential Voltage Analysis (DVA). Advancements for aging diagnostics are presented and a novel coulometry method, termed

"Coulomb Tracking," is introduced, which allows identification of side reactions during storage periods.

As battery aging during nonoperating periods plays an important role in the life of EV batteries, two calendar aging studies are presented in Chapter 4. The capacity fade and resistance increases of cells that were stored at different temperatures and SoCs are analyzed. By combining several methods of aging diagnostics, such as capacity measurements, DVA, Coulomb Tracking, EIS, and pulse measurements at different SoCs, the root causes and driving forces of capacity fade and resistance increase are identified. Moreover, projections for the calendar life of the examined batteries are made.

Chapter 5 contains the first cycle aging study, in which the impact of the charging protocol on battery aging is examined. Extensive parameter variations are presented for constant current constant voltage (CCCV) charging, which is the most common charging strategy for lithium-ion batteries. In addition, charging protocols combining different charging currents are examined. The impact on charging time and capacity utilization is analyzed. Moreover, battery life is analyzed by capacity measurements, EIS and pulse measurements, as well as DVA. This demonstrates the strong impact of charging current and cycle depth on battery aging. Lithium plating is confirmed to be a critical issue for fast charging.

In Chapter 6, the impact of EV driving conditions on battery aging is investigated in a second cycle aging study based on representative dynamic load profiles. Specifically, the effect of recharging sequences related to regenerative braking is examined. For different temperatures, SoCs, and cycle depths, cycle aging is presented and compared to calendar aging. Results from long-term testing, representing up to 200,000 km, are presented. Aging under dynamic load conditions is also compared to constant current discharging, which is typically found in the aging literature. Low-temperature degradation, which can cause a substantial reduction in cycle life, is examined separately for charging and discharging. DVA is used to identify the origins of temperature-dependent degradation and the utilization of Coulomb Tracking enables identification of the root causes of capacity recovery after long-term operation at high SoC.

The conclusion of each of the three aging studies is presented at the end of the respective chapter. Based on the findings and conclusions from the three preceding main chapters, Chapter 7 derives strategies for improving battery operation in an EV to maximize battery life. This demonstrates that by optimized operating strategies, a battery life equal to the life of a typical passenger vehicle can be achieved already today at moderate temperatures. This avoids costly battery replacements and as such can reduce the total cost of ownership, which is an essential prerequisite for a widespread adoption of EVs. However, low-temperature performance is still a critical issue and has to be further improved. This thesis ends with a brief outlook on further research work that arises from the results of this thesis.

Although the studies presented in this thesis examine one specific type of lithium-ion cell, the general aging trends and degradation mechanisms also apply for other high-energy lithium-ion cells containing graphite anodes and NCA or NMC cathode materials. However, the extent of aging owing to a specific degradation mechanism can vary notably among different cell types.

2 Fundamentals of Lithium-Ion Battery Aging

Although less rapid than other battery technologies, lithium-ion batteries exhibit a deterioration of their performance over time, which comprises a loss of available energy and power [9]. This results from a capacity fade and resistance increases. The capacity fade can originate from a loss of electrode active material, from a loss of cyclable lithium, or from increasing internal resistances which cause an earlier termination of the charging or discharging process [10,11]. Furthermore, the increasing cell resistances reduce the power capability and decrease the available energy due to higher losses during discharging.

The specific degradation mechanisms which lead to a capacity fade and increasing internal resistances are presented in this chapter. Moreover, the concept of calendar and cycle aging as well as the end of life (EoL) of a lithium-ion traction battery in an EV are covered.

2.1 Components of a Lithium-Ion Battery Cell

As illustrated in Figure 3, lithium-ion battery cells consist of two composite electrodes and a separator in-between. The anode, which represents the negative electrode, typically consists of a copper current collector foil coated with carbonaceous active material. The cathode, which represents the positive electrode, typically consists of an aluminum current collector foil coated with transition-metal-oxide active material, such as lithium cobalt oxide, lithium nickel oxide, lithium manganese oxide, or compositions thereof; another widely used cathode material is lithium iron phosphate (LFP) [12]. In today's EV traction batteries, NMC and NCA are used as cathode materials due to the high energy density of these lithium-ion cell chemistries [13,14]. The separator of a lithium-ion cell is typically a porous polymer foil. The pores of the active materials and the pores of the separator are filled with electrolyte, which consists of organic solvents, a conducting salt, and additives. [15]

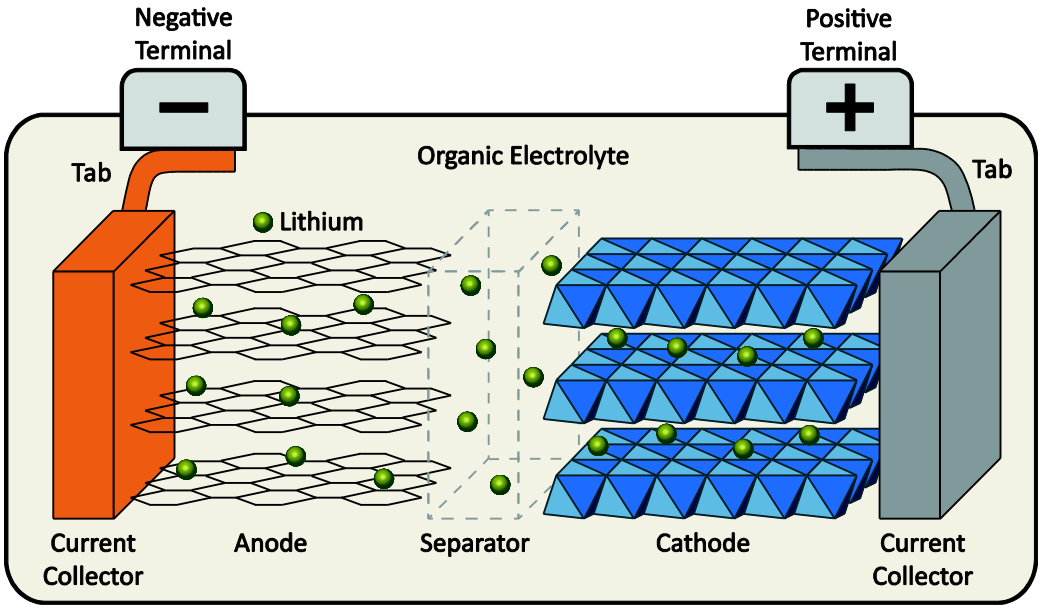

Figure 3. Components of a lithium-ion battery cell

During charging, lithium stored in the cathode is oxidized and deintercalated. The lithium ions go into the electrolyte solution and move from the cathode to the anode while electrons are released to the external current path at the positive terminal of the cell. Via the negative terminal of the cell, electrons from the external current path reach the anode active material, where lithium ions from the electrolyte are intercalated into the active material while being reduced to neutral lithium atoms. During discharging, this process is reversed. [16]

2.2 Degradation of Cell Components

The different components of a lithium-ion cell are all subject to degradation. This section describes the major degradation mechanisms of the anode active material, the cathode active material, the electrolyte, the separator, and the current collectors. As the experimental studies that are presented in this thesis were performed with lithium-ion cells containing a graphite anode and an NCA cathode, this section focuses particularly on the degradation mechanisms of these electrode materials.

2.2.1 Anode Active Material

Graphite is the prevailing material for the negative electrode of the lithium-ion cells that are used in EVs [5]. The aging effects at graphite anodes can be mainly attributed to changes at the electrode/electrolyte interface, where the growth of passivating surface films and metal lithium deposition are the major degradation mechanisms [17]. In addition to that, mechanical degradation can be observed in the graphite structure and the surface films.

2.2.1.1 Surface Film Formation: Solid Electrolyte Interphase

As the graphite anodes of lithium-ion cells are operated beyond the thermodynamic stability of the organic electrolytes, decomposition reactions occur along with lithium intercalation. These reactions include the reduction of the electrolyte solvent and the decomposition of the conducting salt. The resulting reduction products form passivating films at the surface of the anode active material, the so-called solid electrolyte interphase (SEI). [18,19]

The composition and structure of the SEI depends largely on the active material, the solvent, conducting salt, and additives used in the electrolyte, and the formation process [20–23]. Typical reaction products of the decomposition of carbonate-based electrolytes (e.g., EC, EMC, DMC) with $LiPF_6$ as conducting salt are Li_2CO_3, $ROCO_2Li$, $(CH_2OCO_2Li)_2$, and LiF [19,24–26]. The SEI is often described with a bilayer structure: A dense inner layer, containing inorganic salts, and a soft outer layer, mainly based on organic reaction products [26–28].

An ideal SEI has a low electrical conductivity and is permeable for lithium ions, but impermeable for other electrolyte components [17,29]. Thus, the SEI inhibits further electrolyte decomposition and anode degradation [17,26]. Moreover, an ideal SEI has a uniform morphology and chemical composition to ensure homogeneous current distribution [18]. The formation and growth of the SEI consume cyclable lithium which leads to an irreversible capacity fade, particularly during the initial charging of the cell and the first few cycles [18,30]. On a long time scale, the SEI penetrates into the pores of the electrode and in addition may also penetrate into the pores of the separator, which

may result in a decrease of the accessible active surface area of the electrode [17]. This reduces the capacity and increases the internal resistances of the battery cell.

The growth of the SEI can also be affected by aging reactions at the cathode; the corresponding mechanism of transition metal dissolution will be described in the section on cathode active material degradation.

2.2.1.2 Lithium Plating

When charging a lithium-ion battery, lithium plating can take place. Lithium plating describes the reduction of lithium ions, which are dissolved in the electrolyte, to metal lithium at the surface of the anode active material. This reaction takes place instead of the regular intercalation of lithium into the lattice structure of the active material [31]. It can originate from limitations in charge transfer or lithium solid diffusion [32,33]. Lithium plating can occur when the anode potential drops below the standard potential of Li/Li^+ [32]. Some of the plated lithium later reacts irreversibly with the electrolyte and forms insoluble side products [34,35]. This leads to a growth of the anode surface films, which can also be detected by an increasing thickness of the cell [36,37]. The side products can also fill pores of the active material and the separator and insulate certain electrode regions [38]. Excessive lithium plating can be identified by a specific plateau in the cell voltage at higher SoCs, as illustrated in Figure 4. This plateau can be observed after the charging process and it disappears again during a subsequent rest period [39–41] or when the battery is discharged [42]. Small amounts of lithium plating can be detected through calorimetry or high accuracy measurements of the coulombic efficiency [43,44].

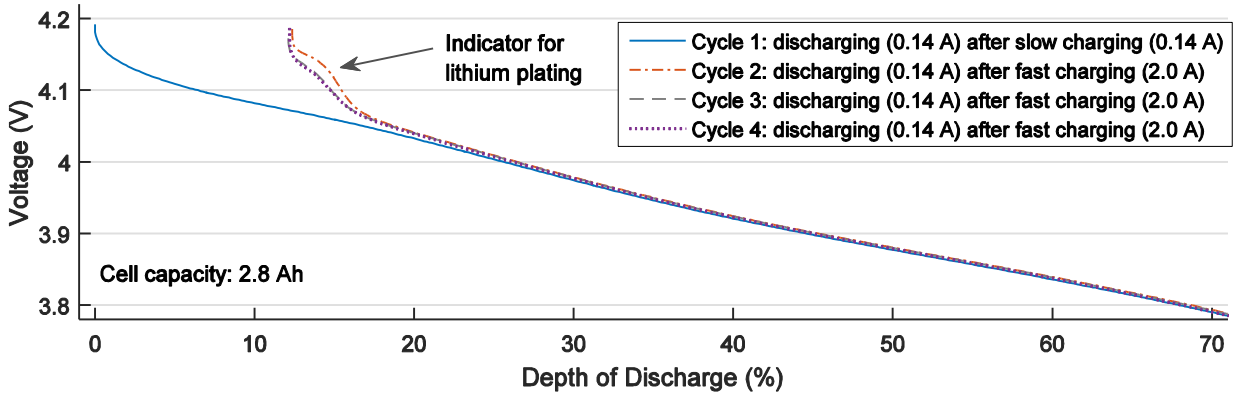

Figure 4. Cell voltage of four low-current discharging sequences at 10°C of a high-energy NCA lithium-ion cell with a capacity of 2.8 Ah after charging with low and high charging currents

Although plated lithium dissipates during rest periods after the charging sequence and leads to an intercalation into the anode active material [45], parts of the deposited lithium react with the electrolyte. The reaction of deposited metal lithium with the electrolyte consumes cyclable lithium and, thus, reduces the cell's capacity [46]. Graphite anodes are very prone to lithium plating due to their low equilibrium potential, particularly at a high state of charge (SoC) [47]. As a general trend, lithium plating increases with higher SoC, higher charging current, and reduced temperature [32,48]. Furthermore, thicker electrodes with larger particles and a lower porosity are more prone to lithium plating than thinner electrodes with smaller particles and a higher porosity [34,49]. High-energy cells are particularly susceptible to lithium plating and can exhibit lithium plating already at

25°C and charging rates of only 0.5 C [50]. As shown by Schuster et al. [51], aged cells can become more susceptible to lithium plating. Overall, metallic lithium plating can be considered as a parasitic side reaction during charging, which leads to a consumption of cyclable lithium and thus reduces the capacity [17].

2.2.1.3 Mechanical Stress

The intercalation and deintercalation of lithium ions into graphite leads to volume changes in the active material. The distance between parallel graphene layers expands by up to 10% during intercalation [52]. The changes in the thickness of graphite battery electrodes typically amount to about 5% throughout the cycling process, as the anodes are not fully utilized [53,54]. The volume changes can cause cracks in the SEI, weaken particle-to-particle contacts, and lead to structural damage of the graphite anode material owing to a breakage of C-C bonds. These effects are described in the following paragraphs.

It is widely believed that the graphite expansion and contraction during cycling results in cracks in the SEI, particularly for cycling at higher rates; At the cracks, bare active material comes newly in contact with the electrolyte and new SEI is formed [55–60]. This intensified SEI growth causes an increased consumption of cyclable lithium.

For graphite anodes cycled at a low lithium content of less than 10%, the relative volume changes are largest and, thus, the stress onto the graphite structure is more severe than in regions of higher degrees of lithiation, where the relative volume changes are considerably lower [61]. The local stress at the edges of the graphene layers is supposed to cause a breakage of C-C bonds [61]. Further structural degradation is ascribed to graphite exfoliation owing to solvent co-intercalation [59,62]. All this leads to a loss of active material, resulting in a capacity fade.

In addition to cracks in the SEI and structural damage, the volume changes throughout charge-discharge cycling can weaken the electrical contact between the particles of the active material and can also cause a delamination from the current collector [60,63]. This increases the internal resistances of the cells.

2.2.2 Cathode Active Material

The degradation of the cathode active material is driven by structural changes during cycling, dissolution reactions, and surface film formation [64]. In this section, the degradation mechanisms are presented with special focus on NCA, as the lithium-ion cells examined in this thesis contained NCA cathodes.

2.2.2.1 Structural Changes and Mechanical Degradation

Structural changes and phase transitions occurring with the electrochemical delithiation and lithiation of the cathode active material are origins of irreversible capacity fade [65]. Structural disordering in lithium nickel oxides, where nickel atoms occupy sites of delithiated lithium layers, can be reduced by a certain substitution of nickel by cobalt and by a doping with aluminum [66]. The most commonly used composition for NCA cathodes is $LiNi_{0.8}Co_{0.15}Al_{0.05}O_2$ [12]. Although this material composition provides substantial improvements in the structural stability, there is still a

certain cubic rock-salt layer emerging at the particle surface, which is several nanometers thick and has a low lithium-ion conductivity [67]. The formation of this sub-surface rock-salt layer is accompanied by oxygen release and electrolyte oxidation, which contributes to an increasing cathode impedance [68]. Furthermore, a high degree of delithiation of NCA cathodes can cause irreversible phase transitions. Above ca. 55–60% delithiation, depending on the composition of the NCA active material, an irreversible distortion of the lattice structure occurs, which leads to an irreversible capacity fade [69,70]. Hence, an overcharging of the cells has to be avoided.

At high and low SoC of the lithium-ion cells, volumetric changes of the cathode occur during intercalation and deintercalation of lithium into the NCA particles, which cause mechanical stress for the active material [69,70]. The resulting mechanical degradation of the active material structure, which is typically accompanied by a substantial impedance increase, was identified as a dominant degradation mechanism in several aging studies. Increasing microcracks and smaller, fragmented NCA particles were observed after cycling [69,71,72]. The impedance increase of aged NCA cathodes appeared to be strongly affected by the contact loss between the NCA particles and the conductive matrix [73]. Thick electrodes of high-energy lithium-ion cells were shown to be more sensitive to mechanical stress and exhibited faster degradation than thin electrodes [74]. Typically, the impedance increase of aged graphite/NCA lithium-ion cells origins mainly from the cathode [38,75,76].

2.2.2.2 Transition Metal Dissolution

Cathode active materials of lithium-ion cells often suffer from a dissolution of transition metals, such as manganese, cobalt, and nickel, which occurs particularly at high cathode potentials and aggravates with higher temperature [6,77–79]. Transition metal dissolution occurs most pronouncedly for manganese spinel cathode materials [80,81].

The dissolved metal ions migrate to the anode, where they aggravate the SEI growth, which consumes cyclable lithium and leads to a capacity fade [82,83]. Although NCA electrodes are less prone to transition metal dissolution than manganese-based cathodes, a certain amount of nickel and cobalt can still be found incorporated into the SEI of aged anodes of lithium-ion cells with graphite anodes and NCA cathodes [67,71].

2.2.2.3 Surface Film Formation: Solid Permeable Interface

Electrolyte decomposition and the formation of surface films at the electrode/electrolyte interface occurs not only at the anode but also at the cathode of a lithium-ion cell. Several studies reported surface films on the cathodes of aged lithium-ion cells [75,84–86]. The surface film at the cathode is often referred to as solid permeable interface (SPI) [87]. The SPI of NCA cathodes is composed of organic species from electrolyte solvent oxidation and inorganic species from conductive salt decomposition [88]. As described above, oxygen is released when NCA lattice structures transform into rock-salt type. This aggravates oxidation reactions and leads to a growth of the SPI [17,89]. The composition of the SPI exhibits similarities to the outermost layer of the SEI [24]. Yet, Abraham et al. [89] demonstrated that the SPI is created by reactions at the cathode and is no result of SEI components migrating from the anode to the cathode.

2.2.3 Electrolyte

As presented above, the electrolyte is involved in decomposition reactions leading to surface film formation at both electrodes. Day et al. [90] demonstrated by differential thermal analysis that a considerable amount of conductive salt is decomposed during cycling operation. As the concentration of the conductive salt determines the ionic conductivity between both electrodes, the decomposition reactions affect the ohmic resistance of the lithium-ion cell [91,92].

The electrolyte reduction at the anode consumes cyclable lithium and leads to a capacity fade [56,93]. By contrast, the electrolyte oxidation at the cathode does not consume cyclable lithium and lead to a capacity fade; instead, it causes a reintercalation of lithium into the cathode, which represents a reversible self-discharge [94,95].

Both types of electrolyte decomposition can be accompanied by a release of gaseous reaction products and increase the internal cell pressure [96,97]. Furthermore, the ongoing electrolyte decomposition can result in a local drying out of the lithium-ion cell [98,99], which leads to inhomogeneous current distribution and a further acceleration of the degradation [100].

2.2.4 Separator

Although the porous separator of a lithium-ion cell is electrochemically inactive, it can affect the performance of the lithium-ion cell considerably. Aging studies revealed that deposits from electrolyte decomposition clog pores of the separator, which leads to an increasing ionic impedance and may also result in a decrease of the accessible active surface area of the electrodes [17,86]. Furthermore, mechanical stress can alter the porosity and tortuosity of the separator. Mechanical compression and viscoelastic creep may lead to pore closure, which in turn reduces the ionic pathway and results in an increased high-frequency resistance [101,102].

Pore clogging can lead to an inhomogeneous current distribution, as pore closure acts as an “electrochemical concentrator”, creating locally high currents and overpotentials in the adjacent electrode areas, which increase the risk of lithium plating [46,103]. A direct impact of compression on lithium plating was also reported by Bach et al. [104], where local lithium plating was observed together with a local damage of the separator.

2.2.5 Current collectors

There are two main degradation mechanisms related to the current collectors of a lithium-ion cell. On the one hand, the current collectors can corrode electrochemically. This occurs particularly at the aluminum current collector of the positive electrode when acidic species, such as HF, are present and lead to an increasing contact resistance between the current collector foil and the cathode active material [65,105]. The copper current collector of the negative electrode can dissolve under overdischarge conditions when the anode potential rises to 1.5 V vs. Li/Li^+ [65].

On the other hand, mechanical stress can deform the current collector foils. Particularly for high-current cycling of cells with wound electrodes, the volume changes of the active materials due to the intercalation and deintercalation of lithium cause high and inhomogeneous mechanical stress that can lead to a local deformation of the jelly roll [106]. This can weaken the contact between the

electrodes and the separator so that certain regions can no longer contribute to the cell's capacity [106,107].

2.3 Calendar Aging and Cycle Aging

In addition to the classification of aging mechanisms by cell components, two categories of aging conditions are usually employed to classify aging reaction in lithium-ion batteries: Aging under nonoperating conditions, which is typically referred to as calendar aging, and cycle aging under charging and discharging operation [9]. While cycle aging generally comprises the aging mechanisms that damage the materials reversibility, calendar aging results mainly from interactions between the active materials and the electrolyte [108].

Calendar aging is strongly linked to electrolyte reduction and oxidation and the growth of surface films on the active materials. It strongly depends on time, SoC, and temperature [109]. Cycle aging comprises also the mechanisms of structural and mechanical changes in the battery components. It is substantially more complex than calendar aging and depends also on a variety of additional parameters, such as charging and discharging currents, cycle depth, and charge throughput [110,111].

Usually, calendar aging and cycle aging are considered as additive [108]. In practical aging studies where the cells are cycled continuously, it is not possible to measure the individual contributions of cycle and calendar aging, as calendar aging also occurs during the periods of charge-discharge cycling. Typically, the concept of superposition is applied which assumes that calendar and cycle aging add linearly [111,112].

2.4 End of Life

The EoL of a battery is reached when the energy content or the power capability is no longer sufficient for the particular application. For battery aging studies, standardized EoL criteria would be beneficial. However, standards on "test specifications for lithium-ion traction battery packs and systems of electrically propelled road vehicles" (ISO 12405-1, ISO 12405-2) do not include EoL criteria. The standard on the "performance testing of secondary lithium-ion cells for the propulsion of electric road vehicles" (IEC 62660-1) also contains no EoL criteria. This is particularly demonstrative, as there is a similar standard for "performance and endurance tests of secondary batteries **(except lithium)** for the propulsion of electric road vehicles" (IEC 61982) which defines the EoL as 80% of the nominal capacity. The "USABC Electric Vehicle Battery Test Procedures Manual" [113] from 1996 defined two EoL criteria: the net delivered capacity is less than 80% of the rated capacity or the peak power capability is less than 80% of the rated power at a depth of discharge of 80%. However, these criteria had not been incorporated into binding standards yet.

Overall, it appears to be difficult or unwanted to define standardized EoL criteria. This might result from divergent requirements on the performance at the EoL of the battery, which can vary substantially among different vehicles and user needs. For EVs with large and small battery systems, a loss of 20% in capacity is supposed to have a different impact on the usability of the vehicle: For an EV with a larger battery system, more capacity fade and, thus, a higher loss of driving range might

be tolerable than for an EV with a small battery system, until the EV is no longer able to provide the driving range required by the customer.

In many publications, the EoL for the lithium-ion traction battery of an EV is assumed as a remaining capacity of less than 70%–80% [114–118]. In this thesis, a capacity fade of more than 20% is considered as the EoL. Yet, cycling procedures were not automatically stopped when a capacity fade of 20% was reached so that the cells were often cycled beyond this point.

2.5 Limitations of Aging Studies Presented in the Literature

In general, the aging studies of lithium-ion batteries published in the literature investigated individual electrochemical effects with only a small set of parameters varied. As the lithium-ion cells differ among the many aging studies, no direct comparison of the results is possible. Furthermore, the test conditions and methods for degradation monitoring vary substantially. To obtain comparable results for different operating conditions with different predominant degradation mechanisms, aging studies performed with the same type of lithium-ion cell, identical test conditions, and similar methods for degradation monitoring are required.

The operating conditions of an EV battery can be categorized into the following three operating states: nonoperating, charging, and driving. In all three states, the aging behavior differs substantially. As the aging studies presented in the literature usually did not examine dynamic load profiles like they occur when operating an EV, explicit aging studies related to the different operating conditions of an EV battery are necessary to obtain a thorough understanding of the aging of lithium-ion batteries in EVs.

To overcome the above-mentioned limitations, experimental aging studies on nonoperating periods, charging protocols, and driving operation are presented in this thesis, which were conducted with the same type of lithium-ion cell, under comparable test conditions, and with similar methods for degradation monitoring. The methods and results are presented in the following chapters.

3 Analysis Techniques Used for Degradation Monitoring

All experimental aging studies presented in this thesis followed an identical base structure. At first, the cells underwent an initial characterization. Then, the cells were aged under the respective operating conditions. In periodic intervals, checkup measurements under identical environmental conditions were performed to monitor the degradation of the cells. The checkup procedures contained various sequences of electrical characterization for noninvasive and nondestructive analysis of battery degradation.

The core objective of the experimental aging studies was to identify the predominant aging mechanisms for the different operating conditions of an EV battery. To achieve this, appropriate methods for degradation monitoring were required. Capacity measurements, Electrochemical Impedance Spectroscopy (EIS), and current step response analysis represent commonly used techniques for degradation monitoring, which were also applied in this thesis.

In addition to the above-mentioned standard techniques, Differential Voltage Analysis (DVA) and coulometry were used. DVA enables the separation of aging contributions from anode degradation, cathode degradation, and shifts in the electrode balancing without opening the cells and performing post-mortem analyses. Moreover, a new coulometry technique is presented in this section which enables the identification of anodic and cathodic side reactions in calendar aging studies.

As a detailed knowledge of the different techniques is required for an optimal application and for the correct interpretation of the results, the fundamentals of the various techniques are introduced and discussed in detail in this section. The explicit implementation of each analysis technique is then described in the respective chapter of each study.

Before presenting the different analysis techniques, a general section provides basic information on the experimental work, which is of relevance for all subsequent chapters presenting the aging studies and their results.

3.1 Basic Information on the Experimental Work

This section introduces the lithium-ion cells examined in this thesis and the technical equipment used. Moreover, it provides some general definitions and considerations.

3.1.1 Lithium-Ion Cells Examined

In the experimental calendar and cycle aging studies presented in this thesis, commercial 18650 cells from a well-established manufacturer with mature production processes were examined. Stable production processes were expected to guarantee reliable results without considerable variation from production. High-energy lithium-ion cells of type Panasonic NCR18650PD with an NCA cathode and a graphite anode were examined in this thesis. Table 1 lists characteristic properties of this cell type. The cells had a capacity of ca. 2.8 Ah and an opening of the cells disclosed the lengths and widths of the coated electrode areas. This helped to estimate the areal capacity of

3.65 mAh/cm² which was necessary to obtain comparable current densities for measurements with coin cells fabricated from the electrode materials of the commercial 18650 cells.

For the NCR18650PD cells, the manufacturer stated a high specific energy of 220 Wh/kg, a high energy density of 570 Wh/l, and a low internal resistance of about 20 mΩ [119]. A capacity utilization above 95% at an elevated discharging current of 10 A and a good discharging performance at low temperature, even below 0°C, also qualify these cells for EV applications [119]. Moreover, the cells exhibit similarities to those cells used in the Tesla Model S, which confirms the practical relevance of selecting this cell type for investigating the aging behavior of lithium-ion batteries in EVs.

Table 1. Characteristic properties of the lithium-ion cells examined in this thesis

Manufacturer		Panasonic
Type		NCR18650PD
Nominal capacity (datasheet values)		Minimum: 2.75 Ah, typical: 2.9 Ah
Nominal capacity (C_N used in this thesis)		2.8 Ah
Maximum voltage (V_{max})		4.2 V
Nominal voltage (V_N)		3.6 V
Minimum voltage (V_{min})		2.5 V
Highest charging current presented in datasheet		1.375 A
Highest discharging current presented in datasheet		10 A
Weight		45 g
Anode material		Graphite
Cathode material		$LiNiCoAlO_2$ (NCA)
Coated cathode area	inner side of electrode	667 mm x 57.5 mm = 383.5 cm²
	outer side of electrode	667 mm x 57.5 mm = 383.5 cm²
	total (A_c)	767 cm²
Coated anode area	inner side of electrode	715 mm x 58 mm = 414.7 cm²
	outer side of electrode	661 mm x 58 mm = 383.4 cm²
	total (A_a)	798 cm²
Areal capacity* (C_N/A_c)		3.65 mAh cm^{-2}

*related to the coated cathode area, as it is slightly smaller than the anode area

In the aging studies, more than 250 cells were examined and tested with different load profiles under different operating conditions. The cells were all of the same type but stemmed from two different production lots. The cells from the first lot were used in the first calendar aging study and in the cycle aging study on driving operation; the cells from the second lot, produced about six months later, were used in the second calendar aging study and in the cycle aging study on charging protocols.

To facilitate cycle life testing, most of the cells were equipped with standardized 4-pole luster terminals. As shown in Figure 5, strips of Hilumin (nickel-plated steel) were used for the contacting of the cells, onto which power and sense leads from the luster terminal were soldered before the strips were spot-welded onto the poles of the cell. Figure 5a shows the uncontacted cell and Figure 5b exhibits the contacting version of the first lot of cells. In this first contacting version, the power and sense leads were located at the same end of a ca. 3 cm long Hilumin strip. Figure 5c exhibits an optimized contacting version, where the power and sense leads were located at opposite ends of a substantially shorter Hilumin strip. This reduced the voltage drop measured by the sense lead since

the path from the tip of the sense lead to the welding spots was no longer within the path of the current flow from the power lead to the welding spots. Thus, additional resistance contributions from the Hilumin strip were minimized. This optimized contacting was used for the cells of the second lot which were tested in the cycle aging study on charging protocols. The other cells from the second lot, tested in the second calendar aging study, remained uncontacted. For the measurements, these cells were placed in cell holders with spring loaded contact probes for power and sense at each end. Differences in the ohmic resistances owing to the contacting methods were revealed by the initial characterization measurements and will be presented in Section 3.2.

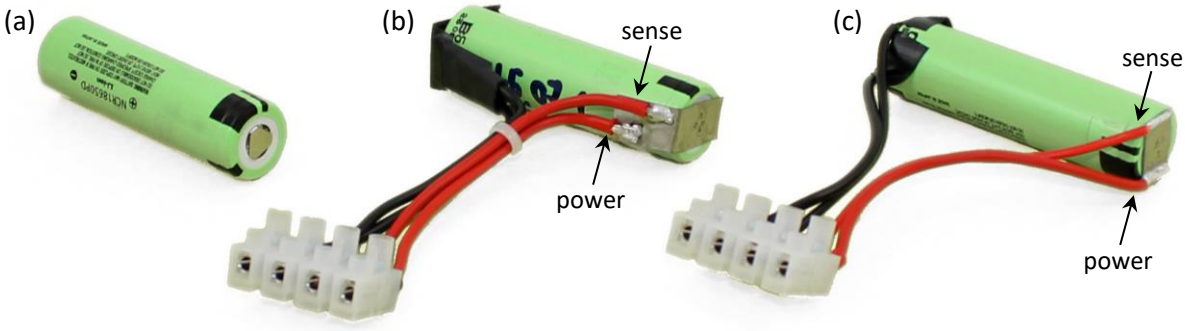

Figure 5. Contacting of the cells with Hilumin strips spot-welded onto the poles and 4-pole luster terminals. (a) Uncontacted cell, (b) cell from the first lot, where power and sense leads were soldered onto the same end of a Hilumin strip; and (c) cell from the second lot with optimized contacting, where power and sense leads were located at opposite ends of the Hilumin strip.

The general dependence of the cell performance on amperage and temperature is illustrated in Figure 6. Figure 6a shows the discharging behavior of the cells for different discharging currents, obtained from own measurements. When discharging with 5 A, the available capacity is ca. 7% lower than for discharging with a low current of 0.25 A. As illustrated in Figure 6b, the performance of the cells depends strongly on temperature. With lower temperatures, the voltage drop owing to the internal resistances increases and the available capacity diminishes. The temperature dependence is also a critical issue for degradation monitoring, as varying measurement temperatures lead to fluctuations in the capacity and resistance measurements. To avoid such distortions, all checkup measurements were performed in thermal chambers at 25°C.

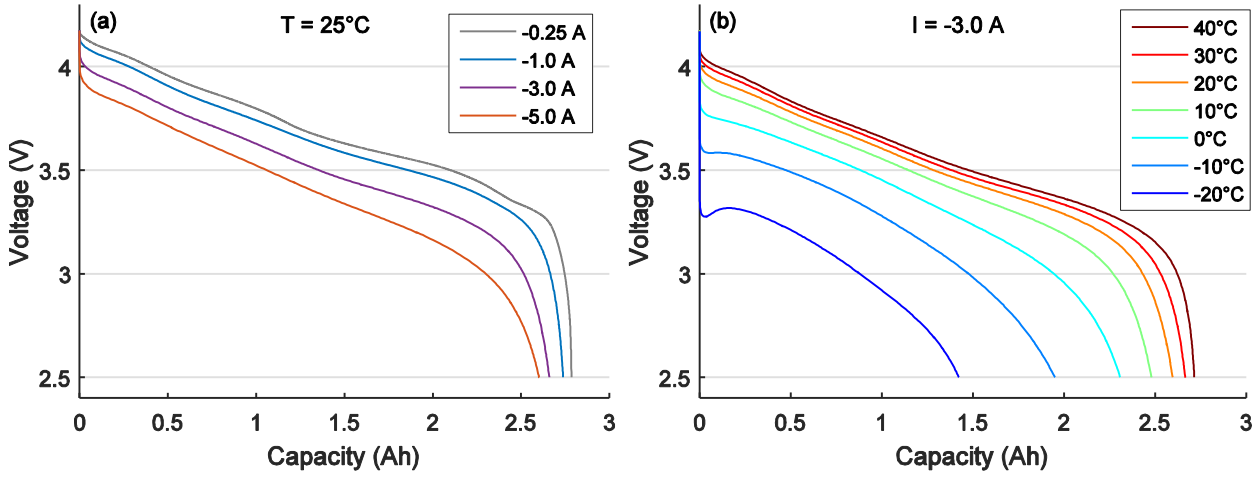

Figure 6. (a) Discharging curves for different currents at the same temperature of 25°C and (b) discharging curves for –3 A at various temperatures

3.1.2 Technical Equipment Used

For the initial characterization of the cells, a Hioki BT3562 tester was used to determine the 1 kHz AC resistance. The subsequent experiments were conducted with BaSyTec CTS battery test systems, which provided multiple independent 5 V/±5 A test channels. For EIS measurements, a Gamry G750 galvanostat/potentiostat was used. The EIS measurements were performed in galvanostatic mode without DC offset (I_{dc} = 0 A) and the cells were typically tested at 50% SoC. In the control software of the galvanostat, the excitation current is always defined as the root mean square (RMS) value and not as the amplitude of the sinusoidal current signal. Hence, all excitation current values presented in this thesis represent $I_{ac,rms}$ values. The examined frequency interval ranged from 10 kHz to 10 mHz. As the measurement duration is mainly determined by the low test frequencies, the frequency points per decade and their repetitions were reduced with increasing frequencies. The explicit frequency and repetition values are listed in Table A-1 in the appendix. The total duration of one EIS measurement was ca. 10 min. In the second calendar aging study, a multiplexer was available, which allowed automatized EIS measurements without a manual disconnection and reconnection of the cells.

As the behavior of lithium-ion batteries is highly temperature-dependent, all measurements were performed in thermal chambers. Several self-built chambers were used, which provided different constant temperatures. These chambers contained resistive heaters, Peltier coolers, and Wachendorff UR3274U5 PID temperature controllers with a PT100 temperature sensor. The temperature calibration of these chambers was performed with a Fluke 1524 reference thermometer and a Fluke 5622-05 PT100 probe. These thermal chambers were able to reduce temperature variations to less than 0.2°C and they were used for measurements at 25°C, 40°C, and 55°C. There were also two thermal chambers with simple on-off controllers for temperatures of 10°C and 60°C which exhibited larger temperatures variations of 1–2°C. For tests with dynamic temperature changes, a Vötsch VT4021 climate chamber was used.

3.1.3 General Definitions and Considerations

For a reproduction of the experimental aging studies and for a correct interpretation of the results, the following definitions and considerations have to be regarded.

Conventions for the Current Flow

In the entire thesis, the current flow is defined in such a way that discharging always represents the direction of the current flow that occurs when both poles of a cell are interconnected by an ohmic resistor. This definition is particularly important when comparing half-cells and full-cells, as differences between the current flow and the flow of the lithium-ions arise. This means that in the half-cells, graphite or NCA is delithiated during charging and lithiated during discharging. In the full-cell, NCA is delithiated during charging whereas graphite is lithiated; and vice versa during discharging. Thus, the direction is opposed for graphite in the full-cell.

The sign of current values is defined so that charging currents are represented by positive values discharging currents are represented by negative values. Analogously, positive or negative ampere-hour values express charged or discharged amounts of charge, respectively.

Absolute Current Values instead of C-Rates

For all checkup and diagnosis routines, the charging and discharging currents were specified as absolute ampere-values. As explained in Refs. [120] and [121], identical absolute current values lead to a better comparability than identical C-rates when testing cells of identical volume.

When comparing different cell types, the objective is to obtain similar current densities. Typically, the coated electrode areas of high-power 18650 cells with about 1 Ah capacity and high-energy 18650 cells with about 3 Ah capacity differ far less than their capacities. The differences in capacity origin mainly from a different thickness and porosity of the active material coatings. Thus, identical absolute ampere-values lead to more homogeneous current densities than identical C-rates for cells of identical volume but different capacity [120]. Furthermore, in practical applications using cells of a specific form factor, such as the cylindrical 18650 format or the prismatic and pouch formats presented in the DIN/VDA SPEC 91252, the number of cells in the battery system is often predetermined by the construction space available. Consequently, the load per cell is also predefined and, thus, independent from the explicit capacity value [121].

As many cell types of format 18650 – which have virtually the same volume – were investigated at the Institute for Electrical Energy Storage Technology at the Technical University of Munich (TUM), the aging studies presented in this thesis also used test protocols based on absolute current values.

Equivalent Full Cycles

As cycle aging often exhibits a strong dependency on the charge throughput, equivalent full cycles (EFC) are used for a better comparability of cells cycled with different cycle depths. To compute EFC, the charge throughput is divided by the nominal capacity C_N of the cells, which is 2.8 Ah for the cells examined in this thesis. For the computation of the charge throughput Q, the combination of 1 Ah charged and 1 Ah discharged is counted as a charge throughput of 1 Ah. This is represented by the following equation for the integration of the battery current I to compute Q:

$$Q = 0.5 \cdot \int_{t_{\mathrm{start}}}^{t_{\mathrm{end}}} |I| \, dt \tag{1}$$

Resistance Definitions

To distinguish between results from impedance measurements in frequency domain and cell resistance measurements in time domain, $R_{\mathrm{ac,f}}$ and $R_{\mathrm{dc},\tau}$ were defined respectively. $R_{\mathrm{ac,f}}$ represents a resistance value derived from a frequency domain measurement at a specific frequency f. It is defined as the real part of the impedance at the frequency f. With this definition, the $R_{\mathrm{ac,1kHz}}$ values measured by the Hioki BT3562 tester and by the Gamry G750 potentiostat/galvanostat are in excellent agreement. For measurements in time domain, the resistance $R_{\mathrm{dc},\tau}$ is derived from the voltage response corresponding to a current step, which is evaluated for the pulse duration τ. $R_{\mathrm{dc,10s}}$ is the resistance value obtained for a pulse duration of 10 s.

3.2 Constant Current Constant Voltage Capacity Measurement

The actual capacity of a battery cell is the most prominent value to evaluate the aging progress. It is usually determined by discharging a fully charged cell with a constant current (CC) until the minimum voltage is reached. However, reaching the minimum voltage level does not mean that the cell is completely discharged. Typically, concentration gradients inside the cells equilibrate and the cell voltage rises again after a certain pause; another short discharge period becomes possible [122]. This effect occurs more pronouncedly for higher discharging currents. Thus, a low discharging current has to be used to determine the maximum storage capability of a cell. To circumvent unnecessarily long measurement durations, a constant current constant voltage (CCCV) discharging procedure can be used. This combines a CC discharging sequence and a constant voltage (CV) sequence at the minimum voltage level until the amperage of the discharging current drops below a predefined cut-off threshold. As the capacity measurements are sensitive to temperature, all capacity measurements were performed in thermal chambers at 25°C to obtain comparable results.

Figure 7a shows a capacity histogram for the 105 cells of the first production lot and Figure 7b shows a capacity histogram for the 175 cells from the second production lot. The capacity values result from initial characterization tests, where the cells were CCCV charged and then discharged with a CCCV procedure to determine the actual capacities of the cells. After that, the cells were charged again to the initial SoC, which was ca. 30% at the delivery of the cells. The explicit test procedures and the respective parameters for both lots of cells can be found in the appendix (see Table A-2 and Table A-3). The mean capacity values for both lots cannot be directly compared since the two initial characterization procedures had different parameter values for the discharging voltage and for the cut-off currents of the CV phases. For the first lot, the absolute cut-off currents for CCCV charging and discharging were higher and the cells were only discharged to 2.75 V. This led to lower capacity values than for the second lot.

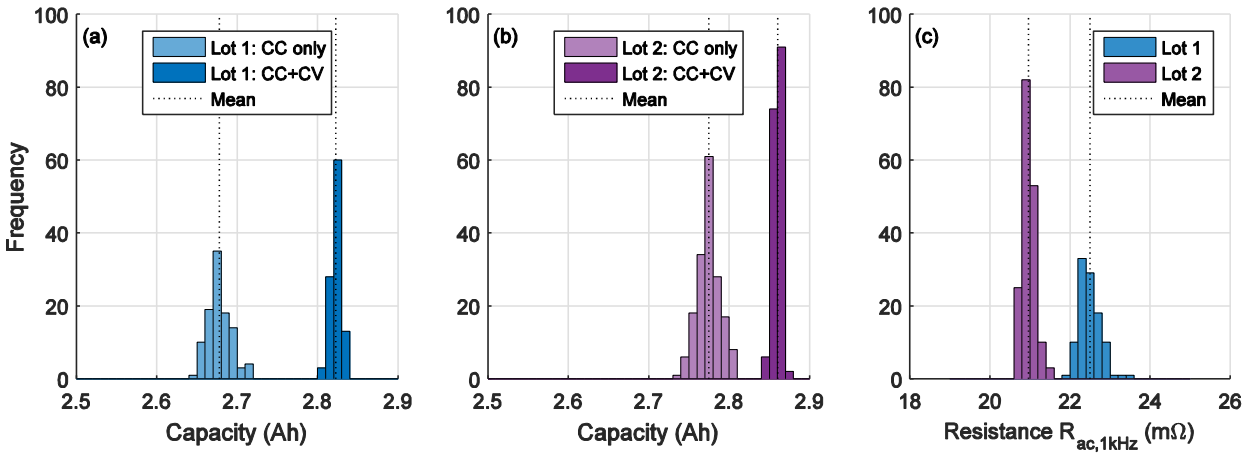

Figure 7: (a,b) Histograms of cell capacities and (c) histograms of internal resistances obtained from the initial characterization tests of the two lots of lithium-ion cells examined in this thesis. The width of each bin is 0.01 Ah for the capacity histograms and 0.1 mΩ for the resistance histogram. The differences in the mean value of the capacity and resistance between both lots were caused by variations in the parameters of the checkup procedures and by different ways of contacting the cells, respectively.

Although the mean values of the capacity measurements are not directly comparable, Figure 7a and Figure 7b demonstrate for both lots that the capacity values exhibit substantially lower variations

for CCCV discharging compared to sole CC discharging. This is also confirmed by Table 2, which lists the mean values μ and the standard deviations σ for the capacity and resistance measurements of the initial cell characterization. A normal distribution is characteristic for new cells [123,124]. The standard deviation decreases for both lots from 14 mAh for the CC measurements to 5–6 mAh for the CCCV measurements, which corresponds to a decrease from 0.5% C_N to ca. 0.2% C_N. These standard deviations are notably lower than those of other lithium-ion cells presented in the literature, which ranged between 0.8% C_N and 1.9% C_N for new cells [123–125]. This confirms the mature production processes of the cell type examined in this thesis which provide minimal cell-to-cell variation.

Before these initial capacity measurements, the cells were connected to a Hioki BT3562 battery tester to determine the $R_{ac,1kHz}$ resistance. Figure 7c shows the resistances measured for both lots of cells. The higher cell resistances measured for the first lot can be ascribed to a different contacting method. All cells from the second lot performed the initial resistance measurements in uncontacted state in a four-probe spring-contact-based fixture. The cells of the first lot were equipped with the contacting version presented in Figure 5b, where the voltage drops over a considerable section of the Hilumin strips were also part of the voltage measurement. The resistance increase of ca. 1.6–1.8 mΩ was mainly caused by the ohmic resistance of Hilumin as the contact resistance of a spot-welding connection of Hilumin typically lies below 0.2 mΩ [126].

The lower standard deviations for CCCV discharging demonstrate that an additional CV phase can compensate variations in the CC discharging time span resulting from resistance variations or small temperature variations due to an inhomogeneous, turbulent air flow in the thermal chamber which leads to an inhomogeneous convection and thus an uneven warming up of the cells. Overall, the CCCV discharging procedure provides a very robust and reliable identification of the actual capacity of the cells. Therefore, it was used in all aging studies presented in this thesis.

Table 2. Mean values μ and standard deviations σ of the capacity measurements performed with CC or CCCV discharging and of the $R_{ac,1kHz}$ resistance measurements

	Capacity Measurement CC			Capacity Measurement CCCV			Resistance Measurement 1 kHz		
	μ_{CC}	σ_{CC}	σ_{CC}/μ_{CC}	μ_{CCCV}	σ_{CCCV}	σ_{CCCV}/μ_{CCCV}	μ_R	σ_R	σ_R/μ_R
Lot 1	2.678 Ah	0.014 Ah	0.0052	2.823 Ah	0.006 Ah	0.0021	22.5 mΩ	0.3 mΩ	0.013
Lot 2	2.775 Ah	0.014 Ah	0.0050	2.860 Ah	0.005 Ah	0.0017	21.0 mΩ	0.2 mΩ	0.010

3.3 Electrochemical Impedance Spectroscopy

The internal resistances of a lithium-ion battery have a substantial impact on the power capabilities of the battery. When the resistances rise, the power capability decreases. Moreover, the maximum and minimum voltage limitations are reached earlier during CC charging or discharging, which can reduce the available capacity for a specific application notably.

3.3.1 Fundamentals

EIS is an established and frequently used technique to determine the dynamic behavior of electrochemical systems [127,128]. From a periodic excitation, the complex impedance is derived, which describes the transfer function of the examined system in a system-theoretical manner and contains information about the amplitude ratio and phase shift between the voltage and the current signal for a specific frequency. For sinusoidal current and voltage signals, *i(t)* and *u(t)*, of a specific frequency *f* and with the amplitudes $\hat{I}$ and $\hat{V}$, the complex impedance *Z(f)* computes as follows:

$$i(t) = \hat{I} \cdot e^{j(\omega t+\varphi_\mathrm{i})} = \hat{I} \cdot e^{j(2\pi f t+\varphi_\mathrm{i})} \tag{2}$$

$$v(t) = \hat{V} \cdot e^{j(\omega t+\varphi_\mathrm{v})} = \hat{V} \cdot e^{j(2\pi f t+\varphi_\mathrm{v})} \tag{3}$$

$$Z(f) = \frac{v(f)}{i(f)} = \frac{\hat{V} \cdot e^{j(2\pi f t+\varphi_\mathrm{v})}}{\hat{I} \cdot e^{j(2\pi f t+\varphi_\mathrm{i})}} = |Z(f)| \cdot e^{j\varphi} \text{ with } |Z(f)| = \frac{\hat{V}}{\hat{I}} \text{ and } \varphi = \varphi_\mathrm{v} - \varphi_\mathrm{i} \tag{4}$$

$|Z(f)|$ provides the information about the amplitude ratio and φ about the phase shift. EIS measurements can be performed with either a voltage excitation or a current excitation. According to the excitation mode, the measurements are named potentiostatic or galvanostatic, respectively. A combination of both modes is performed in pseudo-posentiostatic EIS measurements, where the measurement itself is performed galvanostatically but the amplitude of the excitation current is constantly adjusted to obtain a constant voltage amplitude for all frequencies examined. For batteries cells, the measurements are typically performed galvanostatically or pseudo-potentiostatically since the batteries are voltage sources themselves and since galvanostatic EIS measurements prevent SoC drifts as the same charge quantity is transported in positive and negative direction within one period. [129,130]

3.3.2 Interpreting Impedance Spectra

In an EIS measurement, the complex impedance is determined for a wide frequency range to obtain a characteristic impedance spectrum. Typical excitation frequencies for batteries range from the kilohertz region down to the millihertz region [131,132]. In this thesis, the examined frequency interval ranged from 10 kHz to 10 mHz. From the resulting impedance behavior, different physical and electrochemical properties of a battery cell can be identified and characterized. Figure 8 shows an exemplary EIS spectrum of the cell type examined in this thesis. In this Nyquist plot, characteristic points and sections are highlighted, which will be described in the following paragraphs.

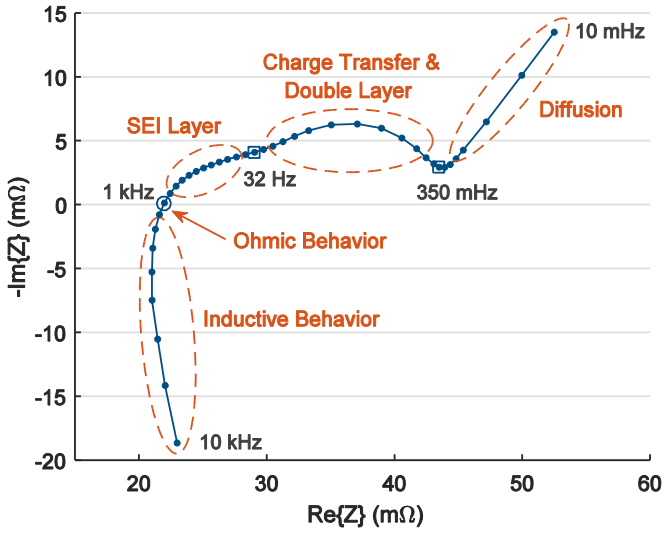

Figure 8. Impedance spectrum of the examined Panasonic 18650 lithium-ion cell at 50% SoC and 25°C with characteristic points and sections highlighted

3.3.2.1 Ohmic Behavior

A characteristic point in the impedance spectrum is where the imaginary part of the impedance becomes zero. For the excitation frequency corresponding to this point, the cell exhibits purely ohmic behavior. This means that the phase shifts from inductive and capacitive effects are compensating each other and the cell behaves like an ohmic resistor. For the lithium-ion cell type examined in this thesis, this occurs very close to 1 kHz. As a consequence, the real part of the impedance at 1 kHz, the $R_{ac,1kHz}$, is a well-suited indicator to identify changes in the ohmic behavior. Ohmic contributions to the cell impedance typically origin from the electrolyte resistance, the resistances of the current collectors and active masses, and the contact resistances between the current collectors and active masses [133]. The electrolyte resistance depends on its conductivity, which changes with the concentration of conductive salt dissolved in it [91,92]. As this concentration changes with aging, $R_{ac,1kHz}$ can be used to identify electrolyte degradation. The contact resistances between current collector and active material typically generate high-frequency capacitive semicircles in the impedance spectrum [134,135]. In cylindrical 18650 cells, however, these effects are superposed by a pronounced inductive behavior, which dominates the overall cell impedance in the high-frequency region and results in negative y-values in Figure 8 for frequencies above 1 kHz. As a consequence, the capacitive semicircles from the contact resistances between current collectors and active materials cannot be determined individually and their resistive contributions become part of the ohmic resistance value $R_{ac,1kHz}$ [136].

3.3.2.2 Inductive Behavior

The lower part of the impedance spectrum depicted in Figure 8 represents the inductive behavior of the cell, which results mainly from the geometric design of the cell and its electrodes. In cylindrical cells, the spiral windings of the jelly roll lead to considerably higher inductivities than for the planar electrodes of coin cells or pouch cells with stacked electrode sheets [136,137]. Furthermore, the position of the tabs, which connect the current collector foils with the external poles of the cell, also have a marked impact on the cell's inductance. A longer distance through the spiral windings of the jelly roll between both tabs leads to a substantially higher inductance [138]. The cell type examined

in this thesis has the negative tab located at the outer end of the jelly roll and the positive tab located at about one third of the distance from the inner end to the outer end of the current collector foil. Hence, a considerable inductive behavior is observed. The inductive contributions to the cell impedance exhibit usually only minor changes with aging.

3.3.2.3 Capacitive Behavior

The upper part of the impedance spectrum depicted in Figure 8 represents the capacitive effects and comprises two depressed semicircles and a sloping line at the right end. For the cells in new condition, the two semicircles overlap in such a way that they cannot be clearly distinguished. The semicircles cover effects from passivation layers as well as charge transfer resistances at both electrodes and double layer capacities [17,139]. The sloping line at the low-frequency end represents limitations in mass transport due to diffusion processes [133,140]. The square markers in Figure 8 highlight the cell impedances at 32 Hz and 350 mHz, which represent the transition point between the two semicircles and between the second semicircle and the sloping line, respectively. These markers are used throughout the entire thesis to visualize the transformations of the different sections of the impedance spectrum with aging and to separate sections dominated by anode influence and cathode influence.

3.3.3 Identification of Anode and Cathode Contributions by Symmetric Coin Cells

The individual impedance characteristics of both electrodes of a lithium-ion battery can be determined by examining symmetric cells [141–143]. Thus, symmetric 2032-sized coin cells were fabricated from the electrodes of a new cell at 50% SoC. From the graphite anode material and the NCA cathode material, electrode samples with a diameter of 14 mm were punched out. These electrode samples were reassembled in symmetric coin cells with either only graphite or only NCA samples. In addition to the symmetric cells, full-cells with one graphite and one NCA electrode sample were built. These cells were the link for the validation between the symmetric coin cells and the original 18650 full-cell. The coin cells of size 2032 were built with a polymer separator of 16 mm diameter and 30 µl of fresh electrolyte (1 M $LiPF_6$ in EC:EMC (3:7)).

As the electrode samples obtained from the jelly roll of a commercial 18650 cell were generally coated on both sides, distortions in the impedance measurements occurred, particularly for the NCA samples. An additional high-frequency capacitive semicircle was observed, which was thought to be caused by the contact resistance between the back side of the electrode sample and the conducting metal of the coin cell. This undesired high-frequency, capacitive semicircle in the spectra of the symmetric NCA cells and of the full-cells could be reduced by an increasing pressure onto the coin cell. As a consequence, all coin cell impedance spectra presented in this section were recorded inside a press setup, which was used to press both halves of the coin cell housing together with a force of ca. 3 kN. This effectively minimized the undesired high-frequency semicircle related to the contact resistances of the NCA electrode material.

Figure 9a-c depicts the measured impedance spectra of the coin cells, with the same characteristic frequencies highlighted as in the impedance spectra above. The coin cell measurements exhibit only impedance values above the x-axis, which represents a very low inductive behavior. This confirms

that the inductive contributions in the impedance spectra of the commercial 18650 cells origin from the spiral winding of the electrodes.

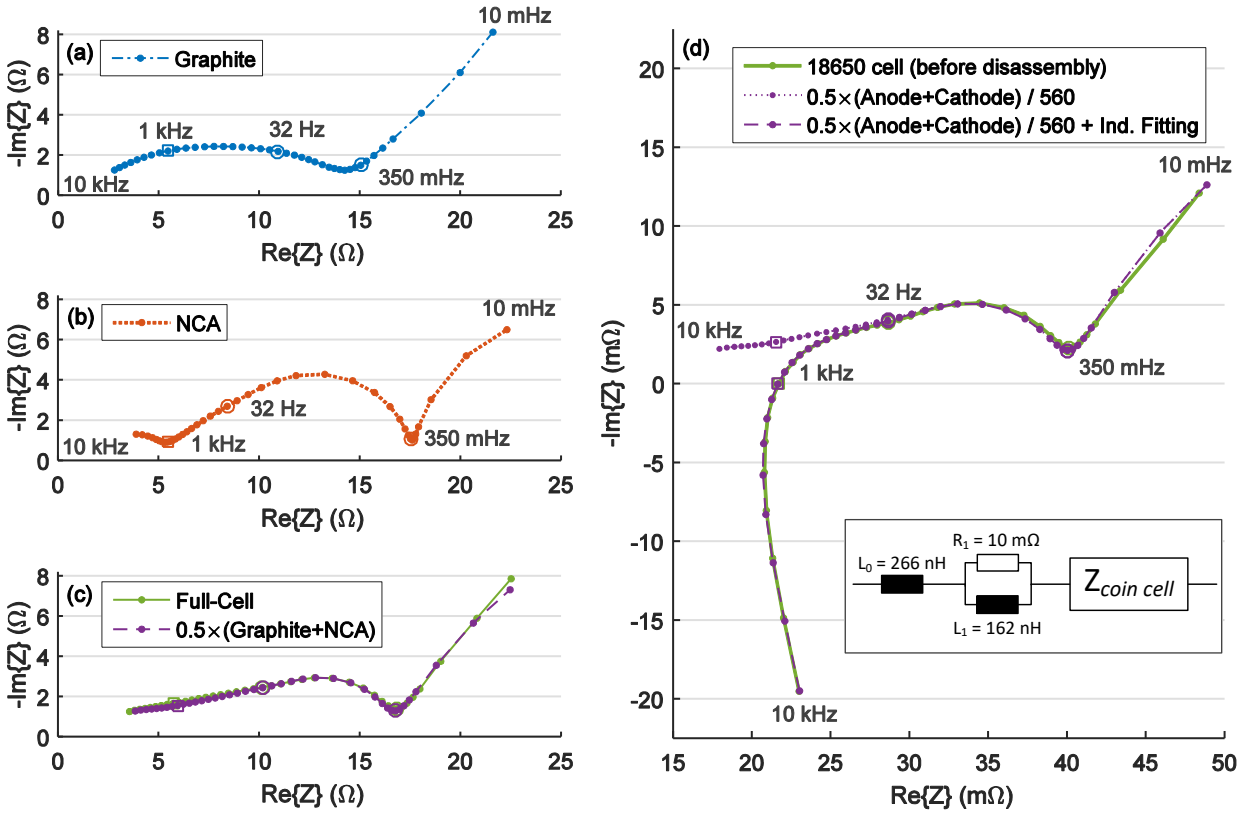

Figure 9. Impedance spectra from coin cell measurements. (a) Symmetric graphite coin cell, (b) symmetric NCA coin cell, (c) comparison of full-cell coin cell and the superposition of the previous graphite and NCA spectra. (d) Comparison of the impedance spectra from the original 18650 cell and the scaled results from superimposed symmetric graphite and NCA spectra, also in combination with the additional inductive components illustrated by the equivalent circuit model at the bottom. The superposed spectra were shifted horizontally to visualize the excellent agreement.

Figure 9a exhibits a flat arc segment for the graphite anode between 1 kHz and 32 Hz, where the real part increases by ca. 6 Ω. For the same frequency interval, Figure 9b shows considerably smaller changes in the real part of the cathode impedance of only ca. 3 Ω and also lower imaginary parts as in the graphite spectrum. In the frequency interval from 32 Hz to 350 mHz, the characteristics of the impedance spectra are reversed. The real part in the graphite spectrum increases by only ca. 4 Ω, whereas it increases by more than 9 Ω in the NCA spectrum. Also the imaginary parts in the NCA spectrum are substantially higher. In Figure 9c, the spectrum of a full-cell in the coin-cell format and the superposition of the graphite and NCA spectrum from Figure 9a and b are compared. The superposition was performed by adding the impedance values of both spectra after dividing the individual impedance values from both spectra by 2, since the impedances of the symmetric cells represent the sum of two identical electrodes. Moreover, a horizontal offset of 0.5 Ω was added to obtain similar positions of the characteristic frequencies of 32 Hz and 350 mHz. The two curves depicted in Figure 9c demonstrate that an excellent agreement can be obtained in the superposition process. This confirms that the linear superposition of electrode-individual impedance values is feasible.

The impedance reconstruction illustrates that in the frequency range between 1 kHz and 32 Hz, the graphite anode is the dominant source of impedance, whereas the semicircle between 32 Hz and 350 mHz origins largely from the NCA cathode.

To compare the results of coin-cell measurements with the impedance spectra of the conventional 18650 cells, the superposition of graphite and NCA impedances is scaled by 1/560 in Figure 9d, which is close to the factor of 1/500, resulting from the comparison of active electrode areas between the coin cells and original cell in 18650 format. The ca. 12% higher divisor indicates somewhat higher relative resistances for the coin cells. This might be caused by the back side coating of the NCA sample that lies in the current path and thus increases the impedance as the electrons have to flow through an additional layer of active material compared to the conventional current path in the 18650 battery cell, where the electrons only flow through the metal current collectors to reach the active material.

To adjust the inductive behavior, an inductor and a parallel connection of inductor and resistor were assumed in series to the cell. The parameter values of these three components were varied to obtain a good fit between both curves. Figure 9d demonstrates an excellent qualitative agreement between the two curves. Thus, the reconstruction of the impedance spectrum of the 18650 cells from symmetric coin cell measurements confirms that the frequency range between 32 Hz and 350 mHz serves as an indicator for degradation of the NCA cathode, whereas the frequency interval from 1 kHz to 32 Hz can be ascribed to the graphite anode.

3.3.4 Prerequisites for Reliable EIS Measurements

To employ EIS in experimental studies on battery aging, it has to be guaranteed that reliable spectra are recorded. According to the mathematical fundamentals of EIS, impedance measurements correctly describe the transfer function of an electrochemical system if the system meets the conditions of causality, linearity, and time-invariance [144,145]. Typical sources of measurement errors originate from the applied excitation signal, temperature variations, and relaxation times. Their impact and identification are presented in this section.

3.3.4.1 Proper Lissajous Figures

By evaluating online Lissajous figures, which visualize the voltage data versus current data during the measurements, the measurement quality can be assessed and violations of the above-mentioned mathematical prerequisites can be identified. In an ideal case, the Lissajous figure exhibits a perfect ellipse, as illustrated in Figure 10a. Typical deviations in practical EIS measurements are noisy ellipses, distorted ellipses, and degenerated ellipses where the endpoint of one period is not identical to its starting point. Figure 10b shows a noisy ellipse, which typically occurs when the signal-to-noise ratio is low due to an excitation signal which is too small for the resolution and precision of the employed measurement hardware. Distorted ellipses, as illustrated in Figure 10c, are a result of nonlinear behavior. They occur when the voltage response to the sinusoidal current excitation is no longer a sinusoidal signal itself. For lithium-ion batteries, this can be observed at very low or very high SoCs when the potential begins to change disproportionately and the voltage response becomes a distorted sinusoidal signal. In these cases, the cell violates the linearity criterion. Figure 10d illustrates a degenerated ellipse, which exhibits a spiral-like behavior.

This occurs when there are additional changes in the cell potential that are no result from the AC excitation and, thus, violate the causality condition. Such drifts occur when the AC current signal is superimposed with a DC offset or when there is a pronounced relaxation of the cell voltage after charging or discharging sequences. Since the voltage of the endpoint differs from the voltage of the starting point, the criterion of time-invariance is also violated.

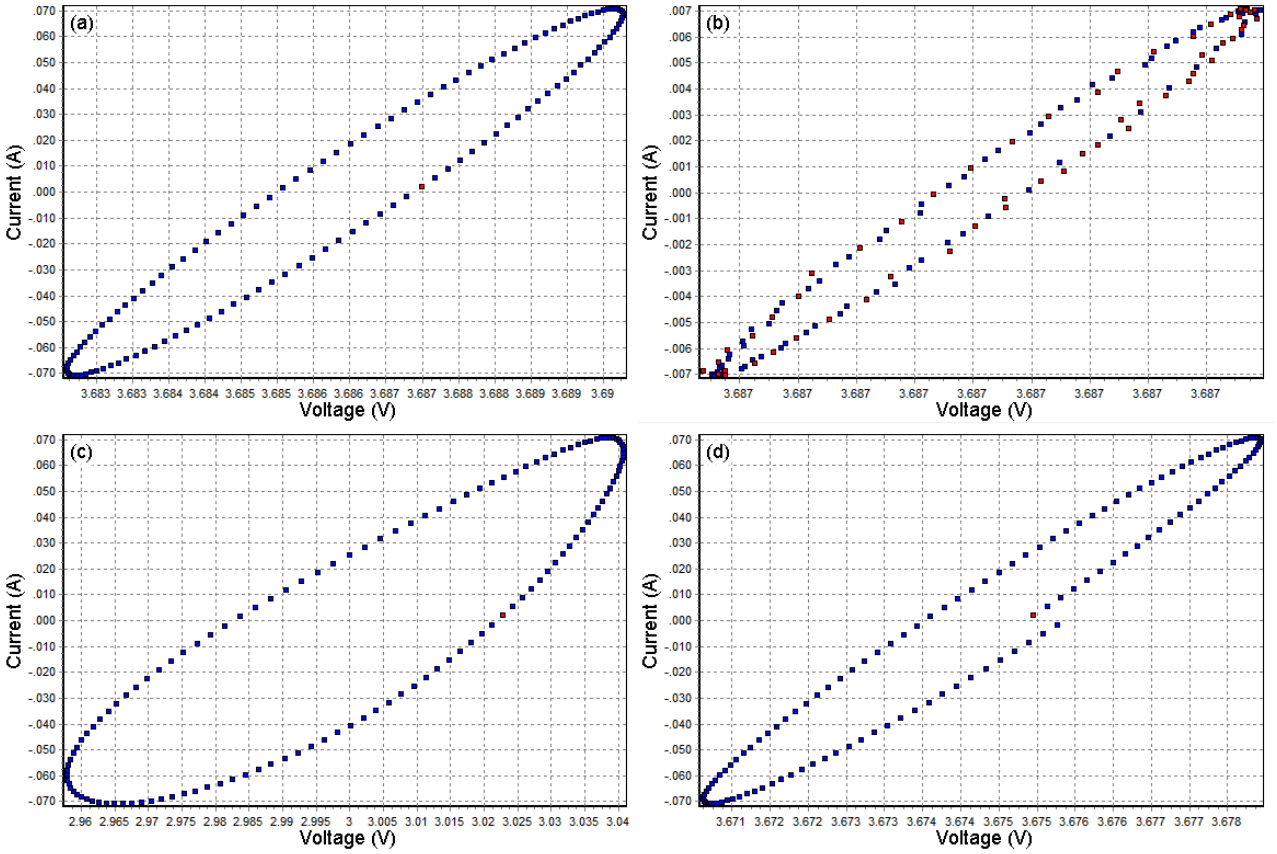

Figure 10. Screenshots from Lissajous figures obtained during EIS measurements: (a) good measurement, (b) noisy ellipse due to a low signal-to-noise ratio, (c) distorted ellipse due to nonlinear behavior, and (d) degenerated ellipse where the beginning and the endpoint of the period are not identical, resulting from a superimposed voltage drift.

3.3.4.2 Appropriate Excitation Amplitudes

When specifying an appropriate amplitude for the AC excitation of an EIS measurement, it has to be ascertained that on the one hand, the excitation is large enough to obtain a good signal-to-noise ratio for a robust measurement and that on the other hand, the linearity criterion is not violated. Depending on the SoC, the maximum excitation amplitude can vary substantially. Excitations of only 5–10 mV are typically recommended whereas in quasi-linear regions, amplitudes of 50–100 mV or even more are also applicable [146].

To evaluate the measurement quality and the impact of the excitation amplitude on the impedance results, EIS measurements at 50% SoC were performed with different AC current settings. The results are compared in Figure 11. This demonstrates that the impact of the excitation amplitude is negligible over a wide range of excitation currents for the EIS measurements performed without DC offset at 50% SoC. Thus, the cell is in a quasi-linear region at 50% SoC. Moreover, Figure 11 demonstrates that the overpotentials do not decrease with higher currents, as it was observed for

lead-acid batteries and ascribed to the Butler-Volmer relationship [147,148]. Monitoring the online Lissajous figures revealed noisy measurements only for very small excitation signals of $I_{ac,rms}$ = 12.5 mA and below, but very smooth results for all higher excitation currents. Thus, $I_{ac,rms}$ values of 50 mA and 100 mA, which were used in the different aging studies, provided robust, reliable, and comparable results which fulfilled the mathematical prerequisites of EIS.

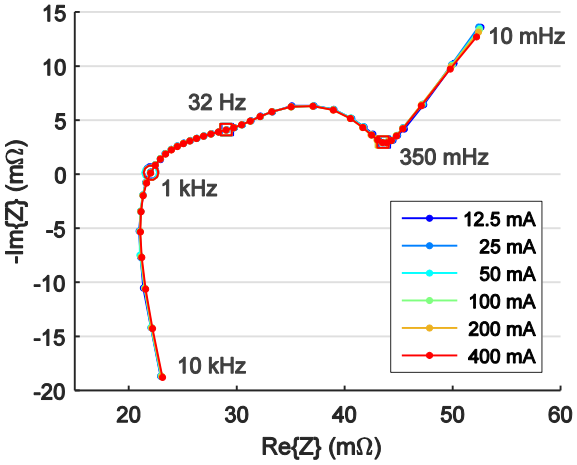

Figure 11. Impedance spectra of the examined 18650 cells at 50% SoC for different excitation currents $I_{ac,rms}$

3.3.4.3 *Constant Measurement Temperature*

As the impedances of a lithium-ion battery depend strongly on temperature [149–151], it is essential to perform the EIS measurements under identical temperature conditions. Otherwise, impedance fluctuations owing to temperature variations among the different checkup measurements can be considerably larger than the changes from preceding degradation. Figure 12a shows the substantial changes in the cell impedances with lower temperatures. In Figure 12b, the variations for 25±5°C are demonstrated. Particularly in the low and medium frequency domain, the impedance spectra differ markedly. As a consequence, all EIS measurements were performed in thermal chambers at 25°C, which was the standard checkup temperature for capacity and resistance measurements.

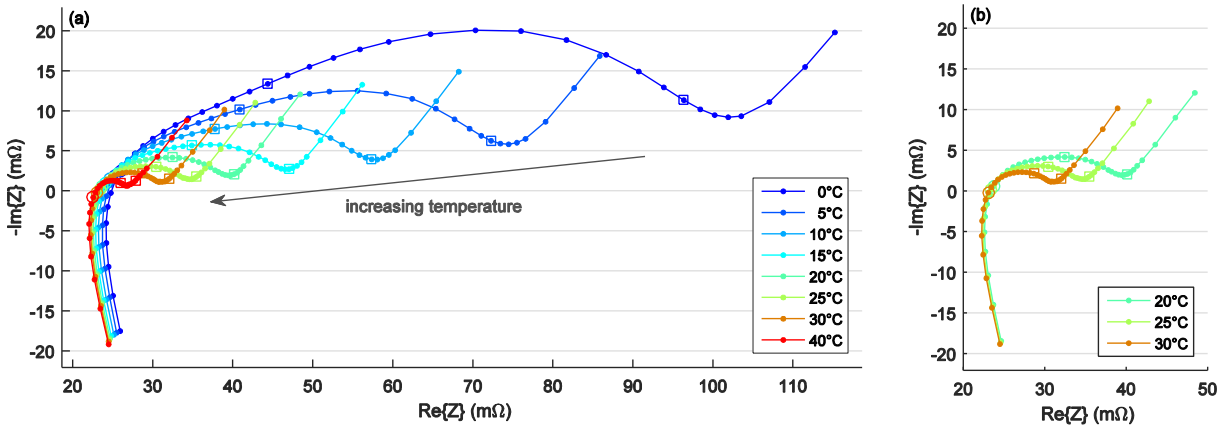

Figure 12. Impedance spectra of a new 18650 cell at different temperatures ranging (a) from 0°C to 40°C and (b) a detailed view for 25±5°C

3.3.4.4 Identical Relaxation Times

Another source of error in impedance studies is the relaxation time [152,153]. The relaxation time represents the pause between charging or discharging a cell to the target SoC and performing the actual EIS measurement. To demonstrate the impact of relaxation, a cell at 50% SoC performed a sequence of complete discharging, charging, and discharging with pauses of 15 min between all steps. After that, the discharged cell was charged to 50% SoC and EIS measurements were repeated after different relaxation times. The first EIS measurement was performed after 20 min and the entire experiment lasted almost 50 days. As visualized in Figure 13, substantial changes in the impedance spectrum occur with increasing relaxation times. These changes affect predominantly the medium-frequency domain. The impedances in the high-frequency domain of 1 kHz and above remain unchanged. For the cell type examined, a considerable growth of the semicircle between 32 Hz and 350 mHz is observed. The sloping line at lowest frequencies, representing the diffusion processes, is right-shifted accordingly. Hence, there must be long-term equalization processes, such as a lithium redistribution inside the electrodes, which lead to the altering EIS results [153].

Although the altering impedance spectra over time constitute time-variant behavior, no signs of time-variance were observed in the online Lissajous figures, such as voltage offsets between the beginning and the end of a sinusoidal period. Thus, the cells were in a quasi-steady state throughout each individual EIS measurement, so that the time-invariance criterion could still be considered as fulfilled.

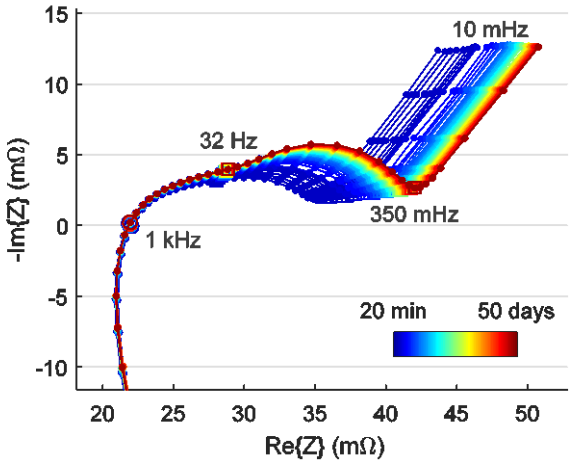

Figure 13. Impedance spectra with $I_{ac,rms}$ = 50 mA for different time spans after charging a cell to 50% SoC. Before that, the cell performed a charge-discharge sequence with pauses of 15 min after each step.

Figure 14 depicts the impedance changes over time for four characteristic frequencies. The most pronounced increases are observed between the impedance graph for 32 Hz and the impedance graph for 350 mHz. This represents the growing semicircle in the medium-frequency domain. Figure 14a shows that particularly within the first relaxation hours, the impedances change notably.

Figure 14b demonstrates that the impedance changes persist even after several weeks of storage at 25°C, which is substantially longer than the 4 h and 48 h of relaxation which were described in literature [152,153]. Almost half of the entire impedance change observed after 49 days of relaxation occurred within the first day. For robust battery aging diagnostics based on EIS measurements, it is important to minimize sources of error due to the measurement procedure and the test schedule.

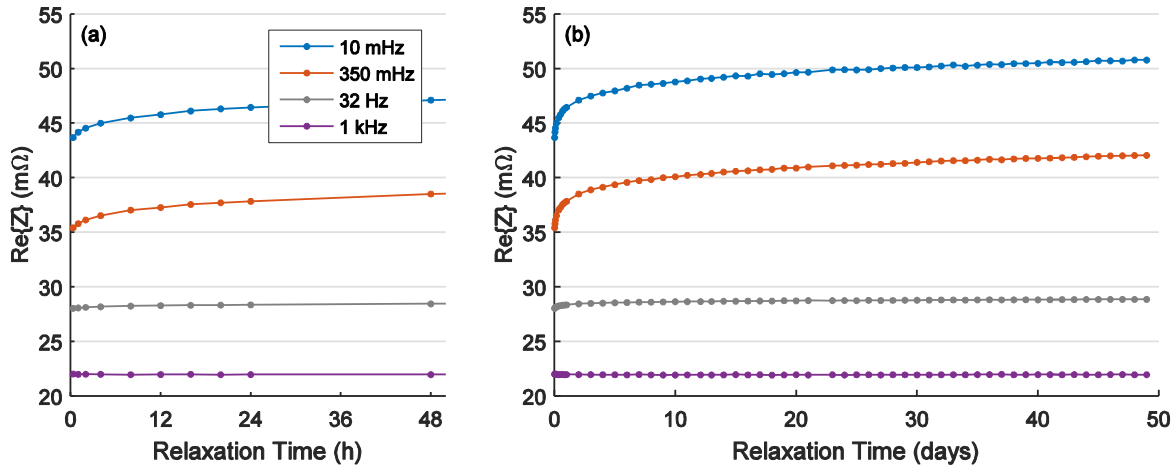

Figure 14. Impact of relaxation time on the impedance at different characteristic frequencies for a cell charged to 50% SoC at 25°C. (a) First 50 h of relaxation. (b) Entire relaxation period of almost 50 days.

To minimize deviations, the EIS measurements either have to be performed always after exactly the same relaxation period or it has to be waited several days between charging or discharging to the target SoC and performing the EIS measurement. After several days of relaxation, the rate of the impedance changes has decreased substantially. Thus, deviations in the relaxation times in the order of minutes and hours do not cause such large deviations in the impedance values any longer, compared to the deviations caused within the first 24 h of relaxation. Overall, impedance changes due to relaxation have a massive impact on the results of battery aging studies. They have to be carefully controlled because otherwise, robust and reliable results are obtained only in the high-frequency domain, which remains unaffected by relaxation.

The relaxation times had a substantial impact on the results of the impedance measurements of the different aging studies presented in this thesis. In most studies, the cells had to be disconnected from the battery test system and connected to the galvanostat for the EIS measurements and since only one measurement device was available for the studies presented in this thesis, it was not possible to obtain comparable EIS results for relaxation periods shorter than 24 h. Since waiting several days between the end of the capacity measurements and the EIS to become more robust to variations in relaxation times was also not feasible, varying relaxation times and a decreasing precision of the EIS results were inevitable. As a consequence, the results of the EIS measurements could only be used to precisely assess changes in the high-frequency domain, such as the changes in $R_{ac,1kHz}$. When characterizing the low-frequency behavior, which also includes the effects of passivation layers, charge transfer, double layers, and diffusion, the impedance changes due to varying relaxation times were larger than the aging-induced impedance changes.

Only in the second calendar aging study, comparable impedance results could also be obtained in the low-frequency domain. In that study, an EIS multiplexer was available which allowed combined capacity and EIS measurements without manually disconnecting and reconnecting the cells; the entire test procedure could be controlled by the battery test system. This enabled checkup procedures with identical relaxation times, which were set to 1 h and provided impedance data of high significance also in the medium-frequency and low-frequency domain.

3.4 Current Step Response

As presented in the previous section on the EIS, the dynamic behavior of a battery is strongly affected by temperature and relaxation periods. Since the relaxation times before EIS measurements could not be kept constant in most of the experimental aging studies, current pulses were applied to complement the EIS measurements. As the current pulses were performed at the battery test systems without any disconnection of the cells, the relaxation periods before the current pulses could be precisely controlled by the checkup test procedure and were identical in all checkup measurements of one respective aging study.

The voltage response of the battery to the current step is evaluated to compute DC resistance values. Since the voltage response to a 10 s pulse was used in many aging studies on lithium-ion batteries [154–158], this pulse duration was also employed in this thesis. The amperage of the pulses, I_{pulse}, ranged between 1 A and 5 A in the checkups of the aging studies presented in this thesis. Figure 15 illustrates the current and voltage values used for the computation of $R_{\mathrm{dc,10s}}$.

$$R_{\mathrm{dc,10s}} = \frac{V_{10\mathrm{s}} - V_{0\mathrm{s}}}{I_{\mathrm{pulse}} - I_{0\mathrm{s}}} = \frac{V_{10\mathrm{s}} - V_{0\mathrm{s}}}{I_{\mathrm{pulse}}} \quad \text{for} \quad I_{0\mathrm{s}} = 0\ \mathrm{A} \tag{5}$$

Since the dynamic behavior of battery cells depends strongly on temperature, the resistance measurements have to be performed at controlled temperatures which are similar in all checkups. To obtain a good signal-to-noise ratio, but keeping the SoC changes and the warming of the cells owing to irreversible losses at a minimum, discharging pulses of 3 A (ca. 1.1 C) were evaluated for this thesis.

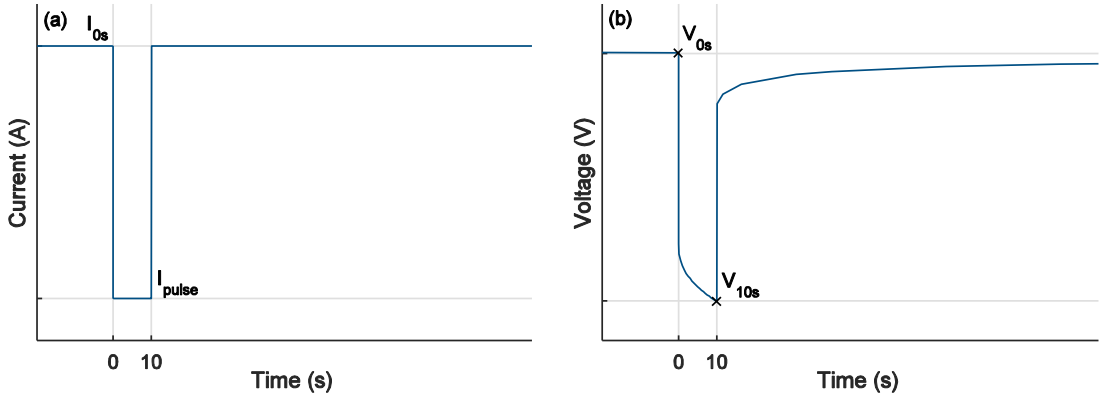

Figure 15. Illustration of (a) current pulse and (b) voltage response used for the calculation of $R_{\mathrm{dc,10s}}$

Although current step response evaluations are also sensitive to relaxation, distortions are generally prevented by the battery test system, which precisely controls the pause lengths and guarantees identical relaxation times in all checkup measurements. This enabled a reliable monitoring of changes in the electrochemical effects with higher time constants, such as charge transfer and diffusion. By contrast, pulse measurements were not suitable for measuring high-frequency resistances, due to the limited sampling rate of the battery test systems. Since the first measurement after applying the pulse could only be taken after several milliseconds, the resulting 'high-frequency' resistance values were always higher than the values for $R_{\mathrm{ac,1kHz}}$ from the EIS measurements.

Thus, resistance values from current step responses are ideal for low-frequency resistances, whereas EIS measurements are superior for high frequencies. Overall, EIS and current step response

analysis are a valuable combination which enables to determine changes in the electrolyte conductivity by $R_{ac,1kHz}$ from EIS and changes in the sum of resistances with higher time constants by $R_{dc,10s}$ from the voltage response to current pulses.

3.5 Differential Voltage Analysis

The behavior of a battery which is measured at its poles is always a superposition of contributions from the positive and the negative electrode. For aging studies, analysis techniques are beneficial which enable the identification of aging processes of the individual electrodes without opening the cells for inserting a reference electrode or destroying the cells for post-mortem studies. Such an analysis technique is DVA, which is introduced in this section and applied in the different calendar and cycle aging studies.

3.5.1 Fundamentals

DVA is a technique for noninvasive, nondestructive electrical characterization of battery cells, which bases on a differentiation of voltage curves. From a CC charging or discharging sequence, the derivative *dV/dQ* is computed and plotted versus capacity. For the low-current charging sequence depicted in Figure 16a, the corresponding differential voltage spectrum is illustrated in Figure 16c.

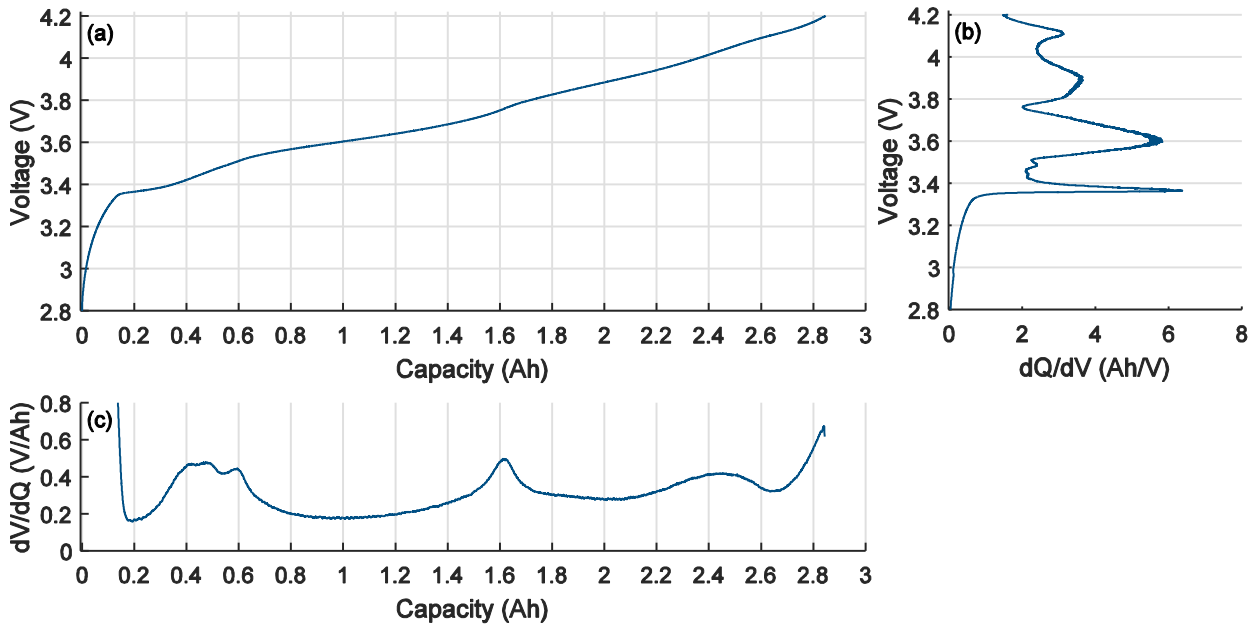

Figure 16. (a) Low-current charging curve of a new NCA cell and the derived (b) differential voltage spectrum and (c) incremental capacity spectrum

As the individual contributions of both electrodes can be identified in the full-cell derivative, DVA can be used to determine the balancing and the utilization of the two electrodes without inserting a reference electrode [159]. In aging studies, DVA is employed to separate different aging mechanisms, such as anode degradation, cathode degradation, and shifts in the electrode balancing [10,160]. As the peaks in the differential voltage spectrum appear more pronouncedly with lower currents, charging and discharging currents of C/20 and below are typically used [161,162].

The two electrodes of a battery can be regarded as a series connection, where the full-cell voltage V_{cell} is the difference between the potentials v_{p} and v_{n} of the positive and the negative electrode, respectively. Due to the series connection, it is always the same current that flows through both electrodes. As a consequence, *dV/dQ* represents a linear superposition of the derivatives of the half-cell potential of the positive and negative electrode [163]:

$$V_{\mathrm{cell}} = v_{\mathrm{p}} - v_{\mathrm{n}} \tag{6}$$

$$\frac{dV_{\mathrm{cell}}}{dQ} = \frac{dv_{\mathrm{p}}}{dQ} - \frac{dv_{\mathrm{n}}}{dQ} \tag{7}$$

The reciprocal of this derivative is evaluated in Incremental Capacity Analysis (ICA), which is also often used for battery aging diagnostics [164–166].

$$\frac{dQ}{dV_{\mathrm{cell}}} = \frac{1}{\frac{dv_{\mathrm{p}}}{dQ} - \frac{dv_{\mathrm{n}}}{dQ}} \tag{8}$$

For the same charging sequence as regarded above for DVA, Figure 16b illustrates the corresponding incremental capacity spectrum, where *dQ/dV* is plotted versus the cell voltage. Whereas peaks in DVA indicate phase transitions, peaks in ICA represent phase equilibria [167,168]. Comparing Equations (7) and (8) shows that in DVA, the contributions of both electrodes always add linearly. The superposition of both electrodes in ICA is substantially more complicated. It only generates spectra which are simple to analyze when the potential of one electrode remains constant (see Ref. [169]). Then, *dV/dQ* of one electrode is zero and the derivative of the full-cell is identical to the derivative of the other electrode. For that reason, ICA is frequently employed in aging studies examining LFP cells, where the cathode potential remains unchanged over a wide SoC range [169–171].

Another disadvantage of *dQ/dV* is that *dV* can become zero when the cell voltage remains constant for a certain period of time during the charging or discharging sequence, e.g., in phase equilibria [163,172]. This means that the derivative cannot be computed for this time step as it causes a division by zero. This problem cannot occur for DVA, as *dQ* is always a constant value unequal zero during CC charging or discharging. To avoid divisions by zero, *dQ/dV* can preferably be computed from voltage sweeps with a constant *dV/dt*, as they are performed in cyclic voltammetry, also called electropotential spectroscopy.

Overall, DVA based on *dV/dQ* is preferred to the evaluation of *dQ/dV* for the degradation monitoring of the NCA cells examined in this thesis. As the central peak at ca. 1.6 Ah appeared somewhat more pronouncedly for charging the cells than for discharging the cells, DVA was performed with data from charging sequences in this thesis. All DVA evaluations presented in this thesis were derived from low-current charging curves obtained with a current of 100 mA. Together with the 767 cm² of active electrode area, presented in Table 1, this results in a current density of ca. 0.13 mA cm^{-2}.

3.5.2 Half-Cell Voltage Curves

To demonstrate the linear superposition of anode and cathode derivative in DVA and to assign the different peaks and slopes of the differential voltage spectrum to both electrodes, half-cells were built from the active materials of the commercial 18650 cells in new condition. For building the half-cells, one cell at 0% SoC and one cell at 100% SoC was opened. The jelly roll was extracted and

electrode samples with a diameter of 14 mm were punched out for 2032-sized coin cells. The samples were used to build half-cells together with metal lithium electrodes of 15 mm diameter. For the fabrication of the coin cells, fiberglass separators with a diameter of 16 mm and ca. 160 µl of electrolyte (1 M $LiPF_6$ in EC:EMC (3:7) + 2% VC) were used.

Single-sided anode samples could be extracted from the NCA cells, since the outermost anode winding was coated only on the inner side. Hence, no side effects from the back side of the electrode sample occurred during the measurements. The cathode samples had double-sided coatings, for which capacity drifts due to an interfering back side coating had to be expected during cycling [173].

For the coin cells, similar current densities as for the DVA measurement of the commercial cells were applied. Thus, the charging and discharging currents were defined as follows:

$$I_{\mathrm{coin}} = \pm(1.4\,\mathrm{cm}/2)^2 \cdot \pi \cdot 0.13\ \mathrm{mA\ cm^{-2}} = \pm 0.2\ \mathrm{mA} \qquad (9)$$

The graphite half-cells were cycled between 0.1 and 1.5 V and the NCA half-cells between 2.5 and 4.3 V at 25°C. Before the charge-discharge cycling, the coin cells were stored for at least 12 h to provide sufficient time for the electrolyte to soak into the pores of the active material and the separator. At least three half-cells were fabricated from each electrode material. Since the cycling behavior was highly reproducible, the results of only one half-cell sample are presented.

Figure 17a shows three charge-discharge cycles of the graphite anode half-cells. They clearly reveal the different voltage plateaus, which correspond to the different stages of lithium intercalation into graphite [52,174,175]. Each charge or discharge step has a duration of up to 32 h.

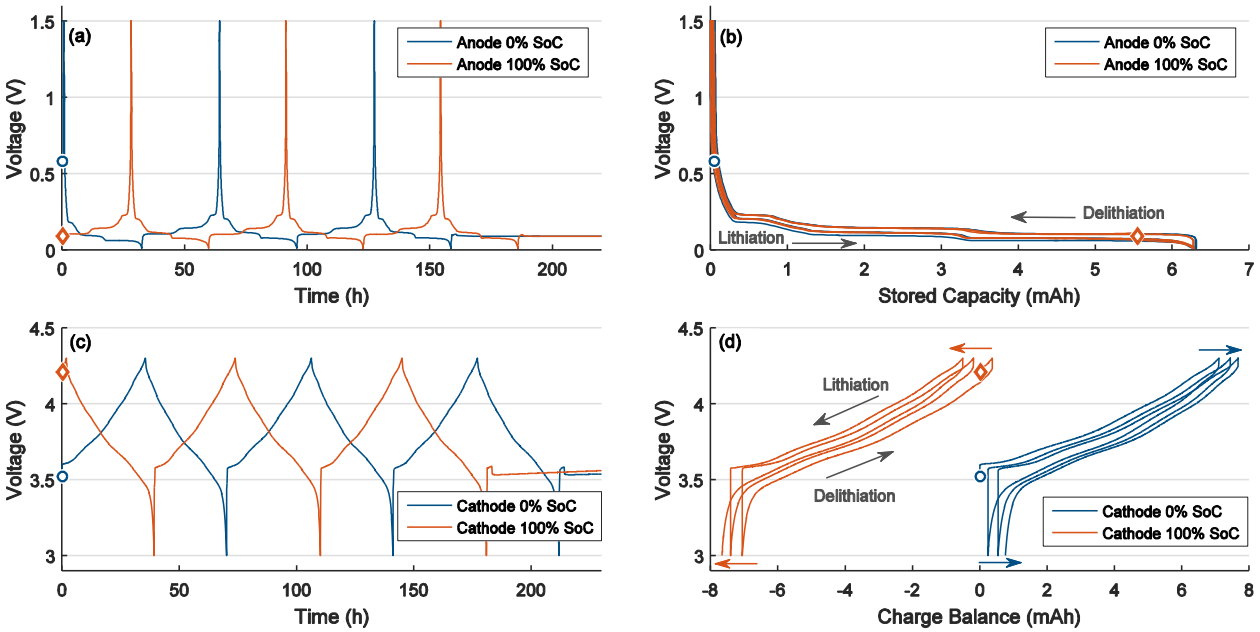

Figure 17. Three charge-discharge cycles of the graphite and the NCA half-cells from an empty (0% SoC) and a full (100% SoC) cell in new condition. (a, c) Voltage over time; (b, d) voltage over capacity. Markers indicate the initial potential and charge content for the electrodes from the full-cells at 0% (blue circles) and 100% SoC (orange diamonds).

In Figure 17b, the same half-cell voltage data are plotted versus stored capacity. Since these coin cells contained electrode samples with only single-sided coatings, the three cycles are similar and no capacity drifts occur. The circle and diamond markers indicate the initial potential and stored

capacity of the half-cells after the fabrication process. The blue circles show that a 0% SoC of the full-cell correlates with a completely delithiated anode; the orange diamonds demonstrate that the anode is utilized less than 90% at 100% SoC. At ca. 50% of the maximum storage capacity, a potential step can be observed, which indicates a different staging configuration of the intercalated lithium. Above 50% lithiation, the two-phase regime of LiC_{12} and LiC_6 can be observed [52,176,177].

Figure 17c shows three charge-discharge cycles of the NCA cathode half-cells. When this voltage data are plotted versus capacity in Figure 17d, a drift toward higher capacity values is observed for the coin cell from the full-cell at 0% SoC and a drift toward lower capacity values is observed for the coin cell from the full-cell at 100% SoC. This is a result of the lithiated or delithiated back side of the double-sided electrode sample, respectively. Since the capacity values were not stable, the utilization of the cathode at 0% and 100% SoC could not be derived from these data. However, further evaluations showed that the charging and discharging curves of the second and third repetition were similar, so that reproducible half-cell curves for the reconstruction of the full-cell spectra could be obtained.

3.5.3 Full-Cell Analysis

The half-cell curves were used to reconstruct the full-cell voltage characteristics. For this reconstruction, a proper scaling and balancing of the anode and cathode curves is necessary. When working with differential voltage spectra from samples with different sizes, such as 18650 cells and coin cells, a capacity normalization is typically performed by multiplying the derivative with the total capacity Q_0 [172].

$$\frac{dV}{dQ} \cdot Q_0 = \frac{dV}{dQ/Q_0} = \frac{dV}{dSoC} \tag{10}$$

As shown in Equation (10), this normed derivative can also be interpreted as the derivative of the voltage with respect to the SoC. For the reconstruction of the full-cell behavior from half-cell data, the normed derivative of the full-cell $\left(\frac{dV_{\mathrm{cell}}}{dQ} \cdot Q_0\right)$ has to be reproduced by the normed derivatives of the half-cells of the positive and negative electrode $\left(\frac{dv_{\mathrm{p}}}{dq_{\mathrm{p}}} \cdot q_{0,\mathrm{p}},\ \frac{dv_{\mathrm{n}}}{dq_{\mathrm{n}}} \cdot q_{0,\mathrm{n}}\right)$.

The scaling between the capacity changes in the full-cell (dQ) and in the half-cells (dq_{p} and dq_{n}) is performed as follows:

$$dQ = s_{\mathrm{p}} \cdot dq_{\mathrm{p}} = s_{\mathrm{n}} \cdot (-dq_{\mathrm{n}}) \tag{11}$$

where s_{p} and s_{n} represent the capacity scaling factors for the positive and negative electrode, respectively. Equation (11) also takes into account that charging the full cell leads to a discharging of the anode, according to the current flow definitions presented in Section 3.1.3.

Based on Equations (7) and (11), the following equations demonstrate how the full-cell derivative can be expressed by a linear superposition of the normed cathode and anode derivative.

$$\frac{dV_{\mathrm{cell}}}{dQ} = \frac{dv_{\mathrm{p}}}{dQ} + \left(-\frac{dv_{\mathrm{n}}}{dQ}\right) \tag{12}$$

$$\frac{dV_{\mathrm{cell}}}{dQ} \cdot Q_0 = \frac{dv_{\mathrm{p}}}{dQ} \cdot Q_0 + \left(-\frac{dv_{\mathrm{n}}}{dQ}\right) \cdot Q_0 \tag{13}$$

$$\frac{dV_{\mathrm{cell}}}{dQ}\cdot Q_0 = \frac{dv_{\mathrm{p}}}{s_{\mathrm{p}}\cdot dq_{\mathrm{p}}}\cdot Q_0 + \left(-\frac{dv_{\mathrm{n}}}{s_{\mathrm{n}}\cdot(-dq_{\mathrm{n}})}\right)\cdot Q_0 \tag{14}$$

$$\frac{dV_{\mathrm{cell}}}{dQ}\cdot Q_0 = \frac{dv_{\mathrm{p}}}{dq_{\mathrm{p}}}\cdot q_{0,\mathrm{p}}\cdot\underbrace{\frac{Q_0}{s_{\mathrm{p}}\cdot q_{0,\mathrm{p}}}} + \frac{dv_{\mathrm{n}}}{dq_{\mathrm{n}}}\cdot q_{0,n}\cdot\underbrace{\frac{Q_0}{s_{\mathrm{n}}\cdot q_{0,\mathrm{n}}}} \tag{15}$$

$$\frac{dV_{\mathrm{cell}}}{dQ}\cdot Q_0 = \frac{dv_{\mathrm{p}}}{dq_{\mathrm{p}}}\cdot q_{0,\mathrm{p}}\ \cdot\ \alpha_{\mathrm{p}}\ +\ \frac{dv_{\mathrm{n}}}{dq_{\mathrm{n}}}\cdot q_{0,\mathrm{n}}\ \cdot\ \alpha_{\mathrm{n}} \tag{16}$$

Equation (16) shows that the two factors, α_{p} and α_{n}, are sufficient for the scaling of the derivatives. In addition this scaling, two ampere-hour offsets, δ_p and δ_n, are used to shift the derivatives horizontally to obtain the correct alignment between both electrodes [160,178]. For an arbitrary charge content ξ of the full-cell, the following equation presents the superposition of the half-cell derivatives:

$$Q_0\left.\frac{dV_{\mathrm{cell}}}{dQ}\right|_{\xi} = \alpha_{\mathrm{p}}\cdot q_{0,\mathrm{p}}\left.\frac{dv_{\mathrm{p}}}{dq_{\mathrm{p}}}\right|_{\xi+\delta_{\mathrm{p}}} + \alpha_{\mathrm{n}}\cdot q_{0,\mathrm{n}}\left.\frac{dv_{\mathrm{n}}}{dq_{\mathrm{n}}}\right|_{\xi+\delta_{\mathrm{n}}} \tag{17}$$

In total, there are two scaling and two shifting parameters which can be adjusted for reconstructing the full-cell behavior from half-cell data. For the NCA cells examined in this thesis, Figure 18a illustrates how the full-cell voltage of the examined NCA lithium-ion cell results from the difference of cathode and anode potential. Figure 18b presents the corresponding derivatives. The comparison of the original 18650 cell and the reconstructed full-cell data shows very good agreement. The various slopes and peaks in the derivatives of the full-cells and half-cells confirm the linear superposition of both electrodes. Hence, the differential voltage spectrum contains valuable information on the scaling and balancing of the two electrodes, which will be used in the following section to deduce degradation indicators.

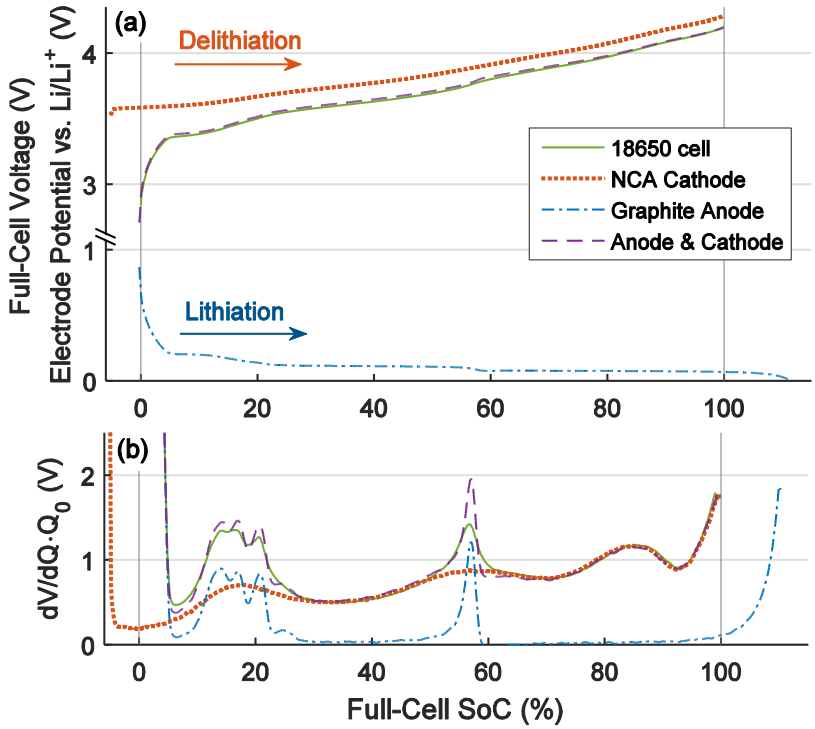

Figure 18. Reconstruction of the full-cell voltage and the differential voltage spectrum of a new cell from half-cell data. (a) Voltage behavior for low-current charging; (b) corresponding differential voltage spectra

3.5.4 Degradation Indicators

As the slopes and peaks of the individual electrodes can be clearly recognized in the full-cell spectrum, DVA can be used to define degradation indicators which provide information about anode degradation, cathode degradation, and changes in the electrode balancing.

Based on the superposition of anode and cathode derivative depicted in Figure 18b, the characteristic slopes at 0% and 100% SoC can be assigned to the individual electrodes. The marked potential drop in the full-cell voltage indicating 0% SoC is linked to the rising potential of the delithiated graphite anode, which is represented by the steep slope in the differential voltage spectrum. Hence, an empty anode determines the discharging endpoint, which represents the lower end of the available capacity window of the full-cell. This was also confirmed by the data from the coin cells fabricated from anode material from the cell opened at 0% SoC. The upper end of the capacity window is not determined by the graphite anode since the anode is generally oversized and the anode potential is constant in the high SoC region, as shown in Figure 17b. Thus, the charging endpoint is determined by the increasing potential of the cathode approaching its maximum permissible degree of delithiation, which is limited to ca. 55% for NCA cathodes to avoid substantial deformations in the lattice structure [69,179]. The discharging and charging endpoints are also of special importance for coulometry evaluations, which will be described in Section 3.6.

Figure 19 shows the complete assignment of slopes and peaks to both electrodes. From this assignment, the three characteristic capacities Q_1, Q_2, and Q_3 can be derived which are used to determine aging contributions from anode degradation, cathode degradation, and changes in the electrode balancing. As illustrated in Figure 19, Q_1 represents the distance between 0% SoC and the central graphite peak at about 1.6 Ah. The central graphite peak indicates the transition from the medium to the low voltage plateau of the anode potential, which occurs when the graphite anode is lithiated more than 50% [52,61]. Since Q_1 bases solely on characteristic anode markers, it provides information about changes in the storage capabilities of the graphite anode. Similarly, Q_3 provides information about the storage capabilities of the NCA cathode, as it bases solely on characteristic cathode markers. Q_2 represents the distance between the central graphite peak and 100% SoC. Hence, it combines an anode and a cathode marker. It sums up together with Q_1 to Q_{actual} and provides information about the balancing of the two electrodes. A change in Q_2 without a change of the anode capacity Q_1 and the cathode capacity Q_3 indicates a sole shift in the electrode balancing, which changes the inventory of cyclable lithium and thus alters the operating window of the two electrodes.

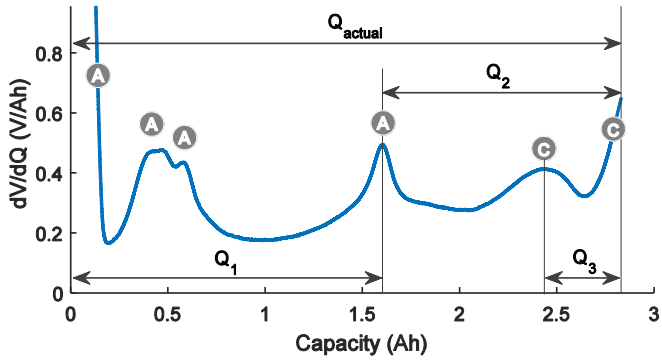

Figure 19. Assignment of slopes and peaks to anode (A) and cathode (C). The characteristic capacities Q_1, Q_2, and Q_3 allow to ascribe aging contributions to different degradation mechanisms.

3.6 Coulometry

Coulometry is a useful method for analyzing side reactions and battery aging. In conventional coulometry studies on lithium-ion batteries, the battery cells are cycled continuously with low currents of C/10 and below; the charged and discharged ampere-hours are recorded together with the cell voltage [180,181]. From these cycling data, coulombic efficiencies are computed and their absolute values and changes over cycle number or time are evaluated [43,182]. Furthermore, the slippage of the charging and discharging endpoints is analyzed, which provides explicit information about anodic and cathodic side reactions [56,183]. Performing coulometry with the low-current cycling approach requires high-precision battery test systems which feature highly precise current measurements that exhibit no offset errors causing drifts in the ampere-hour integration [184,185].

In contrast to the conventional low-current cycling approach, this thesis presents coulometry evaluations with the data from calendar aging studies, in which the cells were not cycled continuously but stored in open circuit condition. Only occasional checkups were performed at the battery test systems to determine the actual capacities of the cells and to bring them back to their respective storage SoCs before they were disconnected from the test system again and returned to the storage compartments. This novel coulometry method is named “Coulomb Tracking” and was introduced in Ref. [186].

3.6.1 Coulomb Tracking Method

Coulomb Tracking consists of two major steps. At first, the measurement data of all tests performed at the battery test system with the cell under test are ordered chronologically and a continuous ampere-hour balance is generated. To obtain this continuous charge balance, the last ampere-hour value of each measurement run is used as an offset for the charge balance of the subsequent measurement. During the time in which the cell is stored, the cell is disconnected from the battery test system. This is an important prerequisite of this coulometry method, as it ascertains that no charge can flow into or out of the cell during the storage periods. Thus, the charge balance remains unchanged. In the second step, the continuous charge balance is used to track the slippage of representative charging and discharging endpoints. To evaluate comparable endpoints, one specific sequence of the checkup procedure is selected from which the charging and discharging endpoints are determined and changes are monitored. The advantage of this method is that it can be performed with conventional battery test systems, as no long-term measurements have to be performed during the storage periods, where the current integration is prone to drifts owing to small offset errors in the current measurement. As the cells are stored in open circuit condition, the change in the charge balance always remains zero, independent of the storage duration lasting several days, weeks, or months.

Figure 20 illustrates the Coulomb Tracking method. Figure 20a shows the periodic sequence of checkups (blue), test protocols bringing the cells to storage SoC (red), and the actual storage periods in open circuit condition (gray). During the checkups, charge-discharge cycles are performed to determine the actual capacity under reference conditions. Figure 20b shows the individual charge balances recorded for each measurement run at the battery test system. From these data, the continuous charge balance is generated as described above and illustrated in Figure 20c. The dotted

lines represent the constant ampere-hour values during the storage periods, in which the cells are disconnected from the battery system. The crosses represent the discharging and charging endpoints of one specific sequence of the checkup where the current is low; and the dashed lines illustrate the slippage of the endpoints over time. The shifts of the charging and discharging endpoints provide information about anodic and cathodic side reactions. As the duration of the checkups is short compared to the storage periods, the errors in the ampere-hour integration, performed by the battery test system, remain small compared to the shifts of the endpoints resulting from the storage periods, particularly at high storage temperatures. The interpretation of the endpoint shifts is similar as for the conventional coulometry approach, based on continuous low-current cycling.

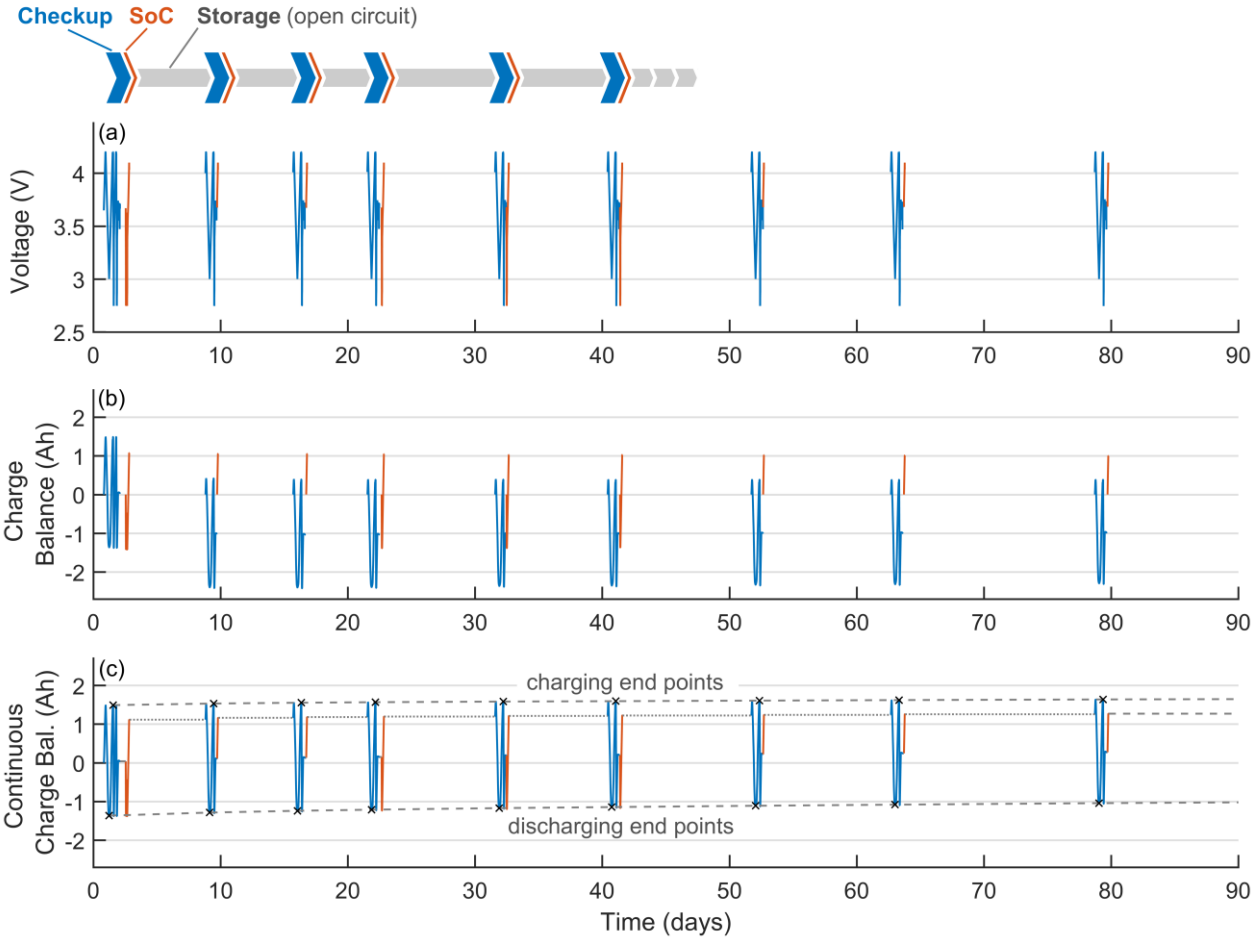

Figure 20. Exemplary representation of the Coulomb Tracking method: (a) Repetitive test sequence of checkup procedure, bringing the cell to storage SoC, and storage period in open circuit condition. (b) Charge balances of the individual measurements. (c) Continuous charge balance after post-processing for Coulomb Tracking, where the last ampere-hour value of each test dataset is used as offset for the subsequent measurement dataset. The dashed lines illustrate the slippage of specific charging and discharging endpoints.

3.6.2 Interpretation of Coulometry Results

In principle, coulometry can detect such side reactions that alter the degree of lithiation of one or both of the electrodes. For lithium-ion batteries, these side reactions can be categorized into the three cases which are illustrated schematically in Figure 21: Anodic side reactions, cathodic side reactions, and coupled side reactions, which represent a combination of the two previous cases.

3.6.2.1 Anodic Side Reactions

Figure 21a and Figure 21d show side reactions that only affect the negative electrode. These anodic side reactions are generally related to electrolyte reduction and SEI growth, which consume intercalated lithium of the anode during storage [56,93,187]. With the altering degree of lithiation of the anode, the operating point shifts to the left during the storage periods, as illustrated by the blue arrow and the cross marker in Figure 21a. As the ampere-hour value of the continuous charge balance does not change during storage, because the cells are always stored in open circuit condition, the side reactions can be interpreted as an internal shift of the anode half-cell curve to the right. The resulting degree of lithiation after the storage period is located at the ampere-hour value of the charge balance at the beginning of the storage period. This is illustrated in Figure 21d. The right-shift of the anode curve also entails a right-shift of the discharging endpoint, represented by the violet arrow, whereas the charging endpoint remains unaffected. This decreases the inventory of cyclable lithium and the utilization of both electrodes, which represents an irreversible capacity fade.

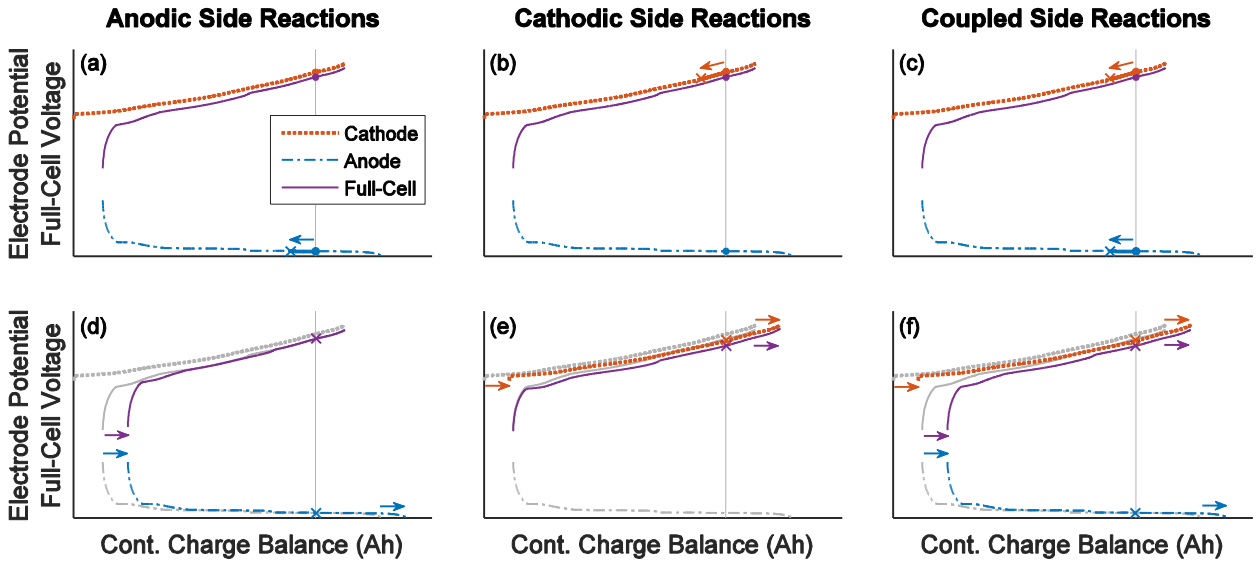

Figure 21. Schematic illustration of the effects of anodic, cathodic, and coupled side reactions based on the composition of the full-cell voltage from half-cell potentials for an arbitrary storage SoC (vertical gray line). (a)-(c) Changes in the degree of lithiation and the potential of the individual electrodes (red and blue arrows). (d)-(f) Resulting shifts of the half-cell curves (blue and red arrows) and of the charging and discharging endpoints (violet arrows) in the continuous charge balance used for Coulomb Tracking. The gray curves represent the states before the side reactions.

3.6.2.2 Cathodic Side Reactions

Figure 21b and Figure 21e depict side reactions that only affect the positive electrode. Cathodic side reactions include electrolyte oxidation and transition-metal dissolution, which provoke a reinsertion of the lithium into the positive electrode that can be observed in form of a potential decrease [188,189]. The changing degree of lithiation and the potential drop are illustrated by the red arrow and cross marker in Figure 21b. Comparable to the shift of the anode curve in Figure 21d, Figure 21e demonstrates that cathodic side reactions lead to a right-shift of the cathode half-cell curve. The violet arrow shows that this shift entails a right-shift of the charging endpoint, while the discharging

endpoint remains at the same location, as long as the cathode is not fully utilized. This expands the inventory of cyclable lithium and the utilization of both electrodes. Thus, cathodic side reactions can increase the actual capacity of the full-cell [190]. However, the stored amount of charge decreases during the storage periods due to the reintercalation of lithium into the cathode. Hence, cathodic side reactions cause a reversible self-discharge [191].

3.6.2.3 Coupled Side Reactions

Figure 21c and Figure 21f illustrate the effects of coupled side reactions, which combine side reactions at the positive and negative electrode. In Figure 21c, the arrows and cross markers represent the changes in the degree of lithiation of both electrodes. Coupled side reactions occur when reaction products generated at one electrode migrate or diffuse to the other electrode and cause additional side reactions there, such as deposition of dissolved transition metals or electrolyte shuttle reactions [56,192]. Although transition-metal dissolution is typically expected for manganese-based electrodes [193,194], post mortem studies have also revealed a deposition of cobalt and nickel at the anode of aged NCA cells [71]. Furthermore, reaction products from electrolyte oxidation at higher cell voltage were identified to diffuse to the anode and increase side reactions there [195]. In this paper, coupled side reactions are such combinations of anodic and cathodic side reactions where the amount of lithium that is intercalated at the cathode and the amount of lithium consumed at the anode are identical. As illustrated in Figure 21f, this leads to an identical right-shift of both half-cell curves and results in an identical shift of the discharging and charging endpoint. As a consequence, these side reactions cause a fully reversible self-discharge without a change in the actual capacity of the cell [196]. Hence, there are no changes in the inventory of cyclable lithium, as long as there is no considerable degradation of the electrodes.

The side reaction mechanisms presented above all base on a delithiation of the anode and/or a relithiation of the cathode. They all have in common that they reduce the energy content of the battery cell – even if the actual capacity of the cell remains unchanged or even increases. In those cases, the energy loss occurs in the form of a reversible self-discharge which can be recovered during the next charging sequence. Other hypothetical side reactions which cause a lithiation of the anode or a delithiation of the cathode are not taken into consideration. They do not appear feasible, as they would increase the energy content of a battery cell during storage, which is considered as thermodynamically unfavorable. An increase in the energy content during storage periods can only be expected when there was a previously generated inhomogeneity of the lithium distribution in the electrodes, e.g., in the “overhang areas” of the anode, which have no opposed cathode counterpart [197,198]. In these cases, the equalization process of previously generated concentration gradients can appear as an increasing energy content during storage. As such effects are no aging-related side reactions, the three side reaction mechanisms presented in Figure 21 were sufficient to reproduce and explain the capacity fades and endpoint shifts which occurred in the two calendar aging studies presented in this thesis.

4 Battery Aging during Nonoperating Periods

Passenger vehicles are typically parked more than 90% of the day [199]. As a consequence, an EV is in nonoperating state most of the time and battery degradation related to calendar aging is of high importance [168]. In this thesis, calendar aging of the high-energy NCA lithium-ion cells was investigated by two experimental studies. The results of these studies exhibit the dependencies of capacity fade and resistance increase on SoC, temperature, and charge-discharge history. Moreover, the origins of capacity fade can be identified by DVA and Coulomb Tracking. Furthermore, projections on calendar life are presented. This provides valuable information for optimized operating conditions for EV batteries. Parts of the results were also presented in Refs. [120,186].

4.1 Insights from the Literature on Calendar Aging

In general, calendar aging comprises all aging processes that lead to a degradation of a battery cell independent of charge-discharge cycling. As presented in Chapter 2, parasitic side reactions at the electrode-electrolyte interfaces are considered to be the predominant degradation processes, which cause electrolyte reduction at the negative electrode and electrolyte oxidation at the positive electrode. Calendar aging is an important factor in many applications of lithium-ion batteries where the operation periods are substantially shorter than the idle intervals, as it is the case for EVs. Furthermore, the degradation owing to calendar aging can also be predominant under cycling conditions, especially when cycle depths and current rates are low [154,200].

Käbitz et al. [154] compared two types of storage conditions: storage at a constant voltage source and storage in open circuit condition. The study revealed that there is generally no dependency of calendar aging on the type of storage. Only for storage at 100% SoC, the examined NMC cells showed a faster degradation when being connected to the voltage source during the storage period. Hence, storage in open circuit condition is applied in this thesis as this represents the typical usage condition of an EV battery and also allows to perform Coulomb Tracking.

There are many studies on calendar aging of lithium-ion batteries which present the capacity fade of the cells over time but do not provide explicit investigations on anodic or cathodic side reactions causing the capacity fade [105,109,154,168,201–205]. In general, accelerated aging is observed for higher temperatures. Moreover, the studies report intensified aging at higher SoCs. However, the studies usually considered only a few storage SoCs or storage voltages. Most of the studies examined only three different values or fewer [105,109,168,202–209], and there is one study that investigated five SoCs from 20% to 100% [154]. Hence, none of these studies covered the entire SoC range from 0% to 100% and none are able to thoroughly report the relationship between SoC and capacity fade.

Only Ecker et al. [201] investigated calendar aging with a finer SoC resolution; they examined the aging of NMC lithium-ion cells at 12 storage voltages. A correlation between the capacity fade and the graphite stages was identified. Since the correlation between open circuit voltage and SoC changes with aging, the SoCs of cells examined with a predefined voltage level tend to drift with

increasing capacity fade [210]. This impedes the assignment of the aging results to explicit SoC values which represent a certain ratio of stored ampere-hours to cell capacity. It also prevents a robust analysis of storage SoCs close to the potential steps of the graphite anode when the balancing of the electrodes shifts due to a loss of cyclable lithium.

Consequently, to further examine and verify the impact of the graphite electrode on the calendar aging of lithium-ion batteries, experimental aging studies with a fine SoC resolution are presented in this thesis. Storage SoCs related to the actual cell capacity were examined in addition to voltage levels. Moreover, side reactions were analyzed to determine root causes of degradation. The investigations on calendar aging are necessary for a separation of calendar and cycle aging.

4.2 Objectives for the Own Aging Studies

Calendar aging plays an important role for EV batteries since they are in nonoperating condition most of the time. The experimental aging studies presented in this chapter had the following objectives:

- Determining the predominant aging mechanisms for capacity fade and resistance increase
- Identifying side reactions during nonoperating periods
- Analyzing the impact of SoC on calendar aging
- Analyzing the impact of temperature on calendar aging
- Providing baseline degradation curves for the aging study on driving operation
- Deducing strategies for minimizing aging during nonoperating periods

4.3 Design of the Experimental Studies

Two calendar aging studies were performed in parallel to the cycle aging studies to obtain baseline aging curves for different SoCs and temperatures. Moreover, the impact of the graphite anode was investigated by fine resolutions of the storage SoCs. In addition to that, side reactions were examined by coulometry. Figure 22 provides an overview over both aging studies, where each test condition was examined with one new cell.

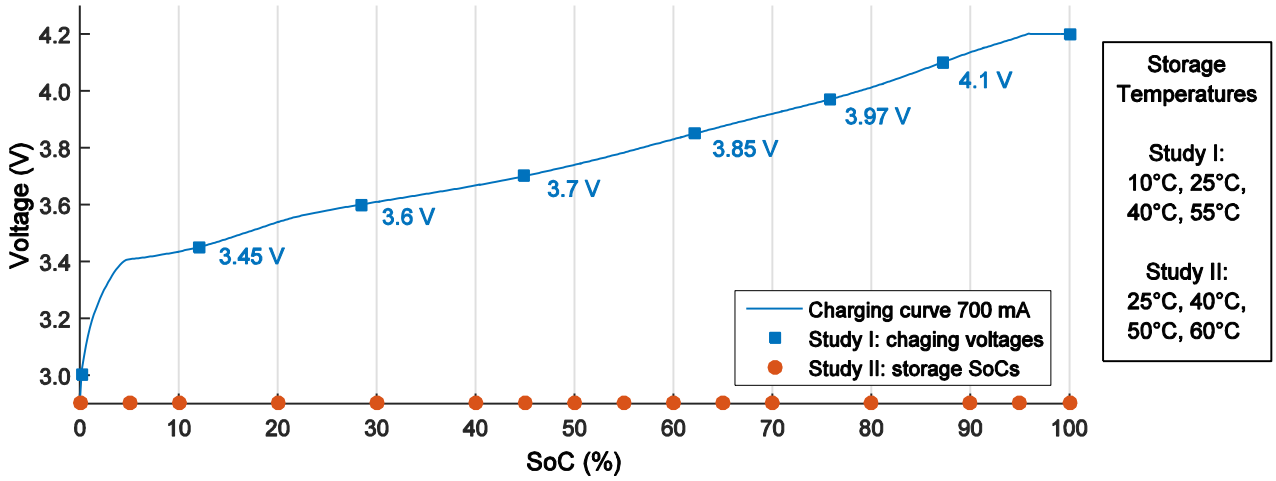

Figure 22. Overview on the storage conditions of the two calendar aging studies.

The first study covered eight different SoCs and a temperature range from 10°C to 55°C. The second calendar aging study was conducted with an even finer SoC resolution consisting of 16 storage SoCs and a more extensive checkup procedure. This helped to not only determine the extent of calendar aging but also identify origins of capacity loss and resistance increase from calendar aging. In that study, storage temperatures from 25°C to 60°C were examined.

The two studies used different methods for establishing the storage SoC, which will also be explained in the following sections, where the test procedures are presented in detail. In both studies, the cells were stored in disconnected state, as storage in open circuit condition is a prerequisite for Coulomb Tracking evaluations. This storage condition also represents a more realistic scenario for an EV, because the battery pack is explicitly disconnected by opening the relays in the power path when the EV is parked or when the charging procedure at the charging station has been completed.

4.3.1 Calendar Aging Study I

The first calendar aging study was conducted in parallel to the study on driving operation, which will be presented in Chapter 6, to separate usage-independent aging components from aging components related to charge-discharge cycling. In this calendar aging study, cells from the first lot were examined.

4.3.1.1 Test Conditions

This calendar aging study examined eight storage levels from completely discharged to fully charged condition, as illustrated in Figure 22. Furthermore, four temperatures were examined: 10°C, 25°C, 40°C, and 55°C. Hence, 32 combinations of storage SoC and storage temperature were investigated in this study. Whereas the temperatures were defined with uniform intervals of 15°C, the storage SoCs between the fully charged and completely discharged condition were defined discretionary. Except for the maximum and minimum SoC, the SoCs were defined by target charging voltages for a CC charging procedure with a charging current of 700 mA (= C/4), as it is illustrated in Figure 22.

4.3.1.2 Test Procedure

For each of the four temperatures, the eight cells with different SoCs were stored in the respective thermal chamber. Before the test procedure and periodically throughout the entire test period, checkups were performed at 25°C to assess the aging progress. As illustrated in Figure 23, the checkup procedure contained voltage ramps for cyclic voltammetry, CCCV charging and discharging for capacity measurements, and pulses at 50% SoC to monitor changes in internal resistances. A detailed description of all checkup procedures with explicit parameter values is provided by Table A-4 in the appendix.

The checkup procedure ended at 50% SoC. At this SoC, a galvanostatic EIS measurement ranging from 10 kHz to 10 mHz was performed with an RMS excitation amplitude of 50 mA. Finally, each cell was brought to its respective storage level again. Cells with a storage SoC above 50% were directly charged with 700 mA to the particular SoC, whereas the other cells were discharged first before charging to the desired storage SoC (see Figure 23b and Figure 23d).

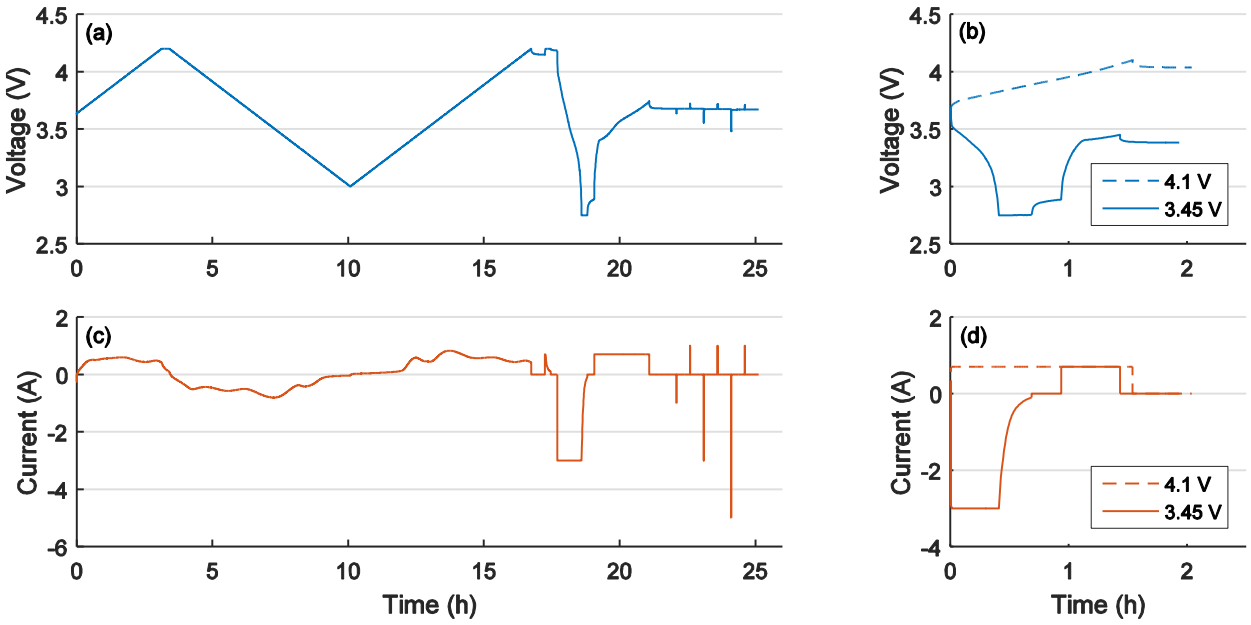

Figure 23. (a) Voltage and (c) current curves of the checkup procedure used in the first calendar aging study. (b,d) Charging the cells to different storage SoCs after the checkup.

In this aging study, the cells had to be disconnected from the battery test system after the checkup to perform the EIS measurement at the galvanostat. After the EIS measurement, the cells were reconnected to the battery test system. As the checkup and the charging to storage SoC were performed with two separate test procedures, the second test procedure had no information about the actual capacity measured in the checkup. As manual adjustments of the test protocols after each checkup were not practicable, the storage levels were defined as voltage levels for the CC charging sequence instead.

4.3.1.3 Degradation Monitoring

To monitor changes in capacity, the actual capacity was determined as the amount of ampere-hours discharged during the CCCV discharging sequence. From the first calendar aging study, the charging ramp before the capacity measurement was also evaluated by Coulomb Tracking to determine the slippage of the charging and discharging endpoints. Resistance changes and differential voltage spectra were analyzed based on the data from the second calendar aging study.

4.3.2 Calendar Aging Study II

Approximately 12 months after the beginning of the first calendar aging study, a second calendar aging study was started with a finer SoC resolution to investigate the interdependencies between SoC, anode potential, and battery aging more comprehensively. Moreover, a different way of defining the storage SoCs was employed and more extensive checkup procedures were applied to identify origins of the capacity fade and the increase of internal resistances. In this study, cells from the second production lot were examined.

4.3.2.1 Test Conditions

As illustrated in Figure 22, the storage SoCs of the second calendar aging study were defined in relation to the actual capacity. In total, 16 SoCs from 0% to 100% were examined. To obtain a fine SoC resolution, test points were defined every 10% SoC. Moreover, 5% and 95% SoC were added to have a finer resolution at the boundaries. As substantial differences in capacity fade were observed between the fourth test point (~45% SoC) and fifth test point (~62% SoC) in the first calendar aging study, additional test points at 45%, 55%, and 65% were specified.

Since this study started later, its focus was on higher temperatures for accelerated calendar life testing. In addition to 25°C and 40°C, which were also examined in the first study, high temperatures of 50°C and 60°C were added. This provided a finer resolution of the accelerated aging at elevated temperatures between 40°C and 60°C.

4.3.2.2 Test Procedure

For each of the four temperatures, 16 cells with different SoCs were stored in disconnected state in the respective thermal chamber. For a thorough investigation of aging effects, an extended checkup and a standard procedure were employed. All checkups were conducted at 25°C.

Extended Checkup Procedure

The extended checkup, depicted in Figure 24, contained voltage ramps for cyclic voltammetry, low-current discharging and charging for DVA, CCCV charging and discharging for capacity measurements, and a sequence of charging and discharging pulses repeated at ten equidistant SoC levels from 100% to 10% to monitor SoC-dependent changes of internal resistances.

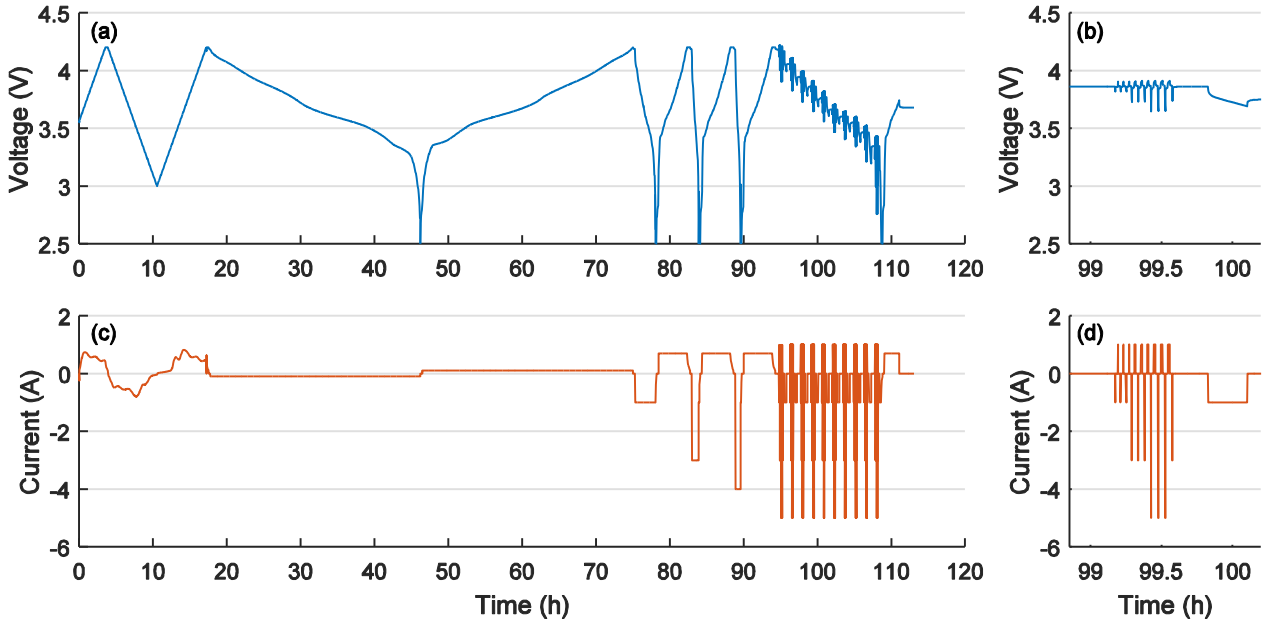

Figure 24. Extended checkup procedure of the second calendar aging study. (a,c) Overview over the entire checkup procedure. (b,d) Example of the pulse test sequence which was repeated at 10 SoCs.

The pulse sequence is illustrated in Figure 24b and Figure 24d and consisted of pairs of discharging and charging pulses. The discharging pulses had a duration of 10 s and amplitudes of 1 A, 3 A, and 5 A. The subsequent charging pulses all had an amplitude of 1 A and charged exactly the amount of charge which was discharged by the preceding discharging pulse. Hence, the pulse length increased

with higher amplitude of the discharging pulse. For each discharging amplitude, three repetitions of the discharging and charging pulse pair were performed. The pauses between the pulses lasted 30 s. Again, a detailed description of the checkup procedure can be found in Table A-6 in the appendix.

Standard Checkup Procedure

In addition to the long-lasting extended checkup, a standard checkup was defined (see Figure 25): It started with an EIS measurement, contained a low-current charging sequence for DVA, a CCCV discharging sequence for capacity measurement, and a second EIS measurement at 50% SoC. In this calendar aging study, the checkup procedure was performed at a battery test system with an EIS multiplexer. This allowed to perform the entire test procedure, comprising the checkup routine, EIS measurements, and establishing the storage SoC, within the same test protocol.

Integrating the different parts of the checkup into a single test procedure provided two advantages: First, the EIS measurements at 50% SoC could be performed after a defined rest period of 1 h, which avoided distortions from different relaxation times between charging to 50% SoC and the EIS measurement. Second, the actual capacity, measured during CCCV discharging, could be used to establish the storage SoC at the end of the test procedure automatically in relation to the actual capacity.

Different Ways of Establishing the Storage SoC

To investigate the impact of different intercalation configurations of the electrodes, two different ways of establishing the desired storage SoC were defined: The standard way, which was applied for all storage temperatures, was to reach the storage SoC from a fully discharged state. Hence, all cells with a storage SoC below 50% were completely discharged after the EIS measurement at 50% SoC before being recharged to the storage SoC (see Figure 25a and Figure 25c). The other cells, with storage SoCs above 50%, continued charging after the EIS measurement.

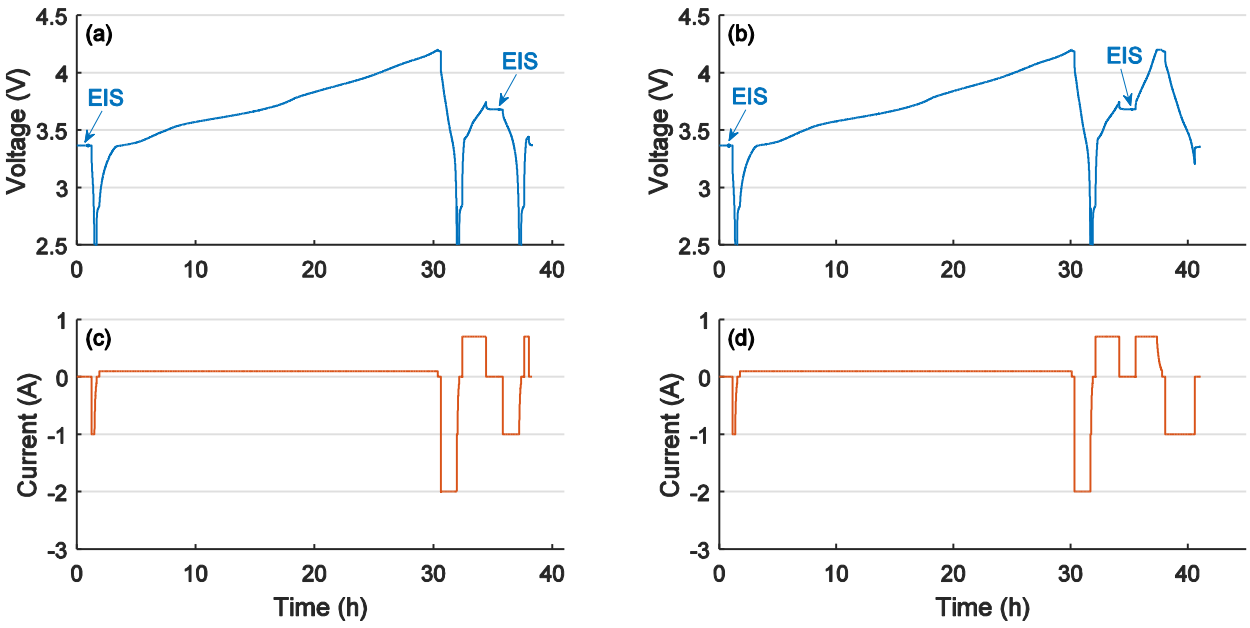

Figure 25. Standard checkup procedure of the second calendar aging study ending either with (a) charging or (b) discharging to the storage SoC. The examples illustrated here end at a storage SoC of 10%.

The second way of reaching the storage SoC, which was only applied for an additional set of 16 cells stored at 50°C, was defined as being discharged from 100% SoC. As shown in Figure 25b and Figure 25d, all cells were fully charged after the EIS measurement and then discharged to the particular storage SoC.

The checkups were performed before the storage periods and in periodic intervals. The standard checkup had been performed more frequently than the extended checkup due to the long duration of the extended checkup procedure. As only the standard checkup included the EIS measurements and the establishing of the storage SoC, it was also performed after each extended checkup. The checkups were performed with decreasing frequency, as the degradation is typically largest in the first months of a calendar aging study.

4.3.2.3 Degradation Monitoring

The changes in capacity presented for cells from the second calendar aging study were computed from the CCCV discharging capacity measured in the standard checkup. The low-current charging sequence of the standard checkup was used to determine the slippage of the charging and discharging endpoints. This charging sequence was also used for the computation of differential voltage spectra.

The results of the extended checkup for cyclic voltammetry, DVA, and ICA revealed that DVA was most suitable for the assessment of individual electrode degradation and loss of lithium inventory. Hence, only the results from DVA are presented and discussed in this thesis.

Resistance changes were analyzed based on EIS measurements at 50% SoC, which were performed in the standard checkup. From the extended checkups, the current pulses were used to compute $R_{dc,10s}$ resistance values to identify changes in cell resistances at 50% SoC as well as at different SoCs.

4.4 Results and Discussion

The two calendar aging studies provide comprehensive insights about the degradation of lithium-ion batteries in EVs during nonoperating periods. This section presents the results on capacity fade, side reactions, and increasing resistances. All time-related results are presented versus storage time. Storage time comprises only the time periods in the thermal chambers and excludes the checkup times at 25°C. At the end of this section, projections for calendar life predictions are made.

4.4.1 Capacity Fade and Its Characteristics

The capacity fade is typically the most important degradation effect in EVs as it limits the available driving range. This section presents and compares the results of both calendar aging studies to identify root causes for the decreasing battery capacity during nonoperating periods.

4.4.1.1 Typical Capacity Curves

Figure 26 shows typical capacity curves for calendar aging and presents data from cells stored at low, medium, and high SoC. These are results from the first calendar aging study, which covered storage temperatures from 10°C to 55°C. The curves demonstrate that degradation aggravates substantially with higher temperature. While the capacity fade after ca. 660 days of storage lies between 2% and 4% at 10°C, the capacity fade at 55°C amounts to 9–17%. However, the capacity fade does not double for every 10°C of temperature increase, as it is often considered as a rule of thumb, which is based on typical reaction kinetics and the Arrhenius law. For the cell type investigated in this thesis, the capacity fade at 55°C is about 4 times the capacity fade at 10°C.

Furthermore, the curves in Figure 26 exhibit the characteristic shape of capacity fade from calendar aging, where the degradation rate is highest in the beginning and slows down over time. This shape is typically described with a square-root-of-time relationship [211,212]. However, the shape of the curves slightly differs among the different storage SoCs. Particularly for the high SoC, depicted in Figure 26c, a substantial capacity fade is observed at the beginning of the aging study for all storage temperatures.

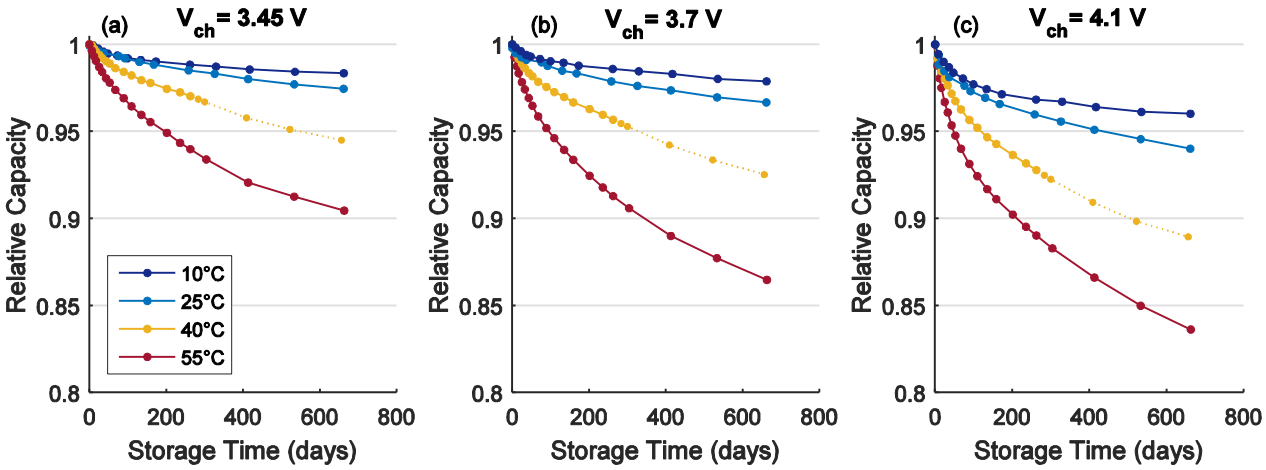

Figure 26: Capacity development of cells from the first calendar aging study stored at temperatures from 10°C to 55°C. The capacity fade is shown for cells stored at (a) low SoC, (b) medium SoC, and (c) high SoC. The dotted segment of the 40°C curve represents corrected data, after the cells had been exposed to more than 70°C for several days due to a defect of the temperature controller of the thermal chamber.

4.4.1.2 Impact of the Short-Term Operating History

When evaluating the results from the second calendar aging study, a certain impact of the short-term operating history was observed. This is illustrated in Figure 27, where the capacity fade is presented for the cells stored at 25°C and 50°C. The capacity values are all obtained from standard checkup measurements. However, these standard checkup measurements were either performed after an extended checkup or directly after a storage period. This is indicated by asterisks and dot markers, respectively. As the degradation rate is typically highest in the beginning and decreases over time, checkups were performed more often in the first months of the aging study. These checkup measurements were mainly performed as standard checkups only, which are illustrated by the dot markers in Figure 27.

Due to the two different checkup constellations, the initial conditions of the cells at the beginning of the standard checkup measurement procedure varied. When only the standard checkup was performed, the cells were at their respective storage SoC at the beginning of the checkup procedure. By contrast, all cells had already performed several charge-discharge cycles and had a uniform SoC of 50% when the standard checkup was performed after a run of the extended checkup procedure.

Figure 27 demonstrates that these different checkup constellations directly affect the capacity measurements. For storage SoCs of 60% and above, an increased capacity fade is observed when the standard checkup is performed without a preceding run of the extended checkup. For storage SoCs below 20%, a lower capacity fade is observed and for the cells stored at 0% SoC, Figure 27 even shows a capacity increase at the beginning. As a consequence, the capacity spread between the cells stored at 0% SoC and the cells stored at 100% SoC is substantially larger when the standard checkup is performed without a preceding extended checkup. Hence, the different short-term operating history and the preceding storage SoC have a considerable impact on the degradation monitoring.

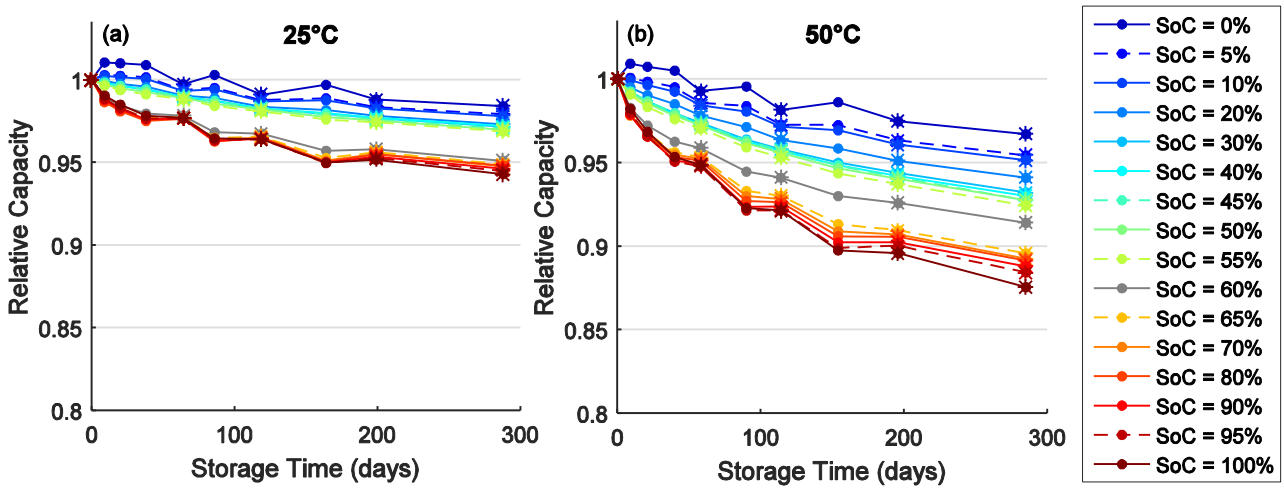

Figure 27: Capacity development obtained by the standard checkup procedure. Asterisks indicate standard checkup runs performed after an extended checkup. For these runs, capacity divergence between 0% and 100% SoC is lower than for those standard checkup runs performed directly after a storage period.

When the standard checkup is performed after an extended checkup, the initial conditions of all cells are similar. As the capacity values lie closer together when the checkup procedure is performed from a uniform start SoC of 50%, these capacity measurements appear more representative. Hence, only these values are evaluated in the subsequent sections. In the first calendar aging study, there

was only one checkup procedure. This checkup procedure contained an initial charge-discharge cycle before the capacity measurement. This helped to avoid distortions from effects of the preceding storage SoC.

Figure 27 also reveals that the capacity fade does not increase steadily with the SoC. Instead, groups of cells can be identified where the capacity fade is similar or lies close together. Such groups can be found particularly at medium and high SoCs and will be examined in the next section.

4.4.1.3 SoC Regions of Similar Capacity Fade

The finer SoC resolution of the second calendar aging helps to obtain a detailed understanding of the impact of SoC on battery aging during nonoperating periods. Figure 28a illustrates the capacity fade versus SoC for different storage periods at 25°C and 50°C. It exhibits no steady increase with higher SoC. Instead, there are plateau regions, covering SoC intervals of more than 20% of the cell capacity, in which the capacity fade is similar. There is one plateau in the high SoC region (65%–90%) and one plateau in the mid SoC region (30%–50%). In the low SoC region (0%–30%), the capacity fade increases steadily with higher SoC.

The fine SoC resolution enables a localization of the marked step between 55% and 60% SoC which separates the plateau regions of medium and high capacity fade for storage at 25°C. This precise localization has not been possible with the data from the first calendar aging study, where only the two test points at ca. 45% and 62% SoC were available. For storage at 50°C, the transition from medium to high capacity fade occurs between 55% and 65% SoC.

Figure 28b illustrates the capacity fade also for the other two storage temperatures. Similar trends and plateau regions can be observed. The more noisy shape of the capacity curve for 60°C can be ascribed to the larger temperature inhomogeneity inside the corresponding thermal chamber, which was of lower quality and precision. For 60°C, the transition zone between medium and high capacity fade widens to 55–70% SoC.

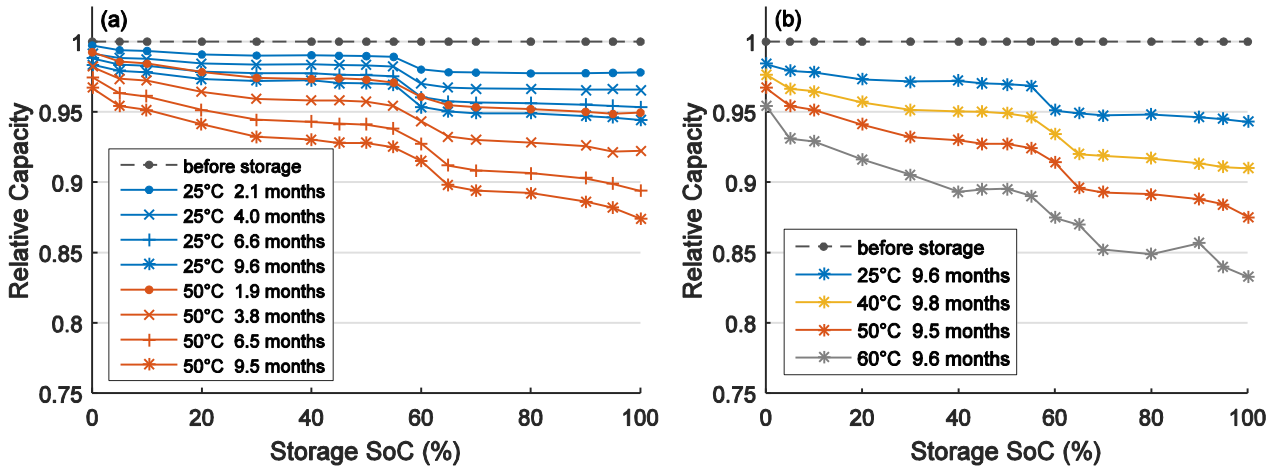

Figure 28. Relative capacity depending on storage SoC (a) after different storage durations at 25°C and 50°C and (b) for different temperatures after ca. 9.5 months of storage.

4.4.1.4 Different Ways of Establishing the Storage SoC

As the initial condition of the cell at the beginning of a checkup measurement has a considerable impact on the degradation monitoring, two ways of establishing the storage SoC at the end of the standard checkup procedure were examined. The standard way was charging to the storage SoC from a completely discharged state; the second way was discharging to storage SoC from a fully charged state. For both ways, a set of 16 cells each was stored at 50°C. The checkups were performed after identical storage intervals for both sets of cells. The purpose of this comparison was to determine whether the way of establishing the storage SoC, which can lead to different internal distributions of the intercalated lithium, has an impact on calendar aging and on the capacity measurements.

Figure 29 presents the capacity fade of both sets of cells after four different storage periods at 50°C. Both sets exhibit similar plateaus of high and moderate capacity fade at high and medium SoC, respectively. Overall, there are only minor deviations among both sets of cells. This demonstrates that the capacity fade does not depend on the way of establishing the storage SoC. Moreover, the additional partial cycle performed at the end of each standard checkup for establishing the storage SoC by discharging from a fully charged state has not increased degradation.

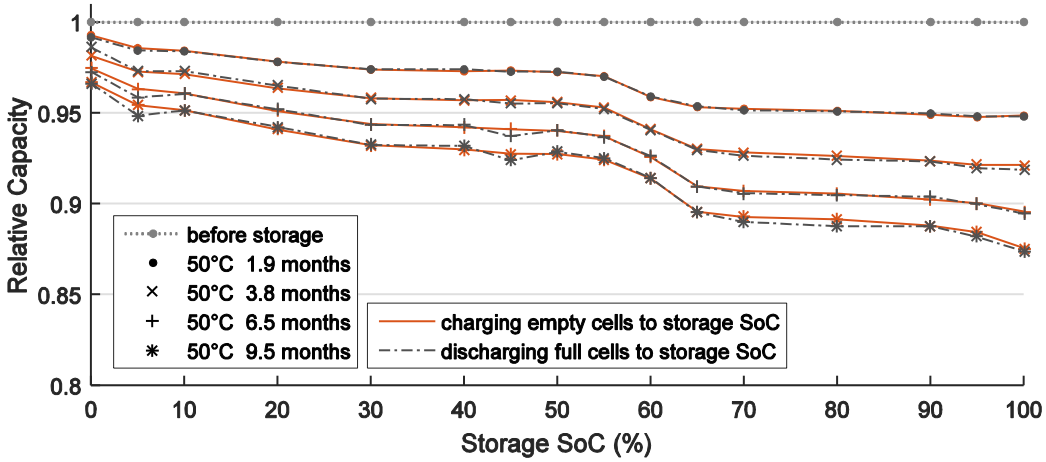

Figure 29. Comparison of the capacity fade under storage at 50°C for two sets of cells with different ways of establishing the storage SoC

4.4.1.5 Reproducibility

The two sets of cells depicted above in Figure 29 exhibit similar degradation. Cell-to-cell variation is almost negligible. After 9.5 months of storage, the mean difference of the 16 SoCs amounts to only 0.1 percentage points. Moreover, there are only three SoCs that exhibit a difference greater than 0.3 percentage points. This confirms the high uniformity of the mass-produced lithium-ion cells investigated in this thesis. As the aging procedure of the second set of cells started 1.5 months after the aging procedure of the first set of cells, these results also confirm the good reproducibility of the aging results. Overall, the calendar aging studies provide reliable aging curves, which can also be used as baseline curves in cycle aging studies to separate the contributions of calendar and cycle aging.

4.4.1.6 *Insights from Differential Voltage Analysis*

To identify root causes of the capacity fade, DVA was performed. For storage at 50°C and various SoCs, Figure 30 depicts the differential voltage spectra after different storage periods. The length in x-direction of a spectrum represents the actual capacity. Although there are considerable capacity reductions, particularly for the higher SoCs, there are zero or only minor changes in the position of the central graphite peak at all SoCs. This indicates that there occur no considerable changes in the storage capabilities of the anode active material.

Between 1.0 Ah and 1.5 Ah, the *dV/dQ*-values increase with higher capacity fades. This appears like an evolving hump at the left side of the central graphite peak. Moreover, the depth of the very first valley at ca. 0.2 Ah decreases and the cross marker, indicating the cathode peak at high SoC, shifts to the left. All these changes agree well with a left-shift of the entire cathode half-cell voltage curve (compare Figure 18, p.36). Hence, the changes in the differential voltage spectra indicate a horizontal displacement of the anode and cathode half-cell curve against each other, which reduces the available cycling window of the full-cell and causes the capacity fade.

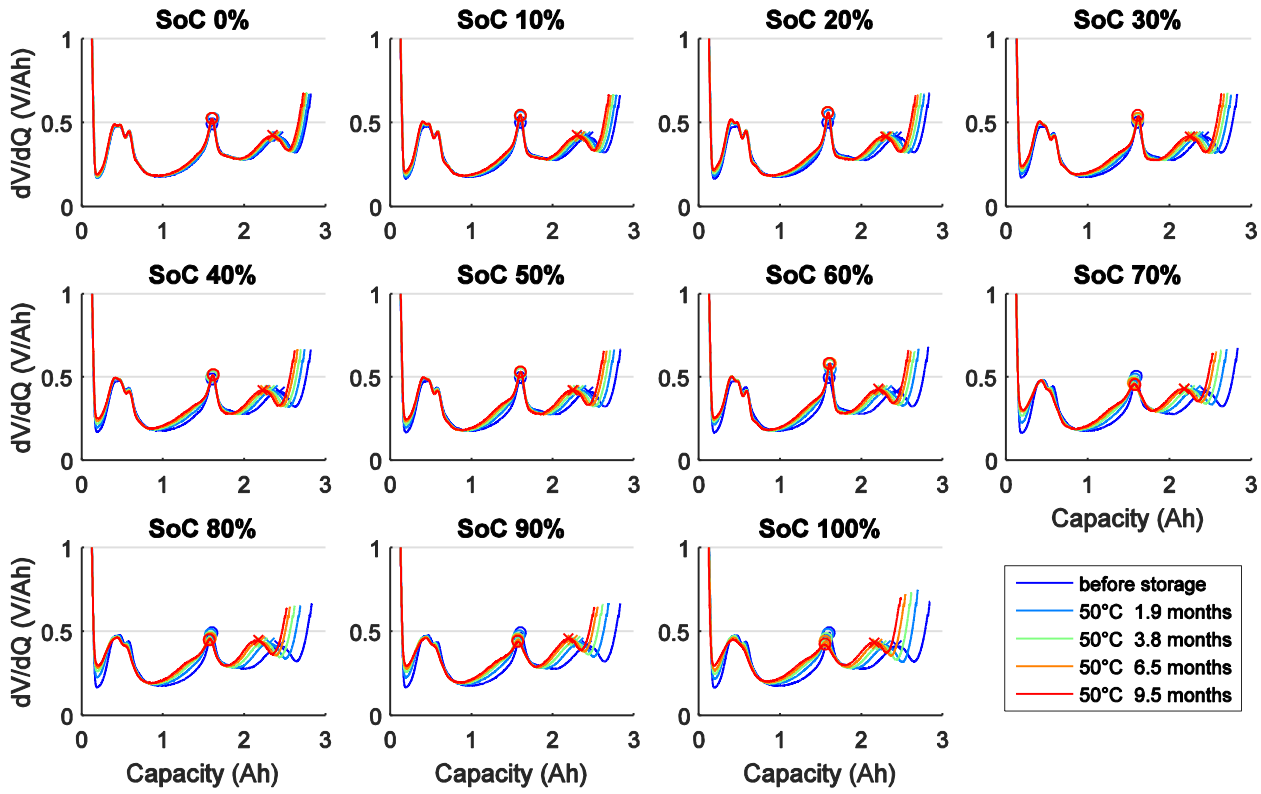

Figure 30: Differential voltage spectra for up to 290 days of storage at 50°C and various SoCs. The circle and cross markers indicate characteristic anode and cathode peaks, respectively.

Evaluation of Degradation Indicators

For a better interpretation of the differential voltage spectra and the contributions of anode and cathode, Figure 31 shows the fade of Q_{actual} for eight selected cells together with the changes in the degradation indicators Q_1, Q_2, and Q_3 of these cells after 9.5 months of storage. The actual capacities of these cells have faded between 60 mAh and 160 mAh for storage at 25°C and between 140 mAh and 350 mAh for storage at 50°C. This corresponds to a capacity fade of ca. 2–6% at 25°C and 5–12% at 50°C. The analysis of Q_1, Q_2, and Q_3 provides information about the origin of the capacity fade. The Q_1 capacities have remained rather unchanged for all cells after the 9.5 months of storage,

which corresponds to the unchanged locations of the central graphite peaks observed in Figure 30. This demonstrates that there has been negligible degradation of the anode itself, as no or only minor changes of the storage capabilities of the graphite active material can be observed. For Q_3, which represents the storage capability of the cathode active material, there are also only small changes detectable. In contrast to Q_1 and Q_3, substantial changes are observed for Q_2. The absolute reductions in the Q_2 capacities are similar to the reductions in Q_{actual}. As the changes in the Q_2 values indicate a shift in the electrode balancing and as the degradation of the individual electrodes has remained comparably low, the utilization of both electrodes decreases: The anode remains less lithiated at 100% SoC, where the cathode approaches its maximum permissible degree of delithiation; and the cathode becomes less lithiated at 0% SoC, where the anode is fully delithiated. This reduces the inventory of cyclable lithium. Overall, the analysis of Q_1, Q_2, and Q_3 has shown that the capacity fade from calendar aging results predominantly from a shift in the electrode balancing related to a loss of cyclable lithium.

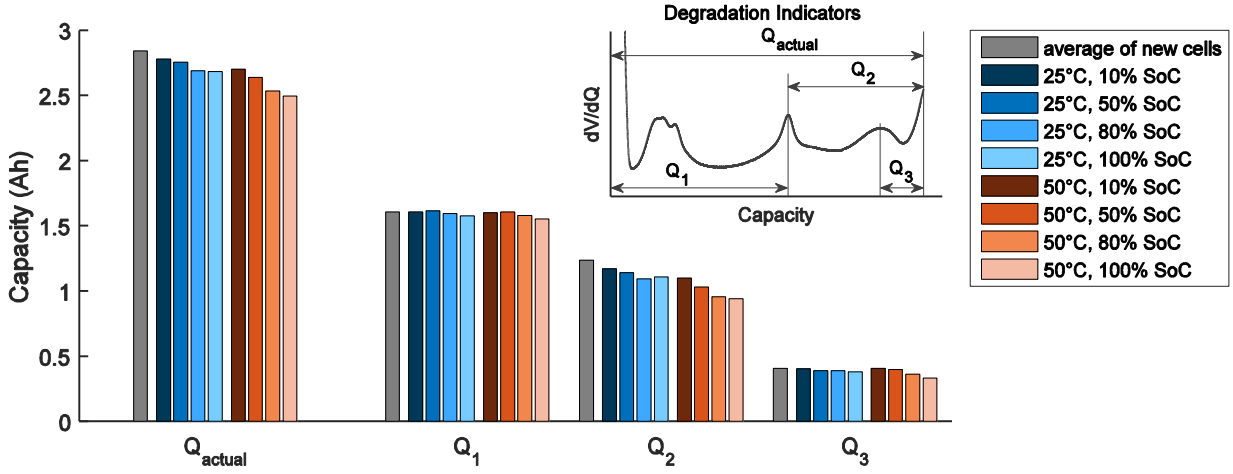

Figure 31. Actual capacity Q_{actual} and degradation indicators Q_1, Q_2, and Q_3 for the cells stored 9.5 months at 10%, 50%, 80%, or 100% SoC in the second calendar aging study

4.4.1.7 Impact of the Graphite Anode

The capacity fade at all storage temperatures has not increased steadily with higher SoC, but exhibits plateau regions, covering SoC intervals of more than 20% of the cell capacity, in which the capacity fade is similar. Figure 32 compares the capacity fade of the full-cells and the anode potential obtained from half-cell measurements, which also exhibits several plateau regions. A strong correlation becomes obvious, particularly for the cells stored at 25°C. The plateaus of high capacity fade, which lie above 60% SoC, correspond to the lowest voltage plateau of the anode potential. The transition between high and medium capacity fade occurs exactly at the transition point between low and medium anode potential, which is located at 57% SoC for the examined cell type in the new condition. This point is represented by the central graphite peak in the differential voltage spectra, as it was shown in Figure 18. It indicates a degree of lithiation of 50%. The medium anode potential between 30% and 60% SoC correlates well with the medium capacity fade for these storage SoCs. In the low SoC regime below 30% SoC, the anode potential rises and the capacity fade diminishes. This correlation between anode potential and capacity fade could also be verified for further lithium-ion cell types with graphite anodes but different cathode materials [120].

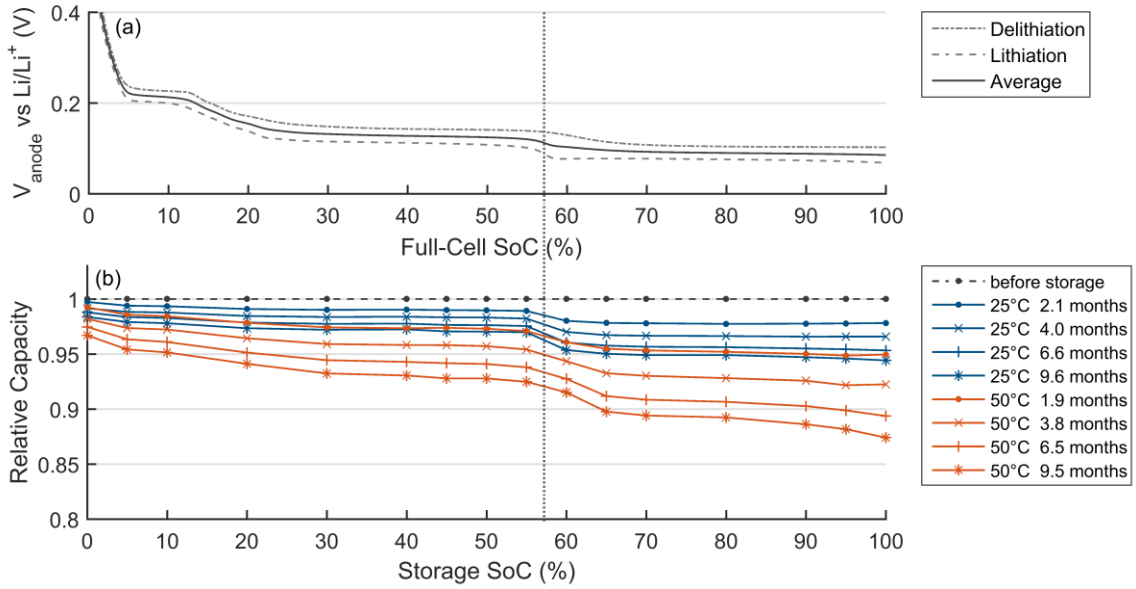

Figure 32. (a) Anode potential over SoC from half-cell measurements. (b) Capacity fade over storage SoC for different storage periods. The location of the central graphite peak in the differential voltage spectrum of the cells in the new condition is highlighted by a dotted vertical line.

In addition to the anode potential, the thickness of graphite anodes is also known to depend on the SoC. The expansion and contraction during lithiation and delithiation can cause cracks in the SEI and an SEI reformation, which consumes cyclable lithium. To determine whether these thickness effects can also be a major cause of calendar aging, the thickness changes of graphite anodes are compared with the observed capacity fade. Graphite anodes exhibit a largely linear expansion from 0% to 25% lithiation, only minor volume changes between 25% and 50% lithiation, and another linear expansion above 50% lithiation, where the LiC_6 phase formation begins [53]. Comparing this thickness behavior of lithiated graphite with the observed trends in capacity fade, an interdependency between graphite expansion and calendar aging can be disregarded: In the high SoC region above the location of the central graphite peak at 57% SoC, corresponding to a lithiation of the graphite anode greater than 50%, a constant capacity fade is observed. The thickness of the graphite anode, however, is continuously expanding above the central graphite peak. If the observed degradation was related to volume expansion, a continuously increasing degradation above the central graphite peak would be observed. Thus, it is not the expansion of the graphite causing the accelerated degradation at higher storage SoCs. Consequently, the accelerated capacity fade above the central graphite peak can be ascribed to the lower anode potential, which aggravates electrolyte reduction and, thus, promotes SEI growth.

For the cells stored at 50°C, Figure 32b shows a substantially higher capacity fade. Moreover, the transition between the different aging plateaus is not as sharp as for the cells stored at 25°C. This is an additional proof for the dependency of the capacity fade on the anode potential: Figure 33 demonstrates that this effect is a result of a change in electrode balancing which shifts the SoC location of the central graphite peak toward higher SoCs. Figure 33a and Figure 33b repeat the capacity fade of the cells stored at 25 and 50°C. The two cells stored at 60% SoC are highlighted. For these cells, Figure 33c and Figure 33d depict the corresponding differential voltage spectra for the different storage periods. The locations of the central graphite peak before the storage test and after about 9.5 months of storage are highlighted.

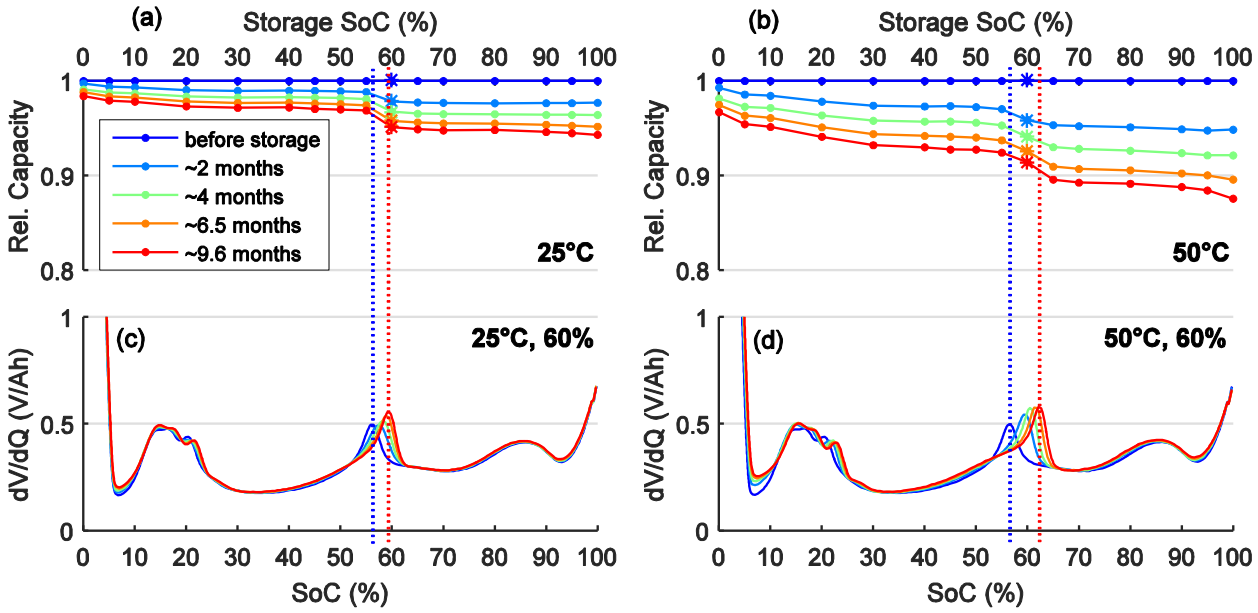

Figure 33. (a, b) Capacity fade over time for the cells stored at 25 or 50°C. Cells stored at 60% are highlighted, for which (c, d) show the corresponding differential voltage spectra. The location of the central graphite peak is highlighted for the new state and that following ca. 9.5 months of storage.

The cells stored at 60% SoC were analyzed because 60% SoC lies slightly above the location of the central graphite peak when the cells are new. For storage at 25°C (Figure 33c), the location of the central graphite peak still remains below 60% SoC after 9.5 months of storage. Hence, the cell stored at 25°C and 60% SoC has always been in the plateau region of high capacity fade. Thus, the transition zone has remained between 55% and 60% SoC. For storage at 50°C (Figure 33d), a higher capacity fade occurs, which has been caused by a greater loss of cyclable lithium. Due to the larger shift in the electrode balancing, the location of the central graphite peak lies above 60% SoC after only ca. 2 months of storage. Hence, the cell stored at 50°C and 60% SoC exhibited high capacity fade only during the first weeks of storage and then slipped into the regime of medium capacity fade. Thus, only the cells stored at 65% SoC and above exhibit the fastest capacity fade. Consequently, the transition zone expands to 55%–65% SoC. This clear correlation between the balancing of the graphite anode and the capacity fade during storage periods confirms that the anode potential has been the major driving force of calendar aging in this study, which aggravates electrolyte reduction and SEI growth.

The identification and evaluation of a widening transition zone was only possible because storage SoCs related to the actual capacity were used instead of voltage levels. They allowed the anode potential at the investigated storage SoCs to change with aging, which resulted in different aging rates over time for storage SoCs slightly above the initial SoC location of the central graphite peak.

Toward 100% SoC, Figure 33a and Figure 33b show some additional aging effects: The cells exhibit a somewhat increasing capacity fade from 80% to 100% SoC. As this does not correlate with the graphite potential, this degradation is thought to be caused by side-reactions driven by high cell voltage, such as oxidation of the electrolyte and transition-metal dissolution. This will be further examined by coulometry measurements in Section 4.4.2.

4.4.1.8 *Comparison of Both Aging Studies*

To compare the aging results of both aging studies, Figure 34 presents the capacity fade after ca. 9 months of storage. The results of the two studies and the different temperatures show that the order of the capacity fade in the low and medium SoC range (< 60% SoC) is similar for cells of the two studies, which stemmed from different production lots. In the high SoC range (> 80% SoC), however, the two groups of cells differ. In general, the capacity fade of lithium-ion cells is expected to increase with higher SoC. As it can be seen in Figure 34a, the capacity fade in the first aging study decreases again toward 100% SoC. Such a decrease is not observed in Figure 34b for the cells of the second aging study. Hence, it is assumed that the cells of the two productions lots were not 100% identical, as the aging mechanisms at high SoC differ considerably. Since the different aging behavior of fully charged cells can be observed at all storage temperatures, an effect solely caused by stochastic cell-to-cell variation within a production lot can be excluded. The origin of these differences is examined in the next section.

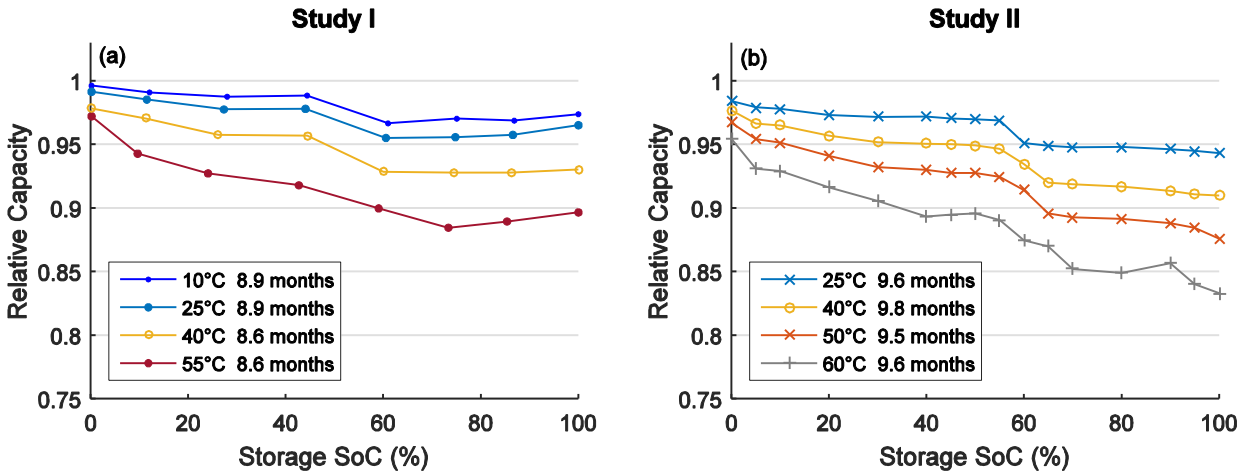

Figure 34. Capacity fade after ca. 9 months of storage at different storage SoCs and temperatures. (a) and (b) present the results from the two calendar aging studies performed with cells of the same type, but from different production lots.

4.4.2 Identification of Side Reactions by Coulomb Tracking

As determined by DVA, the capacity fade from calendar aging results predominantly from a shift in the electrode balancing which reduces the inventory of cyclable lithium. As the electrode materials remain largely intact, side reactions are expected to occur which affect the degree of lithiation of the electrodes and thus alter the balancing of the electrodes. Coulomb Tracking enables to analyze these aging processes.

From the checkup data of the first aging study, Figure 35 shows representative charging curves after different storage periods. Cells stored at different SoCs and temperatures are compared. The ampere-hour value at the beginning of each charging curve represents the ampere-hour value of the discharging endpoint in the continuous charge balance and the ampere-hour value at the end of the curve is the ampere-hour value of the charging endpoint. For all six cells presented, the discharging endpoints shift considerably to the right; and these shifts enlarge with higher SoC and temperature. The shifts of the charging endpoints also increase with SoC and temperature, but they remain substantially smaller than the shifts of the discharging endpoints. As described in the method

section on Coulomb Tracking (Section 3.6.2), only right-shifts of the endpoints occur as a result of the side reactions during the storage periods. From the varying endpoint slippage for different storage SoCs and temperatures, characteristics of anodic and cathodic side reactions can be derived.

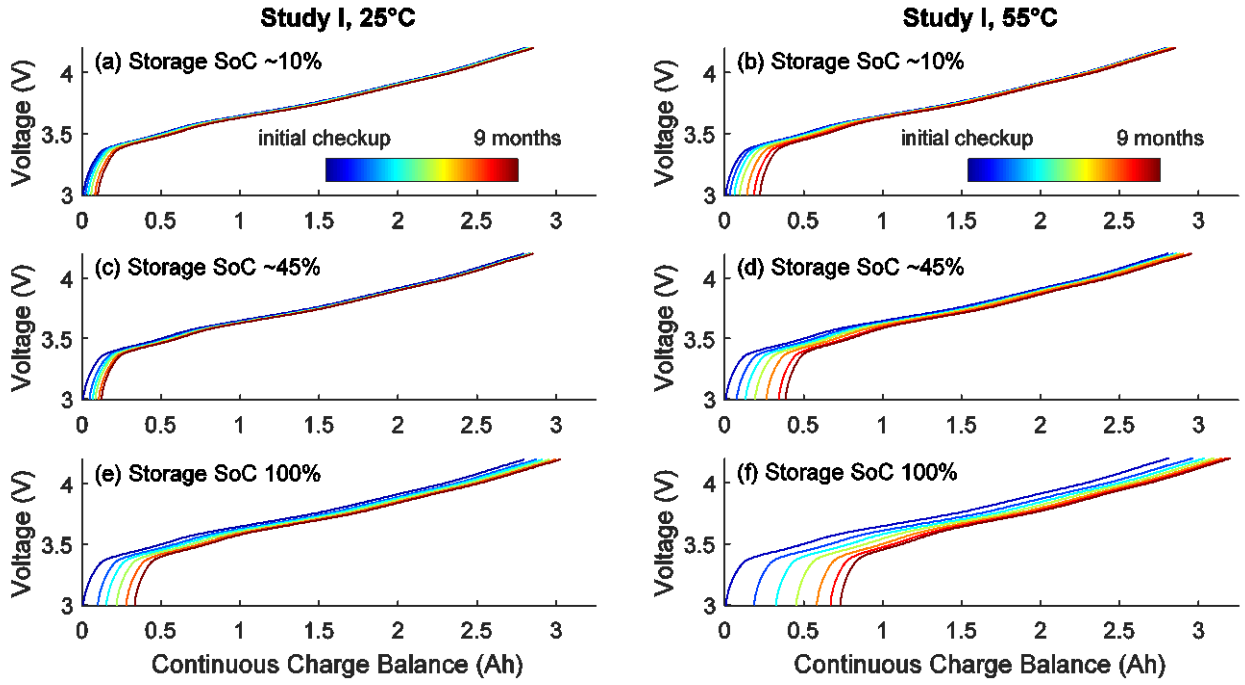

Figure 35. Charging sequence after different storage durations at 25°C and 55°C used for Coulomb Tracking. The shifts of the ampere-hour value of the beginning and of the end of each voltage curve represent the slippage of the discharging and the charging endpoint, respectively.

4.4.2.1 Minimal Cathodic Side Reactions at Low SoC

For storage at 10% SoC (Figure 35a, b), a considerable slippage of the discharging endpoints is observed, whereas the charging endpoints change only marginally. The stable charging endpoints indicate that the extent of cathodic side reactions is very low. Thus, coupled side reactions must also be very low as they always include cathodic side reactions. Consequently, solely anodic side reactions are the predominant aging mechanism at low SoC. These side reactions, which are related to electrolyte reduction and SEI growth, are known to cause right-shifts of the discharging endpoints and this agrees well with the observed changes.

4.4.2.2 Increasing Anodic Side Reactions with Higher SoC

Figure 35 demonstrates that with higher SoC, the slippage of the discharging endpoint increases markedly. Hence, the consumption of intercalated lithium of the anode due to electrolyte reduction and SEI growth aggravates. This can be caused either by solely anodic side reactions or by coupled side reactions, which simultaneously alter the degree of lithiation of the anode and the cathode. For three SoCs from 45% to 100% SoC, Figure 36 illustrates the overall capacity fade over time and the respective contributions of both endpoint shifts. The shifts of the discharging endpoints, presented in Figure 36g-i, exhibit that the rate of the endpoint slippage decreases with time. This is in good agreement with the supposed passivation layer growth, which slows down successively over time. As the anode potential decreases from 45% SoC to 75% SoC (see Figure 32a), increasing anodic side reactions occur as expected. If the slippage of the discharging endpoint was caused by solely anodic

side reactions, it should depend directly on the anode potential. Then, the endpoint shifts for 75%, 80%, and 100% SoC should be similar, as the anode potential remains constant for these SoCs. Instead, considerably larger shifts of the discharging endpoints are observed at 100% SoC. Consequently, there must be increasing coupled side reactions toward 100% SoC.

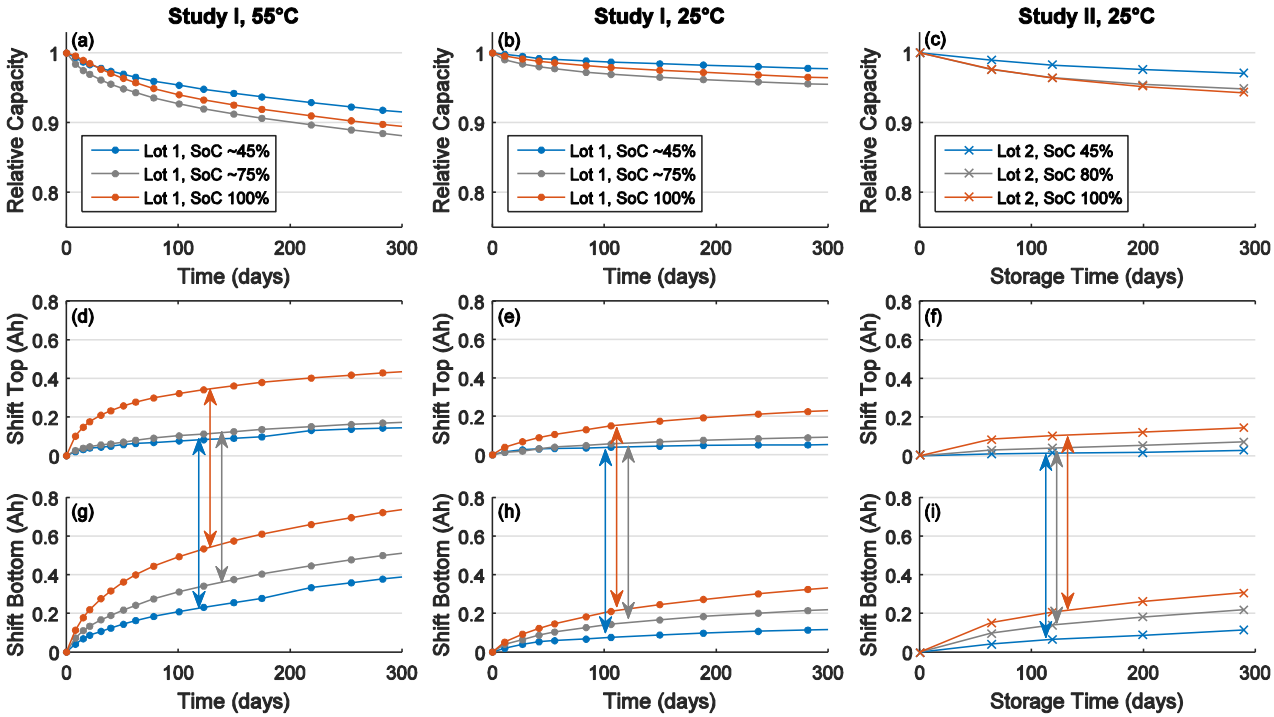

Figure 36. (a)-(c) Capacity fade, (d)-(f) shift of the charging (top) endpoint, and (g)-(h) shift of the discharging (bottom) endpoint for different storage SoCs. Different temperatures are shown for study I (left and center column); and cells from different production lots are compared for the storage temperature of 25°C (center and right column).

4.4.2.3 Coupled Side Reactions above 80% SoCs

In addition to the slippage of the discharging endpoint, Figure 36d-f shows the slippage of the charging endpoint. It is moderate or small for storage SoCs up to 80%. For storage at 100% SoC, however, increased shifts of the charging endpoints are observed at all temperatures. This indicates aggravating cathodic side reactions. As described above, there are also larger shifts of the discharging endpoints for storage at 100% SoC. This supports the assumption of coupled side reactions, e.g., from transition metal dissolution at the cathode and a reduction of the dissolved transition metal ions at the anode. As it can be seen in Figure 36f and Figure 36i for the shifts of the charging and the discharging endpoints of the cells from the second aging study, the differences between the curves for 80% and 100% SoC are similar. This confirms the assumption of a crosstalk between both electrodes which leads to coupled side reactions that alter the degree of lithiation of both electrodes. Deshpande et al. [183] reported interactions between the side reactions at both electrodes: A lithium-ion cell with the electrolyte additive vinylene carbonate (VC) exhibited lower anodic as well as cathodic side reactions than a reference cell without VC in the electrolyte. The authors suggest that reaction products from anodic side reactions migrate to the cathode and intensify cathodic side reactions. From our observations, the opposite direction appears more likely: As the anode potential remains constant in the high SoC regime between 70% and 100% SoC, the amount of reaction products from anode-initiated side reactions can be regarded as similar. Thus,

there is no source for intensified crosstalk behavior toward 100% SoC. At the cathode, however, side reactions – comprising electrolyte oxidation and transition-metal dissolution – aggravate with higher potential. Hence, the successively increasing cathode potential toward 100% SoC is regarded as a source of intensified crosstalk because an increasing amount of reaction products is generated at the cathode, which can migrate or diffuse to the anode and consume intercalated lithium there. This causal relationship also accords well with the above-mentioned reductions in anodic and cathodic side reactions when adding VC to the electrolyte, as VC is known to inhibit cathodic side reactions [189,213].

4.4.2.4 Additional Cathodic Side Reactions in the First Aging Study

The comparison of both aging studies also confirms that the cathodic side reactions do not rely on reaction products from anodic side reactions. According to Figure 36h and Figure 36i, the shifts of the discharging endpoints at 25°C are similar in both aging studies, which represents similar anodic side reactions. The shifts of the charging endpoints, however, are only similar for SoCs up to 80% and differ considerably for storage at 100% SoC. At 100% SoC, the shifts of the charging endpoints are substantially larger in the first aging study, which indicates intensified cathodic side reactions, although the anodic side reactions are similar. Consequently, there must be additional, solely cathodic side reactions. As introduced in section 3.6.2 on the effects of solely cathodic side reactions, they increase the actual capacity as they cause a reversible capacity fade together with a right-shift of the charging endpoint. Since the actual capacity corresponds to the difference between charging endpoint and discharging endpoint – which limit the inventory of cyclable lithium – it is directly affected by the slippage of both endpoints. The double arrows in Figure 36 illustrate the changes in the actual capacity resulting from the endpoint shifts. The arrows demonstrate that the irreversible capacity fade during storage is mainly caused by the slippage of the discharging endpoint, ascribable to electrolyte reduction and SEI growth, which reduces the inventory of cyclable lithium. Solely cathodic side reactions, which cause a reversible self-discharge, can relieve this reduction by right-shifting the charging endpoint. These side reactions are supposed to be oxidative processes which generate no reaction products affecting the anodic side reactions. Such solely cathodic side reactions explain why a lower capacity fade is observed in the first aging study for storage at 100% SoC than for storage at 75% SoC (see Figure 34a), independent of the storage temperature. As these cathodic side reactions are not observed in the second study, it is assumed that slight changes in the functional materials, such as modifications of the electrolyte and its additives, have reduced the cathodic side reactions of the cells examined in the second aging study, which were produced several months later.

4.4.3 Increase of Internal Cell Resistances

As battery aging and the corresponding side reactions do not lead to a capacity fade only but also to rising internal resistances, this section evaluates the resistance changes during nonoperating periods. Results from the second calendar aging study are presented as this study provides the finer SoC resolution and a more detailed examination of cell resistances. In the standard checkup measurements of the second calendar aging study, the resistance changes at 50% SoC were monitored by impedance measurements. In the extended checkup measurements, DC pulse measurements were performed at 10 SoCs between 100% and 10% to detect SoC-dependent resistance changes.

4.4.3.1 Impedance Spectra

For an overview over the changes of different resistance contributions, the impedance spectra obtained by EIS measurements at 50% SoC for new and aged cells are compared in Figure 37. This figure contains the impedance spectra of 16 cells which were stored at 50°C with different SoCs. Figure 37a shows the impedance before the first storage period. The 16 spectra are very uniform, which confirms the high production quality of the cells with very minor variation. The impedance variations amount to only 2%.

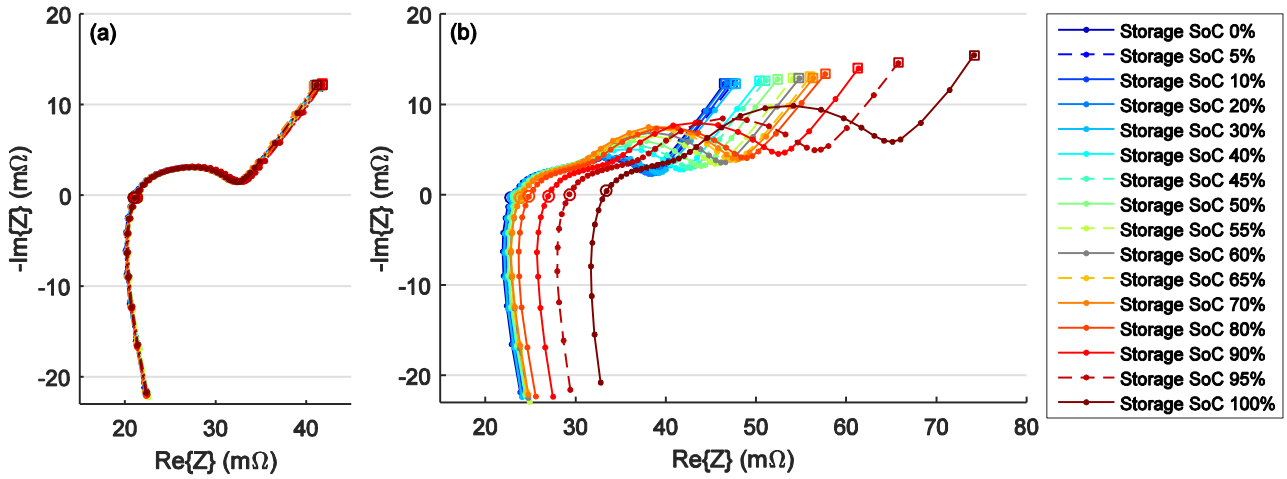

Figure 37. Impedance spectra at 25°C and 50% SoC (a) before and (b) after about 290 days of storage at 50°C

Changes in the Impedance Spectra of Aged Cells

Figure 37b contains the impedance spectra after a storage time of about 290 days at 50°C. The impedances at 1 kHz, where the imaginary part is very close to zero, are highlighted to illustrate changes in ohmic resistance contributions. For storage SoCs above 70%, an increasing shift of the 1 kHz impedance points to the right can be observed, which indicates increasing ohmic resistances.

In the medium frequency range of the aged spectra, a considerable growth of the second capacitive semicircle can be observed. This growth occurs most pronouncedly for storage SoCs above 30% and increases further with higher SoCs. The frequency range of this semicircle is dominated by contributions from the charge transfer reaction of the cathode, as it has been demonstrated by half-cell reconstructions (see Figure 9, p.25). Hence, the impedance spectra reveal an increasing cathode degradation with higher SoC.

In Figure 37, the impedances at 10 mHz are also highlighted to obtain an indicator for the overall impedance changes, covering changes in ohmic resistances, passivation layers, charge transfer resistances, and diffusion resistances.

Evaluation of R_{ac} Values for High and Low Frequencies

The real parts of the 1 kHz and 10 mHz impedances are also illustrated in Figure 38 for the cells stored at 25°C and 50°C. The values depicted in Figure 38b correspond to the impedance points highlighted in Figure 37. Whereas the impedance increase at 25°C is low and exhibits only a slight increase toward 100% SoC for $R_{ac,10mHz}$, more pronounced changes can be observed at 50°C. The $R_{ac,1kHz}$ values exhibit a continuous increase above 80% SoC. These changes indicate increasing ohmic cell resistances, which can be related to a reduced electrolyte conductivity.

For the $R_{ac,10mHz}$ values, a rather linear resistance increase can be observed between 30% SoC and 70% SoC, which is followed by an even more pronounced resistance increase above 80% SoC. As observed in the impedance spectra, this can be mainly ascribed to increasing cathodic charge transfer resistances. Due to the rising ohmic resistances above 80% SoC, the $R_{ac,10mHz}$ values automatically have to increase as well. However, their increase is even larger than the increase of the $R_{ac,1kHz}$ values. Hence, further resistance contributions from increasing charge transfer resistances or diffusion resistances have to apply here.

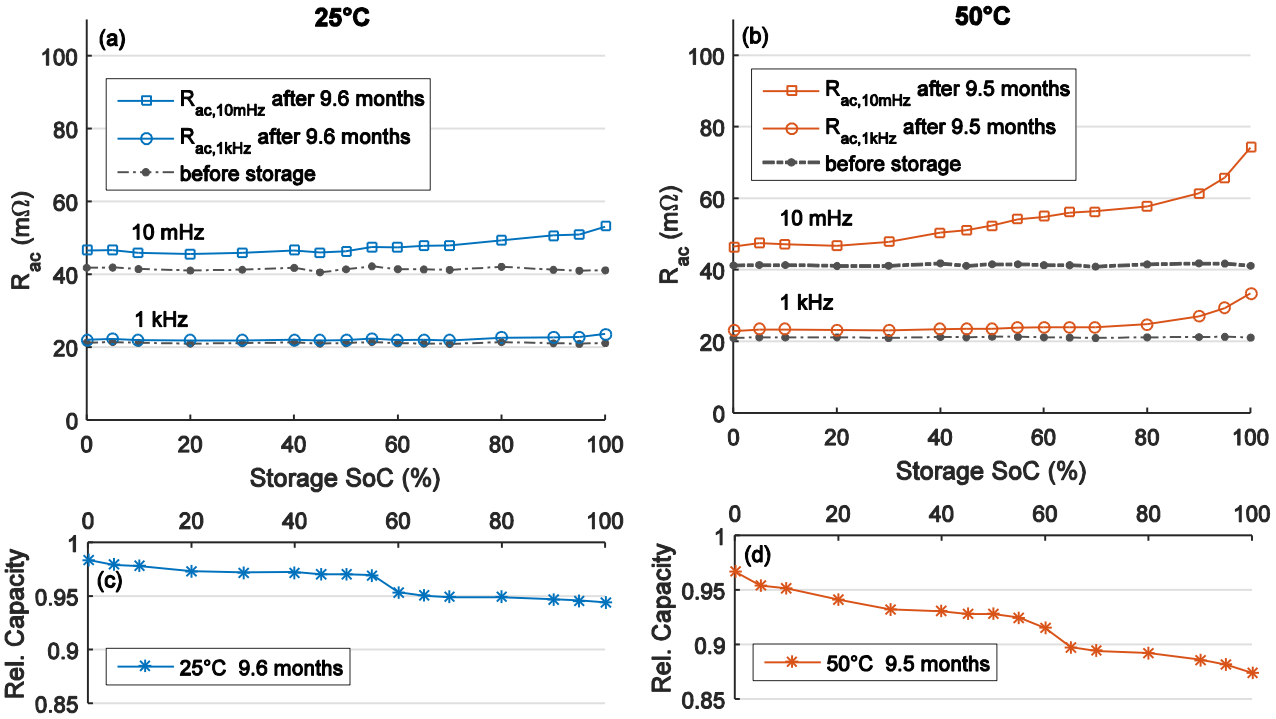

Figure 38. Changes in cell impedances after ca. 9.5 months of storage at (a) 25°C and (b) 50°C. (c) and (d) exhibit the corresponding capacity fade.

Comparison of Resistance Increase and Capacity Fade

Figure 38c and Figure 38d show the corresponding capacity fade of the cells stored at 25°C and 50°C, respectively. This demonstrates that there is no clear correlation between the capacity fade and the resistance increase. In the resistance curves, there is no plateau of medium aging at medium SoC and no plateau of high aging at SoCs above 65%. Thus, the capacity measurements and impedance

analyses detect different aging effects and might reveal separate aging mechanisms, which only correlate partially.

Only the slight increase of capacity fade above 80% SoC appears to correlate with the increases in the $R_{ac,1kHz}$ values. As the anode potential is constant in this SoC region, these aging effects are thought to be driven by cathodic side reactions which increase with higher cell voltage. As already identified by Coulomb Tracking, coupled side reactions occur at very high SoC. As the $R_{ac,1kHz}$ values increase notably, a considerable amount of electrolyte components seem to be consumed by these side reactions, which reduces its conductivity and increases ohmic cell resistances. The DVA results have also revealed that there is some reduction in the storage capability of the cathode active material for storage at high SoC, particularly at elevated temperature. The combination of these findings supports the argumentation that transition metal dissolution occurs at the high SoCs, as this causes a capacity degradation of the cathode as well as coupled side reactions.

Impact of Different Ways of Establishing the Storage SoC and Repeatability

In analogy to the capacity analyses, the two sets of cells stored at 50°C, which were brought to their storage SoCs on different charge-discharge paths, provide information about the sensitivity of the resistance increase to different charge-discharge histories which can lead to different internal distributions of the intercalated lithium. Figure 39 shows the development of $R_{ac,1kHz}$ and $R_{ac,10mHz}$ with respect to the respective value in the new condition. For both resistances, no considerable differences can be identified among the two sets of cells as the differences lie below the differences of the two cells stored at 100% SoC, which were exposed to the exactly the same charge-discharge procedure throughout the entire aging study. Hence, there is no impact of the way of establishing the storage SoC on resistance changes.

Moreover, the curves demonstrate a good repeatability of the results as there are only very minor resistance deviations among the two sets of cells. Hence, the capacity as well as the resistance curves from calendar aging confirm a high uniformity of the cells examined in this thesis.

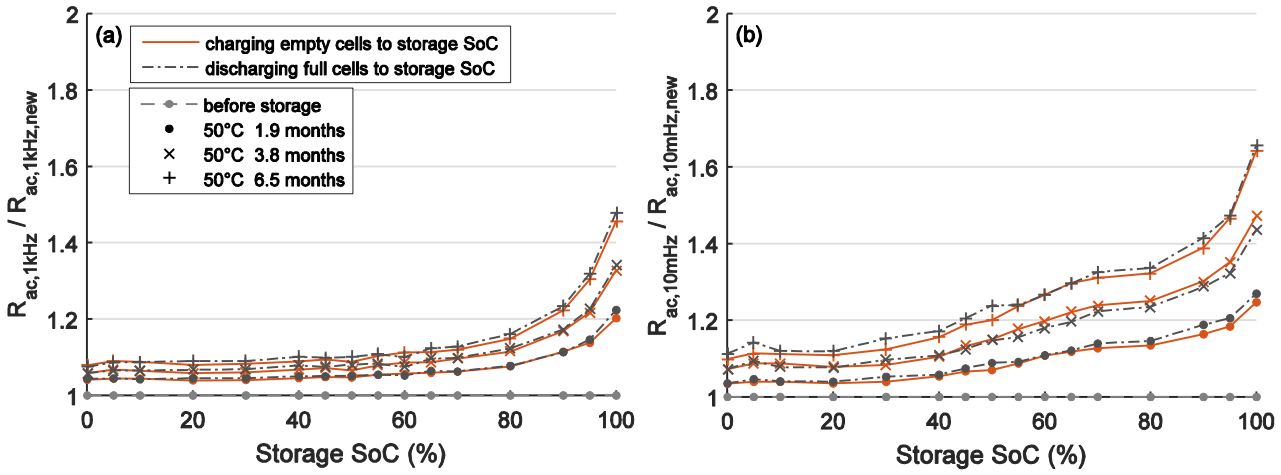

Figure 39. Comparison of resistance rise of (a) $R_{ac,1kHz}$ and (b) $R_{ac,10mHz}$ for the two sets of cells stored at 50°C, which had different directions for establishing the storage SoC.

4.4.3.2 DC Resistances

In the extended checkup measurements of the second calendar aging study, current pulses with a length of at least 10 s and different amplitudes were applied to the cells at various SoCs. Each sequence combining a charging and discharging pulse was repeated three times. For a comparison of the resistance measurements in time domain with the EIS results obtained in the frequency domain, the $R_{dc,10s}$ values computed from the pulses at 50% SoC are evaluated in this section. In the subsequent section, also pulses at other SoCs are evaluated to determine SoC-dependent resistance changes.

Figure 40 illustrates the relative changes of $R_{dc,10s}$ over storage SoC for different storage times at 25°C and 50°C. Furthermore, it compares the resistance changes obtained from the different current amplitudes. After each discharging pulse of –1 A, –3 A, or –5 A, a charging pulse with +1 A followed, which recharged exactly that amount of charge which was discharged by the preceding discharging pulse to keep the SoC level constant. Between each two pulses, there was a short pause of 1 min. As the results of all charging pulses were similar, the results from the third group of +1 A charging pulses, after the –5 A discharging pulses, were omitted in Figure 40 for clarity. Since the results from the three repetitions of each discharging and charging pulse pair were also similar, only the results from the first pulses are presented here.

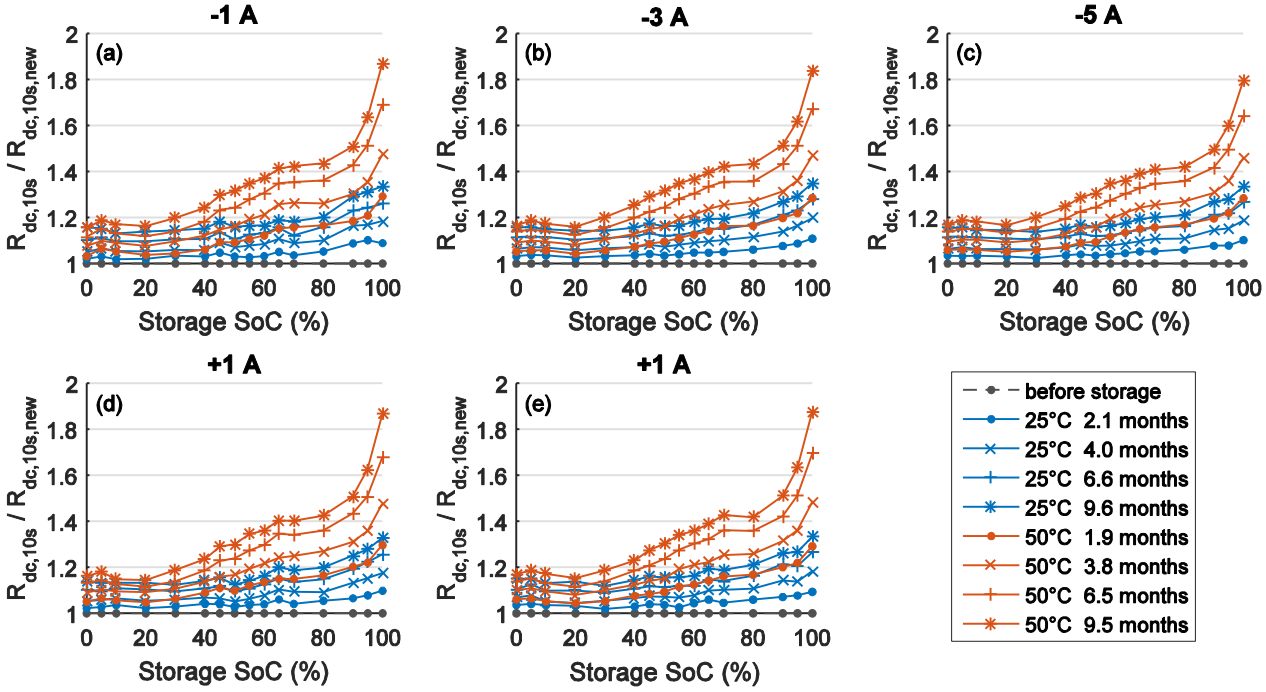

Figure 40. Changes of internal resistances identified by $R_{dc,10s}$ values at 50% SoC which were computed (a-c) from discharging pulses (–1 A, –3 A, –5 A) and (d-e) from charging pulses with constant amperage (+1 A) which followed after the discharging pulses with different pulse currents.

Impact of the Pulse Amplitude

The different current pulses exhibit the impact of the pulse amplitude and the direction of current flow on the changes of the internal cell resistances. As illustrated in Figure 40, the different current pulses all exhibit similar resistance changes for the different storage SoCs and storage temperatures. Only for the cells stored at a high SoC, a somewhat smaller resistance increase is obtained with higher pulse currents. The results from the –3 A and –5 A pulses exhibit somewhat more steady

trends with respect to SoC, particularly for the smaller changes at the storage temperature of 25°C. This can be explained by a better signal-to-noise ratio for the higher currents. Overall, Figure 40 demonstrates that the current amplitude has no considerable impact on the resulting resistance changes computed from the checkup data. To obtain a compromise between measurement accuracy and minimizing the impact on the cell, the discharging pulses with –3 A are selected for further evaluations. Hence, the following analyses present $R_{dc,10s}$ values obtained from the first discharging pulse with –3 A.

Comparison of EIS and Current Step Response Analysis

In Figure 41, the results from EIS and current step response analysis are compared. $R_{ac,10mHz}$ and $R_{dc,10s}$ reveal rather similar aging characteristics with respect to storage SoC and temperature. Hence, both resistance values are suitable indicators to detect changes in the overall cell resistance, which comprises ohmic resistances, passivation layers, charge transfer resistances, and diffusion resistances. The explicit values for the resistance changes obtained by $R_{dc,10s}$ are somewhat higher than that obtained by $R_{ac,10mHz}$. This might be a result from the higher charge throughput of the current pulse, which can reveal changes in diffusion resistances more pronouncedly.

As the $R_{dc,10s}$ measurements reveal the same aging trends as the $R_{ac,10mHz}$ values from EIS, pulse measurements – as part of the checkup routine at the battery test system – can substitute the low-frequency EIS measurements, which are very sensitive to varying relaxation times. Since the pauses before the current pulses can be precisely controlled by the battery test system, the evaluation of $R_{dc,10s}$ values avoids distortions from varying relaxation times. The changes in the purely ohmic behavior of the cells, however, are usually difficult to detect with pulse measurements at conventional battery test systems, as this requires current pulses with steep and well-defined edges as well as current and voltage measurements of high sampling rate, considerably above 1 kHz. Thus, impedance measurements were preferred for the high-frequency domain. Furthermore, the $R_{ac,1kHz}$ values were not affected by varying relaxation times.

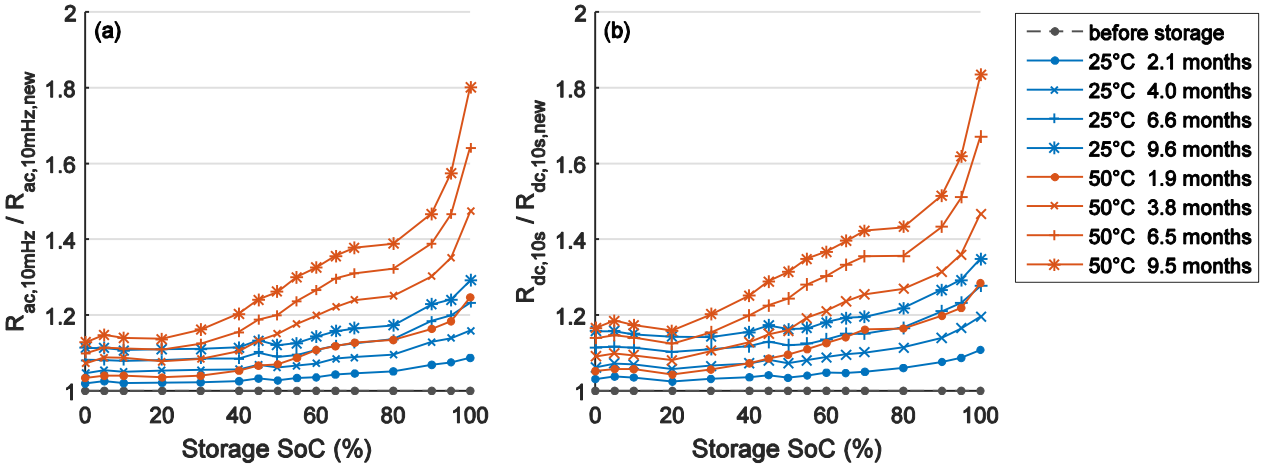

Figure 41. Comparison of changes in (a) $R_{ac,10mHz}$ from EIS and (b) $R_{dc,10s}$ from –3 A discharging pulses for different storage periods at 25°C and 50°C

4.4.3.3 SoC-Dependent Resistances

In many aging studies in the literature, resistance changes are only monitored at one SoC. In this section, resistance changes are examined at various SoCs. The extended checkup applied in the

second calendar aging study included pulse sequences at 10 SoCs, ranging from 100% to 10%. Figure 42 shows the development of $R_{dc,10s}$ measured at 25°C and different SoCs. The absolute values are shown as there are substantial resistance variations with SoC. Particularly at very low SoC and very high SoC, the $R_{dc,10s}$ values are considerably higher than at medium SoC range, even when the cells are new. Again, the resistance curves do not exhibit strong correlations with the plateau regions of medium and high capacity fade.

Similar Resistance Changes Between 30% and 80% SoC

In the medium SoC range between 30% and 80%, Figure 42c-f shows that the resistance changes are similar to the results presented for 50% SoC in the previous section. This highlights that resistance measurements in this SoC region are very robust, as they are not affected notably by SoC changes. This observation can also explain why EIS measurements at 50% SoC delivered the same results even when the excitation amplitude was changed by a factor of more than 30, as presented in Figure 11 (p. 28).

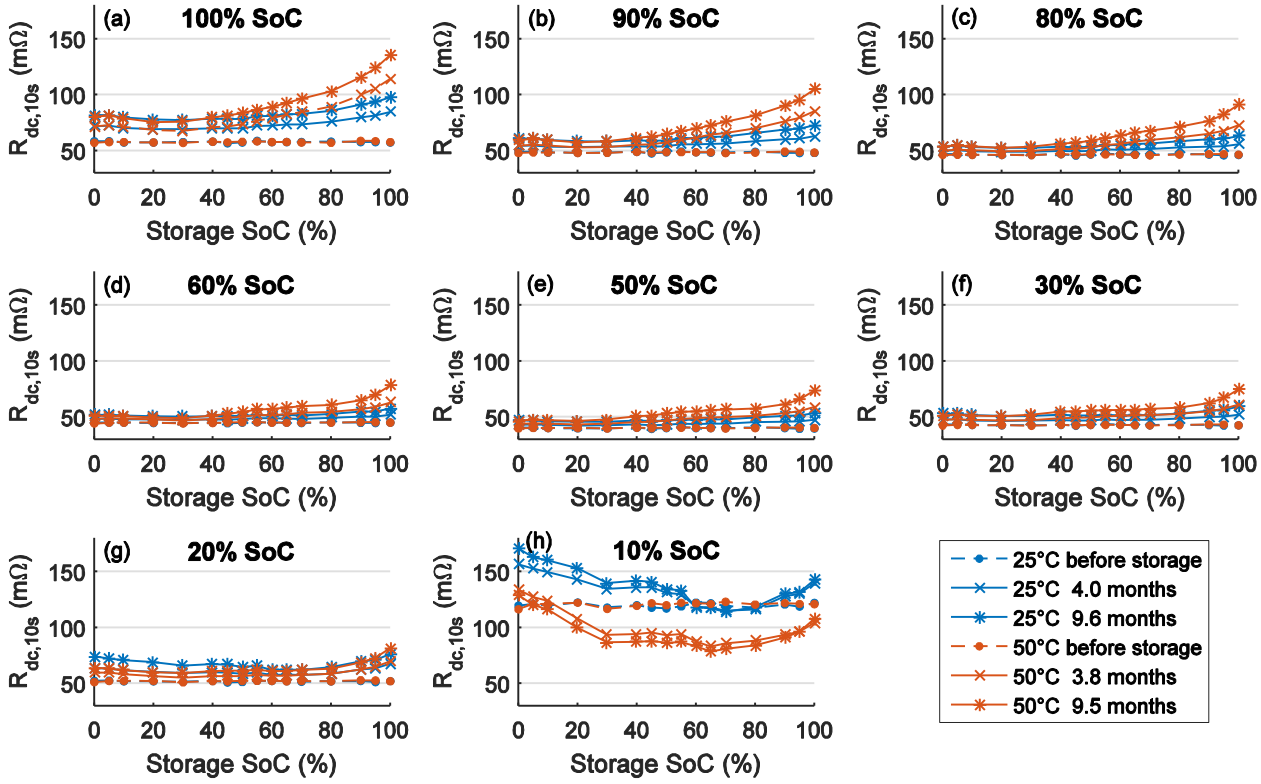

Figure 42: Absolute values of internal resistances measured at different SoCs resulting from different storage SoCs and storage temperatures. The $R_{dc,10s}$ values depicted were obtained from –3 A discharging pulses of the extended checkup procedure, performed at 25°C.

Increasing Resistances at High SoCs Above 80%

At high SoCs of 100% or 90%, Figure 42a and Figure 42b demonstrate that the resistance increase aggravates with higher storage SoC for all storage SoCs above 30%. For the cells stored at 30% SoC and below, the resistance changes are similar. As higher SoCs of a lithium-ion cell correspond to higher degrees of delithiation of the cathode and as there is a maximum permissible degree of delithiation for the cathode, the rising cathode potential determines the end of charge under regular conditions. At 100% SoC, the cathode approaches its maximum permissible degree of delithiation, whereas the anode could still be further lithiated, since the anode is generally oversized. As the

utilization of the anode decreases with higher capacity fade, due to the loss of cyclable lithium, it is unlikely that the increasing resistances at high SoCs originate from a graphite anode which becomes less lithiated. Hence, the substantially increasing resistances observed by the $R_{dc,10s}$ measurements at high SoCs of 100% and 90% are ascribed to the degradation of the NCA active material of the cathode.

Resistance Changes at Low SoC

The reduced utilization of both electrodes due to the loss of cyclable lithium can also explain the resistance changes at very low SoC. Figure 42h reveals decreasing resistances at 10% SoC for the cells stored at 50°C. In the new condition, the resistances measured at 10% lie substantially above those of the aged cells. Investigations on graphite anodes and NCA cathodes showed that the increasing resistances toward lower SoCs originate largely from increasing cathode resistances, when the cathode approaches its fully lithiated state [76]. As the degree of lithiation of the cathode decreases with higher capacity fade due to a lower utilization of the electrodes, the cathode at 10% SoC is less lithiated for an aged cell than for a new cell. As the lower degree of lithiation entails a lower resistance of the NCA cathode in this case, the shift of the electrode balancing caused by the loss of cyclable lithium is responsible for the decreasing $R_{dc,10s}$ values at 10% SoC for the cells stored at 50°C.

Overall, the resistance changes measured at different SoCs confirm that the degradation of the NCA cathode is the main driver of resistance increase for the lithium-ion cells examined in this thesis.

4.4.4 Aging Projections

To estimate the calendar life of a lithium-ion battery, the measurement data from experimental studies are typically extrapolated. As the capacity, which determines the driving range, is typically more important for an EV than the maximum power capability, this section presents calendar life projections based on the capacity fade. Since the capacity fade usually decreases over time and is typically described by a square-root-of-time behavior, this relationship is examined before the calendar life projections are performed.

4.4.4.1 Square-Root-of-Time Behavior

To verify the expected square-root-of-time characteristic of the capacity fade, the results from the first calendar aging study, which provides a longer test period than the second study, are presented in Figure 43. The capacity fade is depicted versus the square-root of storage time for three different SoCs. A linear capacity fade is expected in this representation when the degradation follows a square-root-of-time relationship. For the data presented in Figure 43, a linear degradation can be identified as a first approximation when the first checkup point is neglected. Furthermore, some degradation curves, particularly those obtained at low temperature, reveal a certain change in slope before a rather constant degradation can be observed. The data points after about 1 year of storage exhibit constant degradation rates. Thus, they are suitable for extrapolation. The dashed lines illustrate the linear extrapolation that was performed based on the last five data points in the square-root-of-time representation.

The curves of 40°C exhibit a step in the capacity at about 300 days of storage. Due to a relay failure of the temperature controller, the cells had been exposed to a storage temperature of more than 70°C for about 2–3 days inside the thermal chamber. This led to an accelerated degradation of the cells. To obtain steady degradation curves without this step, the capacity values after the incident were shifted vertically by a constant offset value for each cell. However, this cannot fully compensate the effects of the high-temperature incident. Figure 43 reveals a changing slope of the capacity fade and the degradation rate after 300 days appears to be slightly higher.

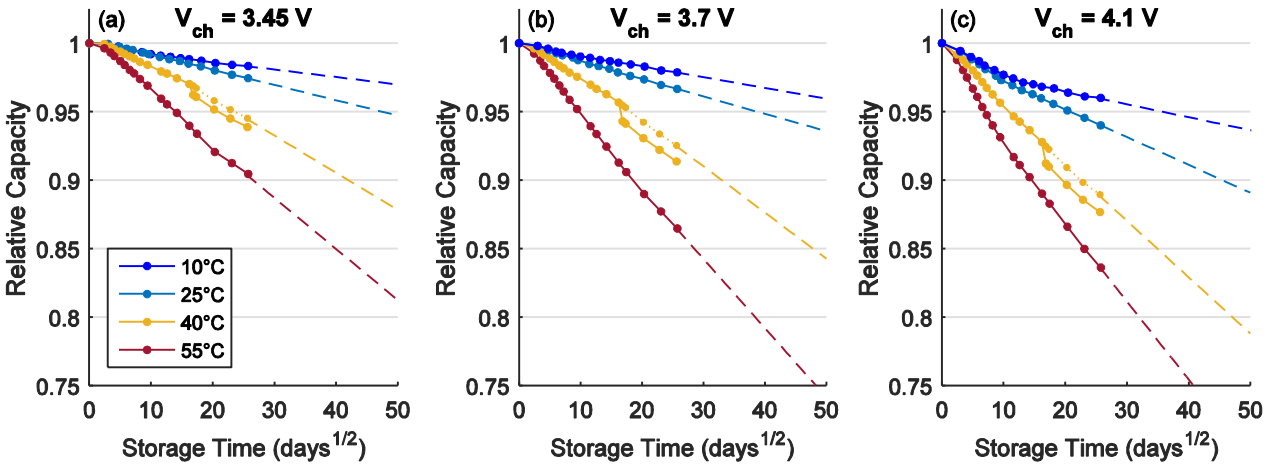

Figure 43. Capacity fade from calendar aging at different temperatures with respect to the square-root of time for (a) low SoC, (b) medium SoC, and (c) high SoC. The dotted segment at 40°C represents vertically shifted data and the dashed lines illustrate the extrapolated capacity fade based on the five last data points.

4.4.4.2 Calendar Life Prediction

Calendar life projections are performed for 10°C since the annual mean temperature in Germany lies around 10°C [214,215]. Moreover, calendar life is extrapolated for 25°C to estimate the capacity fade during nonoperation periods in warmer climate areas. Based on the extrapolations shown in Figure 43, the calendar aging curves were extrapolated to 20 years of storage in Figure 44, which corresponds to a square-root-of-time value of 85 days$^{1/2}$.

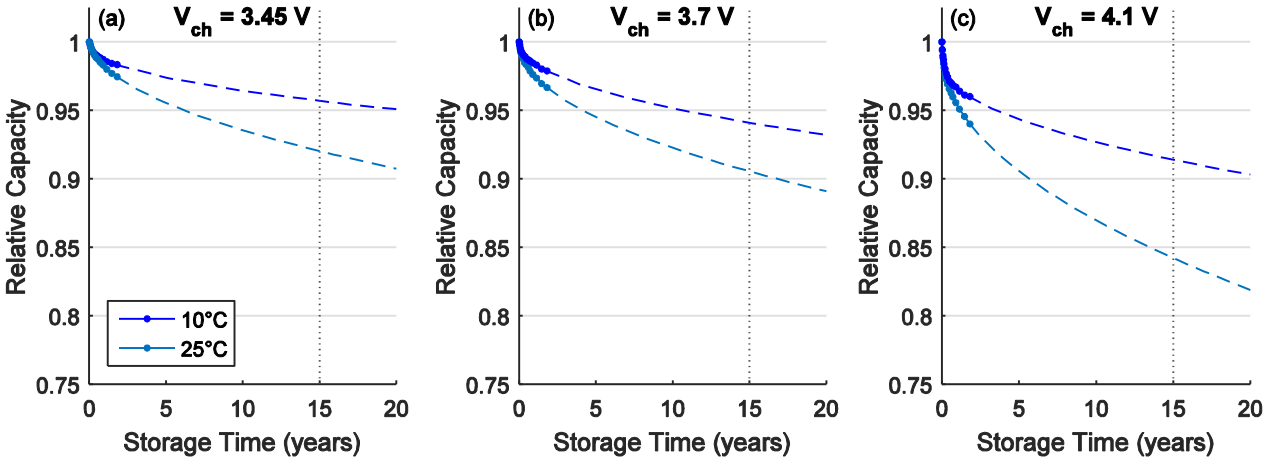

Figure 44. Projected capacity fade for up to 20 years of storage at different temperatures for (a) low SoC, (b) medium SoC, and (c) high SoC.

The USABC EV battery goals demand a battery life of 15 years. For the cell type examined in this thesis, the contributions of calendar aging amount up to 9% capacity fade for 15 years at 10°C and up to 16% capacity fade for 15 years at 25°C. When reducing the SoC to a medium level around 50%, the capacity fade decreases to 6% for 10°C and to 10% for 25°C. This demonstrates that keeping the SoC at a low or medium level during nonoperating periods extends the battery life considerably. When avoiding long time periods at high SoCs, the capacity fade owing to calendar aging can be kept below 10% for a typical vehicle life.

4.5 Conclusions

Loss of Cyclable Lithium Dominates Calendar Aging

The two experimental studies on calendar aging of lithium-ion batteries have shown that the capacity fade during nonoperating periods results predominantly from side reactions which reduce the inventory of cyclable lithium. DVA has disclosed that there is zero or only minor degradation of the storage capabilities of the individual electrodes, but a substantial shift in the electrode balancing. The capacity fade resulting from the loss of cyclable lithium leads to a decreasing driving range for the EV.

Anode Potential is the Main Driver for Capacity Fade

A strong correlation between the capacity fade and the anode potential has been shown for calendar aging. As a consequence, the capacity fade does not increase steadily with the SoC. Instead, plateau regions, covering SoC intervals of more than 20%–30% of the cell capacity, have been observed in which the capacity fade is largely constant. Higher temperatures and lower anode potentials were identified as the main drivers of capacity fade during storage periods, whereas no effects from anode volume changes or different charge-discharge paths for reaching the storage SoC were observed. In the high SoC regime where the graphite anode is lithiated more than 50%, the low anode potential accelerates the loss of cyclable lithium and leads to the fastest degradation.

Coulomb Tracking has confirmed that anodic side reactions are the main aging mechanism behind the capacity fade, as they lead to a slippage of the discharging endpoint which reduces the inventory of cyclable lithium and the utilization of the electrodes. These results confirm that electrolyte reduction and SEI growth at the anode are the predominant aging mechanisms responsible for the irreversible capacity fade of calendar aging.

Cathodic Side Reactions Causing Self-Discharge and Crosstalk Effects

At high SoCs, Coulomb Tracking has revealed some additional cathodic side reactions, which cause a reversible self-discharge. Moreover, a crosstalk between both electrodes has been observed, where cathodic side reactions entailed intensified anodic side reactions. This has led to a somewhat higher capacity fade for the high SoCs in the second calendar aging study. In the first aging study, however, a decreasing capacity fade has been observed for the cells stored above 80% SoC. The reason for this could be determined by Coulomb Tracking: Additional, solely cathodic side reactions at very high SoC caused a larger slippage of the charging endpoint which extended the inventory of cyclable lithium. This relieved the diminishing inventory of cyclable lithium and, thus, reduced the irreversible capacity fade. However, the overall aging reactions increased in that case due to the reversible self-discharge caused by the cathodic side reactions.

Reduced Electrolyte Conductivity at High Storage SoCs

In addition to the capacity fade, resistance increases were also examined. From impedance spectroscopy measurements, a correlation between the increase of ohmic cell resistances and the coupled side reactions occurring at SoCs above 80% could be derived. This has indicated a consumption of a considerable amount of electrolyte components. A certain degradation of the storage capabilities of the cathode was also observed by DVA, which supports the argumentation that transition metal dissolution is the reason for the increasing high-frequency resistances and the somewhat faster capacity fade toward 100% SoC.

Increasing Charge-Transfer Resistances of the NCA Cathode

The comparison of low-frequency impedance measurements and the evaluation of current step responses in the time domain has demonstrated that both methods reveal the same aging trends for the overall cell resistances. Moreover, the results have exhibited only very minor dependency on the current amplitude. Thus, simple current pulse measurements in time domain can substitute low-frequency impedance measurements, which are very prone to variations in relaxation time. For the pulse measurements, identical relaxation times in all checkup measurements can easily be maintained by the battery test system, which executes the entire checkup procedure. The changes in the low-frequency resistances, which cover changes in ohmic resistances, passivation layers, charge transfer resistances, and diffusion resistances, have revealed that there is a considerable increase in the charge transfer resistance of the NCA cathode for storage SoCs above 40%. However, these resistance changes do not correlate with the capacity fade. Overall, cathode degradation has been identified as main driver for increasing cell resistances. Performing resistance measurements at various SoCs has also revealed that the effects of cathode degradation on the overall cell resistance can be observed particularly strongly at high SoCs. For EV applications, the increasing resistances lead to higher voltage drops during driving periods, which can lead to a reduced discharge power of the battery. Moreover, the end of discharge can be reached earlier with markedly increasing battery resistances. This leads to a reduction in acceleration performance and also in driving range.

Minimizing Battery Aging in Nonoperating Periods

To reduce battery aging during nonoperating periods, lithium-ion batteries should be kept at a low temperature and at SoCs which lie below the SoC location of the central graphite peak in the differential voltage spectrum. This avoids storage periods at lowest graphite potential, which leads to fastest capacity fade. The location of the central graphite peak can change with the aging of the battery. For cells stored at 50°C, the location of the central graphite peak has shifted from 57% SoC in the new condition to 62% SoC after a capacity fade of ca. 9%. Thus, the EV battery should be kept at a low temperature and at a low or medium SoC during nonoperating periods. When avoiding long time periods at high SoCs, the capacity fade owing to calendar aging can be kept below 10% for a typical vehicle life of 15 years.

5 Impact of Charging Protocols on Battery Aging

In addition to calendar aging during nonoperating periods, the lithium-ion battery of an EV also ages by cycling operation. This chapter focuses on the aging caused by the charging process. Charging means a deintercalation of lithium from the cathode and an intercalation of lithium into the anode. Toward the end of the charging process, the cathode approaches its maximum permissible degree of delithiation which must not be exceeded to maintain the structural integrity of the cathode active material. In addition to that, the intercalation process of lithium into the graphite anode is considered as a critical step, particularly for fast charging with high currents and for charging at lower temperatures. Under these conditions, large drops of the anode potential are known to cause lithium plating [32,48]. This undesired reaction at the anode can be regarded as the major degradation mechanism when charging lithium-ion batteries. Side reactions between plated lithium and the electrolyte lead to a shift in the electrode balancing owing to a loss of cyclable lithium, which reduces the capacity of the battery.

To analyze the charging-induced battery degradation, an aging study comparing different charging protocols was conducted. This chapter provides a general overview over charging protocols for lithium-ion batteries and presents the charging protocols selected for the experimental study. Moreover, it presents the explicit details on the test procedure and the parameter variations examined, such as charging current and charging voltage. The results provide valuable insights into major degradation mechanisms and ways for optimizing the charging procedure of EVs to prolong the battery life. Moreover, this study provides first insights on the impact of cycle depth on battery degradation.

5.1 Insights from the Literature on Charging Methods

This section provides an overview on charging methods applied for lithium-ion batteries. In general, optimized charging procedures aim to provide a short charging time and a good capacity utilization while maintaining a long cycle life. This sections presents a classification of charging protocols into five main categories: CCCV charging, multistage constant current (MSCC) charging, pulsed charging, boost charging (BC), and other charging protocols.

5.1.1 Constant Current Constant Voltage Charging

The standard charging protocol for lithium-ion cells is CCCV charging [216]. Figure 45a illustrates the two phases of CCCV charging: At first, the cell is charged with a constant current I_{ch}, until the cell voltage reaches the specified charging voltage V_{ch}. Then, the cell voltage is kept constant at V_{ch}, entailing a continuous reduction of the charging current. This CV phase is terminated, when the charging current drops below a predefined threshold value I_{end} or when a predefined maximum charging time t_{max} is exceeded. The speed of the charging process is mainly influenced by I_{ch}; the capacity utilization is determined by V_{ch} and I_{end}. As demonstrated by Choi et al. [217], higher

charging voltages and higher charging currents can deteriorate cycle life considerably. Thus, it is necessary to choose I_{ch} and V_{ch} appropriately to minimize degradation.

Setting $I_{end} = I_{ch}$ results in sole CC charging, which is considered as a special case of CCCV charging within this classification of charging protocols. Due to the missing CV phase, the capacity utilization for sole CC charging is generally lower. High capacity utilization with sole CC charging can only be achieved with very low charging currents. As this extends charging times massively, CCCV charging is usually preferred to CC charging.

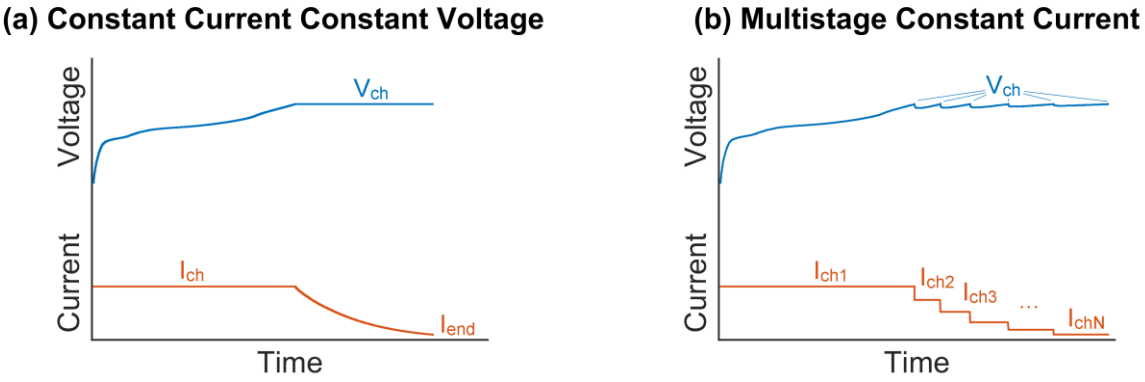

Figure 45: Schematic illustration of (a) constant current constant voltage and (b) multistage constant current charging protocols

5.1.2 Multistage Constant Current Charging

In MSCC charging (Figure 45b), the CV phase of the CCCV protocol is replaced by a series of CC periods with monotonic decreasing charging currents ($I_{ch1} > I_{ch2} > \ldots > I_{chN}$) [218,219]. Each time the cell voltage reaches the charging voltage V_{ch}, the charging current is reduced to the next level. The charging process is terminated, when V_{ch} is reached at the lowest current stage I_{chN}. The MSCC protocol is an approximation of CCCV charging, which reduces implementation costs as no additional circuitry or software algorithms for voltage regulation are required. The speed of the charging process and the capacity utilization can be adjusted by the same means as for CCCV charging. Due to the stepwise reduced charging current, MSCC charging is somewhat slower than CCCV charging with the same initial and final charging currents ($I_{ch1} = I_{ch}$, $I_{chN} = I_{end}$).

5.1.3 Pulsed Charging

As an alternative to CC or CV charging, several pulse charging profiles can be found in literature. They base on periodic changes in amperage and/or direction [220]. The charging current can be reduced, interrupted, or replaced by short discharging pulses for a certain period of time. In this overview, two categories of pulsed charging protocols are distinguished: Charging protocols where the CV phase from CCCV charging is replaced by pulsed charging and charging protocols consisting solely of pulsed charging.

5.1.3.1 Constant Current + Pulsed Charging

Figure 46a illustrates constant current + pulsed charging (CCPC), where pulsed charging replaces the CV phase of CCCV charging [221]. The lithium-ion cell is charged with a constant current I_{ch} until a

predefined voltage level V_{switch} is reached. Then, the charging mode changes to pulsed charging: Charging pulses of amperage I_{ch} and duration t_{pulse} are applied to the cell. After each pulse, the current flow is interrupted, until the cell voltage has dropped below V_{float} again. Usually, a minimum pause length $t_{pause,min}$ is also specified. In most implementations, V_{switch} and V_{float} are identical. With increasing SoC, the pauses become longer. Typical values for minimum pulse and pause lengths lie between 0.1 s and 0.5 s [222]. The charging procedure is terminated when the pause after a charging pulse exceeds a predefined time span $t_{pause,max}$.

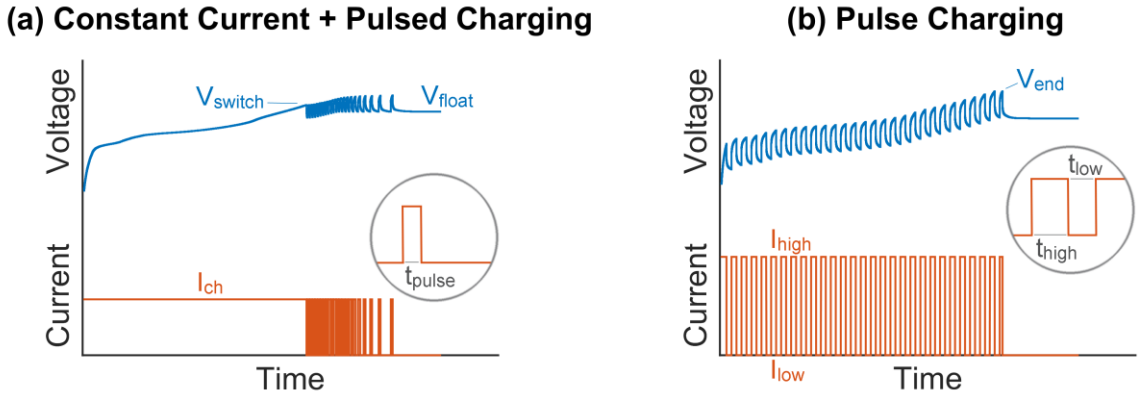

Figure 46: Schematic illustration of (a) constant current + pulsed charging and (b) pulse charging protocols

This charging protocol can be implemented at very low cost, as it requires neither voltage control nor variable charging currents. Capacity utilization and cycle life depend on V_{float} and $t_{pause,max}$: Setting V_{float} close to the maximum voltage specification (V_{max}) of the lithium-ion cell and increasing $t_{pause,max}$ maximizes capacity utilization. However, this can deteriorate cycle life, as the charging pulses lead to an exceedance of V_{max} for a certain period of time.

5.1.3.2 Pulse Charging

In addition to CCPC protocols, there are also the pulse charging (PC) protocols, where the entire charging procedure is performed by charging pulses [220,223]. Figure 46b illustrates such a PC profile, where the current alternates between I_{high} and I_{low}. The time period $t_{total} = t_{high} + t_{low}$ and the duty cycle $D = t_{high} / t_{total}$ define the shape of the pulse profile. There can also be a change of the pulse parameters during the charging process, such as a decreasing charging current or duty cycle toward higher SoCs [224]. Reaching a predefined charging voltage V_{end} terminates the charging procedure. The combination of I_{high} and V_{end} determines the capacity utilization. In Ref. [220], pulse frequencies ranged between 100 Hz and 0.2 Hz.

The motivation of PC protocols is to reduce gradients in the lithium-ion distribution and eliminate concentration polarization [223]. Some studies report beneficial effects of PC for lithium-ion batteries, such as reduced diffusion resistance, better active material utilization, improved cycle life, and reduced charging time, as a CV phase becomes redundant [33,223,225]. Other studies, however, showed that PC had no or even detrimental effects on the performance and cycle life of lithium-ion batteries [220,226]. Numerical simulations based on a 1D physicochemical model indicated that pulse charging with fixed frequency and fixed duty cycle does not have any advantages over CC charging with the same mean charging current [33,224]. Another study showed that for an identical mean current, losses rose and efficiency decreased with an increasing deviation

of the charging current from a CC profile [220]. Purushothaman et al. [224] and Fan et al. [227] presented specific PC profiles with low or decreasing charging currents which reduced battery aging. However, it was not analyzed whether the improved cycle life was a benefit from PC or simply a result of the reduced mean charging current or reduced cycle depth of these profiles.

In a preliminary study on charging protocols [121], it could be demonstrated for different high-power lithium-ion cells that the cycle life obtained with PC is similar to CCCV charging with the same mean charging current and the same cycle depth. Furthermore, capacity utilization was always lower for PC, as the maximum voltage was reached earlier due to the pulses with higher current.

5.1.4 Boost Charging

BC is derived from CCCV charging and features an additional CC or constant power interval at the beginning of the charging process [228]. This additional boost interval shall reduce charging time without deteriorating cycle life, as the batteries are less susceptible to lithium plating at lower SoC. In Figure 47a, the cell is charged with a high current I_{boost} in the beginning, until a substantial amount of charge is transferred into the cell. The boost interval is either limited by a time value t_{boost} or a maximum voltage V_{boost}. It can also be implemented as a CCCV period defined by these three parameters. After the boost interval, the charging procedure changes to a conventional CCCV protocol with the parameters I_{ch}, V_{ch}, and I_{end}. The charging speed can be adapted by I_{boost} and t_{boost}. Moreover, the same rules for adjusting capacity utilization and charging speed as for CCCV charging apply here.

P. Notten et al. [228] showed that a lithium-ion cell could be charged substantially faster with a BC protocol, while providing the same cycle life as a cell that was charged with a standard CCCV protocol without the high boost current in the beginning. Another study from D. Anseán et al. [229] also attributed short charging time and good cycle life to a BC protocol. However, none of the studies compared the BC protocol with a fast-charging CCCV protocol where $I_{ch} = I_{boost}$. Hence, it remained unclear whether reducing the charging current at higher SoCs is beneficial for the cells' cycle life or whether the cells used in these studies were not susceptible to high charging currents and could have been charged with a high-current CCCV protocol as well. In the preliminary aging study on charging protocols, it was shown that the SoC location of the boost period also affected the battery life notably [121].

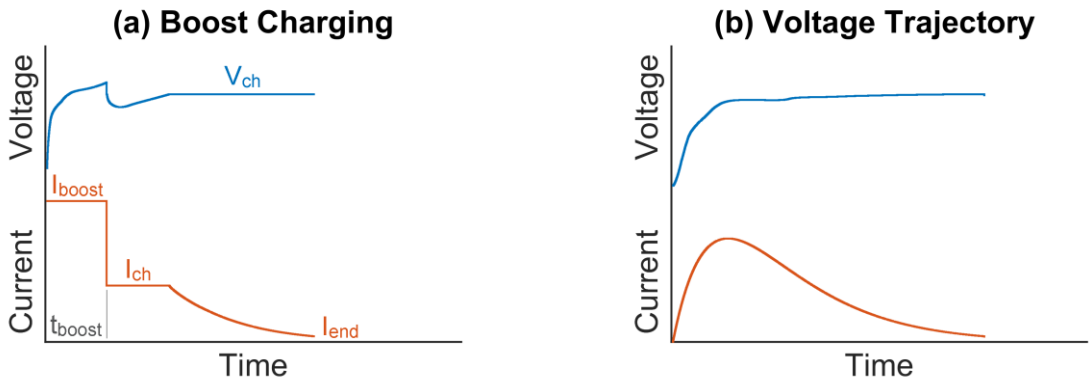

Figure 47: Schematic illustration of (a) boost charging and (b) an example of a predefined voltage trajectory.

5.1.5 Other Charging Protocols

This section gives an overview on some more exotic charging protocols proposed in the literature. It also comprises adaptive procedures, which adjust the charging current in dependence on the internal properties of the lithium-ion cell at its actual condition. The main characteristics of these charging strategies are presented in the following paragraphs.

5.1.5.1 Varying-Current Profile

Several charging procedures are based on varying-current profiles, which start with high charging currents and decrease currents with increasing SoC. Moreover, there are some charging protocols featuring a lower charging current in the beginning of the charging process, as the internal resistances generally have the highest values at low SoC. A period with a low charging current or steadily rising current can be used to minimize losses at very low SoC (see Figure 47b) [230,231]. Optimization methods were also used to achieve fast charging without exceeding certain voltage, temperature, stress, or concentration limitations [232–234]. Charging profiles with adapted currents were either determined experimentally [235] or derived from simulation models in order to obtain the maximum charging current which is applicable without provoking lithium plating [32,236–239]. Such protocols have hardly been used in practical applications, as determining the maximum charging currents appears to be challenging, since these currents vary considerably with temperature and degradation of the cell. As precise information about the actual polarization or concentration gradients inside the cell are necessary, additional state estimation routines are required to determine internal variables of the cell [240], which are also influenced by the short-term and long-term load history.

Many of the studies presenting more exotic charging strategies provided only few experimental data for validation. Furthermore, there were also different investigations on charging lithium-ion batteries which are solely based on simulation and present no experimental validation for the charging process (e.g. [241–244]).

5.1.5.2 Voltage Trajectory

Guo et al. [231] proposed a charging protocol that was no longer based on predefined charging currents, but used a voltage trajectory. This trajectory, which was the result of charging a new cell with a reference current profile similar to that shown in Figure 47b, remained identical over the entire battery life. Thus, charging currents decrease with proceeding capacity fade, while the charging time remains constant.

5.1.5.3 Supercharging

The fast-charging protocol Tesla uses at their supercharging (SC) stations combines BC and charging by voltage trajectory. A screen recording of the vehicle's dashboard during SC was uploaded to youtube by a user of a Tesla Model S in 2014 [245]. Current and voltage data extracted from this video were also available [246]. After manually correcting some wrongly extracted current values of the initial boost period, Figure 48 shows the voltage, current, and power curves, which demonstrate the four phases of this charging protocol. At first, the battery is charged with an approximately constant power. After that, the charging is continued with two voltage ramps, of which the second

ramp has a lower slope than the first. When reaching the maximum charging voltage, the charging procedure is completed with a constant voltage phase. For the vehicle's 85 kWh battery pack with 7104 cylindrical 18650 cells in a 96s x 74p configuration, this leads to the following charging protocol on cell level: In the beginning, the battery is charged by a boost interval with a constant power of ca. 14 W per cell until the voltage reaches 3.9 V per cell. Then, charging continues with the first voltage ramp, which has a slope of ca. 8.3 mV/min per cell connected in series. When the battery voltage reaches 4.0 V per cell, the second voltage ramp starts with a lower slope of ca. 5.7 mV/min. Finally, the charging is completed with a CV phase when a voltage of 4.2 V per cell is reached.

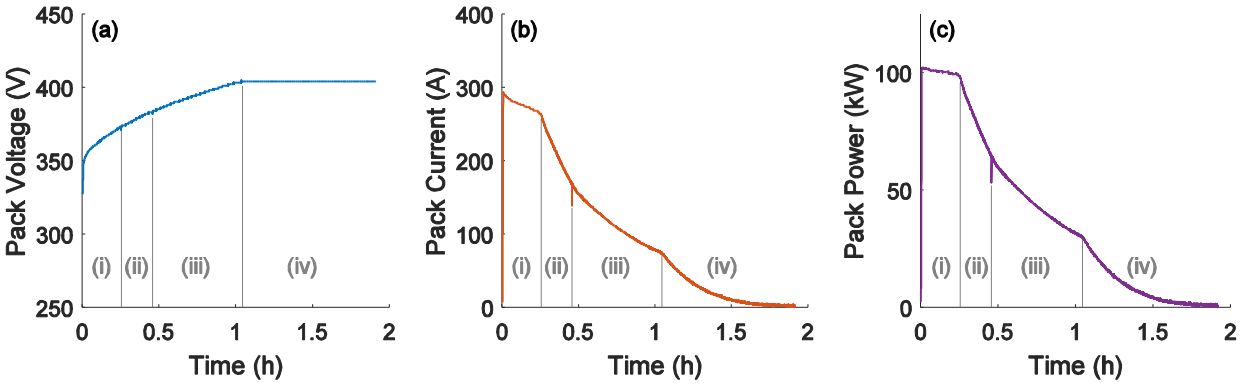

Figure 48. Charging procedure of a Tesla Model S at a supercharging station in 2014 (based on [245,246]). (a) Voltage, (b) current, and (c) power in the four phases of (i) constant power charging, (ii,iii) voltage ramps with different slopes, and (iv) constant voltage charging.

5.2 Objectives for the Own Aging Study

As high-energy lithium-ion cells are typically more susceptible to degradation that is caused by the charging procedure than high-power lithium-ion cells, the experimental aging study on charging protocols had the following research objectives:

- Selecting and examining a representative set of charging protocols
- Determining the impact of the charging protocols on charging time and capacity utilization
- Identifying the predominant aging mechanisms for capacity fade and resistance increase
- Performing thorough parameter variations for charging currents and charging voltages
- Evaluating standard CCCV charging protocols and fast-charging protocols
- Analyzing the impact of capacity utilization on cycle life
- Deducing strategies for reducing charging-induced degradation

5.3 Design of the Experimental Study

To investigate the impact of the charging strategy on the aging of the lithium-ion traction battery of an EV, different charging protocols were examined. Based on the results of the previous study [121], relevant charging strategies were selected and parameter variations were defined. In this section, the charging protocols examined are presented and the test procedure is described.

5.3.1 Charging Protocols Examined

For the experimental study on the impact of the charging procedure on battery aging, a representative set of charging protocols was selected and key parameters were varied. The selected charging protocols comprised CCCV charging, BC, and charging protocols with varying charging currents. MSCC protocols were not examined, as they are very similar to CCCV charging. Furthermore, no pulsed charging was examined, because the preceding study showed that pulsed charging protocols led to similar aging as CCCV protocols with the same mean charging current. As pulsed charging led to a lower capacity utilization and higher losses, no advantages could be ascribed to charging procedures with intermittent current flow. Parameter variations of the standard CCCV charging protocol were identified to have a substantial impact on the cycle life of lithium-ion batteries. The previous study also confirmed that the standard CCCV charging protocol is a reasonable and well-established charging method for lithium-ion batteries. Thus, a large number of parameter variations of CCCV protocols were tested in this study. Table 3 lists the parameter combinations used to determine the impact of different charging currents and Table 4 lists the parameter combinations applied to examine the impact of the charging voltage. To investigate the influence on different depths of discharge on charging-induced cycle aging, Table 5 lists the examined variations of the discharging voltage. All test protocols used a cut-off current threshold I_{end} of 100 mA for the final CV charging sequence. Also the discharging procedure was similar for all test cases: All cells were CCCV discharged with 2 A until the absolute value of the discharging current fell below 500 mA; unless noted otherwise, the discharging voltage was 2.5 V to completely empty the cells.

Table 3. Parameter combinations of CCCV protocols for investigating the impact of the charging current

Charging Voltage V_{ch}	4.2 V					4.1 V					4.0 V		
Charging Current I_{ch}	3.0 A	2.0 A	1.0 A	0.7 A	0.5 A	3.0 A	2.0 A	1.0 A	0.7 A	0.5 A	3.0 A	2.0 A	1.0 A

Table 4. Parameter combinations of CCCV protocols for investigating the impact of the charging voltage

Charging Current I_{ch}	1.0 A								
Charging Voltage V_{ch}	3.7 V	3.8 V	3.9 V	4.0 V	4.05 V	4.1 V	4.15 V	4.2 V	4.25 V

Table 5. Parameter combinations of CCCV protocols for investigating the impact of the cycling depth

Charging Parameters V_{ch}, I_{ch}	4.2 V, 1.0 A		4.1 V, 1.0 A				3.7 V, 1.0 A	
Discharging Voltage V_{dis}	2.5 V	3.2 V	2.5 V	3.0 V	3.2 V	3.4 V	2.5 V	3.2 V

In addition to CCCV charging, BC and SC protocols were investigated as they represent promising approaches of quick charging, where part of the battery's capacity is charged with a higher current. Table 6 lists the parameter variations of the BC protocols, where the duration of the boost interval is always 22.5 min but the onset of the boost interval varies to examine whether the high boost currents provoke different degradation at different SoC regions.

Table 6. Parameter combinations of the BC protocols, including a varying onset of the boost interval

Charging Voltages V_{ch}, V_{boost}	4.2 V, 4.2 V					4.1 V, 4.1 V				
Charging Currents I_{ch}, I_{boost} (t_{boost})	1.0 A, 3.0 A (22.5 min)					1.0 A, 3.0 A (22.5 min)				
Onset of Boost Interval $Q_{StartBoost}$	0 Ah	0.1 C_N	0.2 C_N	0.3 C_N	0.4 C_N	0 Ah	0.1 C_N	0.2 C_N	0.3 C_N	0.4 C_N

Table 7 lists the parameter combinations of the SC protocols. The parameters were derived directly from the charging procedure of a Tesla Model S. As the cells used in the Model S and the cells examined in this study were comparable but not completely identical, a reduced boost interval of 3 A instead of 14 W was also examined as a rapid capacity fade was obtained for the 14 W boost intervals.

To investigate whether low charging currents at the beginning of the charging process are beneficial for cycle life, soft-start protocols were examined which charge the first 10% C_N with a very low charging current of 100 mA. As listed in Table 8, the rest of the charging procedure was performed as 1.0 A CCCV charging to either 4.1 V or 3.7 V.

Table 7. Parameter combinations of the SC Protocols with different boost intervals and discharging voltages

(i) Boost Interval P_{boost} / I_{boost}	14 W		14 W		3 A	
(ii) Slope of Ramp 1 from 3.9 V to 4.0 V	8.33 mV/min					
(iii) Slope of Ramp 2 from 4.0V to V_{ch}	5.71 mV/min					
(iv) Charging Voltage V_{ch}	4.2 V	4.1 V	4.2 V	4.1 V	4.2 V	4.1 V
Discharging Voltage V_{dis}	2.5 V		3.2 V		3.2 V	

Table 8. Parameter combinations of the soft-start protocols

Soft-Start Period I_{soft}, Q_{soft}	0.1 A, 0.1 C_N	
CCCV Charging Parameters V_{ch}, I_{ch}	4.2 V, 1.0 A	3.7 V, 1.0 A

5.3.2 Test Procedure

The test procedure for comparing the charging protocols described above consists of cycling periods and periodic checkup measurements. All tests were performed at 25°C. The checkup procedure used in this aging study is depicted in Figure 49.

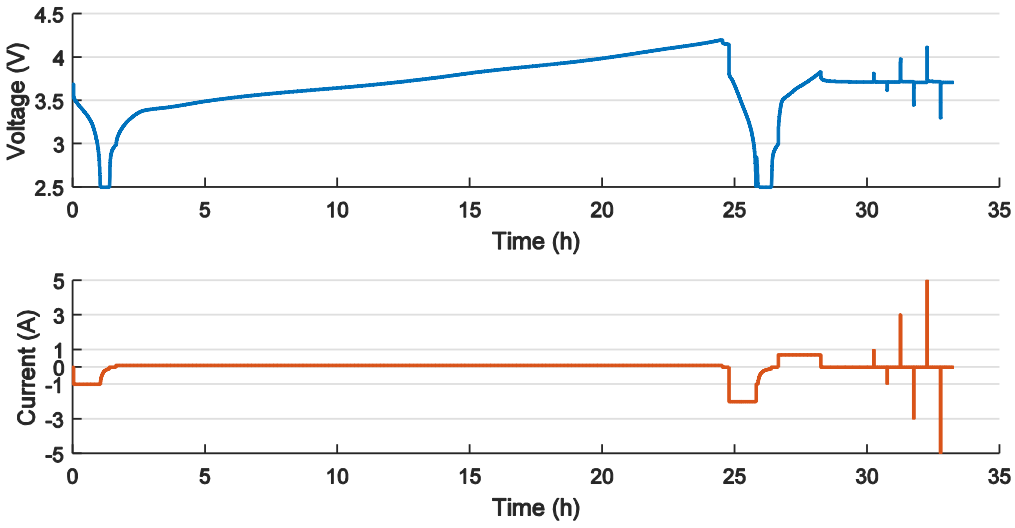

Figure 49. Checkup procedure of the aging study on charging protocols

It contained a low-current charging sequence with 100 mA for DVA, followed by 2.0 A CCCV discharging to 2.5 V with a current threshold of 100 mA to determine the actual capacity. After that, the cells were charged to 50% SoC, where a sequence of charge-discharge pulses was applied. The

entire checkup sequence with all explicit parameter settings can be found in Table A-7 in the appendix. After this sequence at the battery test system, the cell is also connected to the galvanostat to perform an EIS measurement at 50% SoC covering the frequency interval from 10 kHz to 10 mHz with an RMS excitation current of 50 mA.

The cycling procedure consisted of the individual charging protocol of each cell and an identical CCCV discharging sequence for all cells. The applied discharging current was 2.0 A and the default discharging voltage was 2.5 V. The CV discharging sequence was terminated when the amperage of the discharging current dropped below 500 mA. CCCV discharging was used to obtain a similar condition at the end of each discharge process for the beginning of the subsequent charging sequence. If the cells were only discharged with a CC current, the discharge depths would have decreased more pronouncedly with increasing cell resistances. A CCCV discharging procedure was employed to reduce the impact of increasing cell resistances on cycle depth.

5.3.3 Degradation Monitoring

The capacity fade was determined by the capacity measured in the CCCV discharging sequence of the checkup after fully charging the cells. DVA was performed with the data from the low-current charging sequence. The changes in internal resistances were evaluated at 50% SoC based on the $R_{ac,1kHz}$ from the EIS data and the $R_{dc,10s}$ was computed from the 3 A discharging pulse of the checkup sequence. Moreover, entire EIS spectra were evaluated.

5.4 Results and Discussion

In this cycle aging study, the impact of different charging protocols on battery aging was examined with cells from the second production lot. In total, results from 40 different cycling scenarios are presented. Most of them examined CCCV charging, where parameters for charging current, charging voltage, and also discharging voltage were varied. In addition to CCCV charging protocols, advanced charging protocols which combine different charging currents are analyzed and evaluated. All aging data are presented versus EFC to provide a better comparability for charging protocols with different cycle depths.

5.4.1 Constant Current Constant Voltage Charging

As CCCV charging is the standard protocol for charging lithium-ion batteries, an extensive parameter study was performed for this charging method. The impact of different parameter combinations on charging time, capacity utilization, and cycle life is presented and discussed in this section.

5.4.1.1 Impact of Charging Current

Lithium plating was expected to be the dominant aging mechanism when charging lithium-ion batteries. As lithium plating depends strongly on the charging current, five charging currents were examined, which ranged from 0.5 A (ca. 0.18 C) to 3.0 A (ca. 1.1 C). As lithium plating generally aggravates with higher SoC, the different charging currents were combined with three different charging voltages of 4.2 V, 4.1 V, and 4.0 V. The cut-off current for the CV phase of 0.1 A was identical for all charging protocols.

Charging Time and Capacity Utilization

The charging progress for the different combinations of charging current and charging voltage is illustrated in Figure 50. When charging to the maximum voltage of 4.2 V, the charging procedure lasts almost 350 min with the lowest charging current of 0.5 A. As shown in Figure 50a, a doubling of the charging current to 1 A reduces the charging duration to less than 190 min. Another doubling of the charging current to 2 A results in a charging duration of ca. 115 min. The maximum charging current of 3 A led to a total charging duration of ca. 95 min. This demonstrates that the charging time does not decrease linearly with increasing charging currents because the CV phase prolongs due to the higher overpotentials and covers an increasingly larger share of the overall charging duration.

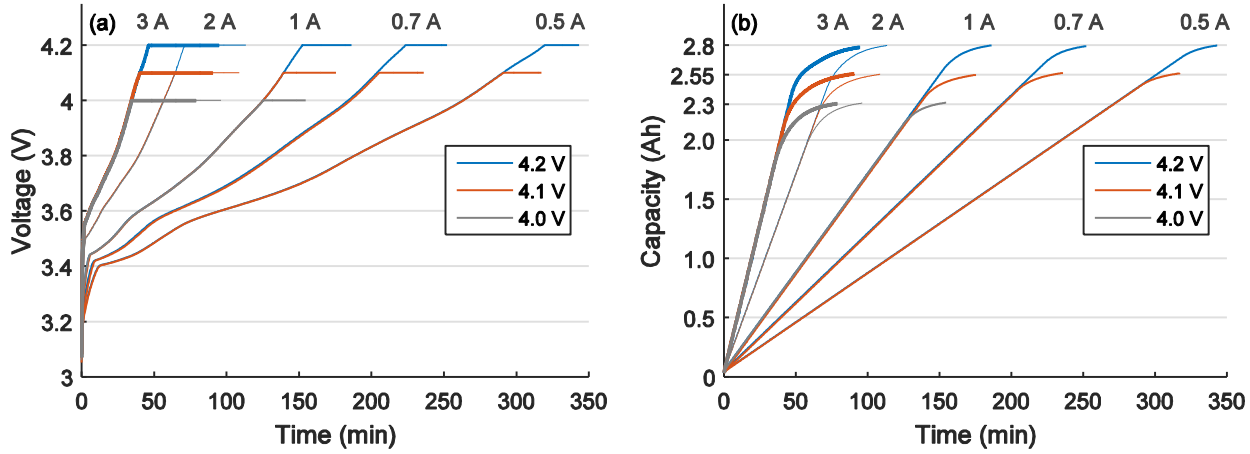

Figure 50. Charging progress of new cells charged with CCCV protocols with different charging currents: (a) Voltage curves and (b) charged capacity for charging to 4.2 V, 4.1 V, and 4.0 V.

Figure 50b shows the charged capacity over time. All capacity graphs start with a straight line, corresponding to the CC phase of the charging protocol, and fade into a curved arc, which represents the CV phase. When charging only to 80% of the respective end capacity, the charging times reduce linearly with higher charging currents, as this SoC is still reached in the CC phase. Figure 50b also reveals that the cells were not completely discharged in the cycle aging study. As the cut-off current for CCCV discharging was set to 0.5 A, compared to 0.1 A in the checkups, the last ca. 40 mAh were not discharged in the cycle aging study.

For each charging voltage, there is no considerable deviation in capacity utilization for the different charging currents. The deviation in capacity utilization remains below 0.5%. Hence, the capacity utilization is rather independent from the charging current of the CC phase. It is mainly affected by the charging voltage and the cut-off current of the CV phase.

Cycling Sequences

To analyze the cycle life for the different combinations of charging current and charging voltage, Figure 51 shows the changes of the capacity available in each discharging sequence of the continuous charging-discharging procedure of the cycle aging study. For all three charging voltages, the high charging currents of 3 A and 2 A exhibit a rapid capacity fade. It has to be noted that these charging currents were beyond the recommended charging current from the manufacturer. For charging with 3 A, the available capacity drops below 80% within less than 100 EFC for all three

charging voltages. For charging with 2 A, the same capacity fade is reached after ca. 150 EFC for the charging voltage of 4.2 V, after ca. 270 EFC for 4.1 V, and after ca. 500 EFC for 4.0 V. This shows an interdependency between charging current and charging voltage. The observed trends clearly affirm the assumption of lithium plating to be the predominant aging mechanism for fast charging lithium-ion batteries, since the capacity fade increases massively with higher charging currents and also with higher charging voltages. Moreover, a pronounced capacity recovery is observed each time the cycling procedure is interrupted for a checkup measurement. This short-term recovery effect is not observed for the lower charging currents. Hence, they are supposed to be directly linked to reactions occurring after substantial lithium plating.

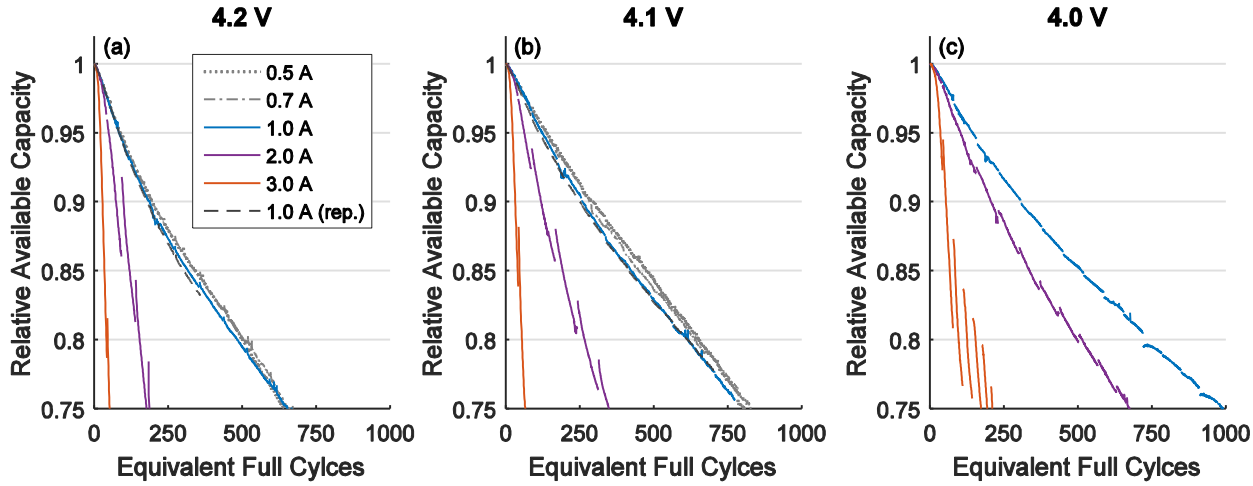

Figure 51. Capacity fade during cycling for charging voltages of (a) 4.2 V, (b) 4.1 V and, (c) 4.0 V. Relative capacity for CCCV discharging with 2 A and a cut-off current of 0.5 A.

For charging with 1 A (ca. 0.36 C), Figure 51 shows that the degradation is considerably lower than for the two higher charging currents. Moreover, the degradation is only somewhat higher than for the low charging currents of 0.7 A (= C/4) and 0.5 A (ca. 0.18 C), which exhibit a similar capacity fade in Figure 51a and Figure 51b. To examine reproducibility, the CCCV protocols charging with 1 A to 4.2 V and to 4.1 V were repeated ca. 11 months later; as illustrated by the dashed black lines, similar results are obtained. This confirms the high uniformity of the cells examined in this thesis and the repeatability of the results. The deviation among each pair of curves obtained with the same charging protocol is substantially lower than the deviations obtained for the different parameter variations. As cycle life does not improve considerably when reducing the charging current from 1 A to 0.5 A, lithium plating appears to be no longer the dominant aging mechanism for these charging protocols. With a charging current of 0.7 A and lower, intensified aging of the cells is reliably prevented at 25°C, also when the cells exhibit an advanced state of aging.

Checkup Results

In addition to the results from the cycling procedure, Figure 52 shows the results of the checkups. Figure 52a-c exhibits similar trends as before: The capacity fade increases markedly for 3 A and 2 A, whereas only small differences are observed for the charging currents of 1 A and below. In general, the capacity values measured by the checkups lie about 2–4 percentage points higher than that observed during the continuous cycling procedure. This can be ascribed to the lower cut-off current for CCCV discharging in the checkup procedure, which compensates at least partially the increase of cell resistances. Hence, the rising resistances lead to a notable degradation of the rate capability.

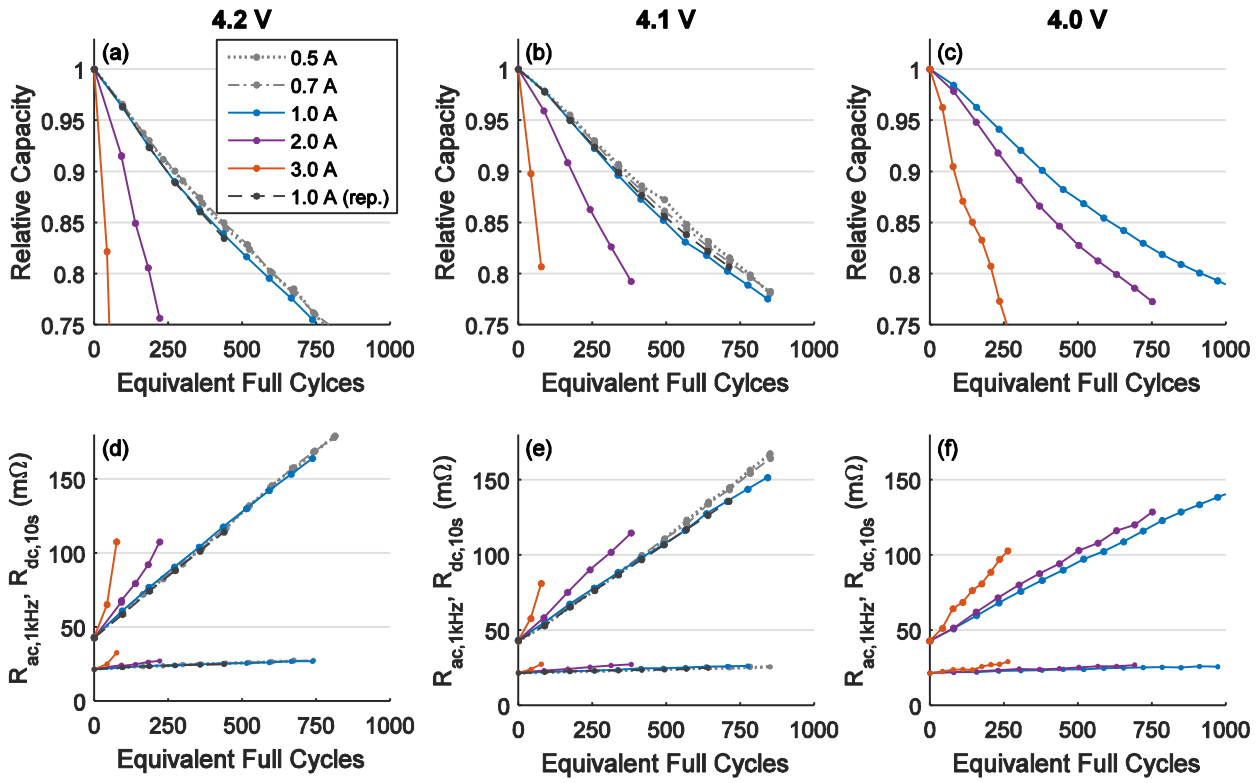

Figure 52. (a-c) Capacity fade and (d-f) resistance increase from the checkup measurements for the different combinations of charging current and charging voltage for the CCCV charging procedure

The resistance measurements, depicted in Figure 52d-f, reveal marked increases of the $R_{dc,10s}$ values. After 750 EFC, the $R_{dc,10s}$ values have more than tripled. The high internal resistances also aggravate the rate capability of the cells, as the high resistances cause a large voltage drop so that the minimum cell voltage is reached earlier in the discharging process. A small increase of $R_{ac,1kHz}$ is also observed when charging with 1.0 A or lower charging currents. Considerable increases in $R_{ac,1kHz}$ are observed when charging with high charging currents that provoke substantial lithium plating. When the metal lithium reacts partially with the electrolyte, it causes a decomposition of electrolyte components and leads to a lower conductivity. When the charging current remains low, there is only a small increase in $R_{ac,1kHz}$, which indicates only minor side reactions with the electrolyte. Hence, lithium plating has remained low.

Figure 53 illustrates the changes in the impedance spectra of the two cells charged to 4.0 V with charging currents of 1.0 A and 3.0 A. Both cells exhibit substantial changes in the capacitive semicircle below 30 Hz which can be ascribed particularly to the charge transfer resistance of the cathode. The impedance spectra in Figure 53b, which correspond to the charging protocol with the higher current that is causing massive lithium plating, the entire spectrum exhibits a right-shift which represents increasing ohmic resistances due to a lower electrolyte conductivity. The other group of spectra, depicted in Figure 53a, shows substantially smaller right-shifts. Overall, lithium plating and the subsequent reactions of the metal lithium with the electrolyte degrade the electrolyte conductivity and increase the ohmic resistance of the cell when charging with elevated currents. The increasing cathode resistances are typically ascribed to the NCA active material, which is known to suffer from weakening particle contacts and microcracks [69,70].

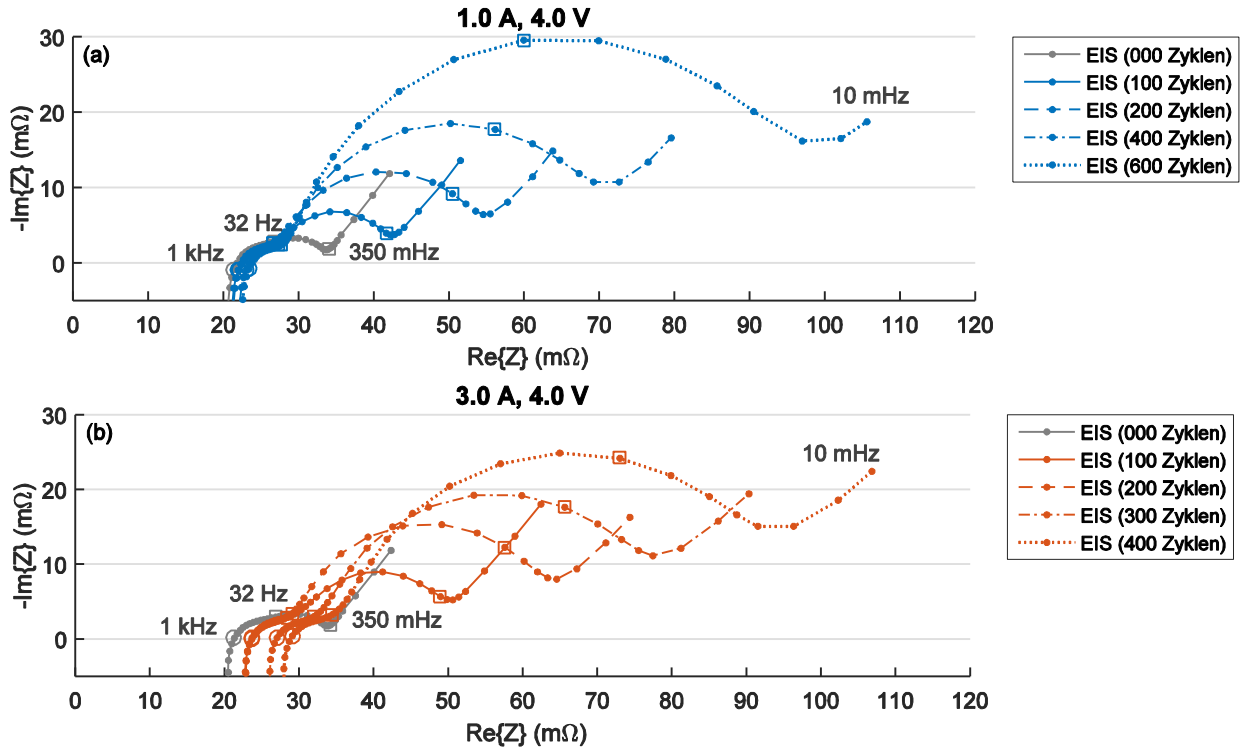

Figure 53. Impedance spectra for cells charged to 4.0 V with (a) 1.0 A and (b) 3.0 A. The second plot shows that the $R_{ac,1kHz}$ changes notable which indicates a consumption of electrolyte by lithium plating.

Additional Insights from Differential Voltage Analysis

To further investigate the effects of lithium plating, the differential voltage spectra of the cells charged with 2.0 A to 4.2 V and 4.1 V are shown in Figure 54. In both cases, substantial reductions in the storage capabilities of the anode can be identified since the location of the central graphite peak shifts considerably to the left with increasing cycle numbers. Evaluating also the spectra of other cells revealed that this peak shift aggravates with higher charging currents.

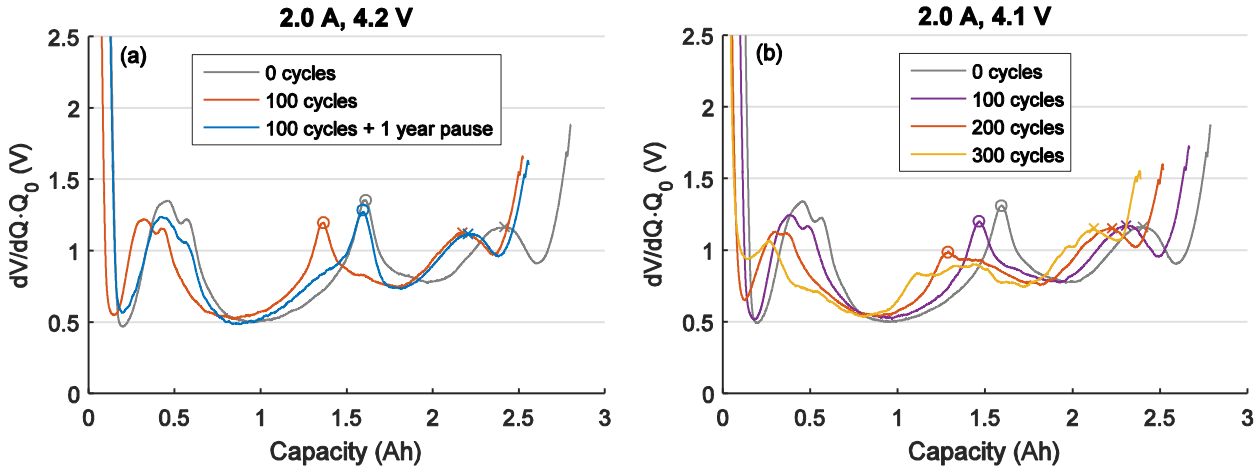

Figure 54. DVA for CCCV charging with 2.0 A to (a) 4.2 V and (b) 4.1 V. The central graphite peak is highlighted by circle markers. A substantial recovery of the graphite anode is observable after a long pause in subplot (a).

However, Figure 54a discloses that a graphite anode which was exposed to substantial lithium plating can recover its storage capabilities. After a pause of ca. 1 year after suffering from 100 charge-discharge cycles with high charging current and high charging voltage, the location of the

central graphite peak had returned to its initial position. Hence, the storage capabilities of the anode had largely recovered. This occurred without notable changes in the capacity measurements, as the capacity values of both checkups can hardly be distinguished in Figure 52a. Furthermore, a Coulomb Tracking analysis for the pause of 1 year revealed no considerable slippage of the charging and discharging endpoints. Consequently, the amount of cyclable lithium has not changed during the pause. From these observations, it is concluded that parts of the anode could not be charged any longer after the occurrence of lithium plating. It is speculated that the deposition of waste products from reactions of the plated lithium with the electrolyte isolates certain anode areas and prevents them from participating in the charge-discharge cycling. This assumption is supported by the findings of Abraham et al. [38], who showed that the capacity of aged graphite anodes could be restored by DMC rinsing, which indicated that the capacity loss resulted from pore-clogging or isolation of graphite particles by electronically insulating surface films. During the 1 year of inactivity, the waste products are supposed to have dissolved or redistributed so that the full capacity of the graphite anode has become accessible again.

The mid area of the differential voltage spectra depicted in Figure 54b shows that the central graphite peak shifts considerably to the left and is attenuated also for the combination of 2.0 A and 4.1 V. Yet, a broadening of the elevated central area can be observed in this case which also exhibits some small peaks side by side after 300 cycles. Owing to this deformation, it is supposed that there is an inhomogeneous degradation of the anode active material that leads to a coexistence of local areas with different actual storage capabilities. If the entire graphite anode had had a degree of lithiation of ca. 50% at the small remaining peak at 1.1 Ah in the checkup after 300 cycles, the anode would have been fully lithiated at 2.2 Ah. As the cell could be charged to almost 2.4 Ah without considerable distortions in the differential voltage spectrum, the total storage capability must have been higher. Thus there must have been areas which had a higher local capacity. An inhomogeneous anode degradation after cycling with higher currents was also observed by Rieger et al. [37] and Somerville et al. [247].

5.4.1.2 Impact of Charging Voltage

As observed in the previous section, the charging voltage has a considerable impact on the cycle life of lithium-ion batteries. In this cycle aging study, a variety of charging voltages was examined for CCCV charging with 1 A. A charging current of 1 A was selected, as it did not cause a pronounced capacity fade owing to lithium plating. This section presents the impact of charging voltage on capacity utilization and cycle life.

Charging Time and Capacity Utilization

To examine charging duration and capacity utilization, an aged and a new cell were charged to 12 different charging voltages from 3.7 V to 4.2 V. The aged cell was the cell charged 500 times to 4.2 V with 1.0 A for the verification of repeatability. As observed in Figure 52d, this aged cell had a pronounced resistance increase. Figure 55a depicts the capacity utilization of the new and the aged cell for the different charging voltages. It also illustrates the amount of charge which is transferred into the cells during the CC and the CV phase. This shows that for aged cells, the CC phase shortens while more charge is transferred in the CV phase. Figure 55b illustrates the corresponding durations of the charging procedure. Whereas the CC phase exhibits a continuously increasing duration with

higher charging voltage, the duration of the subsequent CV phase varies considerably and exhibits no steady trend with respect to the charging voltage. Comparing the new and the aged cell reveals that only the CC phase shortens considerably with the aging of the battery, whereas the total charging duration decreases substantially less. Although the capacity fades, the prolonged CV phase prevents a notable shortening of the charging duration.

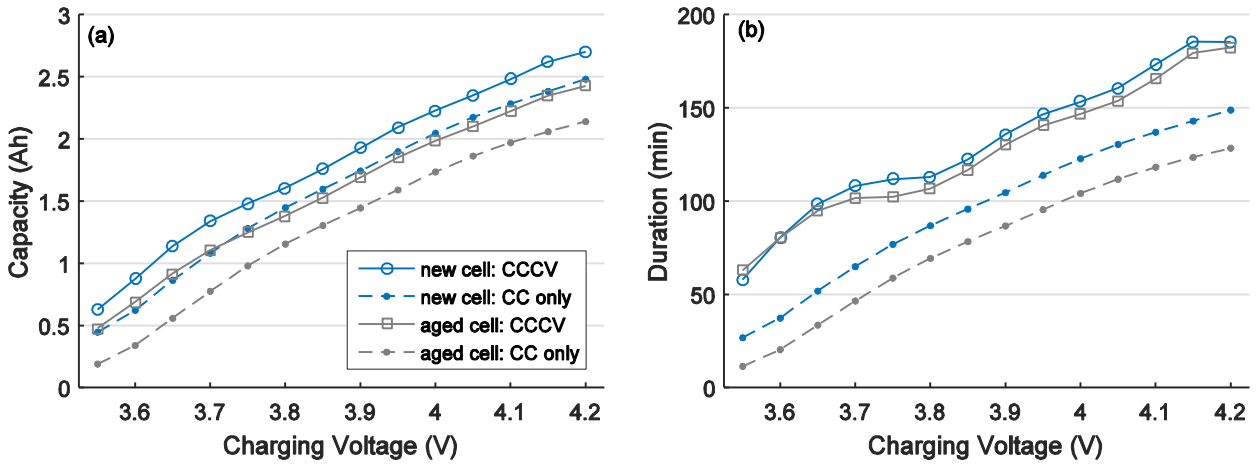

Figure 55. Impact of charging voltage on (a) capacity utilization and (b) charging duration for CC and CCCV charging. (The capacity values and charging durations in this figure are somewhat lower than in Figure 50, as the two cells here were discharged only with a CC instead of a CCCV sequence.)

Cycling Sequences

The charging voltage is often reduced in practical applications to increase the cycle life of the battery. In Figure 56, cycling data from Figure 51a-c are plotted for a comparison of the absolute capacity fade instead of the relative capacity fade for the different charging voltages. Comparing the curves for charging to 4.1 V or 4.2 V with 1 A or less in Figure 56a shows that the curves of the different charging voltages do not intersect before ca. 750 EFC. This means that the absolute available capacity remains greater for higher charging voltages, even if the relative capacity fade is larger, as it was shown in Figure 51.

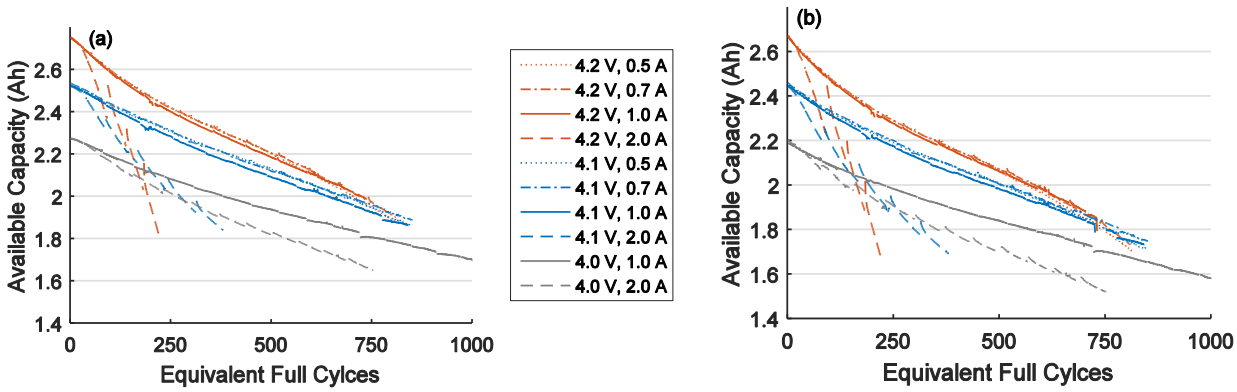

Figure 56. Capacity fade for different charging voltages. The absolute available capacity over EFC is compared for (a) the entire CCCV discharging sequence and (b) CC discharging part only. (Results from Figure 51)

For charging with 2 A, benefits from reduced charging voltages can be observed. For this charging current, the capacity curves intersect. By reducing the charging voltage from 4.2 V to 4.1 V, a higher absolute capacity is available for the lower charging voltage after ca. 150 EFC. When further

reducing the charging voltage from 4.1 V to 4.0 V, the absolute available capacity for charging to 4.0 V is greater after ca. 280 EFC. This demonstrates that when a charging current is applied that provokes considerable lithium plating, a lower charging voltage can be beneficial for the cycle life of the battery.

To assess the impact of the discharging current on the available capacity – particularly for the cells in aged condition – Figure 56b shows the available capacity when only the CC discharging with 2 A is considered and the subsequent CV phase is neglected, in which the current is continuously decreased until it reaches the cut-off threshold of 0.5 A. For CC discharging only, the available capacity is ca. 30–40 mAh lower for the new cells and up to ca. 100 mAh lower after 750 EFC. This represents ca. 1.1%–1.5% C_N and 3.6% C_N, respectively. This confirms that the rate capability decreases for the aged cells due to the increasing resistances.

In addition to the comparison of the three different charging voltages combined with different charging currents, CCCV protocols with an identical charging current of 1.0 A and nine different charging voltages were examined. Figure 57a illustrates the absolute capacity available in the charge-discharge cycling procedure for the different charging voltages. Figure 57b shows the corresponding relative capacity evolution, where all curves from Figure 57a were divided by their first capacity value. The relative capacity fade decreases continuously for the charging voltages from 4.2 V to 3.8 V. For charging to 3.7 V, a higher relative capacity fade is observed again, which will be further analyzed by DVA. A capacity fade of 20% is reached between ca. 400 EFC for charging to 4.25 V and ca. 750 EFC for charging to 4.0 V. For charging voltages below 4.0 V, substantially higher cycle lives of 1000 EFC and more are observed.

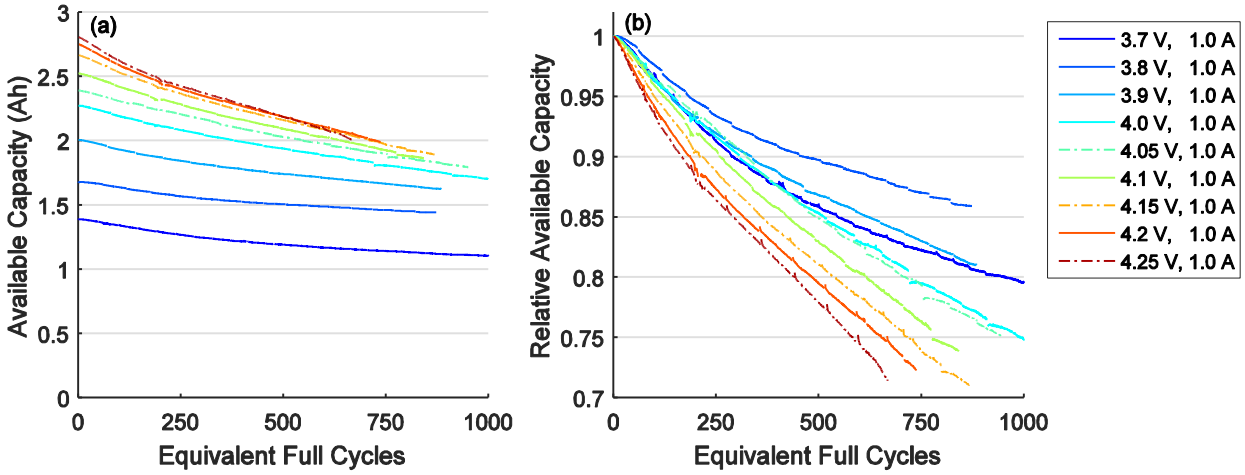

Figure 57. Available Capacity for different charging voltages in (a) absolute and (b) relative representation

The curves of the absolute values of the available capacity, depicted in Figure 57a, illustrate the initial differences in capacity utilization for new cells and visualize the changes in the available capacity over time. The capacity curves for the different charging voltages hardly intersect each other. Only for charging to 4.25 V, which is beyond the maximum voltage specification of the manufacturer, Figure 57a exhibits a somewhat accelerated fade in the available capacity. For all other charging voltages, no intersections can be observed. This means that a reduced charging voltage does not necessarily provide a better absolute capacity retention over the cycle life of the battery, although the relative capacity fade remains lower.

When defining the charging voltage for an EV, the manufacturer has to find an appropriate balance between maximizing the driving range and minimizing the battery degradation perceived by the customer. When the maximum charging voltage is reduced, the relative capacity fade decreases. However, the vehicle provides a shorter driving range. When using the maximum charging voltage, a higher driving range is obtained. As the driving range corresponds to the absolute available capacity and as the absolute capacity curves do not intersect in Figure 57a, a higher charging voltage provides still a higher driving range for the aged cells. Yet, the capacity fade perceived by the customer is substantially higher since it corresponds to the fade in relative available capacity. Considering a vehicle age corresponding to 750 EFC for example, the absolute available capacity and, thus, the driving range is still ca. 10% higher for charging to 4.2 V than for charging to 4.0 V, although the relative capacity fade amounts to ca. 28% for the higher charging voltage and only to ca. 20% for the lower charging voltage.

Checkup Results

To complement the cycling data, the capacity fade and the resistance increase determined by the checkups are depicted in Figure 58. Reducing the charging voltage reduces the cycle depth and thus increases the cycle life of the battery. In contrast to the relative fade of the available capacity, depicted in Figure 57b, the actual capacities exhibit no faster decrease for charging to 3.7 V compared to 3.8 V or 3.9 V. In Figure 58a, the capacity fade increases with higher charging voltages and an almost identical capacity development is observed for charging to 3.7 V and 3.8 V. The resistance measurements in Figure 58b also reveal a progressively larger increase of the $R_{dc,10s}$ values for higher charging voltages. Overall, reduced charging voltages for charging with 1 A have led to lower cycle aging at the cost of capacity utilization but they have not provided a better retention in absolute capacity for most cases.

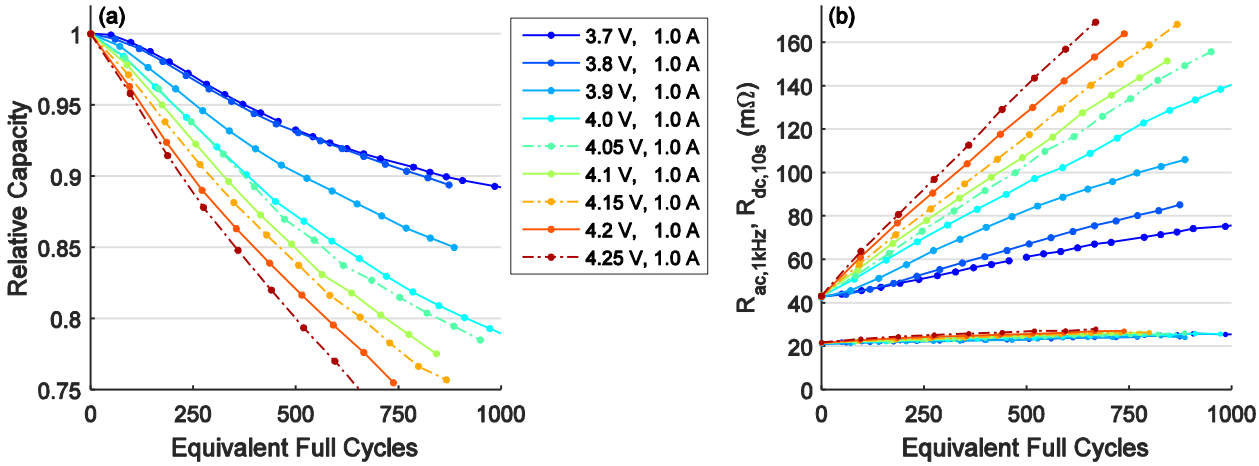

Figure 58. (a) Capacity and (b) resistance measurements from the checkups illustrate the capacity fade and resistance increase for CCCV charging with 1 A to different charging voltages

As illustrated in Figure 58b, the charging voltage also has a strong impact on the resistance increase. Whereas the $R_{ac,1kHz}$ increases only slightly, the $R_{dc,10s}$ values exhibit a marked deterioration. The small changes in $R_{ac,1kHz}$ confirm that side reactions consuming electrolyte were generally low but somewhat increasing toward higher charging voltages. The corresponding impedance spectra confirmed again that the marked increase in the $R_{dc,10s}$ values is caused by the growth of the capacitive semicircle below 30 Hz, related to the charge transfer resistance of the NCA cathode.

Hence, microcracks of the NCA cathode and weakened particle contacts are assumed to aggravate with larger cycle depths and cause the marked impedance increase.

Additional Insights from Differential Voltage Analysis

The reason for the very small reduction of available capacity during cycling which was observed in Figure 57 for the cell charged to 3.8 V can be explained by DVA. Figure 59 shows the differential voltage spectra obtained from the low-current charging sequence of the checkup routine every 100 cycles. The differential voltage spectra are plotted with different x-axes and exhibit the changes of the central graphite peak, which is highlighted by circle markers and indicates the transition from the medium to the low anode potential (see Figure 18, p.36).

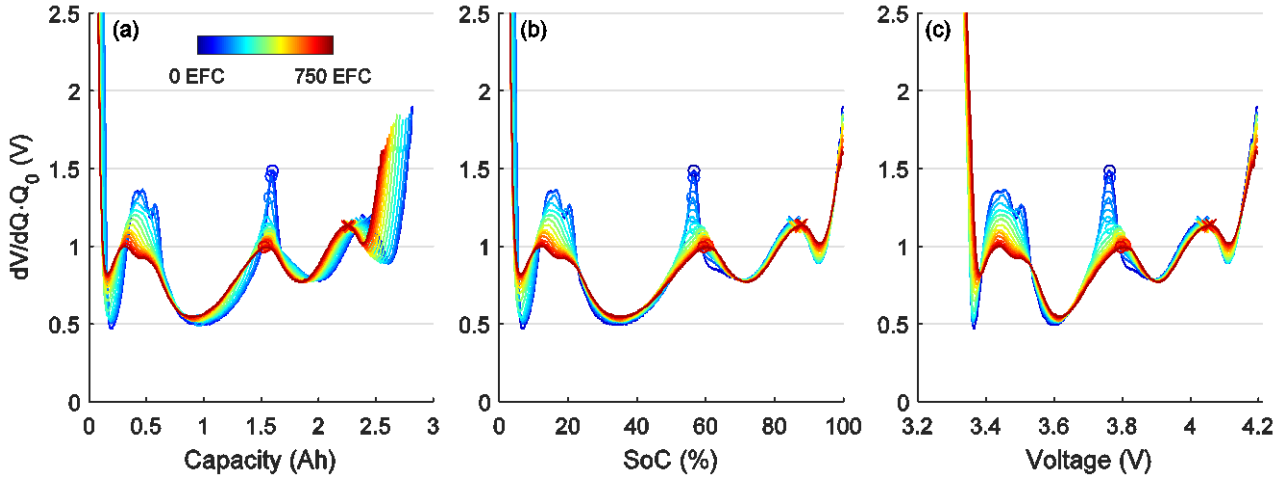

Figure 59. Differential voltage spectra from the checkup data of the cell charged with the 1 A CCCV protocol to 3.8 V, comprising up to 1300 charge-discharge cycles, depicted (a) over actual capacity, (b) over SoC, and (c) over cell voltage. The circle markers highlight the central graphite peak.

As shown in Figure 59a, the peak is attenuated and shifts to slightly lower capacities throughout the first hundreds of cycles. After ca. 400 cycles, the peak remains at a similar capacity. As the actual capacity of the cell decreases further, the peak consequently shifts toward higher SoCs. This is illustrated in Figure 59b and indicates a shift in the electrode balancing. In Figure 59c, the spectra are depicted versus cell voltage. This demonstrates that the central graphite peak is initially located at about 3.75 V and shifts toward 3.8 V with the aging of the cell. As the voltage transition of the anode potential shifts toward higher SoC, the cell potential in the medium SoC region remains longer at a lower level because the anode potential remains longer at a somewhat higher potential. Hence, the cells can be charged longer in the CV phase at 3.8 V before reaching the cut-off current threshold. Overall, the shift in the electrode balancing leads to a longer CV charging duration and, thus, enables a higher available capacity, which explains the lower fade of the relative available capacity depicted in Figure 57b. Charging to 3.7 V remains unaffected from the shift in the electrode balancing because the location of the central graphite peak always lies above this charging voltage.

5.4.1.3 Impact of Cycle Depth and Discharging Voltage

As a preliminary study on charging protocols revealed that completely discharged cells cannot automatically tolerate high charging currents [121], different depths of discharge were examined by different discharging voltages for the CCCV discharging procedure.

Capacity Utilization

In analogy to a decreasing charging voltage, an increasing discharging voltage reduces the available capacity of a lithium-ion battery cell. Figure 60 visualizes the effect of different discharging and charging voltages on the available capacity of a cell in new condition. It shows the differences to the measured capacity in the initial checkup.

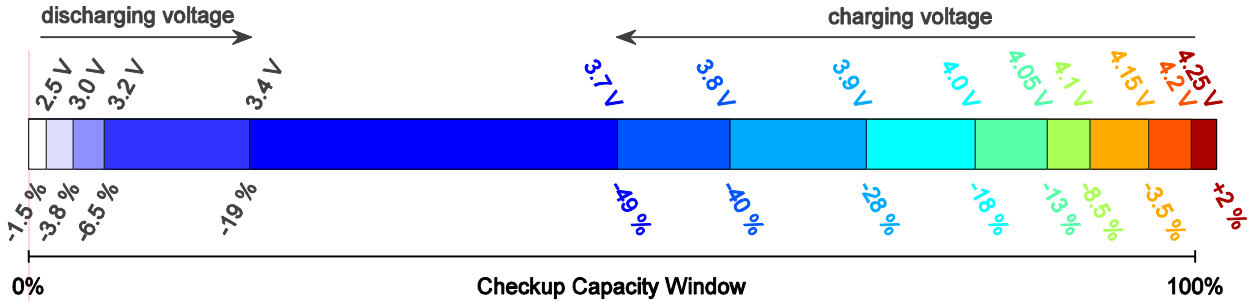

Figure 60. Impact of a higher discharging and a lower charging voltage on the available capacity window during the CCCV discharging and charging test procedure compared to the reference capacity window from the checkup. The values were obtained from cells in new condition.

The 1.5% of unused capacity for discharging to 2.5V show again that the cells were not completely discharged in the cycling sequences due to the cut-off threshold of –0.5 A instead of the –0.1 A which was applied in the checkups. In the cycle aging results presented above, the various charging voltages were all examined together with a discharging voltage of 2.5 V. To examine the impact of the depth of discharge, additional discharging voltages of 3.0 V, 3.2 V, and 3.4 V were defined for the CCCV discharging procedure and examined in combination with a charging voltage of 4.1 V. Figure 60 exhibits their impact on capacity utilization. For a charging voltage of 4.1 V, the capacity utilization amounts to 90% for a discharging voltage of 2.5 V. For the three higher discharging voltages, it decreases to 87.7%, 85%, and 72.5%, respectively. The discharging voltage of 3.2 V, which led to a comparable depth of discharge as sole CC discharging to 2.5 V, was also combined with charging voltages of 4.2 V and 3.7 V. The resulting capacity utilizations, computed as the ratio of the available capacity to the capacity measured in the first checkup, are listed in Table 9. The largest cycling window of 100.5% was obtained for a charging voltage of 4.25 V combined with a discharging voltage of 2.5 V. The smallest cycling window of 44.5% was examined for a charging voltage of 3.7 V combined with a discharging voltage of 3.2 V.

Table 9. Capacity utilization of a new cell during the cycling procedure $C_{cyc,util}$ in relation to the capacity measured in the initial checkup $C_{CU,0EFC}$ for different combinations of charging and discharging voltage

U_{dis} \ U_{ch}		4.25 V	4.2 V	4.15 V	4.1 V	4.05 V	4.0 V	3.9 V	3.8 V	3.7 V
2.5 V	$C_{cyc,util}/C_{CU,0EFC}$	100.5%	98.5%	95%	90%	85.5%	80.5%	70.5%	58.8%	49.5%
3.0 V	$C_{cyc,util}/C_{CU,0EFC}$				87.7%					
3.2 V	$C_{cyc,util}/C_{CU,0EFC}$		93.5%		85%					44.5%
3.4 V	$C_{cyc,util}/C_{CU,0EFC}$				72.5%					

Cycling Sequences

To analyze the impact of different discharging voltages on cycle aging, Figure 61 shows the available capacity for the cycling procedure with different combinations of charging and discharging voltage.

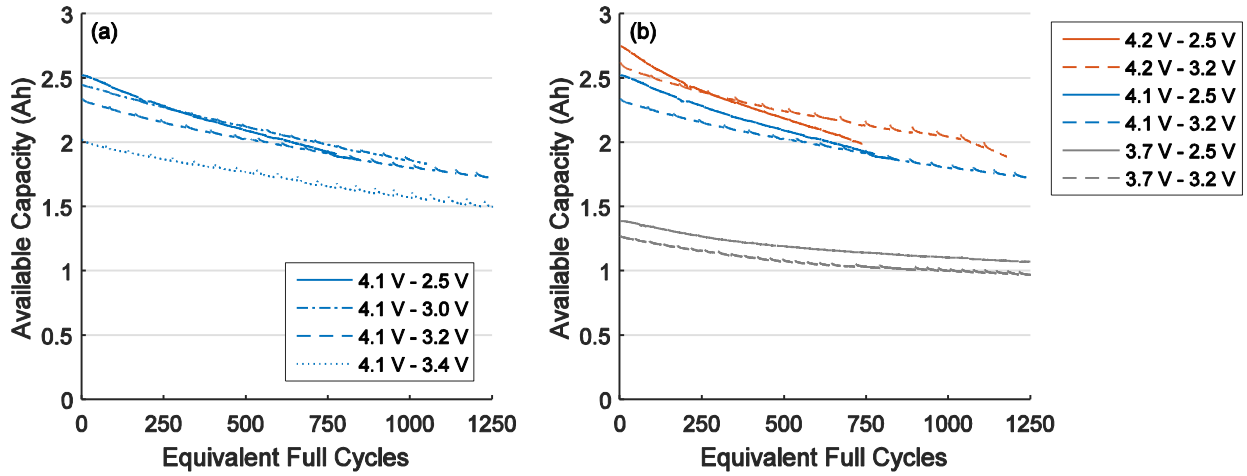

Figure 61. Available capacity over cycle life. (a) Cells with a charging voltage of 4.1 V and different discharging voltages, (b) cells with different charging voltages and discharging voltages of 2.5 V and 3.2 V.

Figure 61a compares the available capacity over EFC of cells with an identical charging voltage of 4.1 V and different discharging voltages of 2.5 V, 3.0 V, 3.2 V, and 3.4 V. The curves of 3.0 V and 3.2 V intersect the curve of 2.5 V discharging voltage at ca. 300 EFC and 750 EFC, respectively. This demonstrates that these reductions of the depth of discharge increase the cycle life of the cells, as they provide a higher available capacity for the aged cells. Figure 61b compares discharging voltages of 2.5 V and 3.2 V for different charging voltages. For 4.2 V charging voltage, the discharging voltage of 3.2 V outperforms the conventional cycling window already after 275 EFC. Hence, a higher discharging voltage is particularly beneficial for a high charging voltage. For the small cycling windows obtained for the charging voltage of 3.7 V, the advantages of a further reduction of the cycle depth by a higher discharging voltage are comparatively small. The available capacities still differ by ca. 100 mAh after 1250 EFC, which reveals no benefits from a reduced depth of discharge.

Checkup Results

The checkup results for the four cells charged to 4.1 V and discharged to different voltage levels in the CCCV discharging sequence are depicted in Figure 62 and exhibit substantially lower degradation for higher discharging voltages. After 750 EFC, the capacity fade for the discharging voltage of 3.4 V is only half of the capacity fade observed for discharging to 2.5 V.

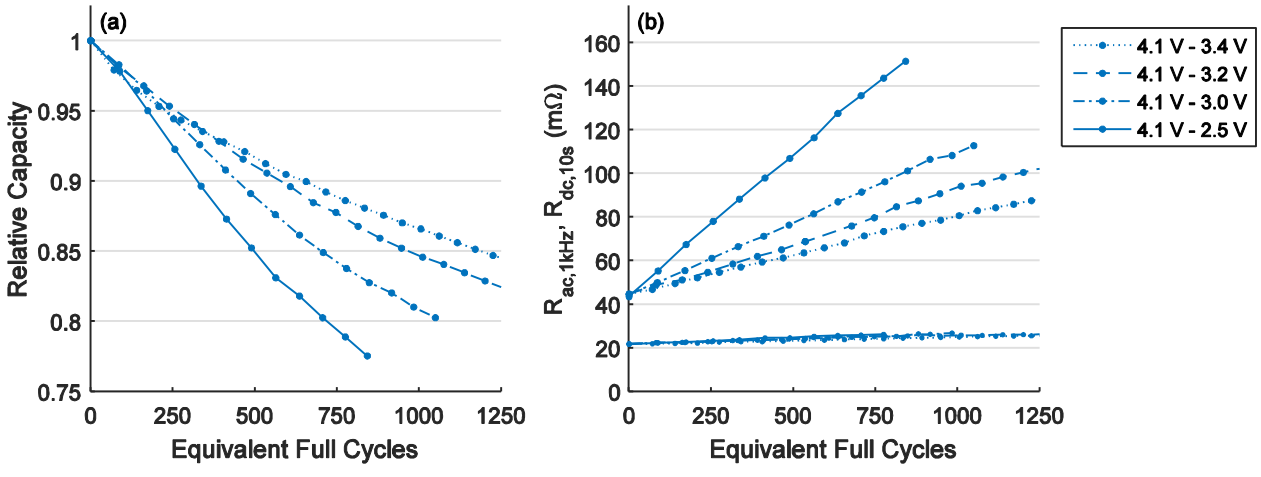

Figure 62. (a) Capacity fade and (b) resistance increase for the four cells charged to 4.1 V and discharged to different voltage levels at 25°C

Also the increase of $R_{dc,10s}$ is substantially lower. $R_{dc,10s}$ has increased by ca. 60% when discharging to 3.4 V, whereas it has increased by more than 200% when discharging to 2.5 V. The impedance spectra after ca. 500 EFC, depicted in Figure 63, demonstrate that it is the enlargement of the capacitive semicircle in the frequency domain below 30 Hz, ascribed to the charge transfer of the NCA cathode, that is responsible for the marked differences in resistance increase. Overall, the reduced cycling windows reduce cycle aging considerably. However, it has to be further investigated whether reducing the cycle depth in general or avoiding the very low SoC regimes has reduced the cycle aging.

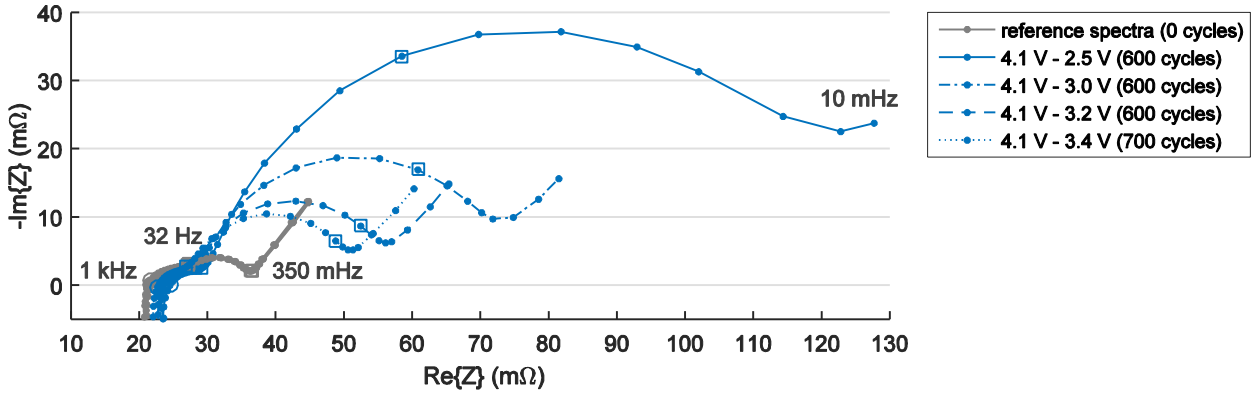

Figure 63. Impedance spectra of the cells in the new state and after 600 or 700 cycles, which corresponds to ca. 500 EFC for the cycling protocols with different discharge depths

Substantial reductions in cycle aging can also be identified for the other two charging voltages. Figure 64 compares the effects of increasing the discharging voltage from 2.5 V to 3.2 V for three different charging voltages. In all three cases, the capacity fade and the resistance increase decrease markedly. More than 1000 EFC can be achieved before reaching a capacity fade of 20%, even for the high charging voltages of 4.1 V and 4.2 V.

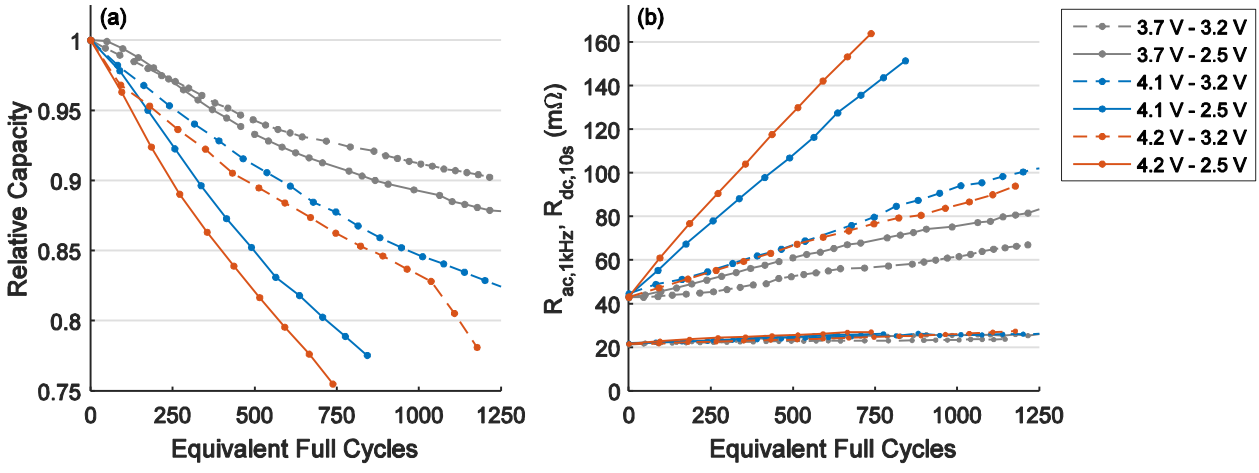

Figure 64. (a) Capacity fade and (b) resistance increase for the cells discharged to 2.5 V and 3.2 V which were charged with different charging voltages.

A moderate increase in $R_{dc,10s}$ can be obtained by either reducing the charging voltage to a low value, such as 3.7 V, while maintaining the same discharging voltage or by increasing the discharging voltage from 2.5 V to 3.2 V while maintaining a high charging voltage of 4.2 V or 4.1 V. Combining both means leads to a massive reduction of the resistance increase, which is highly beneficial for

the peak power performance and the rate capability of the cells as the voltage drops under load remain considerably lower. However, reducing the charging voltage and increasing the discharging voltage always entails a lower capacity utilization.

For all combinations of charging and discharging voltage examined, Table 10 compares capacity utilization and capacity fade. It reveals that in general, the capacity fade decreases with lower cycle depth. Yet, there is no direct relation between cycle depth and the capacity fade. Table 10 shows that reducing the depth of discharge by increasing the discharging voltage reduces cycle aging more effectively than reducing the charging voltage. Taking the cell cycled between 4.1 V and 2.5 V, which exhibits a capacity utilization of 90% and ca. 15% of capacity fade after 500 EFC, as a reference case shows that a reduction of the charging voltage to 4.05 V and increasing the discharging voltage to 3.2 V both decreases the cycle depth by ca. 5 percentage points. When reducing the charging voltage to 4.05 V, the capacity fade decreases only to 13.6%; when increasing the discharging voltage to 3.2 V, the capacity fade decreases considerably more to 9.2%. A similar result is also obtained when comparing other combinations of charging and discharging voltages with similar cycle depths. This demonstrates that cycle aging increases disproportionately in the very low SoC region. Thus, deep discharging should be avoided when a long cycle life has to be achieved.

As the battery of an EV will seldomly be completely discharged in every-day use and as the manufacturer defines a certain safety margin for the discharge depth, the cycle life of the battery will be better in the practical application than in the artificial laboratory tests with deep discharging performed in this study. These test conditions represent worse case scenarios and illustrate the lower boundaries of cycle life. More representative cycle depths will be examined in the aging study on driving operation, presented in Chapter 6.

Table 10. Extension of Table 9 by the capacity fade measured in the checkup after 500 EFC for different combinations of charging and discharging voltage

U_{dis} \ U_{ch}		**4.25 V**	**4.2 V**	**4.15 V**	**4.1 V**	**4.05 V**	**4.0 V**	**3.9 V**	**3.8 V**	**3.7 V**
2.5 V	$C_{cyc,util}/C_{CU,0EFC}$	100.5%	98.5%	95%	90%	85.5%	80.5%	70.5%	58.8%	49.5%
	C_{CU} after 500 EFC	–20.0%	–17.9%	–16.1%	–15.1%	–13.6%	–12.8%	–9.8%	–6.9%	–6.7%
3.0 V	$C_{cyc,util}/C_{CU,0EFC}$				87.7%					
	C_{CU} after 500 EFC				–11.4%					
3.2 V	$C_{cyc,util}/C_{CU,0EFC}$		93.5%		85%					44.5%
	C_{CU} after 500 EFC		–10.4%		–9.2%					–5.7%
3.4 V	$C_{cyc,util}/C_{CU,0EFC}$				72.5%					
	C_{CU} after 500 EFC				–8.6%					

Additional Insights from Differential Voltage Analysis

For the four discharging voltages which were examined together with the charging voltage of 4.1 V, Figure 65 illustrates the changes in the differential voltage spectra within 500 EFC. For CCCV discharging to 2.5 V, Figure 65a exhibits an early attenuation of the characteristic graphite peaks. As no clear central graphite peak is visible after ca. 200 EFC, no distinct potential change from medium to low anode voltage plateau occurs any longer. This is supposed to be caused by an inhomogeneous degradation of the graphite active material. The differential voltage spectra of the cells discharged to 3.0 V, depicted Figure 65b, are similar to those for 2.5 V. Only in the high SoC

regime, the valley from the NCA cathode appears still more pronouncedly, which indicates lower cathode degradation. This reduced degradation of the NCA cathode is in good agreement with the EIS measurements, since the increase of the charge transfer resistance of the cathode is substantially lower for discharging to 3.0 V than for 2.5 V (see Figure 63). When decreasing the depth of discharging by defining 3.2 V as discharging voltage, the central graphite peak in Figure 65c can still be detected for higher numbers of EFC. This indicates a lower anode degradation. The best cycle life was obtained for CCCV discharging to only 3.4 V, which means that the lowest ca. 20% of the capacity were not utilized (see Figure 60). For this case, Figure 65d discloses that the shape of the characteristic graphite peaks exhibits the least changes of all four cases, which indicates the lowest anode degradation. Overall, the differential voltage spectra provide additional information on the degradation of the active materials beyond the loss of cyclable lithium which reduces the actual capacity. Aggravated active material degradation has been observed for the deep discharging.

In the literature, mechanical stress onto the graphite active material was reported to be highest for the intercalation of lithium at very low SoCs [61]. This was related to the large relative volume changes that occur at low degrees of lithiation of the graphite active material. These volume changes exert high stress onto the C-C bonds, which can lead to a damage of the active material structure. Thus, the mechanical stress onto the graphite active material can be an explanation for the accelerated aging when cycling to lower SoCs.

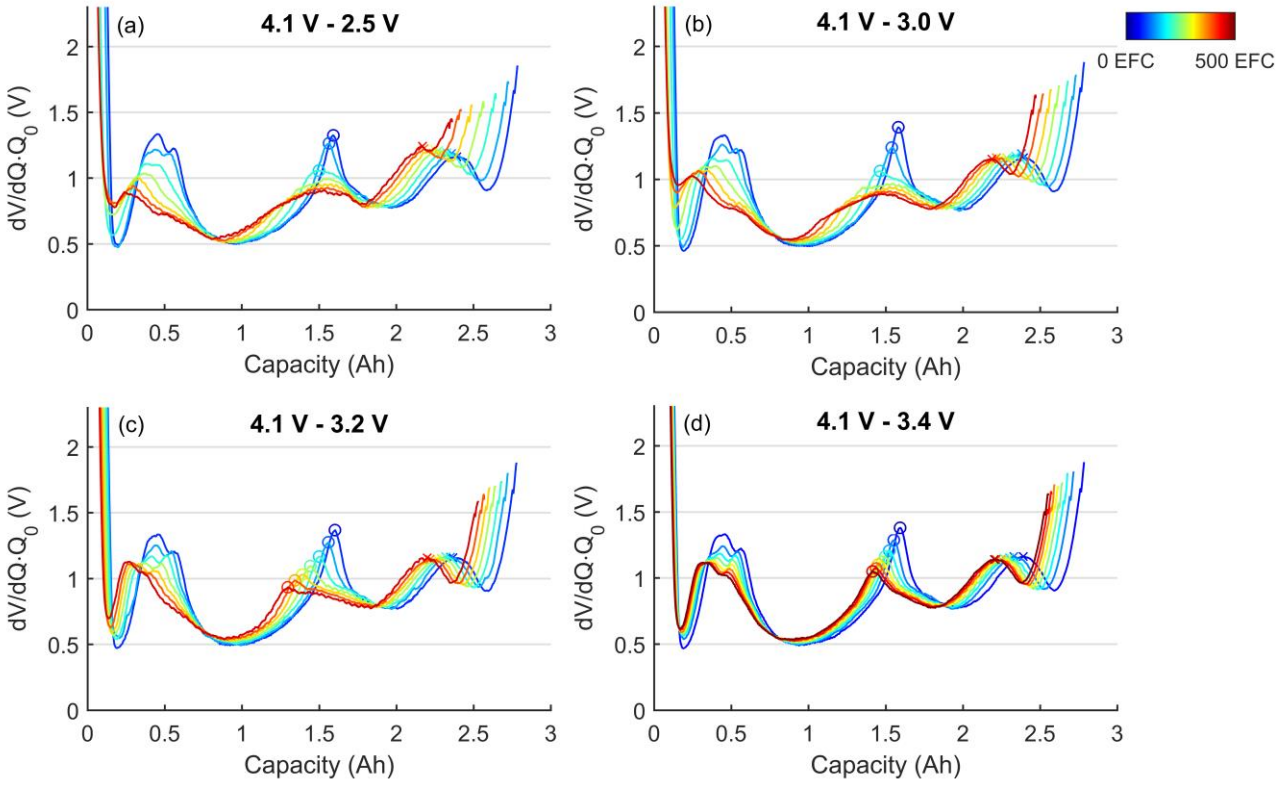

Figure 65. Differential voltage spectra for up to 500 EFC from the cells charged with the 1.0 A CCCV to 4.1 V and CCCV discharged to (a) 2.5 V, (b) 3.0 V, (c) 3.2 V, (d) 3.4 V. The circle markers indicate the central graphite peak and the cross markers indicate the NCA peak at high SoC.

5.4.2 Boost Charging

As demonstrated by the results of CCCV charging, high charging currents lead to a rapid degradation due to lithium plating, which occurs particularly strongly at high SoC. To accelerate the charging process while still maintaining a good cycle life, BC protocols were examined which combine an interval of high charging current and a lower charging current throughout the rest of the charging procedure. The BC protocols extend the conventional CCCV charging procedure by a boost interval, where a higher charging current is applied for a limited time. In this thesis, the BC protocols were based on 1.0 A CCCV charging and contained an additional boost interval, in which up to 40% of the nominal capacity were charged in form of a 3.0 A CCCV interval which lasted 22.5 min. To determine whether different SoC regions have different susceptibilities to high charging currents, boost intervals at different SoC locations were compared. The onset of the boost interval was varied between 0% C_N and 40% C_N.

Charging Time and Capacity Utilization

Figure 66a illustrates the cell voltages and the charged capacities of the BC procedures for charging voltages of 4.2 V and 4.1 V in combination with five different onset locations of the boost interval. The beginning and the end of all BC protocols are similar, only the location of the boost interval varies. Figure 66a demonstrates that BC shortens the total charging duration by more than 40 min. For the cells in the new condition, the total duration amounts to 143 min when charging to 4.2 V and to 134 min when charging only to 4.1 V. These charging durations lie between those of 1.0 A CCCV charging and 2.0 A CCCV charging. As presented in Figure 50, 2.0 A CCCV charging led to a charging time of 115 min for 4.2 V and 110 min for 4.1 V.

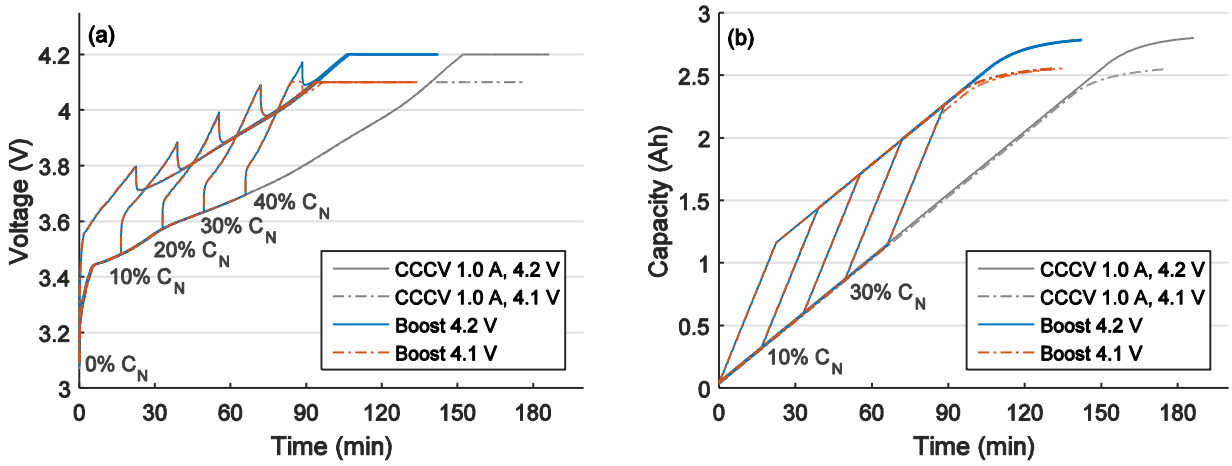

Figure 66. Charging progress of new cells charged with boost charging protocols: (a) Voltage curves and (b) charged capacity for boost protocols with different locations of the boost interval. CCCV protocols are included for comparison. The numbers next to the graphs describe the onset of the respective boost interval.

Figure 66b demonstrates that the capacity utilization remains rather unaffected from the varying charging currents and is similar to the capacity utilization of the 1.0 A CCCV protocols. For charging to 4.1 V with the boost interval starting at 40% C_N, Figure 66a shows that the voltage limitation sets in at the end of the boost interval and restricts the charging current. Due to this limitation, the capacity graph for this charging protocol varies slightly and leads to a somewhat later end of the

charging procedure. Overall, the location of the boost interval has very minor impact on capacity utilization.

Cycle Life

Figure 67 shows the available capacities in the cycling procedures for charging to 4.2 V and 4.1 V. For both charging voltages, the capacity curves lie close together at the very beginning but then diverge markedly after several cycles.

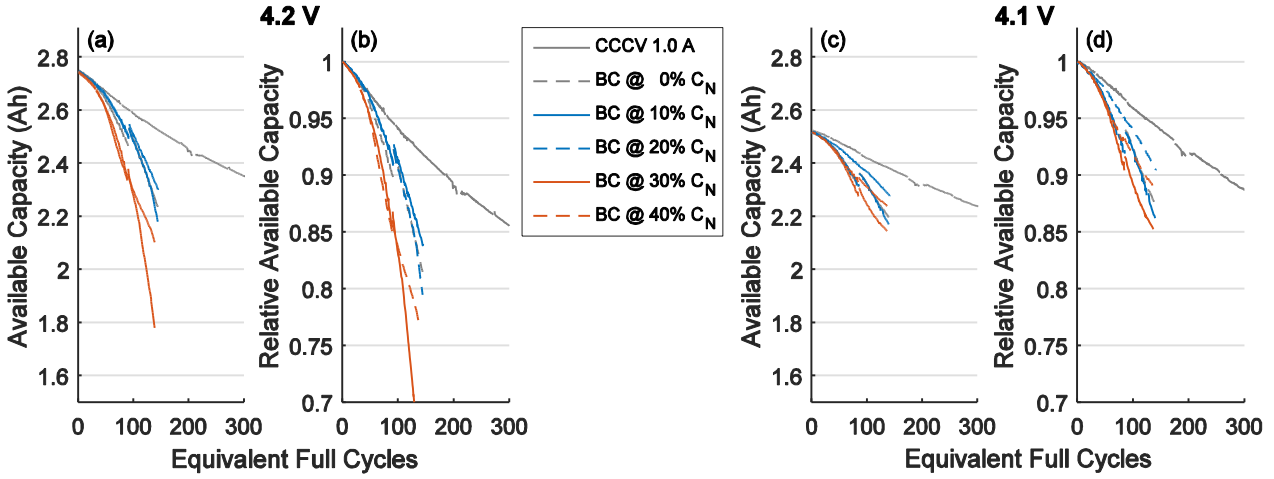

Figure 67. Absolute and relative values of the available capacity using boost charging protocols for (a-b) charging to 4.2 V and (c-d) charging to 4.1 V.

All BC protocols exhibit a considerably faster degradation than the 1.0 A CCCV charging protocols, which serve as a reference. As no adequate cycle life was obtained with the BC protocols, the cycling procedure was terminated early, already after about 150 EFC. For both charging voltages, the worst cycle life was observed for the BC protocols with the boost interval starting at 30% C_N. After less than 150 EFC, a capacity fade of more than 30% was reached for charging to 4.2 V and a capacity fade of ca. 15% was obtained for charging to 4.1 V. Hence, high-current boost intervals have led to disproportionate degradation. For charging to 4.2 V, the BC protocol with the boost interval starting at 40% C_N experienced the fastest capacity fade in the beginning of the cycling procedure but fell behind the 30% C_N variant after ca. 100 EFC. This results from the voltage limitation in the boost interval. With advancing degradation, the charging voltage was reached during the boost interval and the boost period was restricted by the CV boundary. As a consequence, the current at the end of the boost interval decreased, which in turn led to decelerated degradation. This demonstrates that the high charging current during the boost interval causes the substantial capacity fade. Lithium plating appears to be the dominant degradation mechanism for the BC protocols. The results from charging to 4.1 V, depicted in Figure 67c-d, show that the reduced cycle depth leads to a somewhat lower capacity fade. But also in this case, no suitable cycle life for an EV application is achieved.

Checkup Results

The results from the checkups, depicted in Figure 68, reveal similar degradation trends as the results from the cycling procedure. For charging to 4.2 V (see Figure 68a), the capacity fade after less than 150 EFC amounts to 10–31%. For charging to 4.1 V, Figure 68c reveals capacity fades between 7 and 11 % for the different BC protocols. In addition to the rapid capacity fade, the internal resistances rise considerably. As $R_{ac,1kHz}$ also increases notably within the first 150 EFC when charging to 4.2 V

(see Figure 68b), there must occur side reactions causing substantial electrolyte decomposition which lower its conductivity. These side reactions can be explained by plated lithium reacting partially with the electrolyte.

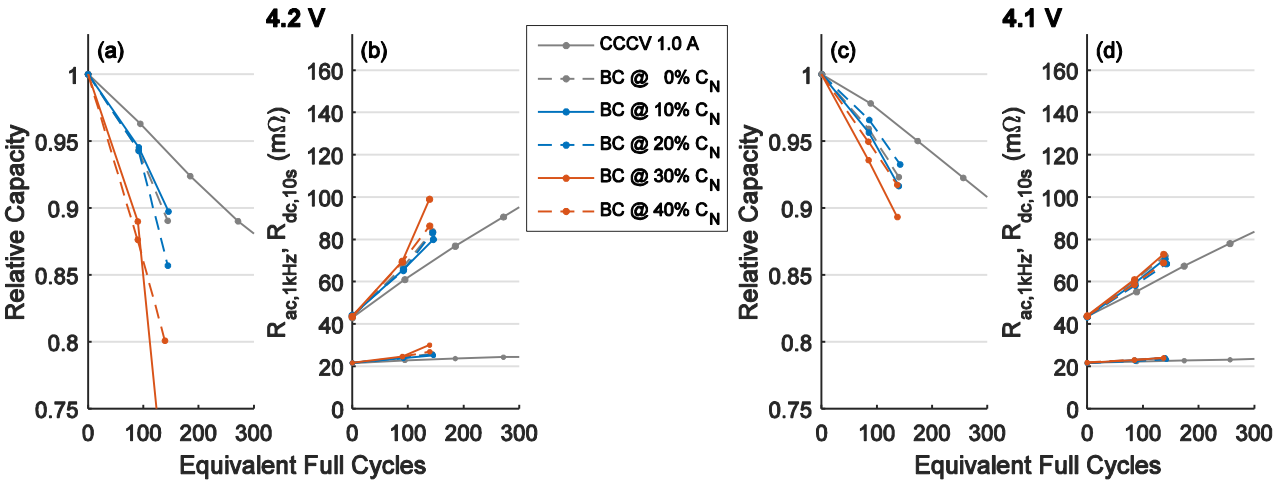

Figure 68. Checkup results comparing boost charging protocols with different locations of the boost interval to 1.0 A CCCV charging. (a, c) Capacity fade and (b, d) resistance increase for charging to (a-b) 4.2 V and to (c-d) 4.1 V.

Similar to the decreasing capacities during cycling, the capacity fade of the cells with the boost intervals at 30% C_N is largest. This confirms lithium plating to be the driving force of capacity fade: The transition of medium to lowest anode potential occurs at ca. 60% C_N. Thus, the cells having the boost interval – which charges 40% C_N with a high charging current – at SoC locations of 20% C_N or below do not reach the SoC regime of lowest anode potential during the boost intervals or the exposure to the high boost currents within the SoC regime of lowest anode potential is only short. By contrast, the BC protocols with the boost interval located at 30% C_N or 40% C_N reach the plateau of lowest anode potential during the boost intervals. Thus, lithium plating aggravates and the capacity fades considerably faster. As described above, the charging currents were reduced for the BC protocols with the boost interval located at 40% C_N due to the voltage limitation during the boost interval. With the charging current having been reduced, also lithium plating and capacity fade have decreased. When charging to only 4.1 V, the charging current in the high SoC regime remains generally lower and less degradation owing to lithium plating is observed in Figure 68c.

Additional Insights from Differential Voltage Analysis

Figure 69 compares the differential voltage spectra of the cells in the new condition and after ca. 150 EFC with the BC protocols. It reveals a considerable left-shift of the central graphite peak, which indicates decreasing storage capabilities of the graphite anode. In Figure 69a, the cell with the boost interval at 30% C_N exhibits not only a larger capacity fade but also a stronger anode degradation than the cell with the boost interval at 40% C_N. Also for the boost intervals in lower SoC regions, substantial degradation of the anode is observed as the location of the central graphite peak shifts considerably to the left. For the cells with the lower charging voltage of 4.1 V, Figure 69b also shows that the storage capabilities of the anode decreased but to a considerably lower extent. Overall, the boost charging protocols examined did not exhibit a superior performance which is suitable for fast charging EVs. Instead, the high-current boost intervals led to an accelerated anode degradation.

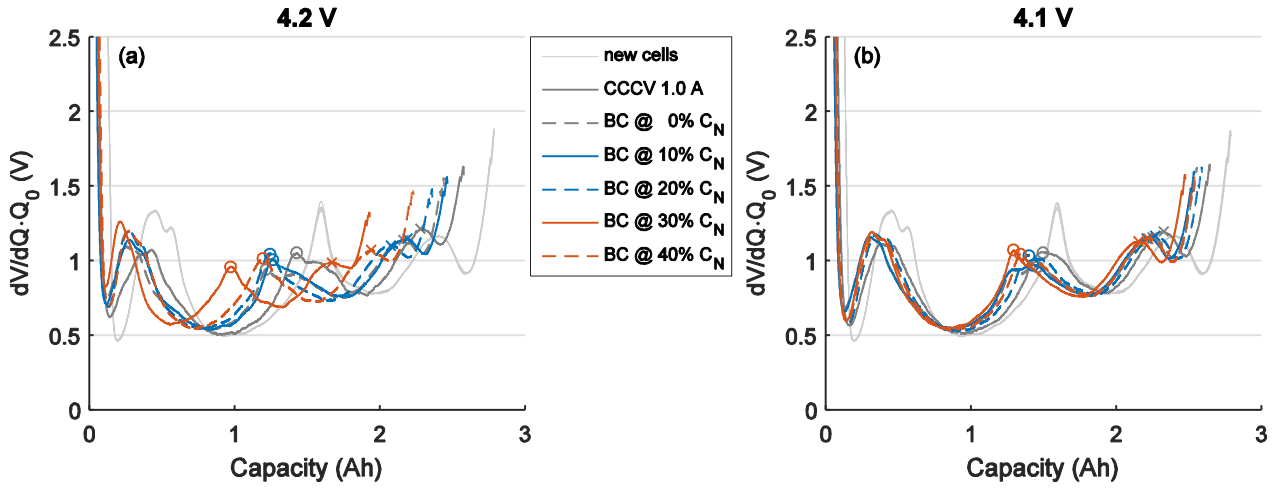

Figure 69. Differential voltage spectra in the new condition and after ca. 150 EFC with the different boost charging protocols for (a) charging to 4.2 V and (b) charging to 4.1 V. The spectra after 200 cycles with 1.0 A CCCV charging serve as a reference.

5.4.3 Supercharging

Another approach of fast charging lithium-ion batteries is SC, which combines an initial boost period with two subsequent voltage ramps to reach the final CV phase. This leads to a continuously decreasing charging current with increasing SoC. Different modifications of the initial SC implementation were also examined to determine major influencing factors on charging-induced degradation.

Charging Time and Capacity Utilization

The charging progress for the SC protocol is illustrated in Figure 70. The charging duration is ca. 100 min for charging to 4.2 V and ca. 90 min for charging to 4.1 V. For both charging voltages, the charging duration is ca. 85 min shorter than for 1.0 A CCCV charging and it is also more than 10 min shorter than 2.0 A CCCV charging. The changing voltage slope at 3.9 V in Figure 70a corresponds to the end of the boost interval. Figure 70b exhibits the bent capacity curves which are the result of the continuously decreasing charging current after the initial boost interval. The capacity utilization at the end of the charging process is similar to CCCV charging.

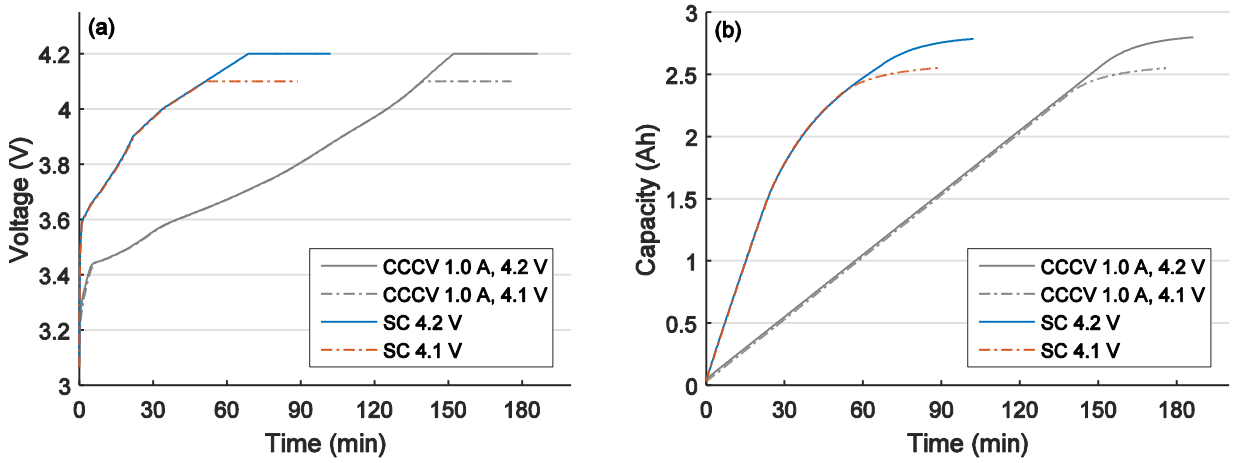

Figure 70. Charging progress of new cells charged with supercharging protocols: (a) Voltage curves and (b) charged capacity. 1.0 A CCCV charging protocols serve as references.

Checkup Results

The capacity fade and the resistance increase for the SC protocols are illustrated in Figure 71 for charging to 4.2 V and 4.1 V. For both charging voltages, a rapid capacity fade is observed in Figure 71a and Figure 71c for the SC protocols (see SC (2.5V)). This capacity fade is substantially larger than that of 1.0 A CCCV charging. A comparison with 2.0 A CCCV charging, depicted in Figure 52, reveals a considerably faster degradation for supercharging, although the total charging time differs only in the order of 10%. Hence, the high initial charging currents have led to disproportionate degradation. The increases in $R_{ac,1kHz}$, shown in Figure 71b and Figure 71d, reveal side reactions entailing a decomposition of the electrolyte. Based on these results, lithium plating can be identified as the main driver of degradation for charging with the SC protocols. Due to the poor cycle life performance, the cycling sequence was terminated already after ca. 120 EFC.

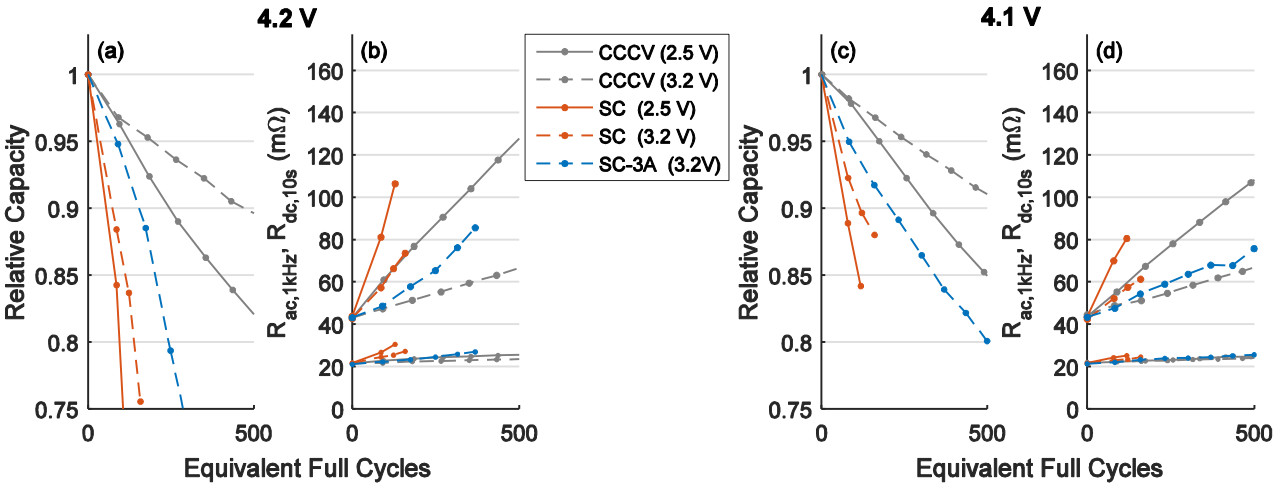

Figure 71. (a,c) Available capacity and (b,d) relative available capacity for different supercharging protocols and 1 A CCCV protocols for charging voltages of 4.2 V and 4.1 V. The respective discharging voltage is given in the parenthesis.

Two modifications of the basis SC test protocols were also examined. At first, the discharging voltage was increased from 2.5 V to 3.2 V to reduce the stress at very low SoC. Furthermore, the boost intensity was reduced: During the boost interval, the charging power of 14 W was replaced by a constant current of 3 A to obtain a better comparability to the experiments on CCCV and BC protocols. The boost periods ended when the cell voltage reached 3.9 V, which was identical to the first SC protocols. As illustrated in Figure 71, the increase of the discharging voltage reduces the degradation also for the SC protocols. Capacity fade and resistance increase are lower (see SC (3.2V)). The lowering of the boost charging currents from ca. 3.7 A to 3 A (see SC-3A (3.2V)) entails a marked improvement compared to the first SC variant. However, the capacity fade and the resistance increase still remains considerably worse than for the 1.0 A CCCV reference protocol, particularly when comparing the curves to those for discharging to 3.2 V only (see CCCV (3.2V)). As shown in Figure 71c, 500 EFC were obtained for the SC-3A protocol in combination with a charging voltage of 4.1 V before reaching a capacity fade of 20%. However, this is more than twice the capacity fade from 1.0 A CCCV charging for the same discharging voltage of 3.2 V. Overall, substantially higher stress is observed for all SC charging protocols due to their high initial charging currents, although the charging currents were adapted to the SoC of the cell.

Additional Insights from Differential Voltage Analysis

For the SC protocols charging to 4.2 V, Figure 72 shows the differential voltage spectra for up to 500 cycles. Figure 72a and Figure 72b reveal a massive fade of storage capabilities of the anode, as the central graphite peak shifts markedly to the left already within a low number of cycles. When increasing the discharging voltage from 2.5 V to 3.2 V, the attenuation of the central graphite peak decreases. Hence, a more uniform degradation of the anode is assumed. Figure 72c demonstrates that for lowering the boost intensity, the shift of the central anode peak decelerates and the aging rate decreases. However, the degradation remains at a very high level. The differential voltage spectra confirm that the high charging currents at the beginning of the charging procedure stress the anode disproportionately and cause a rapid capacity fade. For charging to 4.1 V, the differential voltage spectra revealed a lower degradation rate, but the trends were similar to the observations presented in Figure 72.

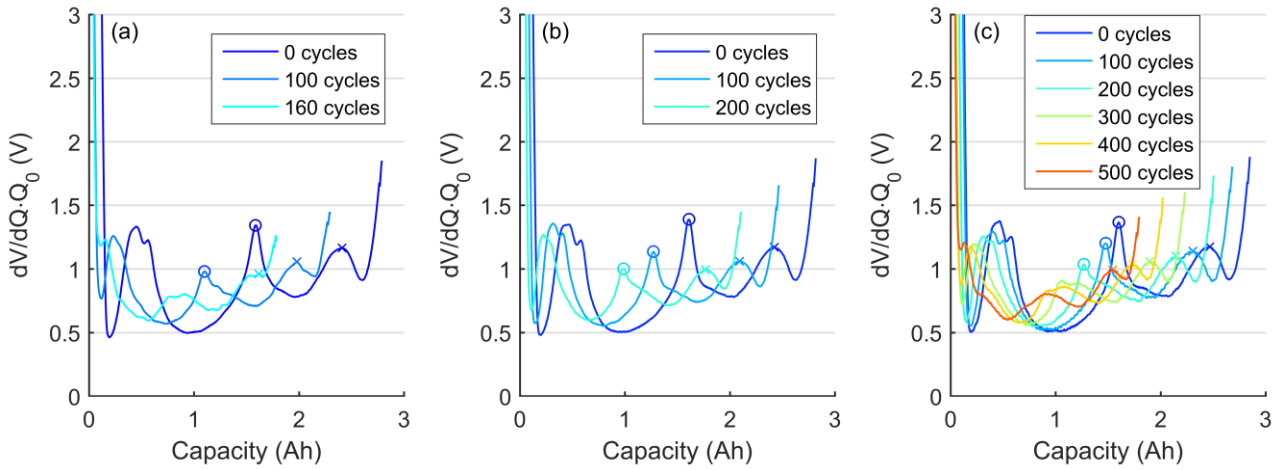

Figure 72. Differential voltage spectra after up to 500 cycles for different supercharging protocols charging the cells to 4.2 V: (a) SC 4.2 V–2.5 V, (b) SC 4.2 V–3.2 V, and (c) SC-3A 4.2 V–3.2 V.

Overall, the cell type examined is very sensitive to high charging currents. Based on the results obtained in this study, the cells exhibit – even for the SC protocols with reduced boost intensity – a capacity fade of 20% already after about 300 cycles from 3.2 V to 4.2 V or 700 cycles from 3.2 V to 4.1 V. In the second case, the cells would still be able to withstand 500 EFC. Combined with an average driving distance of 350 km per full cycle, this corresponds to 175,000 km of driving before reaching the EoL of the battery. For a vehicle with a lower driving range per full cycle, such as 150 km, the cycle life of 500 EFC of the supercharging protocols for the cycling window from 3.2 V to 4.1 V would lead to an insufficient battery life of only 75,000 km.

5.4.4 Charging with Soft-Start Period

As observed in the previous cycling procedures, a deep CCCV discharging to 2.5 V aggravates degradation. To examine whether completely discharged cells are disproportionately stressed by the charging currents at low SoC, charging protocols with an initial soft-start sequence were examined. In these soft-start protocols, the initial 10% C_N were charged with a low current of 100 mA (= C/28).

Charging Time and Capacity Utilization

For charging to 4.1 V and 3.7 V, Figure 73 shows the charging progress with and without a soft-start interval. As the initial 10% C_N were charged at a very low rate, the charging procedure lasts ca. 150 min longer than the 1.0 A CCCV charging protocol and the total duration lies in the order of 0.5 A CCCV charging (see Figure 50). The capacity utilization at the end of the charging procedure is somewhat higher than for the conventional CCCV protocols.

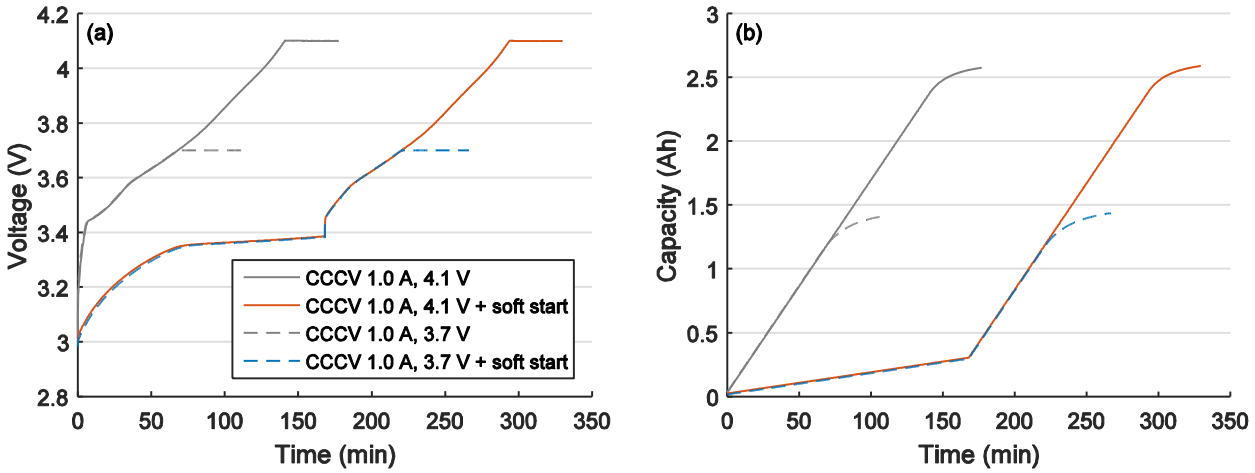

Figure 73. Charging progress of new cells charged with and without a soft-start period covering the initial 10% C_N: (a) Voltage curves and (b) charged capacity for charging voltages of 4.1 V and 3.7 V.

Checkup Results

The capacity fade and the resistance increase of the two soft-start charging protocols are illustrated in Figure 74.

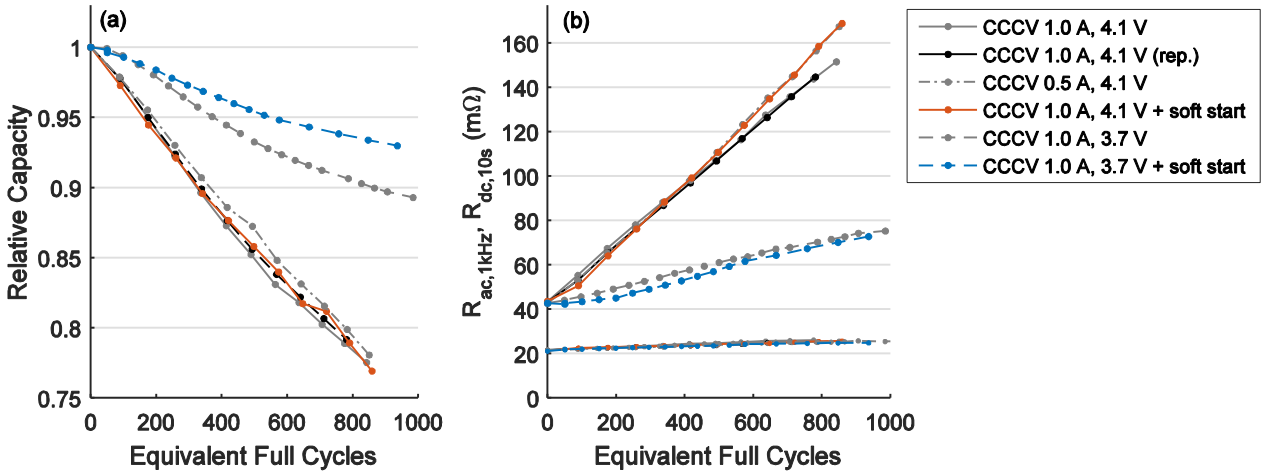

Figure 74. Impact of a soft-start interval on (a) capacity fade and (b) resistance increase, measured by the checkups every 100 cycles.

For charging to 4.1 V and 3.7 V, the soft-start charging protocols are compared to their 1.0 A CCCV counterparts. The capacity fade and resistance increase for charging to 4.1 V is similar for both charging strategies. After 500 EFC, the capacity fade amounts to ca. 14% and $R_{dc,10s}$ has increased by more than 70 mΩ. For charging to 3.7 V, however, a lower cycle aging is observed for the soft-start charging variant. The capacity fade is ca. 2 percentage points lower after 500 EFC and $R_{dc,10s}$ also remains notably lower. This means that for the smaller cycling window, the initial sequence with a low charging current reduces cycle aging.

For charging to 4.1 V, no benefits from a low-current sequence at the beginning can be observed in the capacity fade and resistance increase. The capacity fade is also similar to 0.5 A CCCV charging, which exhibits the same total charging time as the soft-start protocol. Particularly for the internal cell resistances, Figure 74b exhibits an excellent agreement between the soft-start protocol and 0.5 A CCCV charging. There is also an excellent agreement in the resistance values of the two repetitions of 1.0 A CCCV charging. Hence, the differences between the two pairs of resistance curves were not caused by cell-to-cell variation but are supposed to be a result of the different cycle durations.

Additional Insights from Differential Voltage Analysis

To further investigate the effects of a low charging current at the beginning of the charging process, Figure 75a and Figure 75b show the differential voltage spectra of the two cells charged to 3.7 V with the conventional 1.0 A CCCV protocol and with the soft-start protocol, respectively. The most obvious differences can be observed for the graphite peaks at 0.3–0.6 Ah and the central graphite peak at ca. 1.6 Ah. Figure 75b demonstrates that the degradation of the graphite anode is lower for the soft-start protocol since the graphite peaks are less attenuated. As the location of the central graphite peak exhibits only a very small left-shift, the capacity fade results predominantly from a loss of cyclable lithium owing to a shift in the electrode balancing which reduces the available cycling window. This degradation resembles calendar aging, where there has also been observed only a loss of cyclable lithium and very minor degradation of the active materials.

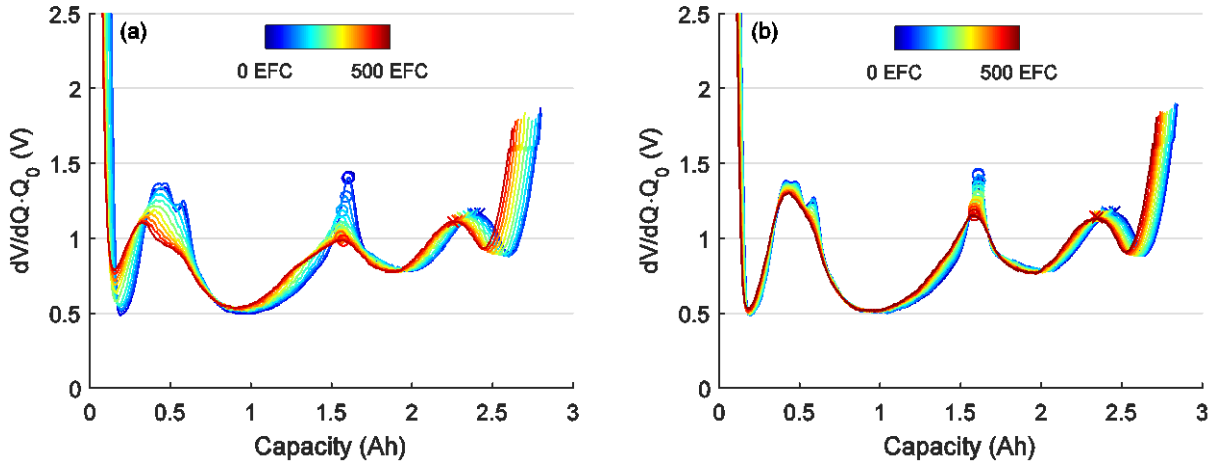

Figure 75. Differential voltage spectra after up to 500 EFC for 1.0 A CCCV charging to 3.7 V (a) without and (b) with a soft-start period, in which the first 10% C_N were charged with a charging current of only 100 mA.

For charging to 4.1 V, Figure 76 compares the differential voltage spectra of three cells which were charged with the soft-start protocol or CCCV protocols. Although there have not been considerable

differences in the capacity fade and resistance increase, notable differences can be observed in the differential voltage spectra.

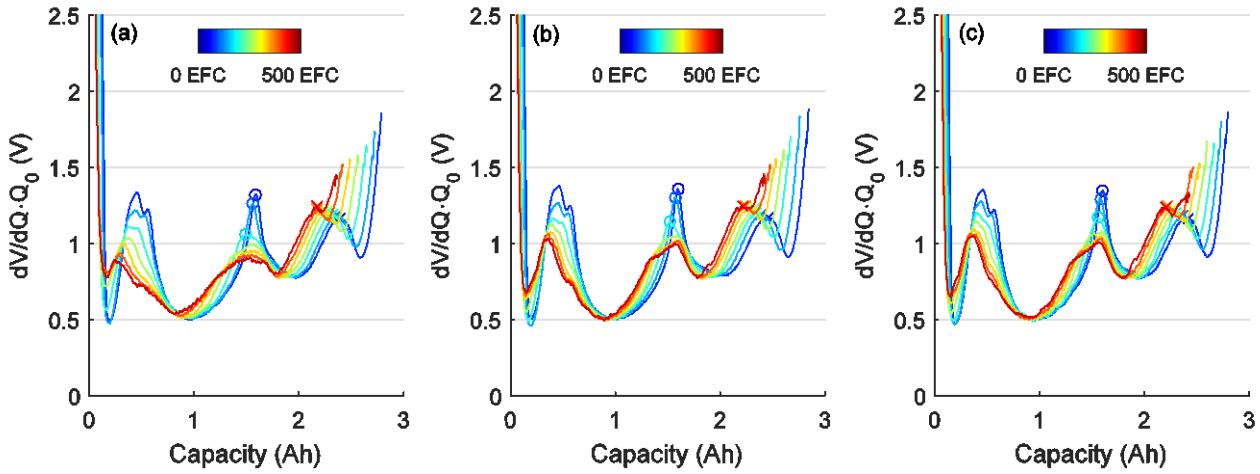

Figure 76. Differential voltage spectra after up to 500 EFC for 1.0 A CCCV charging to 4.1 V (a) without and (b) with a soft-start period, in which the first 10% C_N were charged with a charging current of only 100 mA. (c) 0.5 A CCCV charging, which has a similar charging duration as the soft-start protocol.

In general, the graphite peaks are attenuated considerably more than for charging to 3.7 V, which has been presented in Figure 75. As there is no distinct central graphite peak any longer for the aged cells in Figure 76, an inhomogeneous degradation of the active material is assumed for all cells charged to 4.1 V. Again, the attenuation is lower for the soft-start protocol, depicted in Figure 76b, than for the conventional 1.0 A CCCV protocol, depicted in Figure 76a. It seems that the reduced charging current at low SoC has a positive effect on cycle aging. However, this becomes questionable when regarding Figure 76c, which illustrates 0.5 A CCCV charging to 4.1 V. This charging protocol has a similar total charging duration as the 4.1 V soft-start protocol. As the differential voltage spectra are similar for these two protocols, the lower anode degradation is supposed to be more an effect of time than of the charging current. The slow cycles, which exhibit better anode storage capabilities, might provide the cells enough time for a homogenization of the internal charge distribution or they enable recovery periods in which deposits from side reactions at the electrode surface are dissolved so that certain anode areas are no longer inhibited from participating in the charge-discharge cycling.

Overall, it does not seem that moderate charging currents stress the cells at low SoC but that low charging currents at low SoC, where potential changes in the anode half-cell potential are largest, lead to certain homogenization effects. Investigating these effects can be the subject of further experimental studies.

5.5 Conclusions

Ideal charging protocols for EVs combine a short charging time, a high capacity utilization, and a long cycle life. However, the charging protocol implemented in a practical application is always a compromise that represents a tradeoff between these three criteria.

Charging Time and Capacity Utilization

The charging time is mainly determined by the charging currents applied. With higher charging currents, the charging time decreases. For standard CCCV protocols, the charging time does not change considerably over the battery life. With proceeding aging of the battery cells, the duration of the CC phase shortens. However, the overall charging time decreases only slightly, as the CV phase prolongs.

The capacity utilization is largely independent from the charging current and depends mainly on the charging voltage. Moreover, the cut-off current specified for the CV period also affects the capacity utilization. When starting the charging procedure with a very low current, a somewhat higher capacity utilization has been observed.

Lithium Plating Confirmed as Main Degradation Mechanism

The study on charging protocols for lithium-ion batteries has clearly revealed that high charging currents aggravate degradation. Lithium plating has been confirmed to be the dominant aging mechanism when charging high-energy lithium-ion batteries with high charging currents to high charging voltages. Lithium plating is associated with a rapid capacity fade caused by a loss of cyclable lithium owing to side reactions of the plated lithium with the electrolyte. Increasing high-frequency resistances have revealed a decomposition of the electrolyte, which decreases its conductivity. Also in the differential voltage spectra, reduced storage capabilities of the graphite anode have been observed after charging with high currents.

Resistance Increase Originates Mainly from the NCA Cathode

In addition to the degradation at the anode, the cathode has also exhibited a considerable degradation. The EIS measurements have revealed a massive increase of the charge transfer resistance of the NCA cathode, particularly for deep discharging and large charge-discharge cycles. According to the literature, this can be explained by microcracks in the particles and by weakening particle-to-particle contacts. With the increasing cell resistances, the rate capability of the cells diminishes. Hence, the power capability and the cycle depth under higher discharging currents decreases.

Results of Boost Charging and Supercharging

The BC and SC protocols apply a high charging current only at a certain SoC regime. Although it has been beneficial to avoid high charging currents at high SoC regimes, where the anode potential is lowest, the high charging currents have still caused disproportionate degradation at lower SoCs. No benefits compared to CCCV charging could be identified in this study. This demonstrates that a lithium-ion cell has to be designed for fast-charging capability. Thin anodes with high porosity are typically less susceptible to lithium plating than thick electrodes with low porosity.

Regeneration Effects after Lithium Plating

The cells which were charged with high charging currents and suffered from massive lithium plating have exhibited certain regeneration effects during idle periods. After each checkup procedure, in which the cells were charged and discharged with substantially lower currents than in the high-current charging cycling test procedure, a considerably higher capacity was available in the cycling procedure directly after the checkup measurement than directly before the checkup.

Furthermore, anode storage capabilities recovered after longer pauses. Although the capacity has remained unchanged, the peaks in the differential voltage spectrum have shifted and indicated considerably higher storage capabilities again. This is in good agreement with the theory in the literature that waste products from side reactions between plated lithium and the electrolyte clog pores and inhibit parts of the active material from participating in the charge-discharge cycling procedure.

Means for Reducing Degradation

First of all, fast charging with high charging currents should not be applied for every-day use to avoid lithium plating and high stress for the electrode materials. Furthermore, a lower cycle depth has improved considerably the cycle life of the high-energy lithium-ion cells examined in this thesis. The experimental results have shown that a reduced cycle depth by increasing the discharging voltage has helped to reduce the resistance increase of the NCA cathode considerably more than a reduced charging voltage. In addition to that, the differential voltage spectra have exhibited a lower and more uniform degradation of the active materials for a reduced depth of discharge.

Low charging currents at low SoCs have not directly reduced degradation. Only the longer cycle duration has provided more time for regeneration mechanisms and thus a somewhat slower and more uniform degradation has been obtained.

Effects of Lowering the Charging Voltage

A very prominent method used for increasing the cycle life of a lithium-ion battery is reducing the charging voltage. However, the observed interdependencies between charging voltage and battery degradation have led to an ambiguous result. On the one hand, reduced charging voltages have led to a lower capacity fade. The overall capacity measured in the checkups has decreased more slowly and also the fade in the relative available capacity has been lower.

On the other hand, the capacity utilization has decreased considerably with reduced charging voltages. When regarding the absolute available capacity, there have not been observed any positive effects any longer. Although the capacity fade is lower for a reduced charging voltage, this effect is not sufficiently large that it also has a positive effect on the absolute available capacity. Yet, it is the absolute available capacity that determines the driving range of an EV. The study has shown that even after 1000 EFC, the absolute available capacity was still higher for the cells which were charged to a higher voltage – although their relative capacity fade was larger.

This demonstrates that when designing a battery system for a practical application, a compromise between absolute available capacity and relative capacity fade has to be made. Only when cells suffer predominantly from anode degradation, a reduction of the charging voltage can extend the battery life as it maintains a remaining storage reserve of the graphite anode.

6 Battery Aging under Driving Operation

In EVs, the load for the traction battery during driving is usually very unsteady. There are dynamic load changes which result from the acceleration and deceleration of the vehicle. Furthermore, driving is no pure discharging process because regenerative braking leads to recurring recharging periods. Consequently, these load conditions differ substantially from general laboratory test conditions, where a constant current or a constant power is usually applied for discharging. Thus, to reproduce, predict, and optimize battery life in EVs, it is essential to understand the effects of the typical characteristics of real-world driving profiles on the aging of lithium-ion batteries. Parts of the results on battery aging under driving operation were also presented in Ref. [248].

6.1 Insights from the Literature on Cycling Operation

In the literature, studies on cycle aging of lithium-ion batteries were usually performed with CC discharging (e.g., [154,201,249,250]). They examined the effects of different cycling parameters, such as current rate, SoC, cycle depth, and temperature on battery aging.

Higher current rates were generally observed to cause faster degradation [59,250]. However, the dynamic load changes which occur in EVs were rarely examined in the literature. Several studies on hybrid energy storage systems recommended the combination of high-energy lithium-ion batteries and supercapacitors to improve cycle life [251–255]. They claimed that an additional high-power storage system, which covers all peak loads and recharging pulses, relieves battery stress and, thus, reduces battery degradation. However, no proper validation of this assumption was provided. Due to the highly complex aging behavior of lithium-ion batteries with many interdependencies of influencing factors, realistic load patterns should be applied to verify the results from simplified CC cycling procedures [250]. Gering et al. [256] examined five PHEV pulse profiles with different current amplitudes but comparable charge throughput, which revealed a similar capacity fade. Moreover, Peterson et al. [257] analyzed the degradation of a PHEV battery in driving mode and in vehicle-to-grid mode. However, they did not perform CC cycling for comparison. One major drawback of both PHEV studies is that the operating conditions examined differ substantially from typical EV operating conditions, particularly in current rates and cycle depth.

A strong impact on cycle life is often observed for cycle depth. Battery degradation typically increases with higher cycle depths [258]. The maximum cycle depth of 100% usually leads to highest stress and fastest degradation [70,201]. By contrast, a low cycle depth of 5% minimizes cycle aging and degradation can become similar to pure calendar aging [201,249]. In general, a lower cycle depth enables a higher total charge throughput before the EoL is reached [249]. However, the same cycle depth was observed to cause different battery aging at different SoCs. In an aging study of Ecker et al. [201], the cycling intervals of 0–20%, 80–100%, and 65–85% led to a substantially faster degradation than the cycling interval of 40–60%. Hence, cycle depth and SoC always have to be evaluated jointly.

Many studies also demonstrated a large impact of temperature on cycle aging [72,154,259]. Particularly for temperatures toward 0°C and below, cycle life diminishes due to aggravating lithium plating [157,260]. As lithium plating is an aging mechanism usually related to charging at low temperatures, these results reveal a common limitation of the low-temperature studies presented in the literature. As charging and discharging was always performed at the identical temperature, the degradation owing to charging at low temperature and the degradation owing to discharging at low temperature could not be separated.

Although there are many publications on cycle aging of lithium-ion batteries, it remains unclear how the frequent load changes during driving operation and, in particular, the recharging pulses during regenerative braking affect the cycle life of the lithium-ion batteries in EVs. Moreover, the individual impact of charging and discharging at low temperature has not been examined yet. To overcome these shortcomings, battery degradation was examined for a representative load pattern based on an EV driving load profile. With this load profile, the impact of regenerative braking was investigated together with other influencing factors, such as temperature, SoC, and cycle depth. The aging related to the driving load profile was also compared to aging from pure CC loads. Furthermore, low-temperature degradation was examined separately for charging or discharging at 0°C.

6.2 Objectives for the Own Aging Study

To overcome the shortcomings of the existing aging studies presented in the literature, the experimental aging studies on EV driving operating, presented in this chapter, had the following objectives:

- Selecting a representative load scenario for examining battery aging under EV driving operation
- Determining main drivers of capacity fade and resistance increase
- Identifying the cycle aging contributions, which occur in addition to calendar aging
- Investigating the impact of short recharging sequences owing to regenerative braking on battery aging
- Analyzing the dependency of cycle aging on temperature
- Analyzing the dependency of cycle aging on SoC and cycle depth
- Comparing battery aging under dynamic driving loads and CC loads
- Separate investigation of battery degradation caused by charging or discharging at low temperature
- Identifying operating conditions which enable a long cycle life

6.3 Comparison of Driving Load Profiles

To determine EV battery aging under a more representative load condition than CC discharging, driving load profiles were required. As there had not been any standardized test profiles for EVs when the aging study was designed, load profiles were computed from various driving profiles used for fuel economy measurements of conventional vehicles. For these computations, a vehicle model

was used which comprised all major driving resistances. The resulting load profiles were scaled down to cell level so that an appropriate profile for the experimental aging study could be selected.

Neudorfer et al. [261] analyzed different driving cycles, which are used as standardized references for fuel consumption measurements. They distinguished between “modal” and “stylistic” driving cycles. Modal cycles are artificial driving cycles which consist of several sections with constant velocity. By contrast, stylistic driving cycles represent realistic driving scenarios with permanently changing velocities. For this cycle life study, only stylistic driving cycles were considered, as they generate a more realistic load scenario.

6.3.1 Computation of Driving Load Profiles Using a Simplified Vehicle Model

This section describes the simplified vehicle model that was used to obtain load profiles for the battery of an EV from standardized velocity profiles. This simulation model considered all major driving resistances to compute the necessary driving power at each time step. Thus, the driving cycle’s velocity profile was converted into a power profile. As described by Heissing et al. [262] and Meywerk et al. [263], the driving power $P_{vehicle}$ can be calculated as

$$P_{vehicle} = F_{req} \cdot v = (F_R + F_A + F_C + F_I) \cdot v \quad (18)$$

where F_{req} represents the sum of all driving resistances and v is the velocity of the vehicle. F_{req} consists of the following simplified driving resistances:

- Rolling resistance: $F_R = (m_V + m_L) \cdot g \cdot f_{roll} \cdot \cos(\alpha)$ (19)
- Aerodynamic drag: $F_A = 1/2 \cdot \rho_A \cdot c_W \cdot A_A \cdot (v + v_A)^2$ (20)
- Climbing resistance: $F_C = (m_V + m_L) \cdot g \cdot \sin(\alpha)$ (21)
- Acceleration resistance: $F_I = (e \cdot m_V + m_L) \cdot a$ (22)

where the acceleration a is the derivative of the vehicle’s velocity and $v+v_A$ is the relative velocity between air and vehicle. Table 11 provides a description of all symbols used and their values assumed for the load profile calculation. The values of vehicle A, a sub-compact urban vehicle for up to two passengers, were used for the load profiles employed in this thesis. Vehicle B represents a conventional compact car for four passengers.

Table 11. Parameters for load profile computation

Symbol	Description	Vehicle A	Vehicle B
m_V	Mass of vehicle	625 kg	1350 kg
m_L	Mass of load	150 kg	200 kg
g	Gravitational acceleration	9.81 m/s²	9.81 m/s²
f_{roll}	Rolling resistance coefficient	0.007	0.011
α	Angle of inclination	0°	0°
ρ_A	Density of air	1.2 kg/m³	1.2 kg/m³
c_W	Drag coefficient	0.22	0.30
A_A	Cross-sectional area	1.69 m²	2.20 m²
v_A	Air velocity	0 m/s	0 m/s
e	Factor for rotational masses	1.1	1.1
η	Efficiency	0.75	0.80
P_{aux}	Auxiliary power consumption	500 W	1000 W
N	Number of cells	1296	2500

To translate the driving power P_{vehicle}, required to accelerate and decelerate the vehicle, into the battery load P_{battery}, the drivetrain efficiency η and the power consumption P_{aux} of auxiliary consumers, such as lighting, heating, or driving assistance systems, had to be considered.

According to common sign conventions, positive values of P_{vehicle} indicate acceleration, whereas positive battery currents represent a charging of the battery. The following two equations, depending on the direction of the power flow of the motor, accounted for these conventions:

- acceleration: $P_{\text{battery}} = -(P_{vehicle} / \eta + P_{aux})$ for $P_{vehicle} \geq 0$ W (23)
- deceleration: $P_{\text{battery}} = -(P_{vehicle} \cdot \eta + P_{aux})$ for $P_{vehicle} < 0$ W (24)

For simplicity reasons, a constant drivetrain efficiency of $\eta = 0.75$ and a constant auxiliary power consumption of $P_{\text{aux}} = 500$ W were assumed. These simplifications were tolerable, as for the investigation of battery aging under dynamic driving loads, the qualitative distribution of charging and discharging loads was considered substantially more important than the precise quantitative values at each time step. All presented calculations did not have the aim to describe a specific EV as realistic and accurate as possible, but to generate generic load profiles suitable for the analysis of battery aging related to driving operation and regenerative braking.

As a next step, the load profile was converted from the level of an entire traction battery to cell level by dividing the total power P_{battery} by the number of cells N in the battery pack:

$$P_{\text{cell}} = P_{\text{battery}} / N \quad (25)$$

This yielded the power profile P_{cell} for a single cell. To obtain a demanding load profile, a small battery pack of 1296 cylindrical 18650 cells with a total energy content of ca. 13 kWh was assumed. This amount of energy was sufficient for the regarded sub-compact vehicle to provide a driving range of at least 100 km.

Although the load profile was computed for a sub-compact car, comparable results could also be obtained for a larger vehicle, which had, on the one hand, a higher mass and more engine power, but, on the other hand, a larger battery system. The parameter set of vehicle B, listed in Table 11, led to a rather similar load profile as vehicle configuration A.

Load profiles for battery aging experiments are usually defined as current profiles instead of power profiles, which guarantees an identical charge throughput independent of the battery's SoC or terminal voltage. This provides a better comparability of the results. Therefore, the power profile P_{cell} was divided by a reference voltage U_{ref} to obtain the current profile I_{cell}:

$$I_{\text{cell}} = P_{\text{cell}} / U_{\text{ref}} \quad (26)$$

Since the investigations within this thesis cover a wide SoC range, U_{ref} was set to 3.6 V, which is the nominal cell voltage, specified by the manufacturer.

6.3.2 Evaluation of Driving Cycles

For different European and American driving cycles, the velocity profiles from Ref. [264] were transformed into current profiles for single lithium-ion cells with a numerical fixed-step solver and a step size of 1 s. Table 12 lists the duration, driving distance, and average velocity of the different driving cycles. Furthermore, the discharged ampere-hours per cell and the maximum charge

recovery, which were derived from the simulation, are presented for one run of each driving cycle. Figure 77 depicts the current histograms of six driving cycles, which represent different driving conditions. These results served as a basis for the selection of an appropriate load profile for the cycle life study.

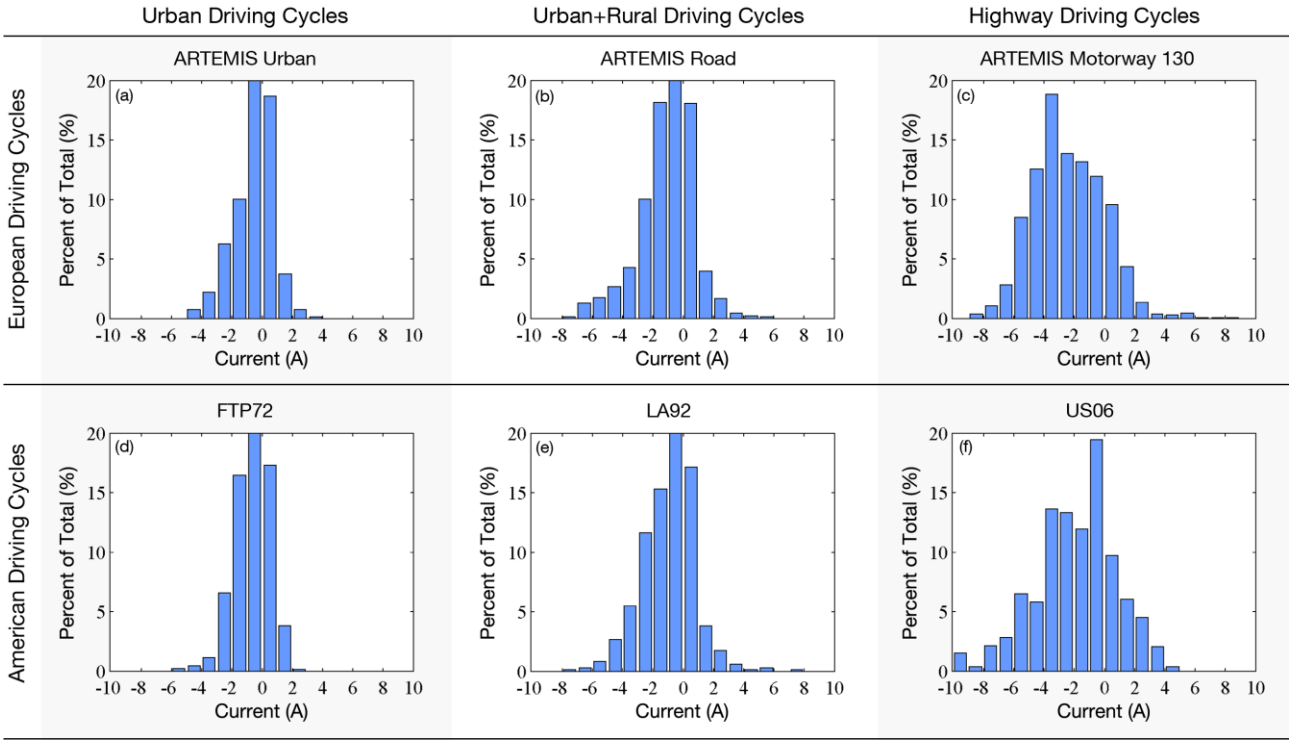

Figure 77. Distribution of cell currents for different European and American driving cycles as percent of total driving cycle duration. The parameters of vehicle A (see Table 11) were used for these calculations.

For investigating the impact of real-world driving loads on battery aging in experimental laboratory studies, highway driving cycles are beneficial as they feature a higher energy consumption than urban and rural driving cycles. This leads to a higher charge throughput and is, thus, simulating a higher driving distance per time (see Table 12). Moreover, this represents a worst-case usage scenario, as EVs are often used in urban traffic conditions, where, despite of more frequent stop-and-go driving conditions, the battery load is considerably lower.

Table 12. Comparison of three European and five American stylistic driving cycles, including the discharged ampere-hours and the maximum amount of charge recovered by regenerative braking from simulations with vehicle configuration A (see Table 11).

	Duration	Driving Distance	Average Velocity	Discharged Ampere-hours	Max. Charge Recovery
ARTEMIS Urban	16.5 min	4.5 km	16.2 km/h	0.151 Ah	25 %
ARTEMIS Road	18.0 min	17.3 km	57.5 km/h	0.354 Ah	17 %
ARTEMIS Motorway 130	17.8 min	28.7 km	96.9 km/h	0.773 Ah	8 %
NYCC	10.0 min	1.9 km	11.4 km/h	0.063 Ah	21 %
FTP72	22.8 min	12.0 km	31.5 km/h	0.244 Ah	19 %
LA92	23.9 min	15.8 km	39.7 km/h	0.401 Ah	20 %
HWFET	12.8 min	16.5 km	77.7 km/h	0.277 Ah	6 %
US06	10.0 min	12.9 km	77.3 km/h	0.369 Ah	15 %

Table 12 also shows that the amount of charge that can be recovered by regenerative braking in highway driving cycles amounts to 8 % for the Artemis Motorway 130, 6 % for the HWFET, and 15 % for the US06 driving cycle. Figure 77 illustrates the distribution of cell currents for different European and American driving cycles. Since the American US06 driving cycle recovers substantially more charge than the other two highway driving cycles and since it contains a considerable percentage of regenerative braking events with a current magnitude above 2 A (see Figure 77f), it was selected for this cycle life study with a focus on the impact of regenerative braking on battery aging.

6.4 Design of the Experimental Study

The objective of this aging study was to investigate the degradation of lithium-ion batteries in EVs under realistic driving load conditions. Therefore, load profiles derived from the American US06 driving cycle were employed. In this section, the various test conditions and the test procedure are presented.

6.4.1 Test Conditions

In this study, highway driving load profiles with different magnitudes of regenerative braking were used. Moreover, the cells were cycled at different temperatures, SoCs, and cycle depths. The dynamic discharging with the driving load profile was also compared to CC discharging with the same mean current and cycle depth. In the following paragraphs, the test conditions are described.

Load Profile

The US06 driving load profile was selected for this aging study. The velocity profile of this highway driving cycle is illustrated in Figure 78a. The corresponding current histogram has been depicted in Figure 77f. As the cycle aging study was conducted on a battery test system with multiple independent 5 V/±5 A test channels, high discharging loads had to be truncated at −5.5 A, which was the limit of the test system. Figure 78b exhibits the truncated discharging currents.

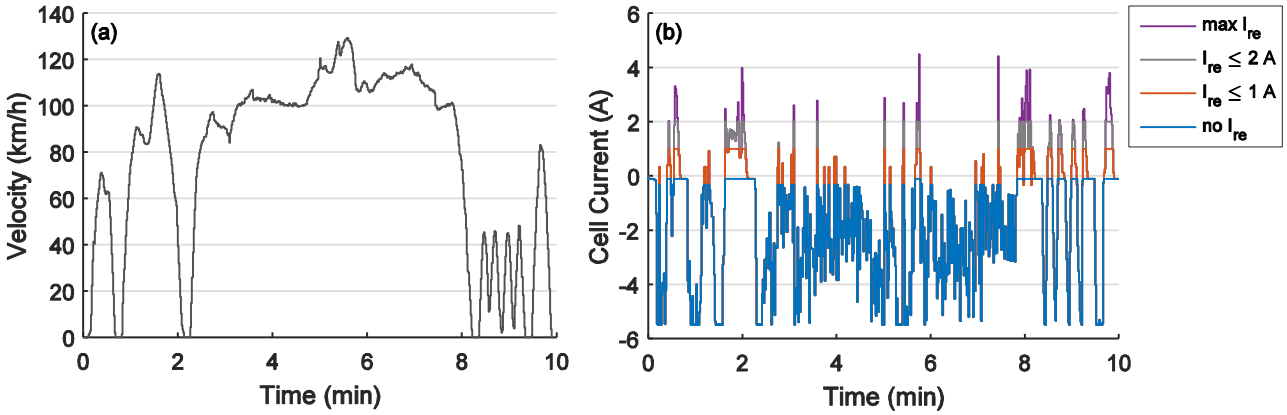

Figure 78. (a) Velocity profile of the US06 highway driving cycle. (b) Load profiles for a single lithium-ion cell with different magnitudes of regenerative braking, represented by different limitations for the recharging currents (I_{re}) during regenerative braking.

Variation of Regenerative Braking

To analyze the impact of regenerative braking on battery aging, four different current levels were defined for the recharging pulses, which are illustrated in Figure 78b by the four different load profiles: The first level is "no recharging" ("no I_{re}"), which corresponds to no regenerative braking at all. The load during the periods of regenerative braking or standstill remains somewhat below 0 A, since the auxiliary load still has to be provided. The second level limits recharging currents I_{re} for the battery cell to 1 A ("$I_{re} \leq 1$ A"). It is able to recover 8% of the ampere-hours discharged during the driving cycle, which corresponds to approximately half of the maximum recoverable amount of charge. The third level of regenerative braking was defined as "$I_{re} \leq 2$ A", covering more than 80% of the maximum recoverable amount of charge. The fourth level of unrestricted regenerative braking is labeled "max I_{re}" and contains recharging pulses up to 4.5 A. This enabled a charge recovery of 16%, which is 1 percentage point higher than the value listed in Table 9 due to the truncation of the high discharging currents.

State of Charge Levels

One run of the US06 driving cycle corresponds to a driven distance of ca. 13 km. To obtain more representative driving distances for the cycle life study, at least two runs of the load profile were performed in series before charging the cell again. Without regenerative braking, two consecutive runs of the US06 highway driving cycle depleted approximately one fourth of the cell's nominal capacity C_N.

In the cycle aging study, different SoC levels were examined. The SoC levels were defined by the maximum voltage for the CC charging procedure with a charging current of 0.7 A (= C/4). As illustrated in Figure 79a, the low, medium, and high charging voltages were 3.7 V, 3.9 V, and 4.1 V, respectively.

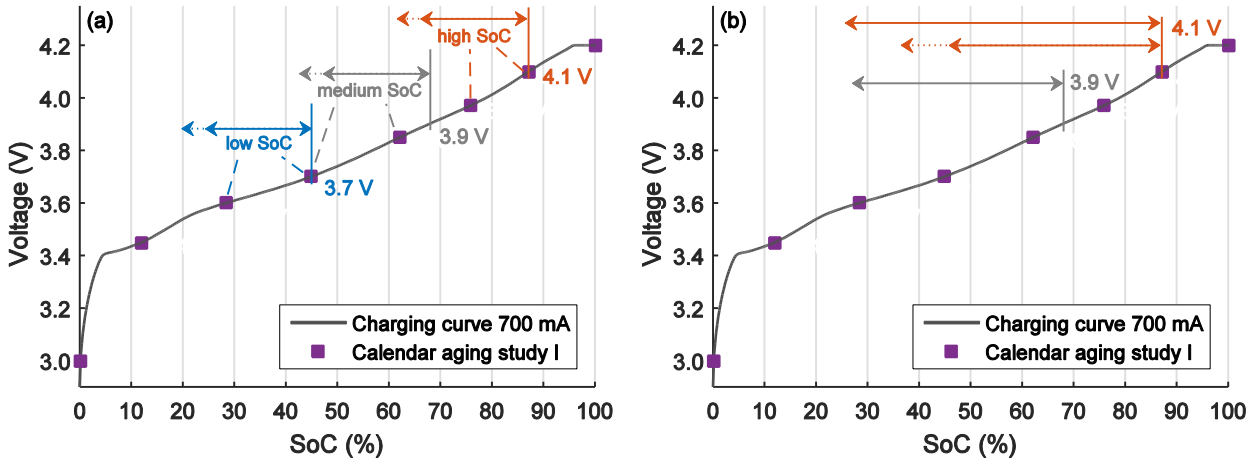

Figure 79. (a) Low, medium, and high charging voltage for constant-current charging at 25°C. The double arrows illustrate the cycle depths for two consecutive runs of the driving load profiles with no regenerative braking at all (25% C_N) and maximum regenerative braking (20% C_N). (b) Cycle depths of four and six consecutive runs of the driving load profiles, used to examine larger cycle depths.

To separate usage-dependent and usage-independent capacity fade, baseline curves for calendar aging were computed for low, medium, and high SoC. This was performed based on the results of the first calendar aging study, which examined cells from the same production lot. Figure 79a

illustrates from which two storage SoCs, an average calendar aging baseline curve was computed for each of the three SoC windows.

A slight correction of charging voltages was applied for 10°C: As higher internal resistances at low temperatures lead to higher terminal voltages during charging, the low charging voltage level was set to 3.75 V and the medium charging voltage was set to 3.925 V. The high charging voltage remained at 4.1 V to avoid any risk of increased lithium plating or electrolyte oxidation resulting from higher cell voltage.

Cycle Depths

The double arrows in Figure 79a illustrate the cycling windows for two subsequent runs of the driving load profiles. Two consecutive runs of the driving load profile deplete 24.8% of the nominal capacity C_N. This corresponds to a depth of discharge of 24.8% C_N when no regenerative braking is used. By recovering charge during braking periods, the depth of discharge at the end of the driving sequence remains smaller. With unrestricted regenerative braking, two consecutive runs of the driving load profile lead to a depth of discharge of 20.4% C_N.

In addition to two consecutive runs of the driving load profile, four and six consecutive runs were also examined for the driving load profile with maximum regenerative braking. This depleted 49.5% and 74.3% C_N. Due to the partial recharging by regenerative braking, the resulting depths of discharge were 40.8% and 61.1% C_N, respectively. These higher cycle depths were examined for the high and the medium charging voltage, as it is depicted in Figure 79b. For the high charging voltage, four consecutive runs of the load profile without regenerative braking were also examined. The remaining SoC margins toward 0% and 100% SoC guaranteed that no overcharging occurred during recharging pulses at high SoC and allowed to perform the cycling procedure also on aged cells with lower capacities approaching the EoL condition of 20 % capacity fade.

Temperature Conditions

To examine the impact of different operating temperatures on battery aging, the cycling sequences with the driving load profiles were performed at 40°C, 25°C, and 10°C. 25°C can be considered as a standard operating temperature for the lithium-ion cells. To cover a representative spectrum of average operating temperatures for an EV, an additional high and low temperature level of 40°C and 10°C was defined. They can be interpreted as summer and winter conditions, where the battery pack cannot be cooled down or heated up to 25°C.

To investigate the impact of charging and discharging at low temperature on battery aging separately, an additional experiment was conducted which based on an alternating operating temperature. A climate chamber was programmed to alternate its temperature between 25°C and 0°C after a predefined time interval. Inside that chamber, two sets of cells were tested. The first set was charged at 0°C and discharged with driving load profiles at 25°C and for the second set, the test scenario was vice versa.

6.4.2 Test Procedure

The entire test procedure was performed with a 32-channel BaSyTec CTS battery test system. Cells from the first production lot were examined. At the beginning of the aging study and every 100 EFC, a checkup was performed to track the degradation of the cells. Figure 80 depicts the checkup routine used in this aging study, which is largely identical to that used in the first calendar aging study (see Figure 23, p.46).

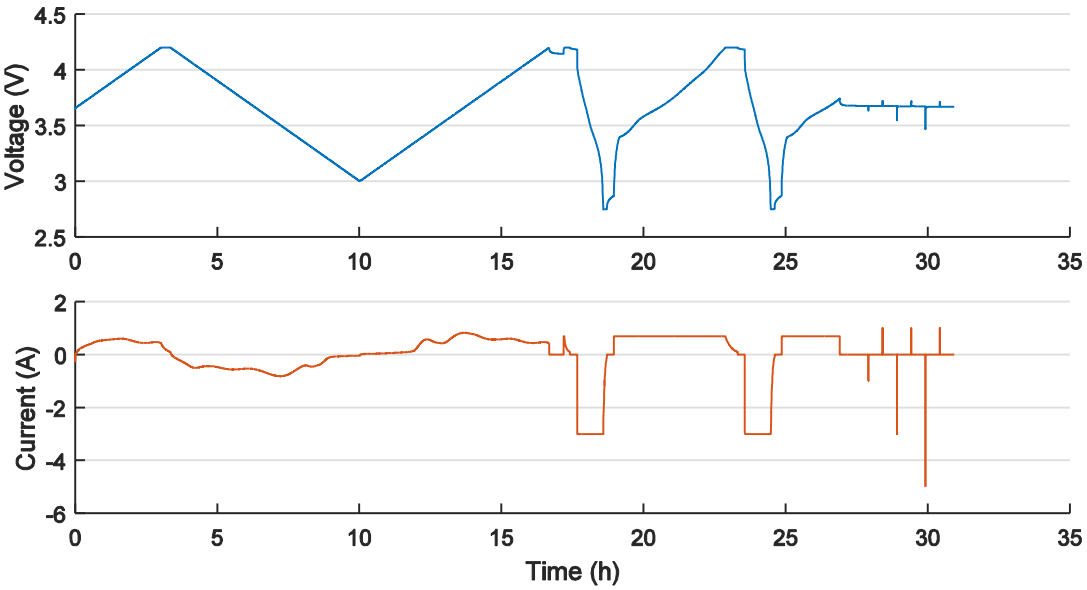

Figure 80. Checkup procedure of the cycle aging study on driving operation

As illustrated in Figure 80, it contained voltage ramps for cyclic voltammetry, CCCV charging and discharging, and pulses at 50% SoC to track changes in internal resistances. The only difference to the checkup of the first calendar aging study is that it contained two CCCV charging-discharging cycles after the initial voltage ramps. This checkup procedure was performed at 25°C for all cells. A detailed description of the checkup procedure is provided by Table A-8 in the appendix. The checkup procedure ended after a pulse sequence at 50% SoC. At this SoC, a galvanostatic EIS measurement ranging from 10 kHz to 10 mHz was performed with an RMS excitation amplitude of 50 mA. To perform the EIS, the cells were manually disconnected from the battery test system and connected to the galvanostat. After the EIS measurements, the cells were reconnected to the battery test system and the cycling procedure was continued at the respective test temperature.

During cycling, the cells were charged to their assigned charging voltages and discharged with different load profiles. The charging was performed by a CC charging procedure with 700 mA until the respective charging voltage was reached. The low charging current of C/4 was employed to minimize degradation caused by charging the cells. For discharging the cells, the driving load profiles with four different magnitudes of regenerative braking were used. Two, four, or six consecutive runs of the load profiles, with a pause of 1 min in between, were applied to obtain different cycle depths. 100, 50, or 33 repetitions were performed, respectively, to obtain about 50 EFC for the different cycle depths. There was a pause of 5 min between each charging and discharging sequence. After the 50 EFC, the cells performed one large cycle of CC charging with 700 mA to 4.1 V and CC discharging with 1.4 A (=C/2) to 2.5 V. In the end, the cells were charged to 50% SoC again. This cycling sequence was performed twice to obtain 100 EFC between two checkups.

Only for the aging experiment with alternating temperatures, the checkups were performed every 50 EFC. In this experiment, the Vötsch VT4021 climate chamber was programmed to change its temperature between 0°C and 25°C every 2.4 h. The charging sequence started always 15-20 min after the temperature change and had a duration of ca. 2 h. As the discharging sequence, depleting 50% C_N within 40 min of driving, was substantially shorter than the charging sequence due to the higher discharging currents, longer pauses were defined before and after the discharging sequences to fill the 2.4 h at the discharging temperature. Hence, the discharging sequence started ca. 50 min after the temperature change and the pause between discharging and the next temperature change was also ca. 50 min. At the beginning and at the end of the aging experiment with alternating temperatures, the standard checkup routine from the aging study on charging protocols (see Figure 49, p.80) was executed since it contained a low-current charging sequence for DVA.

6.4.3 Degradation Monitoring

To track the degradation of the cells, the following indicators were evaluated in this aging study.

Capacity

The actual capacity was determined from the second CCCV discharging sequence. The CCCV capacity values were used to identify the capacity fade with only minor influence of the increasing internal resistances. The two charge-discharge cycles before the capacity measurement were beneficial for reducing effects of the preceding operating history.

Internal Resistances

Two characteristic resistance values were evaluated in this aging study: $R_{ac,1kHz}$ and $R_{dc,10s}$. $R_{ac,1kHz}$, obtained from the EIS measurements at 50% SoC, reveals increasing ohmic resistances. Moreover, $R_{dc,10s}$ was computed from the current step from 0 A to –3 A of the pulse sequence at 50% SoC at the end of the checkup procedure. This resistance value reveals changes in the overall resistances, which also include contributions from passivation layers, charge transfer, and diffusion. Hence, $R_{dc,10s}$ is always considerably higher than $R_{ac,1kHz}$ for the same SoC.

Energy Efficiency

Values for the energy efficiency were calculated from the cycling data. The energy efficiency η of one cycle, consisting of the consecutive runs of the driving load profile and the subsequent recharging to the initial voltage level, was defined as the quotient of cumulated watt-hours discharged during the driving periods divided by the watt-hours charged during the CC charging period. The cumulated watt-hours recovered by regenerative braking were not included in this calculation, as they can always be recovered for free. This recharged amount of charge neither has to be paid by the customer nor increases any power plant emissions.

$$\eta = \frac{E_{\text{discharging}}}{E_{\text{CC\_charging}}} \tag{27}$$

This definition of η leads to increasing efficiencies with higher levels of regenerative braking, as the recovered charge can be used again in a subsequent acceleration period. This can also result in efficiencies above 100% when regenerative braking enables more watt-hours being discharged during driving than watt-hours having been charged at the charging station. To compensate for this side effect from charge recovery during driving, a modified energy efficiency η_{mod} was defined,

which divided η by the quotient of discharged ampere-hours during driving divided by charged ampere-hours of the CC charging sequence.

$$\eta_{\mathrm{mod}} = \frac{E_{\mathrm{discharging}}}{E_{\mathrm{CC\_charging}}} \Big/ \frac{Q_{\mathrm{discharging}}}{Q_{\mathrm{CC\_charging}}} \tag{28}$$

Differential Voltage Spectrum

In the additional experiment with the alternating operating temperature, low-current charging curves were recorded in the first and last checkup. From these data, the differential voltage spectra were computed. The characteristic capacities Q_1, Q_2, and Q_3, as defined in Figure 31, were analyzed to identify origins of capacity fade.

6.5 Results and Discussion

To present the impact of driving operation with dynamic loads and regenerative braking on battery aging, up to 2000 EFC were examined. They correspond to a driven distance of ca. 200,000 km for the vehicle configuration examined. For the first 500 EFC, all four magnitudes of recharging currents for regenerative braking during the driving sequences are compared for the three operating temperatures and the three charging voltages. This reveals the impact of regenerative braking on battery aging at different SoCs. For 1200 EFC at different operating temperatures, the impact of SoC and cycle depth on battery aging is analyzed in more detail. Moreover, the degradation for dynamic driving load profiles is compared to CC discharging. Furthermore, results of long-term cycling at 25°C, comprising 2000 EFC, are presented. In the long-term experiment, regeneration effects were observed after longer pauses, particularly for the cells cycled at higher SoCs only. Finally, the individual impact of charging and discharging at a low operating temperature of 0°C is investigated.

6.5.1 Impact of Temperature

Figure 81 illustrates the degradation of the lithium-ion cells when the cells are charged with 700 mA and discharged without regenerative braking at 40°C, 25°C, and 10°C. The 500 EFC correspond to a driven distance of ca. 50,000 km. As there was no charge recovery during the driving sequences, the cycle depth is ca. 25% C_N. Figure 81 shows the impact of SoC and temperature on capacity fade and resistance increase. To distinguish between usage-independent and usage-dependent battery degradation, baseline curves computed from data of the first calendar aging study are included in the capacity plots. The calendar aging curves are scaled in such a way that they correspond to the 4 weeks of cycling between each two checkups.

Capacity Fade

The capacity fade for the three operating temperatures exhibits a strong dependency on SoC. After 500 EFC, the capacity fade amounts to ca. 5.5% at low SoC, to 6.3–7.2% at medium SoC, and to 8–12% at high SoC. Thus, a higher SoC has led to faster degradation. As this trend can originate to a certain extent from usage-independent calendar aging, the individual contributions of calendar and cycle aging must also be regarded.

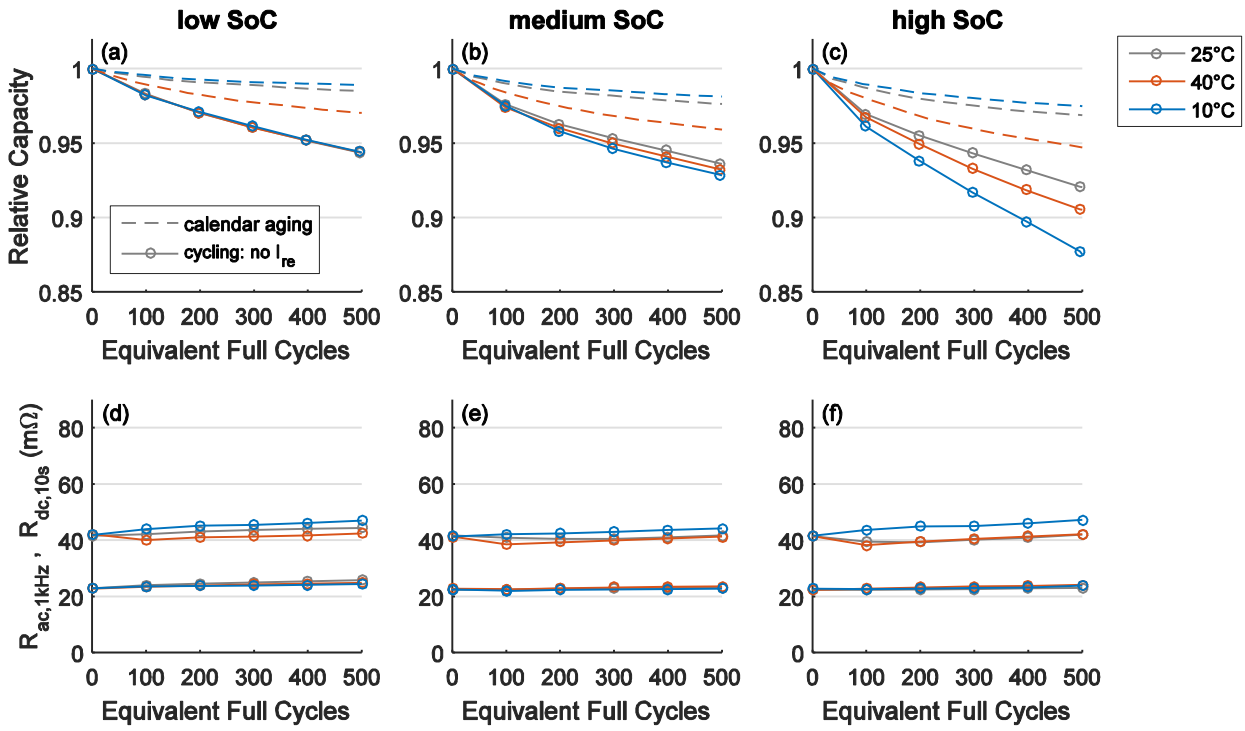

Figure 81. (a-c) Capacity fade and (d-f) resistance increase for 500 EFC without regenerative braking and with a cycle depth of 25% C_N. For the usage-independent capacity fade, results from the calendar aging study are scaled in accordance with the 4 weeks of cycling between two consecutive checkups.

Figure 81a-c demonstrates that the contributions of calendar and cycle aging vary substantially with temperature. For the cells tested at 40°C, calendar aging has a considerable impact on the overall degradation and is responsible for more than half of the capacity fade. The additional capacity fade owing to cycle aging amounts to 2.5% for low and medium SoC, and to 4% for high SoC. For the cells cycled at 10°C, the highest capacity fade is observed at all SoC levels. Since calendar aging is low at this operating temperature, the capacity fade is caused predominantly by cycle aging. The contribution from cycle aging, in addition to the 1–2.5% of capacity fade from calendar aging, amounts to 4.5% at low SoC, to 5.5% at medium SoC, and to 9.5% at high SoC. Hence, the combination of low temperature and high SoC exhibits the largest capacity fade. The lowest aging has been obtained at 25°C. With a capacity fade of 1.5–3%, calendar aging at 25°C is considerably lower than at 40°C. The additional capacity fade owing to cycle aging amounts to 4% at low and medium SoC, and to almost 5% at high SoC. Thus, cycle aging – as the difference between the overall degradation and pure calendar aging – is more severe than at 40°C, but lower than at 10°C.

Due to the different impact of temperature on calendar and cycle aging, there is no steady increase or decrease of the entire capacity fade with temperature. The capacity fade increases toward higher and lower temperatures. 25°C has provided the best cycle life in this aging study. With higher temperatures, calendar aging increases whereas at low temperatures, the cycling operation causes substantial degradation.

These results are in good agreement with other aging studies, which reported an optimal operating temperature around 25°C and increasing degradation toward higher and lower operating temperatures [72,260]. For higher temperatures, Arrhenius-driven reactions were reported as main driving forces of aging, which strongly correlates with calendar aging. For lower temperatures,

degradation is ascribed to lithium plating, which means the deposition of metal lithium during charging.

Resistance Increase

In addition to the capacity fade, battery aging leads to rising internal resistances. Figure 81d-f shows the resistance changes for the different operating temperatures and SoC levels. The increase in $R_{ac,1kHz}$, representing the ohmic behavior, lies below 3 mΩ after 500 EFC for all cells, which means below 15%. The changes in $R_{dc,10s}$ of up to 5.6 mΩ also lie below 15% after 500 EFC, where the largest resistance increase occurs at 10°C. Overall, the resistance changes are small compared to the resistance changes in the preceding aging study on charging protocols. The resistance changes do not exhibit strong dependencies on the operating SoC, as it has been observed for the capacity fade.

In the beginning of the cycling study, $R_{dc,10s}$ has even decreased for all cells cycled at 40°C and for the cells at 25°C that were cycled at the high or medium SoC level. Such reductions in internal resistances have not been observed in the calendar aging studies. Thus, they have to result from the cycling operation. The origin of the resistance reductions can be identified in the impedance spectra depicted in Figure 82. Figure 82a shows impedance spectra for the cell cycled without regenerative braking at 40°C and the medium SoC level. After the first 100 EFC, the width of the arc between 1 kHz and 32 Hz has decreased considerably. This arc is part of the high-frequency capacitive semicircle ascribed to the SEI at the anode. Consequently, the decreasing internal resistances originate from the anode. Lower anode resistances after cycling were also reported in several studies in the literature [158,265,266]. With the capacitive effects decreasing, the vertical position of the impedance at 1 kHz shifts somewhat down, as the inductive effects are less compensated by capacitive effects in the kilohertz domain.

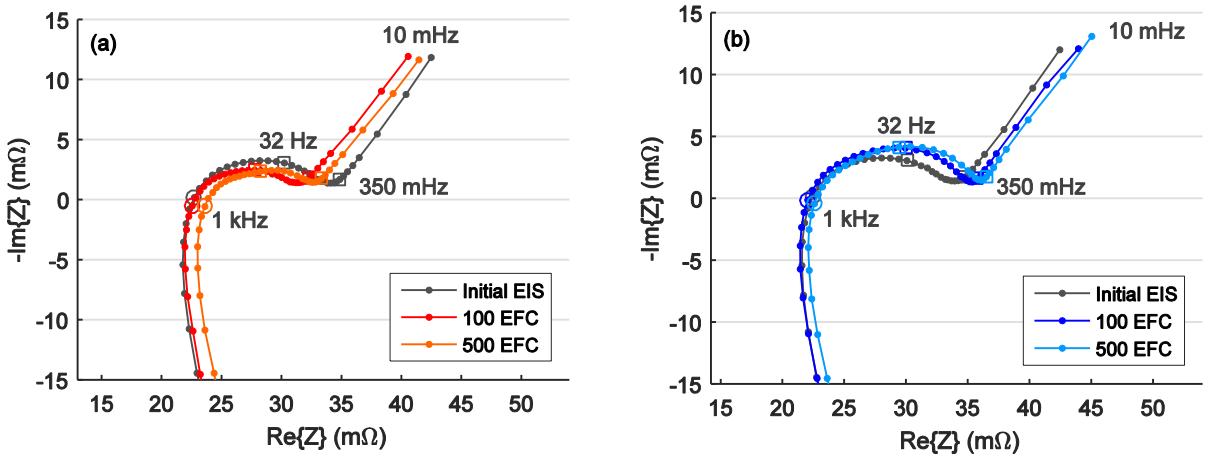

Figure 82. Impedance spectra before cycling, after 100 EFC, and after 500 EFC. The two cells were cycled at (a) 40°C and (b) 10°C without regenerative braking at the medium SoC level with a cycle depth of 25% C_N.

As a comparison, Figure 82b shows the cell cycled at 10°C and medium SoC. This demonstrates that there is no shrinking of the high-frequency capacitive semicircle at lower operating temperatures. Consequently, the impedances rise from the very beginning and, thus, the $R_{dc,10s}$ values lie considerably above the values of the cells cycled at 25°C and 40°C. The increasing $R_{dc,10s}$ values can be ascribed to the increasing arc between 30 Hz and 350 mHz. This indicates increased charge transfer resistances of the cathode.

6.5.2 Impact of Regenerative Braking

For the test procedure with two consecutive runs of the US06 highway driving profile, the impact of regenerative braking on battery aging was examined with four different levels of maximum recharging currents during the braking periods. The four levels ranged from no recharging at all to unlimited recharging pulses. For up to 500 EFC, representing ca. 50,000 km, the impact of regenerative braking on energy efficiency, capacity fade, and resistance increase is analyzed for the different operating temperatures and SoC levels. The cells were always charged and discharged at the same temperature.

Energy Efficiency

Regenerative braking is known to increase the energy efficiency of an EV by recovering energy during braking periods. This can be seen in Figure 83a-c, where the energy efficiency of the cells cycled with regenerative braking is substantially higher. The efficiency curves lie up to 19 percentage points higher. The cells cycled with unrestricted regenerative braking exhibit a depth of discharge after the driving sequence which is only 84% of the depth of discharge of the cells without regenerative braking for the same driving distance. The reciprocal of this value is 119%, which corresponds well to the difference in the energy efficiency curves. Regenerative braking leads to efficiency values above 100%. This occurs because only the energy obtained from the charging station was considered in the efficiency calculations, as only this amount of energy has to be paid by the driver of an EV and has to be considered for emission calculations, e.g., of CO_2.

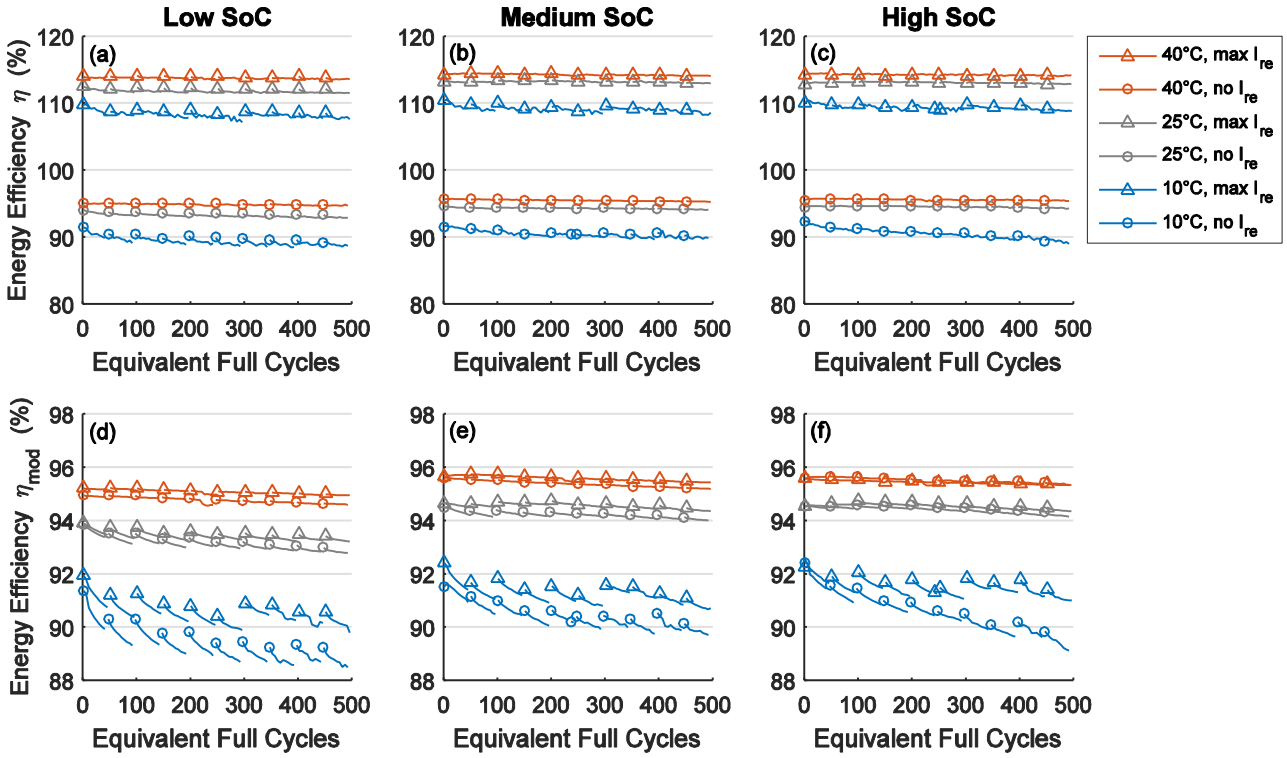

Figure 83. (a-c) Energy efficiency and (d-f) modified energy efficiency during cycling with two subsequent runs of the driving load profile with unrestricted regenerative braking and without regenerative braking

These side effects from charge recovery are compensated by the modified energy efficiency η_{mod}. Thus, the efficiency curves lie closer together in Figure 83d-f. The graphs exhibit only a small impact

of the SoC on the efficiency, but a strong impact of temperature. At 40°C, the efficiency is mostly above 95%. At 25°C, it ranges between 93% and 95%, which means that losses are 20–40% higher. A substantially lower efficiency is observed at 10°C. It ranges between 89% and 92%, which indicates a doubling of the losses compared to 40°C. Hence, the energy available to propel the EV decreases notably with lower temperature. This is one reason for reduced driving range of EVs at low temperatures. The lower efficiency for the larger cycle depth without regenerative braking results from higher voltage drops during the discharging sequence. Reduced electrolyte conductivity, decelerated charge transfer, and slow diffusion increase the internal resistances of the lithium-ion cell and, thus, reduce the efficiency.

Capacity Fade

For the nine combinations of operating temperature and SoC level, Figure 84 depicts the capacity fade for the four levels of regenerative braking. Again, the capacity fade is compared to calendar aging to identify usage-dependent and usage-independent aging contributions.

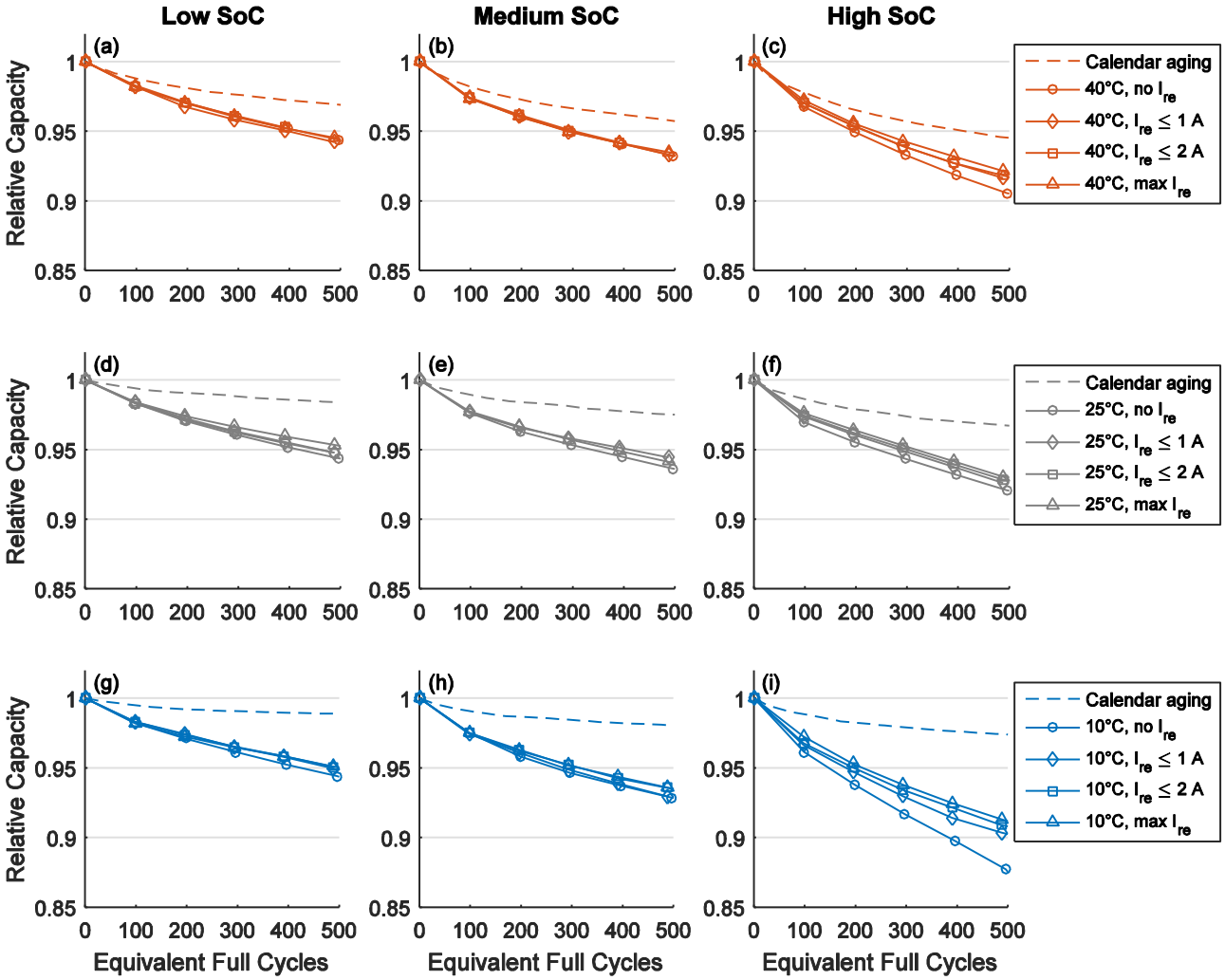

Figure 84. Capacity fade for 500 EFC (ca. 50,000 km) with different magnitudes of regenerative braking. Two subsequent runs of the driving load profile were performed before each recharging. The calendar aging curves are scaled in accordance to the ca. four weeks of cycling between two consecutive checkups.

At 40°C, the cells cycled at the low and medium SoC level show almost no dependency on the magnitude of regenerative braking. All curves lie closely together in Figure 84a and Figure 84b. After

500 EFC, the cells cycled at low SoC exhibit a capacity loss of almost 6% and the cells cycled at medium SoC of almost 7%. The additional capacity loss at medium SoC can be ascribed to increased calendar aging. Thus, cycle aging in addition to the capacity loss from calendar aging is considered identical for both SoC levels and amounts to ca. 2.5% capacity fade after 500 EFC. Regarding the high SoC level at 40°C, Figure 84c demonstrates a dependency on regenerative braking as the capacity curves diverge. A trend becomes apparent: A higher level of regenerative braking reduces the capacity loss. After 500 EFC, the capacity loss in addition to calendar aging is ca. 2.5% for the cell with unrestricted regenerative braking and more than 4% for the cell with no regenerative braking.

In contrast to 40°C, Figure 84d-f shows a dependency of battery aging on the level of regenerative braking for all three SoC levels at 25°C: Cells with a higher magnitude of regenerative braking exhibit lower capacity losses. In analogy to 40°C, the capacity fade increases with higher SoC level. At low and medium SoC, the capacity fade from cycle aging is comparable for the same levels of regenerative braking. At high SoC, intensified aging can be observed again: Capacity losses due to cycling are more than 1 percentage point higher than at medium and low SoC. Compared to 40°C, calendar aging is about 2 percentage points lower and cycle aging is about 1 percentage point higher at 25°C.

At 10°C, Figure 84g-i again presents a dependency on the level of regenerative braking for all SoC levels. The most pronounced impact can be observed at the high SoC level, where capacity curves diverge markedly. Although calendar aging is low at 10°C, the cells exhibit substantial capacity losses. After 500 EFC, capacity losses owing to calendar aging amount to 1% for low SoC, 2% for medium SoC, and 2.5% for high SoC. For the low and medium SoC level, additional losses of 4–5% can be ascribed to cycle aging. At the high SoC level, the additional capacity fade owing to cycle aging amounts to 6% for the cell with maximum regenerative braking. For the cell with no regenerative braking, elevated cycle aging of 10% capacity fade results in a total capacity fade of 12.5% after 500 EFC. This represents the most severe degradation of all load cases depicted in Figure 84.

Analyzing the capacity fade with respect to regenerative braking reveals a common trend: A higher level of regenerative braking has reduced battery aging. This trend has been observed most pronouncedly for the high SoC and low temperature. As these operating conditions are those for which strong degradation owing to lithium plating was expected, the concern of regenerative braking causing more lithium plating in EVs is not affirmed. By contrast, regenerative braking has reduced the capacity fade.

Resistance Increase

The resistance increase of $R_{ac,1kHz}$ and $R_{dc,10s}$ did not reveal a dependency on regenerative braking. The results for all four levels of regenerative braking were similar to those presented in Figure 81d-f for the cells cycled without regenerative braking. A decrease in $R_{dc,10s}$ at the beginning of the cycling procedure occurred for all cells cycled at 40°C and for the cells cycled at 25°C with medium and high charging voltage. As the resistance changes were rather small, the capacity fade turned out to be the predominant aging effect for all the cells cycled with the low cycle depth resulting from two consecutive runs of the driving load profile.

Effects of Reduced Cycle Depth

The lower capacity fade from cycle aging with higher levels of regenerative braking can be explained by the reduced depth of discharge after the driving sequences: The more charge recovered by regenerative braking, the higher the SoC remains at the end of the driving cycle. Thus, the overall cycle depth decreases and the subsequent CC charging period shortens. For the four load profiles with different magnitudes of regenerative braking, the overall charge throughput is similar. They all discharge the same amount of ampere-hours during the two subsequent runs of the US06 highway driving load profiles. Only the time points of recharging differ due to the microcycles generated by regenerative braking. With higher magnitudes of regenerative braking, more ampere-hours are recharged during the driving sequences and less ampere-hours have to be charged afterwards in the CC charging sequence. Without regenerative braking, the cells perform one large discharge-recharge cycle with a cycle depth of 24.8% C_N. With regenerative braking, the cells perform microcycles, in which charge is recovered during braking and discharged again in the subsequent acceleration period. The microcycles become larger with higher magnitudes or regenerative braking. Thus, these cells are less discharged after the driving sequences. The depths of discharge are 22.3% C_N for 1 A and 21.1% C_N for 2 A as maximum charging current during regenerative braking. For unrestricted regenerative braking, the depth of discharge is 20.4% C_N. To analyze the impact of different cycle depths, Figure 85 depicts the capacity fade with respect to “equivalent full cycles without microcycles”. This excludes the charge throughput of the microcycles resulting from charge recovery during braking periods. As a consequence, this regards only the charge throughput of the main discharge-recharge cycle, which corresponds to the ampere-hours recharged during the CC charging period after the driving sequence.

As expected, Figure 85 shows that the EFC without microcycles are considerably lower for cells with higher levels of regenerative braking. For cells with maximum regenerative braking, the cycle number reduces from 500 to 420, whereas it remains unchanged for cells without regenerative braking. Comparing Figure 84 and Figure 85, the adjustments owing to the different scale bases become apparent: At 10°C and 25°C, capacity curves lie closer together in Figure 85 for all SoC levels. At 40°C, this effect can also be observed at high SoC. This confirms the direct correlation between changes in cell degradation and changes in cycle depth under most operating conditions.

As high SoC and low temperature aggravate lithium plating and as decreasing cycle depths with higher magnitudes of regenerative braking have reduced cycle aging particularly under these operating conditions, it is supposed that the lower cycle depth has reduced lithium plating. As the capacity curves lie closer together when the charge throughput of the microcycles resulting from regenerative braking are neglected, it is concluded that the CC charging sequence could be the driving force of capacity fade as it caused small amounts of lithium plating. Consequently, it is not the short recharging with high current rates during regenerative braking that promotes lithium plating, but the long-lasting charging periods when the vehicle is recharged by the grid, although current rates are considerably lower.

Only for the low and medium SoC level at 40°C, the correlation between cell degradation and EFC is in better agreement. Under these operating conditions, lithium plating is unlikely to occur for the charging currents applied in this aging study. As Figure 84a and Figure 84b show, even under these

operating conditions, regenerative braking has not intensified battery aging. Thus, a high level of regenerative braking is beneficial to the cycle life of a lithium-ion battery in an EV.

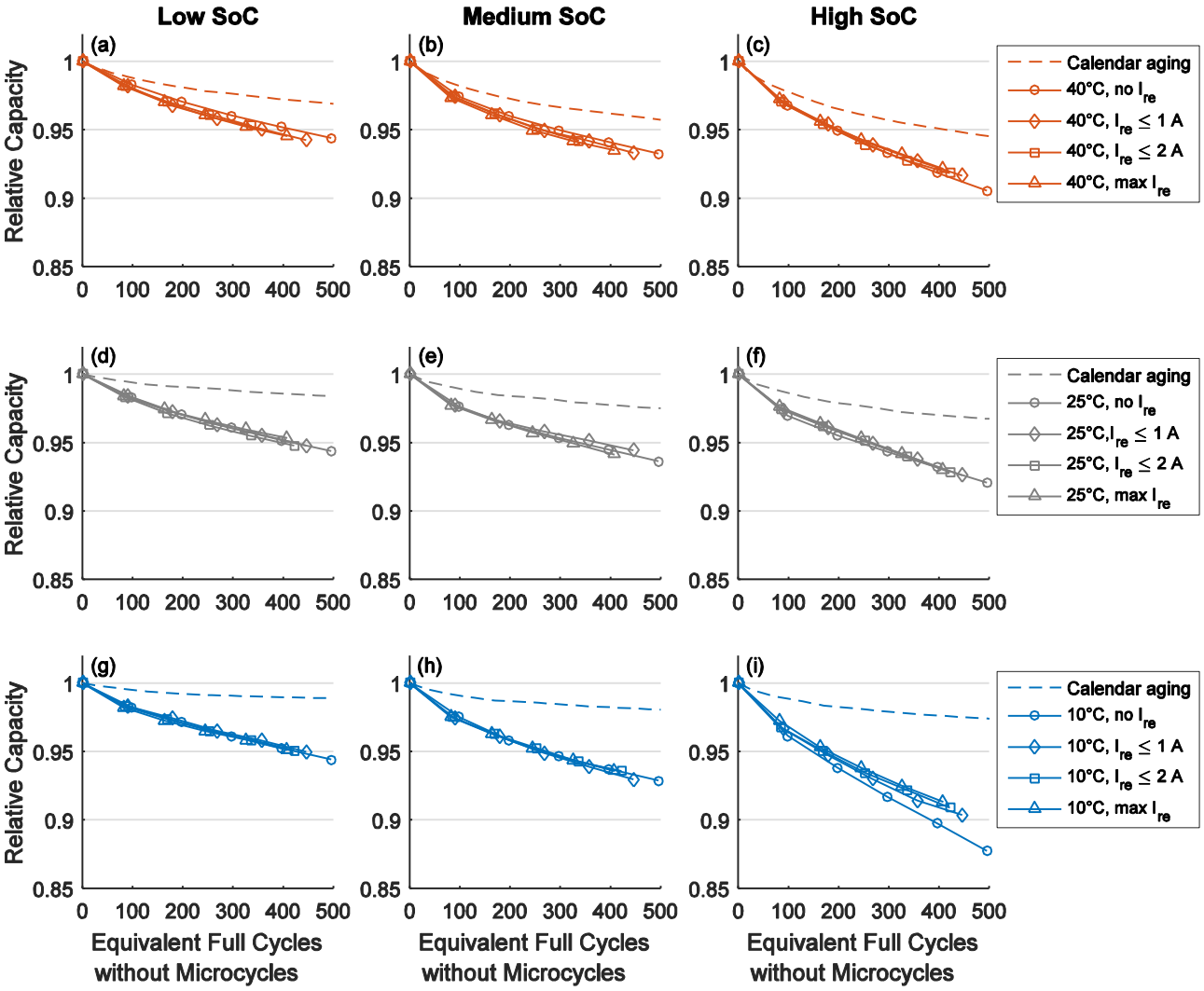

Figure 85. Capacity fade versus EFC without microcyles, which excludes the charge throughput from partial recharging by regenerative braking. Same data as in Figure 84, but with a different values for the x-axis. Scaling of calendar aging identical as in Figure 84.

6.5.3 Impact of Cycle Depth

The results presented in the preceding sections have comprised 500 EFC for cycle depths between 21% and 25% C_N. To further examine the impact of cycle depth, larger cycle depths were tested by test procedures including four and six – instead of two – consecutive runs of the driving load profile. As regenerative braking had been identified as beneficial for the cycle life of the lithium-ion cells, the load profile with unrestricted regenerative braking was used in the test procedures for comparing different cycle depths.

Figure 86 illustrates the capacity fade and the resistance increase for the three operating temperatures and six load scenarios with different charging voltages and cycling depths. The load scenario with two driving cycle runs and a cycle depth of 20% C_N is shown for the high, medium, and low charging voltage. For the high charging voltage, additional cycle depths of 41% and 61% C_N were

tested. The cycle depth of 41% C_N was also tested in combination with the medium charging voltage. Figure 86 presents up to 1200 EFC, which correspond to a driven distance of ca. 120,000 km.

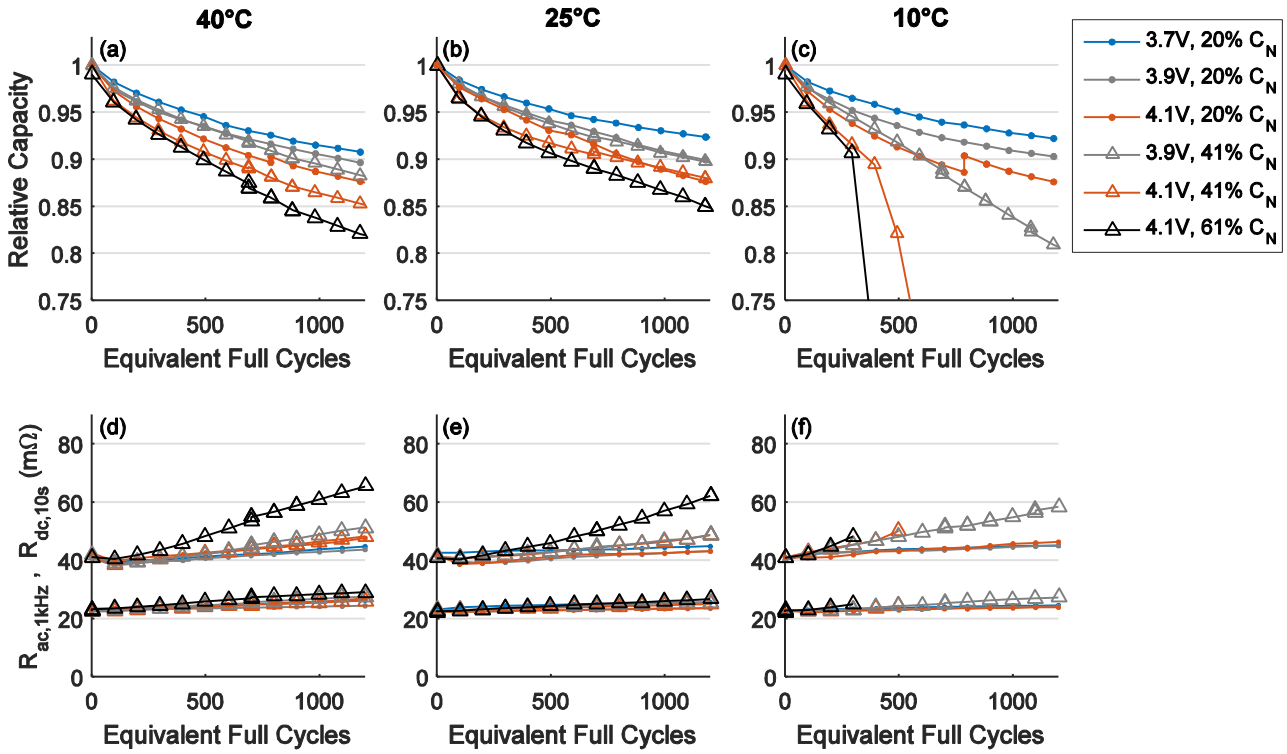

Figure 86. (a-c) Capacity fade and (d-f) resistance increase for up to 1200 EFC with unrestricted regenerative braking, different charging voltages, and depths of discharge of 20%, 41%, and 61% C_N. (For 61% C_N at 40°C and 10°C, the relative capacity curves were shifted 0.01 down, since the cells had already performed several cycles in another study so that their absolute capacity and the initial capacity fade was somewhat lower.)

Capacity Fade

Figure 86a illustrates that the capacity fade after 1200 EFC at 40°C ranges between 9% and 18%. The lowest capacity fade is observed for the low cycle depth of 20% C_N in combination with the low charging voltage. The highest capacity fade is observed for the largest cycle depth of 61% C_N. For the medium cycle depths of 41% C_N, a higher capacity fade has occurred than for the cells with a cycle depth of 20% C_N which have been charged to the same charging voltage.

For an operating temperature of 25°C, Figure 86b reveals capacity fades between 7.5% and 12%. Again, the capacity fade increases with larger cycle depths and higher charging voltages. In the beginning of the aging study, the two cells charged to 4.1 V and discharged with cycle depths of 41% and 61% C_N exhibit a similar capacity fade. After ca. 300 EFC, however, the slope of the capacity curve of the cell with 41% C_N cycle depth flattens and the rate of the capacity fade becomes even lower than for the cell cycled at high SoC with a cycle depth of only 20% C_N. This indicates that the capacity fade can decrease when the time the cell spends in the high SoC region shortens.

The capacity curves depicted in Figure 86c reveal that a higher capacity fade has occurred at the low operating temperature of 10°C. The step at 800 EFC in the capacity graph of the cell cycled with a low cycle depth at high SoC will be explained in a subsequent section. Particularly for higher cycle depths, the capacity fade increases markedly. There have even been premature failures. The cells which were charged to 4.1 V and discharged with a cycle depth of 61% or 41% C_N both failed in the

checkup sequence when the cells were charged to 4.2 V. This occurred after 400 EFC and 600 EFC, respectively. The current path inside these cells was interrupted and no voltage was available at the terminals any longer. This indicates a tripping of the internal current interrupt device (CID) which occurs in case of an overpressure inside the cell [267]. Overpressure inside the cell is typically a result of gaseous reaction products from electrolyte decomposition [97].

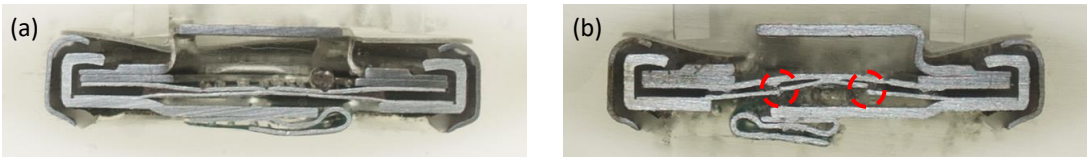

Figure 87. Cross-sections of positive cell terminals from (a) a new cell and (b) a failed cell after cycling with higher cycle depths at 10°C, where the two circles indicate the opening of the current interrupt device.

Figure 87 compares the positive terminals from a new cell and a failed cell after cycling at 10°C. A continuity check between the positive pole, located at the top of the images, and the tab of the cathode current collector, depicted at the bottom of the images, confirmed that the current path was interrupted at the positive terminal. The red circles in Figure 87b show where the current path is interrupted, which confirms a tripping of the CID owing to overpressure inside the cell.

Such a premature failure also occurred after 700 EFC at 10°C for the cell with a charging voltage of 4.1 V and a cycle depth of 25% C_N without regenerative braking. This demonstrates that it is not the short-time recharging from regenerative braking which causes the gassing side reactions. Instead, increasing cycle depths and high charging voltages accelerate the degradation at low temperature.

At all three temperatures examined, the capacity fade has increased considerably with higher cycle depths, in particular at high SoC. The best cycle life has always been obtained for cycling with low cycle depths in the low SoC region below 50% SoC. In this aging study, no deep discharging of the cells occurred, which has shown to be detrimental to cycle life in the study on charging protocols.

Resistance Increase

The resistance developments, depicted in Figure 86d-f, show the changes in the internal cell resistances. The changes in $R_{ac,1kHz}$, representing changes in the electrolyte conductivity, increase with higher temperature and larger cycle depths. However, the absolute changes remain small compared to the changes in $R_{dc,10s}$, which comprises the rising charge transfer resistances of the cathode. The later has, thus, a larger contribution to the increasing energetic losses.

At 40°C, $R_{ac,1kHz}$ rises by 2–6 mΩ whereas $R_{dc,10s}$ exhibits increases of up to 25 mΩ for the cycle depth of 61% C_N. The initial reduction of $R_{dc,10s}$ due to decreasing anode resistances is also observed for the larger cycle depths. Comparable results were also observed for 25°C. $R_{ac,1kHz}$ rises by 1.5–4 mΩ and $R_{dc,10s}$ by up to 21 mΩ for the largest cycle depth. The two cells with a cycle depth of 41% C_N exhibit similar resistance changes, although they have been cycled at different SoC regions. This confirms that the resistance increase depends mainly on the cycle depth and less on the actual SoC interval.

At 10°C, only the cells with a cycle depth of 20% C_N and the cell with a cycle depth of 41% C_N in combination with the medium charging voltage were able to perform 1200 EFC. For the latter, $R_{ac,1kHz}$ has increased by 5 mΩ. For the cells with the low cycle depth of 20% C_N, $R_{ac,1kHz}$ has increased by only 2 mΩ. As observed in the previous sections (see Figure 81d-f), there are no reductions in

$R_{dc,10s}$ at the beginning of the cycling procedure. The increase in $R_{dc,10s}$ after 1200 EFC at 10°C amounts to 18 mΩ for the cell with the cycle depth of 41% C_N. For the cells with the low cycle depth of 20% C_N, $R_{dc,10s}$ has increased by ca. 5 mΩ. The other cells with larger cycle depths died before reaching a comparable resistance increase. As there are no suspicious marks in the resistance developments of $R_{ac,1kHz}$ and $R_{dc,10s}$, these resistance values cannot serve as early indicators for the premature failures in this study.

6.5.4 Long-Term Cycling at 25°C

To analyze the long-term cycle aging of the lithium-ion cells, the test procedures for the cells cycled at 25°C with unrestricted regenerative braking were continued to 2000 EFC, which correspond to a driven distance of ca. 200,000 km. Figure 88 illustrates the capacity fade and the resistance increase for the different charging voltages and cycle depths.

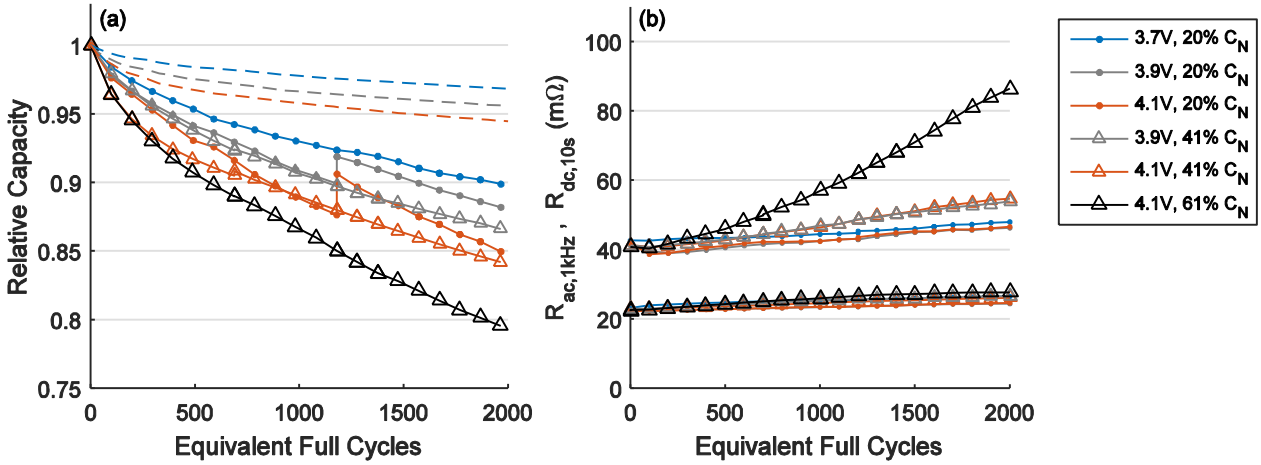

Figure 88. (a) Capacity fade and (b) resistance increase for long-term cycling at 25°C with unrestricted regenerative braking for different charging voltages and cycle depths. The dashed lines represent capacity fade owing to calendar aging at low, medium, and high SoC, with the same time scaling as in Figure 84.

Capacity Fade

The strong dependency of capacity fade on cycle depth is also observed in the long-term aging data depicted in Figure 88a. After 2000 EFC, the cells with a cycle depth of only 20% C_N exhibit a capacity fade of 10% at low SoC, 12% at medium SoC, and 15% at high SoC. The cells with a cycle depth of 41% C_N exhibit a capacity fade of 13.5% for the medium charging voltage and 15.5% for the high charging voltage. The largest capacity fade of more than 20% was observed for cycling with 61% C_N cycle depth.

After 1200 EFC, the cells cycled with the low cycle depth of 20% C_N at medium or high SoC feature a step in the capacity curve of 2–3 percentage points. This corresponds to an interruption of the aging study lasting more than 5 months. The long pause led to a considerable capacity recovery, which will be further analyzed in the subsequent result section.

The difference between the capacity fade of the cycled cells and the calendar aging curves reveals that the additional capacity fade owing to cycle aging for 200,000 km at 25°C can be estimated at 7–16%. The lowest cycle aging is obtained for cycling with low cycle depth of 20% C_N in the low SoC region below 50% SoC. With higher SoC and particularly with increasing cycle depth, the capacity

fade aggravates. In this study, the highest cycle aging is observed for the largest cycle depth of 61% C_N.

For even higher cycle depths, cycle aging will further increase. This has also been observed in the cycle aging study on charging protocols. For high cycle depths above 90%, it was difficult to reach more than 1000 EFC with less than 20% capacity fade. The cell which was CCCV charged and discharged between 4.1 V and 3.4 V exhibited a capacity utilization of ca 70% (see Table 9, p.91) and, thus, its cycle depth is comparable to the cycle depth of the cell in the driving study which was cycled with a cycle depth of 61% C_N, which has been independent of the actual capacity. Comparing the degradation of these two operating scenarios reveals a similar capacity fade. Both cells exhibit a capacity fade of ca. 13% after 1000 EFC. This demonstrates that lithium-ion battery aging strongly correlates with cycle depth. Hence, a direct recharging after partial discharging – even after short driving distances – reduces the cycle depth and might be beneficial to prolong battery life, although the battery spends more time at a higher SoC. Thus, an appropriate compromise between cycle aging and calendar aging has to be found.

Resistance Increase

Also the resistance increase aggravates with higher cycle depth. For the cells with identical cycle depth, Figure 88b exhibits similar trends in the resistance increase. After 2000 EFC, the $R_{dc,10s}$ has increased by 46 mΩ for the cycle depth of 61% C_N. This means that the resistance has more than doubled. For the cycle depth of 41% C_N, the increase of $R_{dc,10s}$ is 14 mΩ and for the low cycle depth of 20% C_N, it is below 6 mΩ.

The resistance curves exhibit no signs of regeneration after 1200 EFC, as it has been the case in the capacity curves of Figure 88a for the cells with low cycle depth. Hence, there is no unambiguous correlation between capacity fade and resistance increase, which allows a robust estimation of the actual capacity fade by measuring the batteries' internal resistances.

Comparing these results again to the cell from the study on charging protocols with a capacity utilization of ca. 70%, the resistance rise of that cell has been even larger. This can be ascribed to the CCCV discharging in the previous aging study. The additional CV discharging phase appears to cause higher intercalation-induced stress in the NCA cathode.

Further insights into the resistance changes of cells cycled at 25°C with cycle depths of 41% and 61% C_N can be obtained from the impedance spectra depicted in Figure 89. For both cells, the impedance spectra exhibit right shifts, representing increasing ohmic resistances, owing to reduced electrolyte conductivity. For the cycle depth of 41% C_N (Figure 89a), the right shift of the 1 kHz impedance amounts up to 3 mΩ and for the large cycle depth of 61% C_N, it amounts up to 5 mΩ. Figure 89 also highlights that the rising charge transfer resistance of the cathode, identifiable by the arc between ca. 30 Hz and 350 mHz, constitutes the by far largest contribution to the resistance increase. For the cycle depth of 61% C_N, the real part of the 10 mHz impedance more than doubles throughout the 2000 EFC.

The impedance spectra in Figure 89 also confirm that there occur no considerable changes in the vertical positions of the impedances in the high-frequency domain above 1 kHz. Consequently, no changes in inductivities occurred, as they would have altered the imaginary parts of the impedances at higher frequencies.

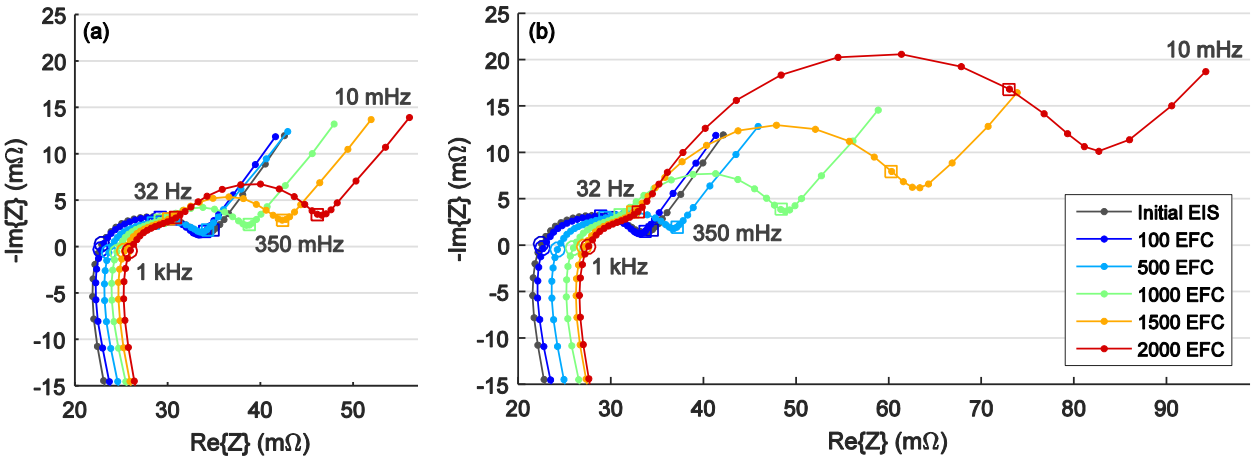

Figure 89. Impedance spectra for cells charged to 4.1 V and cycled with unrestricted regenerative braking and a cycle depth of (a) 41% C_N and (b) 61% C_N.

Energy Efficiency

Due to the increasing internal resistances, the losses of the lithium-ion cells rise and energy efficiency decreases. Figure 90 shows the energy efficiency for the different cells cycled at 25°C with different cycle depths and charging voltages. Similar to the resistance changes, the energy efficiency decreases more pronouncedly with higher cycle depth. For the cycle depth of 20% C_N, the changes are small. After 2000 EFC, the energy efficiency has decreased only by ca. 2%. For the cycle depth of 41% C_N, the efficiency has lowered by 2–3%. For the highest cycle depth of 61% C_N, the efficiency has decreased markedly from 94% to 86% throughout the 2000 EFC. Consequently, losses rise by more than 130%, which is in the same order as the increase of $R_{dc,10s}$. This substantial increase in irreversible heat generation has to be considered when designing the cooling system for the battery.

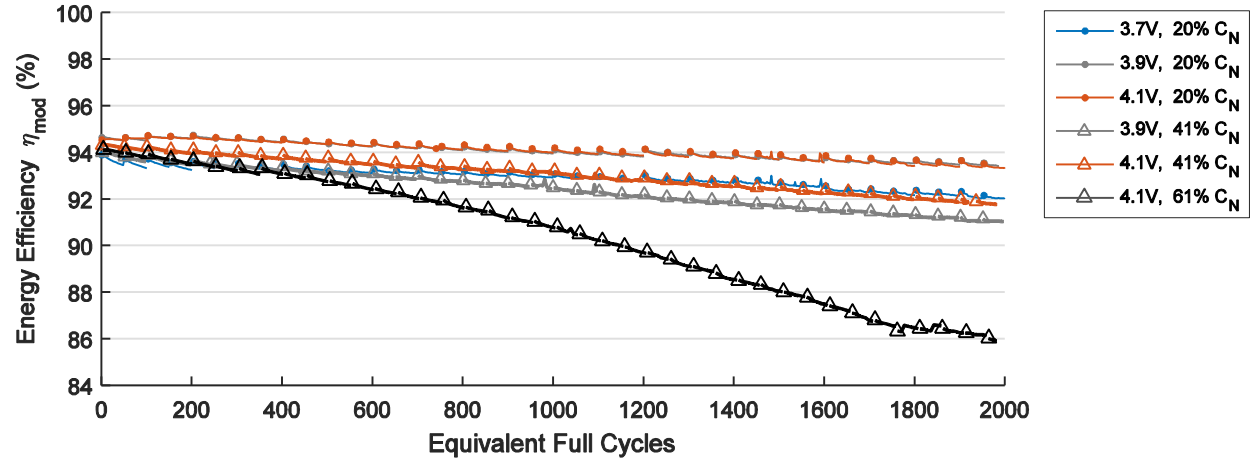

Figure 90. Modified energy efficiency for cells cycled at 25°C with unrestricted regenerative braking and different charging voltages and cycle depths.

6.5.5 Regeneration Effects

In the previous section, capacity recovery has been observed after an interruption of the cycle aging study of several months. The capacity recovery occurred for the cells cycled with low cycle depth of 20% C_N at the high and medium SoC level. To further investigate the capacity recovery during

interrupts, the capacity development is analyzed over time and Coulomb Tracking is used to identify the origin of the reversible capacity fade.

Capacity Fade over Time

Figure 91 depicts the capacity development over time – instead of over EFC, as it was the case in Figure 88a. The markers represent the checkups, the continuous lines represent cycling periods, and the dotted lines indicate pauses with no cycling.

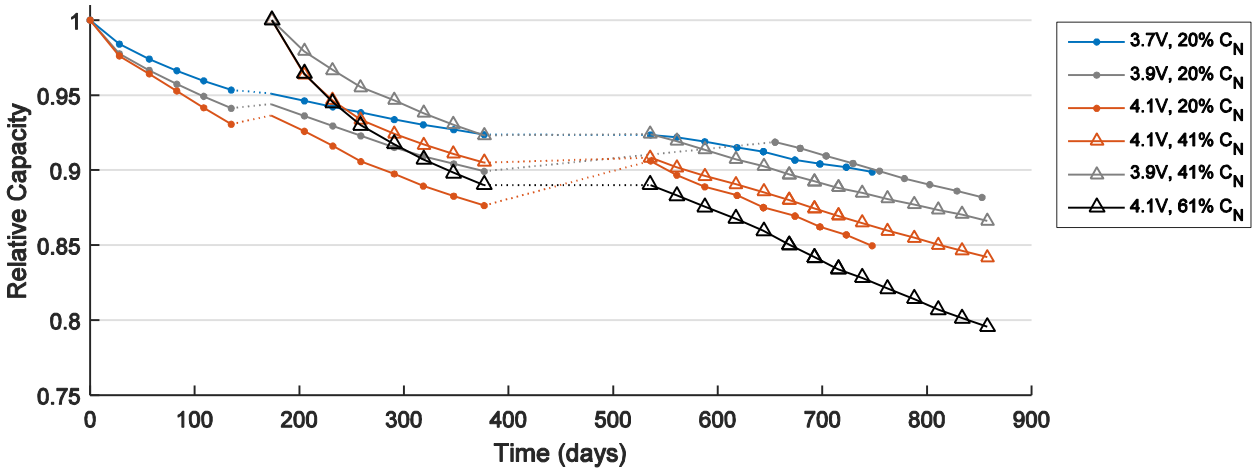

Figure 91. Capacity development over time. The markers represent checkups, continuous lines represent cycling periods at 25°C, and dotted lines indicate storage periods. This demonstrates the capacity recovery of cells cycled in higher SoC regions only.

After the first 140 days, in which 500 EFC with a cycle depth of 20–25% C_N were tested for various combinations of charging voltage, temperature, and magnitude of regenerative braking, the cells with the intermediate levels of regenerative braking were stopped. Their test channels were then used to examine further load scenarios, particularly those with larger cycle depths. Figure 91 shows that the three cells cycled with a low cycle depth of 20% C_N had a pause of ca. 1 month after the first 500 EFC. As no capacity recovery had been expected, no additional checkup was performed after this pause. To estimate afterwards the capacity for these cells after the pause, it was assumed that the capacity fade between the checkups after 500 EFC and 600 EFC was similar to the capacity fade between the checkups after 600 EFC and 700 EFC. Hence, the difference in capacity between the checkups after 600 EFC and after 700 EFC was used to back-calculate to the capacity after the pause of 1 month. As illustrated by the dotted lines between 140 and 175 days, a capacity recovery can be observed for the cells cycled at the high and medium SoC level. However, no capacity recovery is observed for the cell with the low charging voltage.

After 380 days, corresponding to 1200 EFC for the cells cycled from the very beginning and to 700 EFC for the cells newly started after six months, the aging study was interrupted for more than five months. During this long interruption, the cells were stored at 10°C to minimize calendar aging. In all pauses, the cells were stored at 50% SoC, as this is the SoC of the cells at the end of each checkup. When the study continued ca. 160 days later, an additional checkup was performed to determine the actual capacity before starting the new cycling sequences. These capacity measurements reveal substantial capacity recovery for the cells cycled with low cycle depth at high and medium SoC. This capacity recovery caused the steps in the capacity curves which have been presented earlier in Figure 88a. For cycling with low cycle depth at high SoC, Figure 86a and

Figure 86c have also shown a capacity recovery at 40°C and 10°C. These two cells were also started later. As a consequence, the ca. 5 months of pause correspond to the regeneration at 800 EFC. All other cells depicted in Figure 86 were started at the very beginning and, thus, did not experience a longer pause within the 1200 EFC.

For the cells cycled with the low cycle depth of 20% C_N at low SoC, no capacity recovery occurs during the test interruptions. There is also no capacity recovery for the large cycle depth of 61% C_N and for the cycle depth of 41% C_N in combination with the medium charging voltage of 3.9 V. This indicates that all cells that reach the low SoC domain during the cycling procedure do not exhibit capacity recovery. For all cells cycled within the high or medium SoC range only, which means between 90% and 50% SoC only (see Figure 79a), a capacity recovery has been observed.

Identifying the Origin of the Reversible Capacity Fade by Coulomb Tracking

To further study the capacity recovery effect that took place when the cycling procedure was interrupted, the cells cycled with no regenerative braking at 25°C were examined by Coulomb Tracking. For these cells, the cycling procedure was discontinued after 1200 EFC. After the last checkup, an additional test sequence was performed, in which the cells were CCCV charged to 4.2 V with 700 mA, discharged and recharged with 100 mA to 2.5 V and 4.2 V, respectively, and finally discharged to 50% SoC. After this test, the cells were stored 15 months at 50% SoC. Then, the described test sequence with low-current discharging and charging was repeated. Based on the two measurements before and after the storage period, Coulomb Tracking was performed. Figure 92 shows the low-current charging sequences of the two measurements versus a continuous ampere-hour balance.

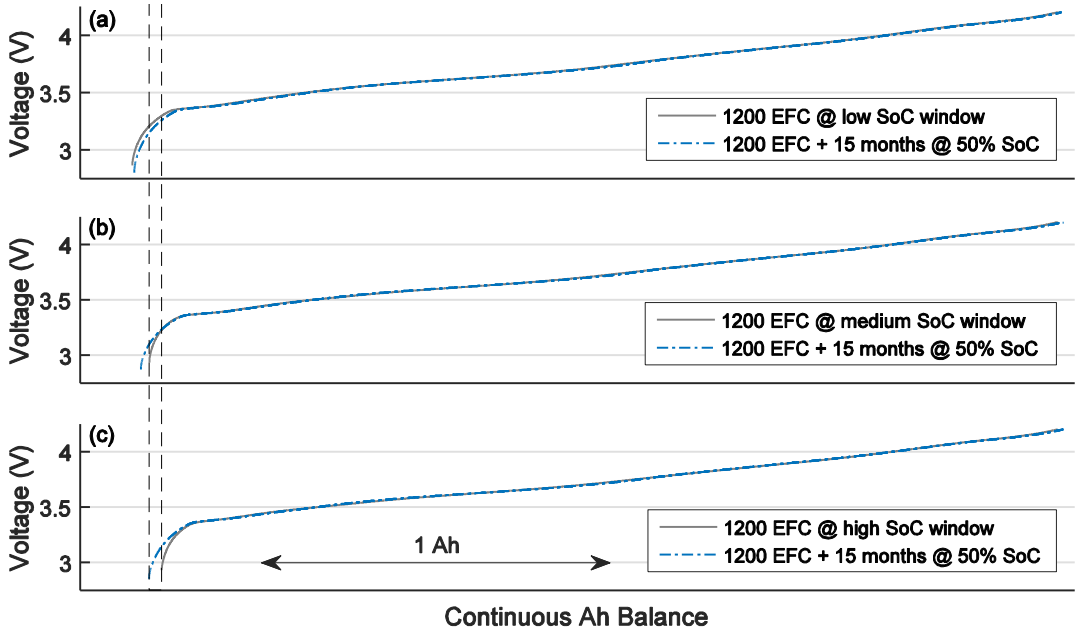

Figure 92. Capacity recovery after 15 months of storage at 50% SoC examined by Coulomb Tracking for the cells cycled 1200 EFC without regenerative braking in the (a) low, (b) medium, and (c) high SoC window with a depth of discharge of 25% C_N. The x-axes are scaled identically for all three cells.

As shown in Figure 92b and Figure 92c, the length of the charging sequence after the long storage period differs considerably for those cells that were cycled in the medium and high SoC cycling window. This corresponds to a capacity recovery, which occurs most pronouncedly for the cell

cycled in the high SoC window. The charging voltage curves are almost identical over a wide SoC range and differ only in the very low SoC region. Here, the slope of each pair of charging curves differs notably. As this steep section of the voltage curve can be ascribed to the large changes of the anode potential (see Figure 18, p.36), the graphite anode is identified as the origin of the capacity recovery.

The mechanism that leads to the recovery of cyclable lithium was described by Gyenes et al. [197] and Lewerenz et al. [198]. Overhang areas of the anode, which face no cathode counterpart, can become a location of inaccessible lithium. Due to potential gradients between the active areas, which face a cathode counterpart, and the overhang areas, lithium can diffuse into overhang areas and become inaccessible for the regular charge-discharge cycling. When a cell is operated at high SoC most of the time, the potential of the anode active area mostly lies within the low voltage plateau of lithiated graphite. This leads to a larger amount of lithium diffusing into the overhang areas and a lower potential in these areas. When the cells are then stored for several months at 50% SoC, the potential of the anode active area lies within the medium graphite voltage plateau. As a consequence, lithium from the overhang areas diffuses back into the active areas and becomes accessible again.

After the storage period, more lithium can be extracted from the anode again, which causes a left-shift of the discharging endpoint. The longer the cell was operated at high SoC, the more capacity is recovered during the storage period. As the cell depicted in Figure 92a was operated only at SoCs below 50% during cycling, the storage period was performed at a minimal higher SoC level than the cycling sequences. Thus, a small amount of lithium has diffused into the overhang areas. This explains why this cell exhibits a small right-shift of the discharging endpoint after the storage period, which corresponds to a somewhat lower capacity. The dashed lines in Figure 92 illustrate the left-shift of the discharging endpoint of the cell previously cycled in the high SoC window. This shift amounts to 36 mAh and leads to a reduction of the capacity difference between the first and the third cell depicted in Figure 92 from 2.9% C_N to 1.6% C_N. It has to be noted that these regeneration effects differ considerably from the short-term capacity regeneration after extensive lithium plating, where a notable capacity recovery has been observed already after one checkup sequence.

6.5.6 Comparison of Dynamic Discharging and Constant-Current Discharging

The US06 driving load profiles used in this study changed the load current every second. To determine the impact of these frequent load changes on battery aging, additional cells were tested with a CC discharging procedure, which featured the same cycle depth and the same mean discharging current as the load profile with unrestricted regenerative braking. The dynamic driving load profile contained load currents between –5.5 A and +4.5 A with a mean discharging current of –1.714 A. Four repetitions of the driving load profile led to a cycle depth of 41% C_N. For both load cases, the charging procedure was CC charging with 700 mA to 4.1 V. Figure 93 compares the capacity fade, resistance increase, and energy efficiency of the two load scenarios at different operating temperatures. Charging and discharging took place at the same operating temperature.

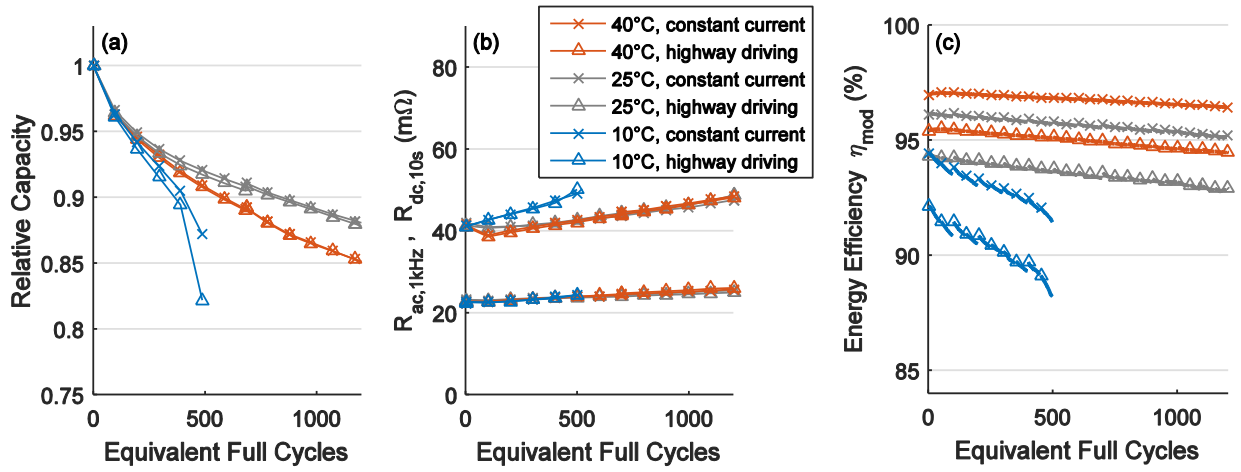

Figure 93. Comparison of battery degradation for the dynamic driving load profile and constant-current discharging with the same cycle depth of 41% C_N and the same mean discharge current of 1.7 A. (a) Capacity fade and (b) resistance increase obtained from the checkups; (c) energy efficiency during cycling.

Capacity Fade

Figure 93a shows that the capacity fade of the two cells cycled at 40°C is similar. At 25°C, the capacity fade is somewhat lower for discharging with the constant current. However, the differences are small and the additional capacity fade due to the dynamic driving load profile with its multiple peak pulse loads lies below 0.4 percentage points. After 700 EFC, where the aging study has been interrupted for more than 5 months, a similar capacity recovery has been observed for both load conditions. The differences in capacity fade between 25°C and 40°C can be ascribed largely to the increasing calendar aging with higher temperature.

For cycling at 10°C, Figure 93a exhibits a substantially faster degradation than for 25°C and 40°C. Moreover, there is a considerable difference in capacity fade between both load scenarios. The dynamic driving load profile has led to a faster capacity fade. At this low temperature, both cells exhibit an accelerated degradation after 400 EFC. As premature failures had been expected after the rapid degradation throughout the last 100 EFC, the cycling of these cells was stopped after 500 EFC.

Resistance Increase

Figure 93b illustrates the resistance increase for the different combinations of load scenario and temperature. For all three operating temperatures, the resistance increase is similar for both load scenarios. This demonstrates that lithium-ion battery aging exhibits a certain low-pass behavior, which means that the resistance increase is driven by the mean load current and the cycle depth and not by short peak loads.

The resistance increase for cycling at 25°C and 40°C is similar, although the capacity fade differs by 3 percentage points after 1200 EFC. This confirms the assumption that the higher capacity fade at 40°C can be ascribed to calendar aging. As shown by the preceding results on charging protocols and driving operation, the resistance increase aggravates with larger cycle depth.

Energy Efficiency

Although degradation was similar for continuous and dynamic discharging, Figure 93c exhibits large differences in energy efficiency. As the resistances of the cells increase similarly and as the charging

procedure is identical for both load cases, the differences in energy efficiency can be ascribed to the different discharging procedures. The energy efficiency of the driving load profile is 1.6–2.0% lower at 40°C, 2.0–2.5% lower at 25°C, and 2.5–3.2% lower at 10°C. As resistive losses usually depend on the square of the current, high peak currents lead to disproportionate losses. As a consequence, the energy efficiency is lower for load profiles with higher dynamics.

6.5.7 Alternating Operating Temperatures

All results presented so far were obtained from cycling at constant operating temperatures. Hence, the individual contributions of the charging procedure and the discharging procedure on battery aging could not be separated. As this is of particular interest for identifying aging mechanisms, especially for the intensified degradation at low temperatures, an additional aging experiment with alternating operating temperatures was performed. For every switchover between charging and discharging, the operating temperature alternated between 25°C and 0°C. This was realized by a climate chamber which changed its operating temperature every 2.4 h. In this climate chamber, two sets of cells were tested: The first set was charged at 0°C and discharged at 25°C, and the second set was charged at 25°C and discharged at 0°C. Figure 94 depicts exemplary beginnings of the cycling procedure of one cell of each set.

Figure 94c and Figure 94d show that it takes 15–20 min after every temperature change until the cell's temperature, which was measured at its surface by an attached temperature sensor, has adapted to the new operating temperature.

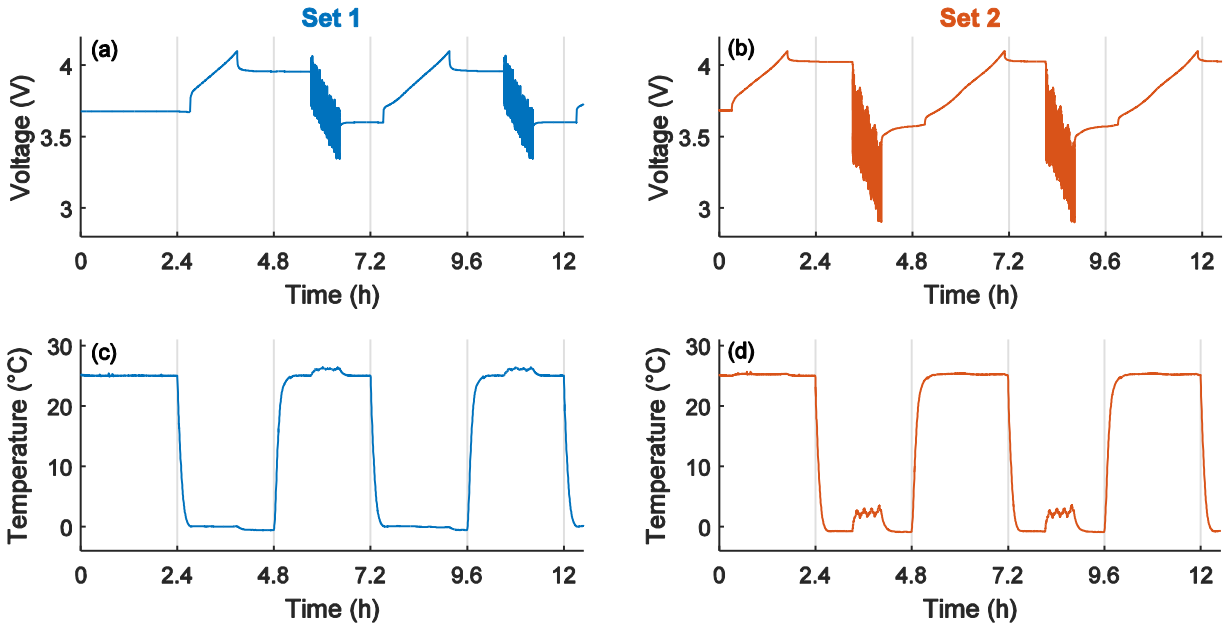

Figure 94. Exemplary test results for both sets of cells. (a) Voltage and (c) surface temperature of one cell of set 1, which was charged at 0°C and discharged at 25°C. (b) Voltage and (d) temperature of one cell with inverse operating temperatures.

This study was also intended to further investigate the impact of charging peaks from regenerative braking on battery aging. The applied test procedures with four consecutive runs of the US06 load profiles led to depths of discharge of 41% C_N and 49% C_N. Previously, it has been shown that regenerative braking reduces battery aging, as it lowers the depth of discharge. However, it remains

unclear whether there are differences in aging when the cycle depth is identical but the recharging peaks from regenerative braking differ. This question is examined by using the load profile without regenerative braking and applying an explicit limitation of the depth of discharge to 41% C_N. For the three load scenarios with different levels of regenerative breaking and/or different cycle depths, Figure 95 exhibits the capacity fade and resistance increase for the two sets of cells.

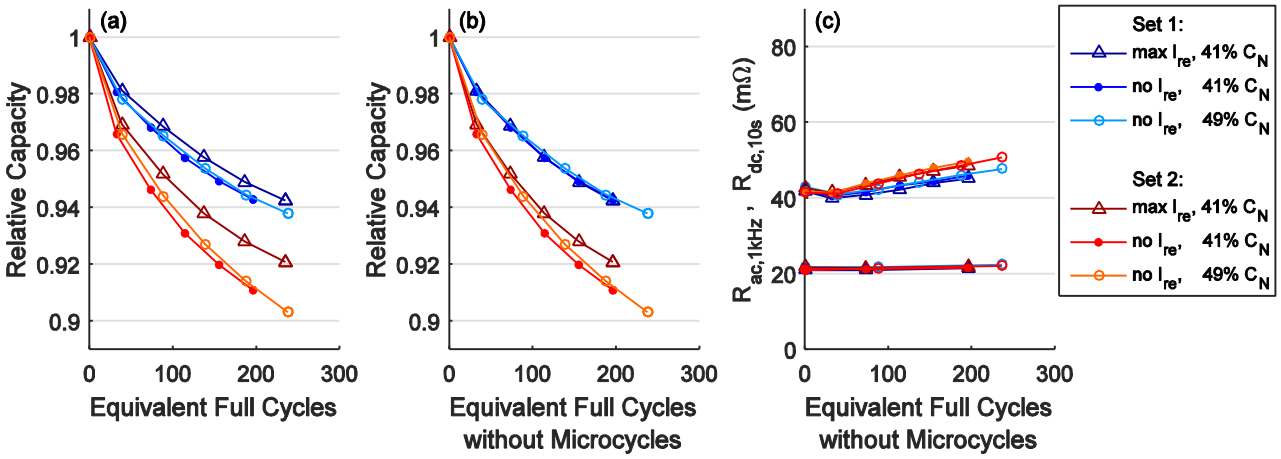

Figure 95. (a, b) Capacity fade for both sets of cells for different levels of regenerative braking and cycle depths. Representation versus charge throughput in (a) EFC and (b) EFC without microcycles generated by charge recovery from regenerative braking. (c) Resistance increase.

Capacity Fade

Figure 95a and Figure 95b illustrate the capacity fade for the two sets of cells, each containing the three different cycling scenarios. In Figure 95a, the capacity fade is depicted versus the overall charge throughput. In the end, the cells had performed up to 240 EFC. Due to the explicit cycle limitation of the cells with a cycle depth of 41% C_N and no regenerative braking, the total charge throughput of these cells is ca. 16% lower. For the first set of cells, which was charged at 0°C and discharged at 25°C, the capacity fade lies between 5.8% and 6.2% at the end of the experiment. For the second set of cells – with inverse operating temperatures – the capacity fade lies between 7.9% and 9.7%.

In analogy to Figure 85, Figure 95b uses the charge throughput without microcycles as x-axis, which excludes the microcycles resulting from charge recovery by regenerative braking. This leads to a horizontal rescaling of the capacity curves for the two cells with regenerative braking. Naturally, the curves of the cells without regenerative braking are identical in Figure 95a and Figure 95b. In this representation, the capacity curves of both sets lie closer together. For set 1, the three curves are almost identical.

Both capacity graphs show that the cells discharged at 0°C age substantially faster than the cells charged at 0°C. At first, this appears counterintuitive, since aging at low temperatures is usually ascribed to lithium plating, which occurs during charging only. However, the charging current has been rather low (700 mA, C/4) in this study. Hence, it is not supposed to cause substantial lithium plating. The discharging procedure with the driving load profiles led to an average discharge current of 0.6–0.7 C with peak discharge pulses up to 2 C. Thus, this study demonstrates that discharging with higher currents at low temperature can also provoke substantial battery degradation.

Neglecting the charge throughput resulting from the charge recovery by regenerative braking, Figure 95b shows that for charging at 0°C, the capacity fade of all three cycling scenarios of set 1 is similar. Hence, it directly depends on the charge throughput of the main cycles. In fact, the cells are all charged by the same CC charging procedure. This shows that for charging at low temperature, the degradation correlates with the long-lasting charging periods after the driving operation. The short recharging periods during driving operation at 25°C have revealed no considerable effects on battery aging.

When the cells are discharged at 0°C, the capacity fade is substantially higher and the differences in regenerative braking lead to a larger spread among the different load conditions. This demonstrates that discharging with higher (peak) loads has a considerable impact on battery aging at low temperature. This reveals that there are aging mechanisms besides lithium plating that degrade lithium-ion cells discharged at low temperatures. Again, the curve for maximum regenerative braking exhibits the best cycle life. Hence, this study also reveals no necessity for limiting the currents during regenerative braking.

Resistance Increase

Figure 95c illustrates that also in this aging experiment, there are only small increases in the ohmic resistances, represented by $R_{ac,1kHz}$. The $R_{ac,1kHz}$ values were extracted from three EIS measurements at 50% SoC, performed before the cycling procedure, after 180 charge-discharge cycles, and after 480 charge-discharge cycles. These cycle numbers correspond to 90 and 240 EFC, respectively, for the cells cycled without explicit limitation in cycle depth. Notable changes in the internal resistances can be observed in $R_{dc,10s}$, depicted in Figure 95c. These values were computed from the pulses at the end of each checkup. Similar to the cells cycled at constant 25°C and 40°C, the $R_{dc,10s}$ values decrease slightly at the beginning of the cycling procedure.

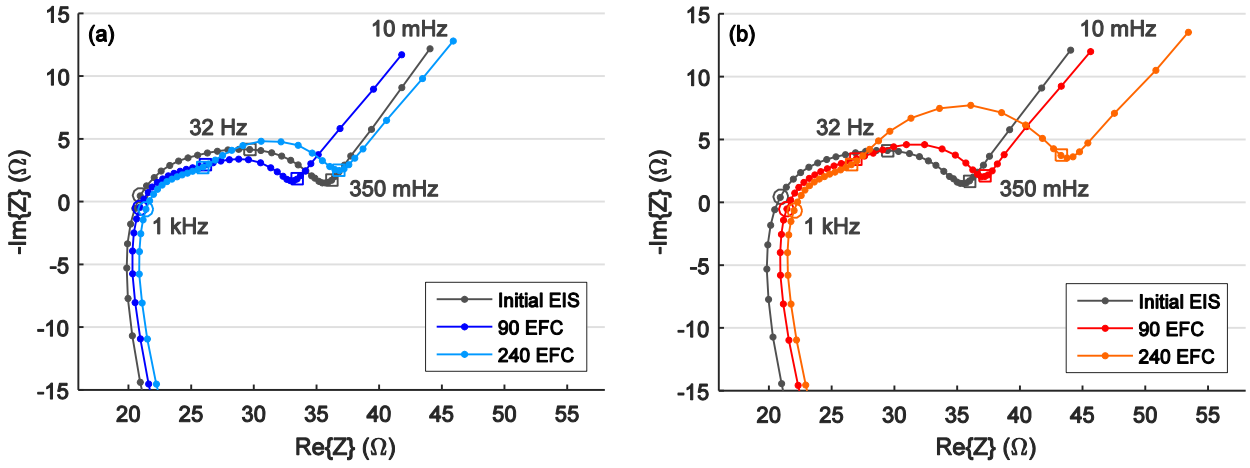

Figure 96. Impedance spectra of the two cells of the alternating temperature study with (a) the lowest and (b) the highest degradation. Characteristic frequency points are highlighted.

The impedance spectra depicted in Figure 96 reveal that performing the discharging sequence at 0°C leads to a larger impedance rise than performing the charging sequence at 0°C. From the six load conditions examined in this experiment, Figure 96a shows the impedance measurements for the best cell (unrestricted regenerative braking, set 1: charging sequence at 0°C) and Figure 96b shows the results for the worst cell (no regenerative braking with 49% C_N cycle depth, set 2:

discharging sequence at 0°C). The characteristic frequencies highlighted are used to separate different resistance components. $R_{ac,1kHz}$ exhibits small changes in the ohmic resistance, which can be ascribed to a reduced electrolyte conductivity. The difference in the real part of the impedances at 32 Hz and 1 kHz, representing mainly contributions from the graphite anode, has decreased for all six cells. The diffusion resistances, represented by the sloping line between 350 mHz and 10 mHz, reveal only minor changes. The most pronounced changes can be observed again for the capacitive semicircle between 32 Hz and 350 mHz. The growing diameter illustrates increasing charge transfer resistances of the NCA cathode.

Differential Voltage Analysis

Additional checkups with a low-current charging sequence were performed at the beginning and at the end of the aging experiment on alternating operating temperatures. DVA was performed with the low-current charging data to disclose the origins of capacity fade.

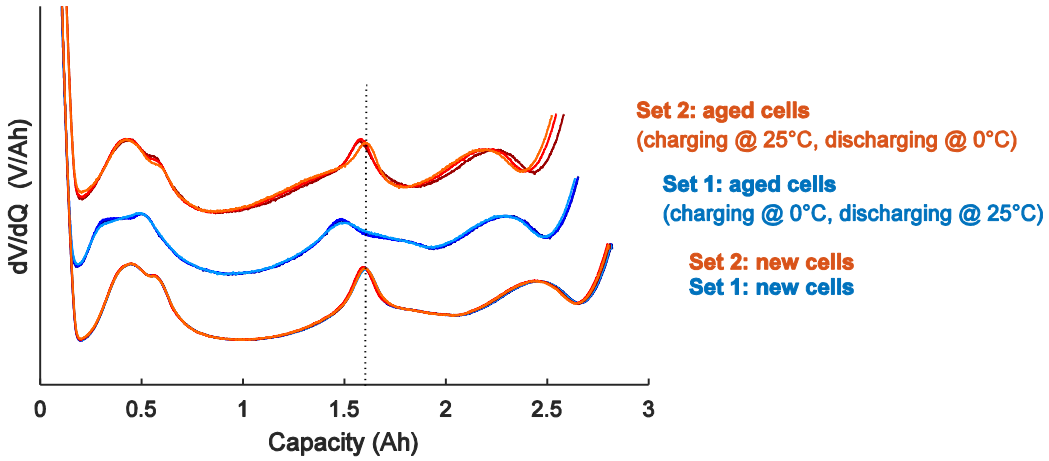

Figure 97. Differential voltage spectra of the cells in new condition and after the cycling experiment with alternating temperatures. The location of the central graphite peak of the new cells is highlighted. The spectra of the aged cells contain vertical offsets for more clarity.

Figure 97 shows the differential voltage spectra for the cells at the beginning and at the end of the aging experiment. For the cells in the new condition, all spectra are similar. The initial location of the central graphite peak is highlighted by the dotted vertical line. The two sets of aged cells are plotted with vertical offsets for more clarity. The first set, containing the cells charged at 0°C, exhibits a shift of the central graphite peak to the left. This indicates a reduced storage capacity of the anode, since the state of 50% lithiation of the anode is reached already at a lower capacity. This anode degradation is also illustrated in Figure 98, where the Q_1 capacity represents the position of the central graphite peak. Thus, charging at 0°C causes notable anode degradation. However, this active material degradation does not directly affect the cell capacity, as the anode is oversized. Instead, it is the loss of cyclable lithium owing to side reactions with the electrolyte that causes the capacity fade. Only if the Q_1 capacity drops to about 50% of the actual cell capacity, the anode becomes the limiting electrode when charging the lithium-ion cells to 100% SoC. Due to the changes in Q_1, Q_2 can no longer be used as a direct indicator for the loss of cyclable lithium owing to changes in the electrode balancing. The Q_3 capacity values for the first set of cells exhibit very minor changes, which demonstrates that there is not much cathode degradation.

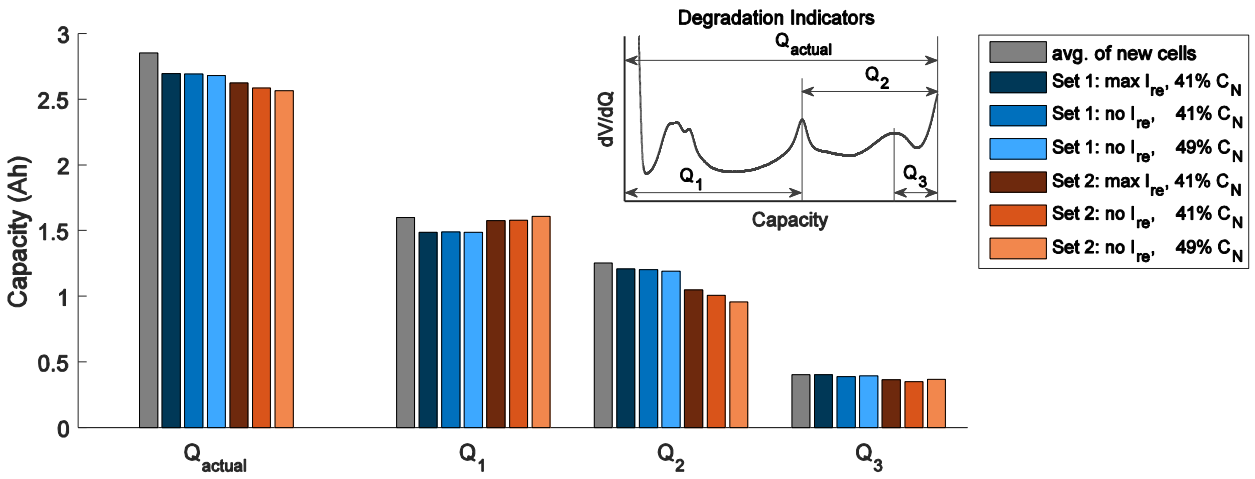

Figure 98. Actual capacity Q_{actual} and degradation indicators Q_1, Q_2, and Q_3 at the end of the cycling experiment with operating temperatures alternating between 0°C and 25°C. At 0°C, the set 1 was charged while set 2 was discharged.

In Figure 97, the differential voltage spectra of the second set, containing the cells discharged at 0°C, exhibit almost no changes in the position of the central graphite peak. Hence, the Q_1 values in Figure 98 remain rather unchanged. Thus, charging at 25°C and discharging at 0°C does not lead to intensified anode degradation, as it has been the case for charging at 0°C. Although these cells exhibit only minor anode degradation, the overall capacity fade is considerably higher than for the first set. Small changes in the Q_3 values indicate some cathode degradation. The higher cathode degradation for set 2 is in good agreement with the impedance measurements shown in Figure 96. The cell from set 2 has revealed a substantially stronger growth of the charge transfer resistances of the NCA cathode than the cell from set 1.

The marked changes of the Q_2 values in combination with stable Q_1 values demonstrate that the capacity fade originates largely from a shift in the electrode balancing, which is caused by a loss of cyclable lithium. Hence, discharging at 0°C must provoke side reactions which consume cyclable lithium. The typical side reactions presented in the literature describe an electrolyte reduction for low anode potentials and an electrolyte oxidation for high cathode potentials. During discharging, the overpotentials at the anode and at the cathode lead to an increasing anode potential and a decreasing cathode potential. This reduces the above mentioned side reactions. Hence, additional types of side reactions occur during discharging at low temperature. They could be further characterized by coulometry. However, this requires high precision battery test systems and could not be performed with the battery test systems available for this thesis, as small offsets in the current measurements led to a drift in the ampere-hour integration and inhibited a localization of the lithium loss.

Overall, the aging experiment with alternating operating temperatures has enabled an identification of individual contributions of charging and discharging on the overall capacity fade of the lithium-ion cells operated at low temperatures. It has confirmed that charging at low temperature leads to anode degradation. However, the reduced storage capabilities of the anode do not directly affect the cell capacity as long as the anode remains oversized. A dominant part of the capacity fade can be ascribed to side reactions consuming cyclable lithium. Particularly for discharging at low

temperatures, where the anode remains intact, this is the major cause of capacity fade. The side reactions effect an irreversible shift of the electrode balancing, which reduces the utilization of both electrodes. It has to be noted that low-temperature discharging does not generally lead to faster degradation than low-temperature charging. This was only the case in this study because the applied discharging currents were considerably higher than the charging currents. For the same charging and discharging current, low-temperature charging causes higher degradation due to lithium plating at the anode.

6.6 Conclusions

This experimental cycle aging study has provided valuable insights into battery degradation under EV driving operation.

Cycle Aging Decreases with Temperature

Comparing different operating temperatures has revealed that the capacity fade from cycling that occurs in addition to calendar aging decreases considerably with temperature. This is opposed to calendar aging which increases with higher temperature. At low temperature, lithium plating becomes the driving force for capacity fade, as it entails a loss of cyclable lithium. When cycling at 10°C, accelerated degradation has been observed, which even led to a tripping of the CID in several cases. This has been caused by a rise of internal cell pressure, which can be related to gaseous reaction products from side reactions between plated lithium and the electrolyte. Overall, the study has demonstrated that a warm battery is beneficial during driving operation.

Regenerative Braking Improves Cycle Life

The comparison on different levels of regenerative braking has demonstrated that the short recharging periods during braking do not increase battery degradation – even at low temperatures of 10°C and 0°C. By contrast, regenerative braking has reduced degradation, in particular at high SoC and at low temperature which are typical conditions that intensify lithium plating. The reduced degradation has been ascribed to the reduced depth of discharge when the battery is partially recharged during braking periods, which leads to shorter durations of the subsequent recharging periods. It has been shown that the capacity fade depends more on the amount of charge recharged at the charging station than on the overall charge throughput. Thus, a high level of regenerative braking is beneficial for an EV. Moreover, no hybridization of the battery system with additional supercapacitors for buffering load peaks is necessary for today's lithium-ion batteries, as typical driving load profiles do not excessively stress the EV batteries.

Cycle Depth as Dominant Factor for Cycle Life

Cycle depth has been identified as a major influencing factor for battery degradation. With higher cycle depths, capacity fade and resistance increase are aggravated. In particular, the resistance increase has revealed a strong dependency on cycle depth and only a small dependency on SoC. Moreover, the resistance increase is mainly caused by rising charge transfer resistances of the NCA cathode. The increasing resistances lead to higher losses and a lower energy efficiency. This has to be considered when designing cooling system for EV batteries. Similar to the calendar aging studies, no direct correlation between resistance increase and capacity fade could be identified. Regarding the resistance contributions from the anode, there has even been a reduction at the beginning of

the cycle aging study when the cells were cycled at 40°C or 25°C – although the capacity was decreasing.

Recovery Effects due to Stored Lithium in the Anode Overhang Areas

Capacity recovery effects without changes in the internal resistances were observed during longer pauses of several months for cells cycled at high SoC. Coulomb Tracking analysis has revealed a left-shift of the discharging endpoint, which means that more lithium could be discharged from the graphite anode again. Such a reversible capacity fade occurs due to lithium diffusing into the overhang areas of the anodes, which face no cathode counterpart. When cells are kept a high SoC, corresponding to the plateau of lowest anode potential, for a longer time, a considerable amount of lithium diffuses into the side areas and becomes inaccessible during the cycling sequences. To avoid an accumulation of inaccessible lithium, prolonged times at high SoC should be avoided and longer times at medium or low SoC help to recover parts of the inaccessible lithium by reversing the potential gradients between active areas and overhang areas of the anode active material.

Degradation under Dynamic Loads Mostly Similar to Constant Loads

The comparison between the dynamic driving load profile and a constant load profile with identical mean current and cycle depth has revealed that degradation is similar in most cases. Only for the low temperature of 10°C, the driving load profile has led to faster degradation than the continuous load. This result, together with the results from different magnitudes of regenerative braking, has demonstrated that lithium-ion batteries exhibit a certain low-pass behavior, which means that the degradation is determined largely by the average load and not by short peak load events. Only for the low temperature of 10°C, fluctuating discharging currents have appeared to be more detrimental than a constant discharging procedure.

Effects of Charging and Discharging at Low Temperature

The aging experiment based on an alternating operating temperature has enabled to study the impact of charging at low temperature and discharging at low temperature separately. DVA has confirmed that charging at low temperature leads to anode degradation. However, the overall capacity fade was lower than for discharging with the driving load profile at 0°C. In that case, no anode degradation occurred for charging at 25°C. Although a certain cathode degradation was observed, the major cause for the capacity fade was a loss of cyclable lithium. As this observation is hard to explain with the current understanding of lithium-ion battery degradation, further research is necessary to better understand the aging mechanisms occurring during discharging at low temperatures. It has to be noted that the discharging currents were considerably higher than the charging currents in this experiment. If the charging currents had been as high as the discharging currents, more lithium plating and a faster degradation would have occurred for charging at 0°C.

Operating Conditions for Long Cycle Life

For cycle life estimations for an EV, cells have been cycled up to 2000 EFC, which is far beyond the USABC development goals for future EV batteries of 1000 cycles. The 2000 EFC could be achieved at 25°C with less than 20% capacity fade for cycle depths up to ca. 60%. Overall, the best cycle life has been obtained for a low cycle depth in combination with a low average SoC. In general, avoiding the SoC regimes of lowest anode potential reduces calendar aging and also the susceptibility to lithium plating.

7 Strategies for Maximizing the Battery Life in Electric Vehicles

To maximize battery life, calendar aging as well as cycle aging has to be minimized. The results of the experimental studies presented in the three preceding chapters have revealed valuable insights into the predominant mechanisms of battery aging under different operating conditions. Based on the findings of the three aging studies, ideal operating strategies are deduced in this chapter. Moreover, battery life estimations are made that demonstrate under which operating conditions, the USABC development goals of 15 years battery life and 1000 cycles for 2020 EV batteries [7] can already be reached with today's battery technology.

7.1 Reducing Calendar Aging

The calendar aging studies have shown that the capacity fade results predominantly from a loss of cyclable lithium owing to side reactions at the anode. Keeping the SoC at a low or medium level and lowering the battery temperature minimizes calendar aging.

Avoiding the SoC Regime Corresponding to the Lowest Anode Potential

The side reactions at the anode have shown a strong dependency on the anode potential and aggravate with lower potentials. As the anode potential exhibits certain plateaus, a reduction of the storage SoC does not automatically reduce these side reactions. Instead, SoC regions covering more than 20–30% of the cell's nominal capacity, exhibit a rather constant degradation. As the LiC_6/LiC_{12} two-phase regime represents the lowest voltage plateau, an SoC in this regime leads to the fastest capacity fade. As a consequence, the degree of lithiation of the graphite anode should be kept below 50% when the cells are kept at the same SoC for a longer time, e.g., during parking.

The low-voltage plateau of the anode typically starts at 55–80% SoC, depending on the electrode balancing of the cell. To identify the beginning of the low-voltage plateau of the graphite anode in the full-cell, a DVA measurement should be performed. The characteristic central graphite peak indicates directly the beginning of the LiC_6/LiC_{12} two-phase regime which is associated with a higher rate of side reactions. DVA measurements should be repeated from time to time because the balancing of the electrodes often changes with the aging of the cells.

For a battery at 25°C, a capacity fade after 15 years of 8–9% has been projected for low and medium SoCs. By contrast, a capacity fade of 16% has been estimated for 15 years of calendar aging at a high SoC within the LiC_6/LiC_{12} two-phase regime.

Keeping the Battery Temperature Low during Nonoperating Periods

As the side reactions at the anode aggravate with higher temperature, the EV battery should be kept cool when the battery is not operated. For the cell type examined in this thesis, lowering the battery temperature from 25°C to 10°C has decreased the capacity fade in the 15-years projections by ca. 40%.

Avoiding Very High States of Charge

For SoCs above 80%, an increasing cathode degradation has been observed. This has led to coupled side reactions and a marked increase of the charge transfer resistance of the NCA cathode. If the SoC cannot be kept in the low or medium SoC regime during long-lasting nonoperating periods to avoid accelerated side reactions at the anode, at least the very high SoCs of 80% and above should be avoided to reduce cathode degradation. However, the beneficial effects of this mean remain limited as the anodic side reactions remain the dominant driver for capacity fade.

Timing of Battery Charging

As a low SoC reduces calendar aging, the battery life can be improved be an intelligent timing of battery charging. When the battery is always recharged directly after driving, it spends the subsequent nonoperating periods at higher SoCs. Thus, a delayed charging, which keeps the battery at a low SoC as long as possible and completes the charging procedure shortly before the next driving period, also helps to reduce calendar aging.

7.2 Reducing Cycle Aging

The aging owing to charging and discharging the EV battery is substantially more complex than pure calendar aging. In addition to SoC and temperature, charge throughput, cycle depth, and current rates have a considerable impact on cycle aging.

Less Cycle Aging at Higher Temperatures

Cycling cells at different temperatures with a highway driving load profile has revealed that the capacity fade in addition to that owing to calendar aging decreases with higher temperature. This is in contrast to calendar aging, where a higher temperature generally accelerates degradation. As a consequence, the battery should be kept warm during cycling. This means that a battery does not have to be cooled down to 25°C during driving or charging. Instead, a heating of the battery to 40°C can reduce the stress and degradation caused by the intercalation and deintercalation processes.

When the EV is parked after a driving sequence, the battery should cool down again to minimize calendar aging during the nonoperating periods. As the operating periods are rather short compared to the nonoperating periods for a typical passenger car, a higher battery temperature during charging or discharging does not have a considerable impact on calendar aging.

Applying Reasonable Charging Currents

High-energy lithium-ion cells are typically more susceptible to lithium plating due to their thick anodes with low porosity. High charging currents should be avoided, particularly at low temperatures and high SoCs, which correspond to the lowest anode potential. But even when higher charging currents are applied only at low SoC, this usually leads to considerably higher stress for the battery cells. Charging with high currents leads to a degradation of the anode active material and lithium plating. Thus, fast-charging protocols should only be applied occasionally and not be used for every-day charging, unless the cell is explicitly designed for high charging currents. In the latter case, however, the required electrode design is generally associated with a lower energy density.

Standard CCCV charging protocols typically provide a reasonable compromise between charging duration and cycle life. The study on charging protocols has shown that below a certain current value, lower charging currents do not further improve battery life.

Lowering Cycle Depth Reduces Resistance Increase

The resistance increase of the lithium-ion cells examined in this thesis has originated largely from rising charge transfer resistances of the NCA cathode. Particularly for large cycle depths and deep discharging, the resistances have increased markedly. When reducing the typical cycle depth to 20–40%, the resistance rise of an EV battery can be minimized. This maintains a higher power capability of the battery also for an aged battery.

Hence, a frequent recharging of the battery can be beneficial as it reduces the average cycle depth. However, this keeps the average SoC at a higher level, which might provoke a faster calendar aging. The combination of a low cycle depth and a low average SoC leads to the longest battery life. However, performing only partial charging is only applicable when not the entire driving range of the EV is needed.

Deep discharging is typically not such a critical issue for EVs as the drivers typically do not drive until the battery is completely discharged, but recharge the vehicle much earlier under most operating conditions. Moreover, the vehicle manufacturers usually program their battery management systems in such a way that a certain capacity reserve remains which is not accessible during the driving operation to prevent a deep discharging and an overdischarging of the battery.

Maximum Utilization of Regenerative Braking Beneficial for Battery Life

The extensive investigations on the impact of regenerative braking on battery aging have shown that regenerative braking always had a beneficial effect on battery life. As a consequence, high recharging peak currents during braking periods should be tolerated, also at low temperatures of 10°C or even 0°C, as they did not harm the battery but reduced the overall cycle depth. The improvements in battery life owing to regenerative braking have been observed particularly at low temperatures and high SoCs. It has been concluded that the shorter recharging sequences at the charging station helped to minimize lithium plating.

Optimizing Capacity Utilization

The aging study comparing different charging protocols has demonstrated that a lower charging voltage reduces the relative capacity fade at the cost of a lower absolute available capacity, which represents the driving range of the EV. After 1000 EFC, the cell with the maximum charging voltage specified in the datasheet still provided a higher remaining driving range than the cells with a lower charging voltage.

From the viewpoint of mathematical optimization, there is no advantage of reducing the charging voltage when it does not retain a higher driving range for aged batteries. However, when taking also effects from psychology and behavioral economics into account, a reduced charging voltage can yet have its benefits. According to the endowment effect, there is the tendency for people who own a good to value it more than people who do not [268,269]. Transferred to battery degradation, this means that losing part of the driving range possessed at the beginning of the vehicle life can be perceived as a more severe loss than a reduced driving range from the very beginning. Such a reduced driving range can result from a restricted utilization of the available battery capacity by a

lower charging voltage; this represents an unused driving range the customer has never possessed. This demonstrates that defining the charging protocol for an EV is not only a mathematical optimization problem but also has to take the psychological perception of the customers into account.

7.3 Battery Life Estimations

For EVs in 2020, the USABC development goals demand a cycle life of 1000 cycles and a battery life of 15 years. For a battery operation at 25°C, different battery life projections can be made based on the results from the aging studies on calendar aging and driving operation. Moreover, the impact of higher and lower temperatures on battery life is discussed.

Cycle Depth of 60% in Combination with Storage at Medium SoC

According to the results of the aging study on driving operation for a cycle depth of 61% C_N at 25°C, 1000 EFC have been achieved with ca. 13% capacity fade (see Figure 88a, p.127). Together with ca. 10% capacity fade from calendar aging after 15 years, when the battery is kept at medium SoCs during nonoperating periods (see Figure 44b, p.69), a total capacity fade of about 23% is obtained.

Cycle Depth of 40% in Combination with Storage at High SoC

When the battery is operated with smaller cycles of only up to 40% C_N but is kept at high SoC during nonoperating periods, Figure 88a has shown that cycle aging decreases by ca. 2 percentage points whereas calendar aging over 15 years increases by ca. 5 percentage points in Figure 44. Thus, the long times at high SoC decrease battery life more than the smaller cycles can prolong it. This demonstrates that always recharging to a high SoC after every short drive does not maximize battery life, although it is beneficial for keeping the resistance increase low.

Cycle Depth of 40% in Combination with a Medium/Low SoC

Only when a reduced cycle depth is combined with an operation predominantly at medium and low SoCs, battery life improves notably. A cycle depth of ca. 40% C_N at medium and low SoCs leads to 10% capacity fade from cycling, as illustrated in Figure 88a, plus ca. 10% of capacity fade owing to calendar aging, as shown in Figure 44b. With this way of operation, a battery life of 15 years and 1000 EFC can already be reached with the cell type examined in this thesis. Moreover, the resistance increase can be kept low

Impact of High Battery Temperatures

High battery temperatures increase calendar aging by accelerating parasitic side-reactions. Thus, the battery temperature should be kept low during the long nonoperating periods. During charging and discharging, a warm battery reduces cycle aging. As long as the battery is only at higher temperatures during operation and cools down again for the nonoperating periods, no disadvantages for the battery life have to be expected. Instead, the battery life prolongs by reducing the cycling-induced degradation. As a consequence, the USABC development goals can also be reached without a strict cooling of the EV battery during operation.

Low-Temperature Operation Remains Critical

While the USABC development goals for future EV batteries can already be reached today for operating temperatures of 25°C and above, low-temperature operation still remains a critical issue.

Operating at temperatures of 10°C or lower does not only reduce the available capacity but also accelerates aging when the cells are cycled. This thesis has demonstrated that not only charging at low temperature, but also discharging at low temperature can cause severe degradation of the lithium-ion battery of an EV. Although the contributions to capacity fade from calendar aging decrease when lowering the battery temperature to 10°C, the contributions from cycling operation increase substantially more. Considering the cycle depths of 60% C_N and 40% C_N in combination with a high charging voltage, only 500 EFC and less have been achieved before a failure of the cells occurred owing to internal overpressure caused by side-reactions releasing gaseous reaction products. Only for low cycle depths of about 20% C_N or a medium cycle depth of 40% C_N at a low or medium SoC, no failures have occurred and more than 1000 EFC have been achieved.

To improve the battery life, the lithium-ion batteries should be heated in winter when there are subzero temperatures. Furthermore, high discharging currents should only be drawn from the battery after a certain warming of the cells.

8 Outlook

Based on the results of the aging studies presented in this thesis, the following topics have been identified as interesting fields for further research.

Low-Temperature Degradation

For the accelerated degradation when discharging the lithium-ion cells with a driving load profile at low temperature, no proper explanation has been found in the literature. Thus, further research is necessary to identify the occurring aging mechanisms that are responsible for the accelerated capacity fade. Applying high-precision coulometry is considered as a promising approach for the separation of anodic side reactions, cathodic side reactions, and losses of active material. With a better understanding of the degradation effects, the low-temperature operation of EVs can be further optimized. Moreover, battery users should become more aware that not only charging but also discharging at low temperatures degrades lithium-ion batteries.

Post-Mortem Studies to Analyze Resistance Changes

Severe degradation of the cathode material has been observed for large cycle depths and deep discharging. These operating conditions have led to marked increases in the charge transfer resistances of the cathode which deteriorates the power capability of the battery. Further post-mortem studies might be beneficial to better understand the mechanisms of mechanical degradation that cause the structural degradation of the cathode materials. Moreover, post-mortem studies can also help to identify the mechanisms behind the resistance decrease ascribed to the anode when cycling at 25°C or 40°C.

Recovery Effects

Different recovery effects have been observed in the three aging studies presented in this thesis. The capacity recovery of cells stored or cycled at high SoC only could be explained by lithium diffusion into the overhang areas of the anode. The amount of lithium stored in the overhang areas becomes inaccessible for charge-discharge cycling. However, a considerable amount of lithium returns when the cells are at low or medium SoC for a longer time. In contrast to this regeneration mechanism, the recovery effects after severe degradation owing to lithium plating have not been fully understood yet. The mechanisms behind short-term capacity recovery and long-term recovery of electrode-specific storage capabilities should be subject to further research.

Battery Aging on System Level

Based on the experimental results presented in this thesis, aging models for the battery system of an EV can be derived and parameterized. As this thesis has examined aging solely on cell level, further research should be performed on system level, where inhomogeneous current distribution among parallel-connected cells can also affect the aging of the individual cells. For online aging diagnostics performed by battery management systems of EVs, advanced diagnosis routines based on DVA appear promising to obtain deeper insights into the actual degradation of the individual electrodes of the lithium-ion traction battery.

Appendix

A.1 Frequency Set Used for Impedance Spectroscopy Measurements

Table A-1 lists all test frequencies together with the respective number of maximum repetitions. It shows the reduced number of frequencies per decade and the reduced number of repetitions for lower test frequencies. This set of frequencies enables a fast measurement time of ca. 10 min.

Table A-1. Frequencies and maximum number of repetitions

Nr	Frequency	Maximum Repetitions
1	**10.0 kHz**	100
2	7.50 kHz	100
3	5.62 kHz	100
4	4.22 kHz	100
5	3.16 kHz	100
6	2.37 kHz	100
7	1.78 kHz	100
8	1.33 kHz	100
9	**1.00 kHz**	100
10	750 Hz	100
11	562 Hz	100
12	422 Hz	100
13	316 Hz	100
14	237 Hz	100
15	178 Hz	100
16	133 Hz	100
17	**100 Hz**	100
18	75.0 Hz	100
19	56.3 Hz	100
20	42.2 Hz	100
21	31.6 Hz	100
22	23.7 Hz	100
23	17.8 Hz	100
24	13.3 Hz	100
25	**10.0 Hz**	100
26	7.50 Hz	4
27	5.11 Hz	4
28	3.48 Hz	4
29	2.37 Hz	4
30	1.61 Hz	4
31	**1.10 Hz**	4
32	750 mHz	4
33	511 mHz	4
34	348 mHz	4
35	237 mHz	4
36	162 mHz	4
37	**110 mHz**	4
38	75.0 mHz	2
39	34.8 mHz	2
40	16.2 mHz	2
41	**10.0 mHz**	2

A.2 Test Protocols Used for Initial Characterizations and Checkups

This sections presents all test procedures in detail. It provides the test protocols with explicit current, voltage, and time settings for all characterization and checkup procedures applied in this thesis.

Table A-2. Initial characterization procedure used for the cells from the first production lot

Step		Parameters	Termination
1	Pause		$t > 1$ min
Loop start			
2	Pause		$t > 15$ min
3	Charge CCCV	$I = 1$ A $V = 4.2$ V	$I < 275$ mA
4	Pause		$t > 15$ min
5	Discharge CC	$I = -2.75$ A	$V < 2.75$ V
6	Discharge CV	$V = 2.75$ V	$I > -275$ mA
Loop end		2 repetitions	
7	Charge CC	$I = 1$ A	SoC > 50%
8	Pause		$t > 60$ min
Pulse sequence at 50% SoC:			
9	Discharge CC	$I = -1$ A	$t > 10$ s, $V < 2.75$ V
10	Pause		$t > 30$ min
11	Charge CC	$I = 1$ A	$t > 10$ s, $V > 4.2$ V
12	Pause		$t > 30$ min
13	Discharge CC	$I = -3$ A	$t > 10$ s, $V < 2.75$ V
14	Pause		$t > 30$ min
15	Charge CC	$I = 1$ A	$t > 10$ s, $V > 4.2$ V
16	Pause		$t > 30$ min
17	Discharge CC	$I = -5$ A	$t > 10$ s, $V < 2.75$ V
18	Pause		$t > 30$ min

Table A-3. Initial characterization procedure used for the cells from the second production lot

Step		Parameters	Termination
1	Pause		$t > 6$ min
2	Charge CCCV	$I = 1$ A $V = 4.2$ V	$I < 50$ mA
3	Pause		$t > 6$ min
4	Discharge CC	$I = -3$ A	$V < 2.5$ V
5	Discharge CV	$V = 2.5$ V	$I > -100$ mA
6	Pause		$t > 6$ min
7	Charge CC	$I = 1$ A	SoC > 30%
8	Pause		$t > 30$ min

Table A-4. Checkup procedure used in the first calendar aging study

Step		Parameters	Termination
1	Pause		$t > 20$ s
2	Calculate Once	$V_{start} = V$	
3	Pause		$t > 20$ s
4	Voltage Ramp	$V_1 = V_{start}$ Slope = 3 mV/min $V_2 = 4.2$ V	$V > 4.2$ V
5	Charge CV	$V = 4.2$ V	$I < 100$ mA
6	Voltage Ramp	$V_1 = 4.2$ V Slope = –3 mV/min $V_2 = 3.0$ V	$V < 3.0$ V
7	Voltage Ramp	$V_1 = 3.0$ V Slope = 3 mV/min $V_2 = 4.2$ V	$V > 4.2$ V
8	Pause		$t > 15$ min
9	Pause		$t > 15$ min
10	Charge CCCV	$I = 700$ mA $V = 4.2$ V	$I < 100$ mA
11	Pause		$t > 15$ min
12	Discharge CC	$I = –3$ A	$V < 2.75$ V
13	Discharge CV	$V = 2.75$ V	$I > –100$ mA
14	Pause		$t > 15$ min
15	Charge CC	$I = 700$ mA	SoC > 50%
16	Pause		$t > 60$ min
Pulse sequence at 50% SoC:			
17	Discharge CC	$I = –1$ A	$t > 10$ s, $V < 2.75$ V
18	Pause		$t > 30$ min
19	Charge CC	$I = 1$ A	$t > 10$ s, $V > 4.2$ V
20	Pause		$t > 30$ min
21	Discharge CC	$I = –3$ A	$t > 10$ s, $V < 2.75$ V
22	Pause		$t > 30$ min
23	Charge CC	$I = 1$ A	$t > 10$ s, $V > 4.2$ V
24	Pause		$t > 30$ min
25	Discharge CC	$I = –5$ A	$t > 10$ s, $V < 2.75$ V
26	Pause		$t > 30$ min
27	Charge CC	$I = 1$ A	$t > 10$ s, $V > 4.2$ V
28	Pause		$t > 30$ min
Connect cell to galvanostat			
	Impedance Spectroscopy	$f_{max} = 10$ kHz $f_{min} = 10$ mHz $I_{ac,rms} = 50$ mA	
Reconnect cell to battery tester			

Table A-5. Standard checkup procedure used in the second calendar aging study

Step		Parameters	Termination
1	Pause		t > 1 min
2	Impedance Spectroscopy	f_{max} = 10 kHz f_{min} = 10 mHz $I_{ac,rms}$ = 50 mA	
3	Pause		t > 1 min
4	Discharge CC	I = –1 A	V < 2.5 V
5	Discharge CV	V = 2.5 V	I > –100 mA
6	Pause		t > 15 min
7	Charge CCCV	I = 100 mA V = 4.2 V	I < 95 mA
8	Pause		t > 15 min
9	Discharge CC	I = –2 A	V < 2.5 V
10	Discharge CCCV	I = –2 A V = 2.5 V	I > –100 mA
11	Pause		t > 15 min
12	Charge CC	I = 700 mA	SoC > 50%
13	Pause		t > 60 min
14	Impedance Spectroscopy	f_{max} = 10 kHz f_{min} = 10 mHz $I_{ac,rms}$ = 50 mA	
15	Pause		t > 15 min
Further procedure depending on storage SoC			
Case A: Storage SoC < 50%			
16	Discharge CC	I = –1 A	V < 2.5 V
17	Discharge CV	V = 2.5 V	I > –100 mA
18	Pause		t > 15 min
19	Charge CCCV	I = 1 A V = 4.2 V	SoC > $SoC_{Storage}$
20	Pause		t > 15 min
Case B: Storage SoC > 50%			
16	Pause		t > 1 min
17	Pause		t > 1 min
18	Pause		t > 1 min
19	Charge CCCV	I = 1 A V = 4.2 V	SoC > $SoC_{Storage}$
20	Pause		t > 15 min

Table A-6. Extended checkup procedure used in the second calendar aging study

Step		Parameters	Termination
1	Pause		t > 60 s
2	Calculate Once	$V_{start} = V$	
3	Pause		t > 2 s
4	Voltage Ramp	$V_1 = V_{start}$ Slope = 3 mV/min V_2 = 4.2 V	V > 4.2 V
5	Charge CV	V = 4.2 V	I < 100 mA
6	Voltage Ramp	V_1 = 4.2 V Slope = –3 mV/min V_2 = 3.0 V	V < 3.0 V
7	Voltage Ramp	V_1 = 3.0 V Slope = 3 mV/min V_2 = 4.2 V	V > 4.2 V
8	Pause		t > 1 min
9	Charge CV	V = 4.2 V	I < 100 mA
10	Pause		t > 15 min
11	Discharge CC	I = –100 mA	V < 2.5 V
12	Pause		t > 15 min
13	Charge CCCV	I = 100 mA V = 4.2 V	I < 95 mA
14	Pause		t > 15 min
15	Discharge CC	I = –1 A	V < 2.5 V
16	Discharge CV	V = 2.5 V	I > –100 mA
17	Pause		t > 15 min
18	Charge CCCV	I = 700 mA V = 4.2 V	I < 100 mA
19	Pause		t > 15 min
20	Discharge CC	I = –3 A	V < 2.5 V
21	Discharge CCCV	I = –1 A V = 2.5 V	I > –100 mA
22	Pause		t > 15 min
23	Charge CCCV	I = 700 mA V = 4.2 V	I < 100 mA
24	Pause		t > 15 min
25	Discharge CC	I = –4 A	V < 2.5 V
26	Discharge CCCV	I = –1 A V = 2.5 V	I > –100 mA
27	Pause		t > 15 min
Pulse sequences every 10% SoC Main loop start			
28	Set	Ah-Set = 0 Ah	
29	Pause		t > 30 min
Loop 1 A start			
30	Discharge CCCV	I = –1 A V = 2.5 V	t > 10 s
31	Pause		t > 1 min

32	Charge CCCV	*I* = 1 A *V* = 4.2 V	Ah-Set > 0 Ah
33	Pause		*t* > 1 min
Loop 1 A end		3 repetitions	
Loop 3 A start			
34	Discharge CCCV	*I* = –3 A *V* = 2.5 V	*t* > 10 s
35	Pause		*t* > 1 min
36	Charge CCCV	*I* = 1 A *V* = 4.2 V	Ah-Set > 0 Ah
37	Pause		*t* > 1 min
Loop 3 A end		3 repetitions	
Loop 5 A start			
38	Discharge CCCV	*I* = –5 A *V* = 2.5 V	*t* > 10 s
39	Pause		*t* > 1 min
40	Charge CCCV	*I* = 1 A *V* = 4.2 V	Ah-Set > 0 Ah
41	Pause		*t* > 1 min
Loop 5 A end		3 repetitions	
42	Discharge CCCV	*I* = –3 A *V* = 2.5 V	*t* > 10 s
43	Pause		*t* > 15 min
44	Discharge CCCV	*I* = –3 A *V* = 2.5 V	Ah_set < –10% C_{actual} *I* > –100 mA
Main loop end		10 repetitions	
45	Pause		*t* > 15 min
46	Charge CC	*I* = 700 mA	SoC > 50%, U > 4.2 V
47	Pause		*t* > 120 min

Table A-7. Checkup procedure used in the cycle aging study on charging protocols

Step		Parameters	Termination
1	Pause		t > 2 min
2	Discharge CC	I = –1 A	V < 2.5 V
3	Discharge CV	V = 2.5 V	I > –100 mA
4	Pause		t > 15 min
5	Charge CCCV	I = 100 mA V = 4.2 V	I < 95 mA
6	Pause		t > 15 min
7	Discharge CC	I = –2A	V < 2.5 V
8	Discharge CCCV	I = –1A V = 2.5 V	I > –100 mA
9	Pause		t > 15 min
10	Charge CC	I = 700 mA	SoC > 50%
11	Pause		t > 120 min
Pulse sequence at 50% SoC:			
12	Charge CC	I = 333 mA	t > 0.5 s
13	Charge CC	I = 1 A	t > 10 s
14	Charge CC	I = 333 mA	t > 0.5 s
15	Pause		t > 30 min
16	Discharge CC	I = –333 mA	t > 0.5 s
17	Discharge CC	I = –1 A	t > 10 s
18	Discharge CC	I = –333 mA	t > 0.5 s
19	Pause		t > 30 min
20	Charge CC	I = 333 mA	t > 0.5 s
21	Charge CC	I = 3 A	t > 10 s
22	Charge CC	I = 333 mA	t > 0.5 s
23	Pause		t > 30 min
24	Discharge CC	I = –333 mA	t > 0.5 s
25	Discharge CC	I = –3 A	t > 10 s
26	Discharge CC	I = –333 mA	t > 0.5 s
27	Pause		t > 30 min
28	Charge CC	I = 333 mA	t > 0.5 s
29	Charge CC	I = 5 A	t > 10 s
30	Charge CC	I = 333 mA	t > 0.5 s
31	Pause		t > 30 min
32	Discharge CC	I = –333 mA	t > 0.5 s
33	Discharge CC	I = –5 A	t > 10 s
34	Discharge CC	I = –333 mA	t > 0.5 s
35	Pause		t > 30 min
Connect cell to galvanostat			
	Impedance Spectroscopy	f_{max} = 10 kHz f_{min} = 10 mHz $I_{ac,rms}$ = 50 mA	
Reconnect cell to battery tester			

Table A-8. Checkup procedure used in the cycle aging study on driving operation

Step		Parameters	Termination
1	Pause		t > 20 s
2	Calculate Once	$V_{start} = V$	
3	Pause		t > 20 s
4	Voltage Ramp	$V_1 = V_{start}$ Slope = 3 mV/min V_2 = 4.2 V	V > 4.2 V
5	Charge CV	V = 4.2 V	I < 100 mA
6	Voltage Ramp	V_1 = 4.2 V Slope = –3 mV/min V_2 = 3.0 V	V < 3.0 V
7	Voltage Ramp	V_1 = 3.0 V Slope = 3 mV/min V_2 = 4.2 V	V > 4.2 V
8	Pause		t > 15 min
Loop start			
9	Pause		t > 15 min
10	Charge CCCV	I = 700 mA V = 4.2 V	I < 100 mA
11	Pause		t > 15 min
12	Discharge CC	I = –3 A	V < 2.75 V
13	Discharge CV	V = 2.75 V	I > –100 mA
Loop end		2 repetitions	
14	Pause		t > 15 min
15	Charge CC	I = 700 mA	SoC > 50%
16	Pause		t > 60 min
Pulse sequence at 50% SoC:			
17	Discharge CC	I = –1 A	t > 10 s, V < 2.75 V
18	Pause		t > 30 min
19	Charge CC	I = 1 A	t > 10 s, V > 4.2 V
20	Pause		t > 30 min
21	Discharge CC	I = –3 A	t > 10 s, V < 2.75 V
22	Pause		t > 30 min
23	Charge CC	I = 1 A	t > 10 s, V > 4.2 V
24	Pause		t > 30 min
25	Discharge CC	I = –5 A	t > 10 s, V < 2.75 V
26	Pause		t > 30 min
27	Charge CC	I = 1 A	t > 10 s, V > 4.2 V
28	Pause		t > 30 min
Connect cell to galvanostat			
	Impedance Spectroscopy	f_{max} = 10 kHz f_{min} = 10 mHz $I_{ac,rms}$ = 50 mA	
Reconnect cell to battery tester			

References

[1] U. Eberle, B. Müller, R. von Helmolt, Fuel cell electric vehicles and hydrogen infrastructure: Status 2012, Energy Environ. Sci. 5 (10) (2012) 8780–8798. (doi.org/10.1039/c2ee22596d)

[2] J.B. Dunn, L. Gaines, J.C. Kelly, C. James, K.G. Gallagher, The significance of Li-ion batteries in electric vehicle life-cycle energy and emissions and recycling's role in its reduction, Energy Environ. Sci. 8 (1) (2015) 158–168.

[3] H. Huo, H. Cai, Q. Zhang, F. Liu, K. He, Life-cycle assessment of greenhouse gas and air emissions of electric vehicles: A comparison between China and the U.S, Atmospheric Environment 108 (2015) 107–116.

[4] O. Egbue, S. Long, Barriers to widespread adoption of electric vehicles: An analysis of consumer attitudes and perceptions, Energy Policy 48 (2012) 717–729.

[5] G.E. Blomgren, The Development and Future of Lithium Ion Batteries, J. Electrochem. Soc. 164 (1) (2016) A5019-A5025.

[6] H. Zheng, Q. Sun, G. Liu, X. Song, V.S. Battaglia, Correlation between dissolution behavior and electrochemical cycling performance for LiNi1/3Co1/3Mn1/3O2-based cells, Journal of Power Sources 207 (2012) 134–140.

[7] United States Advanced Battery Consortium, USABC Goals for Advanced Batteries for EVs - CY 2020 Commercialization, available at http://www.uscar.org/commands/files_download.php?files_id=364 (accessed on February 19, 2017).

[8] O. Gröger, H.A. Gasteiger, J.-P. Suchsland, Review—Electromobility: Batteries or Fuel Cells?, J. Electrochem. Soc. 162 (14) (2015) A2605-A2622.

[9] M.A. Danzer, V. Liebau, F. Maglia, Aging of lithium-ion batteries for electric vehicles, in: Advances in Battery Technologies for Electric Vehicles, Elsevier, 2015, pp. 359–387.

[10] M. Dubarry, C. Truchot, B.Y. Liaw, Synthesize battery degradation modes via a diagnostic and prognostic model, Journal of Power Sources 219 (2012) 204–216.

[11] M. Dubarry, C. Truchot, B.Y. Liaw, K. Gering, S. Sazhin, D. Jamison, C. Michelbacher, Evaluation of commercial lithium-ion cells based on composite positive electrode for plug-in hybrid electric vehicle applications. Part II. Degradation mechanism under 2C cycle aging, Journal of Power Sources 196 (23) (2011) 10336–10343.

[12] M.M. Doeff, Battery Cathodes, in: R.J. Brodd (Ed.), Batteries for Sustainability, Springer, New York, NY, 2013, pp. 5–49.

[13] D. Andre, S.-J. Kim, P. Lamp, S.F. Lux, F. Maglia, O. Paschos, B. Stiaszny, Future generations of cathode materials: An automotive industry perspective, J. Mater. Chem. A 3 (13) (2015) 6709–6732.

[14] N. Nitta, F. Wu, J.T. Lee, G. Yushin, Li-ion battery materials: Present and future, Materials Today 18 (5) (2015) 252–264.

[15] J. Dahn, G.M. Ehrlich, Lithium-Ion Batteries, in: T.B. Reddy (Ed.), Linden's handbook of batteries, 4th ed., McGraw-Hill, New York, N.Y., 2011, 26.1-26.79.

[16] P. Kurzweil, K. Brandt, SECONDARY BATTERIES | Lithium Rechargeable Systems: Overview, in: J. Garche (Ed.), Encyclopedia of electrochemical power sources, Elsevier, Amsterdam, 2009, pp. 1–26.
[17] J. Vetter, P. Novák, M.R. Wagner, C. Veit, K.-C. Möller, J.O. Besenhard, M. Winter, M. Wohlfahrt-Mehrens, C. Vogler, A. Hammouche, Ageing mechanisms in lithium-ion batteries, Journal of Power Sources 147 (1-2) (2005) 269–281.
[18] E. Peled, D. Golodnitsky, SEI on lithium, graphite, disordered carbons and tin-based alloys, in: P.B. Balbuena, Y. Wang (Eds.), Lithium-ion batteries: Solid-electrolyte interphase, Imperial College Press, London, 2004, pp. 1–69.
[19] V.A. Agubra, J.W. Fergus, The formation and stability of the solid electrolyte interface on the graphite anode, Journal of Power Sources 268 (2014) 153–162.
[20] S.S. Zhang, K. Xu, T.R. Jow, Optimization of the forming conditions of the solid-state interface in the Li-ion batteries, Journal of Power Sources 130 (1-2) (2004) 281–285.
[21] P. Verma, P. Maire, P. Novák, A review of the features and analyses of the solid electrolyte interphase in Li-ion batteries, Electrochimica Acta 55 (22) (2010) 6332–6341.
[22] M. Nie, B.L. Lucht, Role of Lithium Salt on Solid Electrolyte Interface (SEI) Formation and Structure in Lithium Ion Batteries, Journal of the Electrochemical Society 161 (6) (2014) A1001-A1006.
[23] M. Nie, D. Chalasani, D.P. Abraham, Y. Chen, A. Bose, B.L. Lucht, Lithium Ion Battery Graphite Solid Electrolyte Interphase Revealed by Microscopy and Spectroscopy, J. Phys. Chem. C 117 (3) (2013) 1257–1267.
[24] S. Malmgren, K. Ciosek, M. Hahlin, T. Gustafsson, M. Gorgoi, H. Rensmo, K. Edström, Comparing anode and cathode electrode/electrolyte interface composition and morphology using soft and hard X-ray photoelectron spectroscopy, Electrochimica Acta 97 (2013) 23–32.
[25] D. Aurbach, B. Markovsky, M. Levi, E. Levi, A. Schechter, M. Moshkovich, Y. Cohen, New insights into the interactions between electrode materials and electrolyte solutions for advanced nonaqueous batteries, Journal of Power Sources 81-82 (1999) 95–111.
[26] M. Gauthier, T.J. Carney, A. Grimaud, L. Giordano, N. Pour, H.-H. Chang, D.P. Fenning, S.F. Lux, O. Paschos, C. Bauer, F. Maglia, S. Lupart, P. Lamp, Y. Shao-Horn, Electrode-electrolyte interface in Li-ion batteries: current understanding and new insights, The journal of physical chemistry letters 6 (22) (2015) 4653–4672.
[27] S.-P. Kim, A.C. van Duin, V.B. Shenoy, Effect of electrolytes on the structure and evolution of the solid electrolyte interphase (SEI) in Li-ion batteries: A molecular dynamics study, Journal of Power Sources 196 (20) (2011) 8590–8597.
[28] K. Edström, M. Herstedt, D.P. Abraham, A new look at the solid electrolyte interphase on graphite anodes in Li-ion batteries, Journal of Power Sources 153 (2) (2006) 380–384.
[29] I.A. Shkrob, Y. Zhu, T.W. Marin, D. Abraham, Reduction of Carbonate Electrolytes and the Formation of Solid-Electrolyte Interface (SEI) in Lithium-Ion Batteries. 1. Spectroscopic Observations of Radical Intermediates Generated in One-Electron Reduction of Carbonates, J. Phys. Chem. C 117 (38) (2013) 19255–19269.
[30] R. Fong, Studies of Lithium Intercalation into Carbons Using Nonaqueous Electrochemical Cells, J. Electrochem. Soc. 137 (7) (1990) 2009–2013.

[31] V. Zinth, C. von Lüders, M. Hofmann, J. Hattendorff, I. Buchberger, S. Erhard, J. Rebelo-Kornmeier, A. Jossen, R. Gilles, Lithium plating in lithium-ion batteries at sub-ambient temperatures investigated by in situ neutron diffraction, Journal of Power Sources 271 (2014) 152–159.

[32] N. Legrand, B. Knosp, P. Desprez, F. Lapicque, S. Raël, Physical characterization of the charging process of a Li-ion battery and prediction of Li plating by electrochemical modelling, Journal of Power Sources 245 (2014) 208–216.

[33] B.K. Purushothaman, U. Landau, Rapid Charging of Lithium-Ion Batteries Using Pulsed Currents, J. Electrochem. Soc. 153 (3) (2006) A533-A542.

[34] P. Arora, Mathematical Modeling of the Lithium Deposition Overcharge Reaction in Lithium-Ion Batteries Using Carbon-Based Negative Electrodes, J. Electrochem. Soc. 146 (10) (1999) 3543–3553.

[35] Z. Li, J. Huang, B. Yann Liaw, V. Metzler, J. Zhang, A review of lithium deposition in lithium-ion and lithium metal secondary batteries, Journal of Power Sources 254 (2014) 168–182.

[36] B. Bitzer, A. Gruhle, A new method for detecting lithium plating by measuring the cell thickness, Journal of Power Sources 262 (2014) 297–302.

[37] B. Rieger, S.F. Schuster, S.V. Erhard, P.J. Osswald, A. Rheinfeld, C. Willmann, A. Jossen, Multi-directional laser scanning as innovative method to detect local cell damage during fast charging of lithium-ion cells, Journal of Energy Storage 8 (2016) 1–5.

[38] D.P. Abraham, J.L. Knuth, D.W. Dees, I. Bloom, J.P. Christophersen, Performance degradation of high-power lithium-ion cells—Electrochemistry of harvested electrodes, Journal of Power Sources 170 (2) (2007) 465–475.

[39] C. Uhlmann, J. Illig, M. Ender, R. Schuster, E. Ivers-Tiffée, In situ detection of lithium metal plating on graphite in experimental cells, Journal of Power Sources 279 (2015) 428–438.

[40] S. Schindler, M. Bauer, M. Petzl, M.A. Danzer, Voltage relaxation and impedance spectroscopy as in-operando methods for the detection of lithium plating on graphitic anodes in commercial lithium-ion cells, Journal of Power Sources 304 (2016) 170–180.

[41] M. Bauer, Multi-phase formation induced by kinetic limitations in graphite-based lithium-ion cells: Analyzing the effects on dilation and voltage response, Journal of Energy Storage (2017) 1–10.

[42] B.V. Ratnakumar, M.C. Smart, Lithium Plating Behavior in Lithium-Ion Cells, ECS Transactions 25 (36) (2010) 241–252.

[43] J.C. Burns, D.A. Stevens, J.R. Dahn, In-Situ Detection of Lithium Plating Using High Precision Coulometry, Journal of the Electrochemical Society 162 (6) (2015) A959-A964.

[44] L.E. Downie, L.J. Krause, J.C. Burns, L.D. Jensen, V.L. Chevrier, J.R. Dahn, In Situ Detection of Lithium Plating on Graphite Electrodes by Electrochemical Calorimetry, Journal of the Electrochemical Society 160 (4) (2013) A588-A594.

[45] C. von Lüders, V. Zinth, S.V. Erhard, P.J. Osswald, M. Hofmann, R. Gilles, A. Jossen, Lithium plating in lithium-ion batteries investigated by voltage relaxation and in situ neutron diffraction, Journal of Power Sources 342 (2017) 17–23.

[46] M. Petzl, M. Kasper, M.A. Danzer, Lithium plating in a commercial lithium-ion battery – A low-temperature aging study, Journal of Power Sources 275 (2015) 799–807.

[47] M. Petzl, M.A. Danzer, Nondestructive detection, characterization, and quantification of lithium plating in commercial lithium-ion batteries, Journal of Power Sources 254 (2014) 80–87.

[48] S.S. Zhang, K. Xu, T.R. Jow, Study of the charging process of a LiCoO2-based Li-ion battery, Journal of Power Sources 160 (2) (2006) 1349–1354.

[49] K.G. Gallagher, S.E. Trask, C. Bauer, T. Woehrle, S.F. Lux, M. Tschech, P. Lamp, B.J. Polzin, S. Ha, B. Long, Q. Wu, W. Lu, D.W. Dees, A.N. Jansen, Optimizing Areal Capacities through Understanding the Limitations of Lithium-Ion Electrodes, J. Electrochem. Soc. 163 (2) (2015) A138-A149.

[50] T. Waldmann, M. Kasper, M. Wohlfahrt-Mehrens, Optimization of Charging Strategy by Prevention of Lithium Deposition on Anodes in high-energy Lithium-ion Batteries – Electrochemical Experiments, Electrochimica Acta 178 (2015) 525–532.

[51] S.F. Schuster, T. Bach, E. Fleder, J. Müller, M. Brand, G. Sextl, A. Jossen, Nonlinear aging characteristics of lithium-ion cells under different operational conditions, Journal of Energy Storage 1 (2015) 44–53.

[52] T. Ohzuku, Formation of Lithium-Graphite Intercalation Compounds in Nonaqueous Electrolytes and Their Application as a Negative Electrode for a Lithium Ion (Shuttlecock) Cell, J. Electrochem. Soc. 140 (9) (1993) 2490–2498.

[53] B. Rieger, S. Schlueter, S.V. Erhard, J. Schmalz, G. Reinhart, A. Jossen, Multi-scale investigation of thickness changes in a commercial pouch type lithium-ion battery, Journal of Energy Storage 6 (2016) 213–221.

[54] M. Hahn, H. Buqa, P.W. Ruch, D. Goers, M.E. Spahr, J. Ufheil, P. Novák, R. Kötz, A Dilatometric Study of Lithium Intercalation into Powder-Type Graphite Electrodes, Electrochem. Solid-State Lett. 11 (9) (2008) A151-A154.

[55] I. Laresgoiti, S. Käbitz, M. Ecker, D.U. Sauer, Modeling mechanical degradation in lithium ion batteries during cycling: Solid electrolyte interphase fracture, Journal of Power Sources 300 (2015) 112–122.

[56] J. Xu, R.D. Deshpande, J. Pan, Y.-T. Cheng, V.S. Battaglia, Electrode Side Reactions, Capacity Loss and Mechanical Degradation in Lithium-Ion Batteries, J. Electrochem. Soc. 162 (10) (2015) A2026-A2035.

[57] T.G. Zavalis, M. Klett, M.H. Kjell, M. Behm, R.W. Lindström, G. Lindbergh, Aging in lithium-ion batteries: Model and experimental investigation of harvested LiFePO4 and mesocarbon microbead graphite electrodes, Electrochimica Acta 110 (2013) 335–348.

[58] R. Deshpande, M. Verbrugge, Y.-T. Cheng, J. Wang, P. Liu, Battery Cycle Life Prediction with Coupled Chemical Degradation and Fatigue Mechanics, Journal of the Electrochemical Society 159 (10) (2012) A1730-A1738.

[59] G. Ning, B. Haran, B.N. Popov, Capacity fade study of lithium-ion batteries cycled at high discharge rates, Journal of Power Sources 117 (1-2) (2003) 160–169.

[60] J.-H. Kim, S.C. Woo, M.-S. Park, K.J. Kim, T. Yim, J.-S. Kim, Y.-J. Kim, Capacity fading mechanism of LiFePO4-based lithium secondary batteries for stationary energy storage, Journal of Power Sources 229 (2013) 190–197.

[61] V.A. Sethuraman, L.J. Hardwick, V. Srinivasan, R. Kostecki, Surface structural disordering in graphite upon lithium intercalation/deintercalation, Journal of Power Sources 195 (11) (2010) 3655–3660.

[62] D. Aurbach, B. Markovsky, I. Weissman, E. Levi, Y. Ein-Eli, On the correlation between surface chemistry and performance of graphite negative electrodes for Li ion batteries, Electrochimica Acta 45 (1-2) (1999) 67–86.

[63] P. Liu, J. Wang, J. Hicks-Garner, E. Sherman, S. Soukiazian, M. Verbrugge, H. Tataria, J. Musser, P. Finamore, Aging Mechanisms of LiFePO4 Batteries Deduced by Electrochemical and Structural Analyses, J. Electrochem. Soc. 157 (4) (2010) A499-A507.

[64] M. Wohlfahrt-Mehrens, C. Vogler, J. Garche, Aging mechanisms of lithium cathode materials, Journal of Power Sources 127 (1-2) (2004) 58–64.

[65] P. Arora, R.E. White, M. Doyle, Capacity Fade Mechanisms and Side Reactions in Lithium-Ion Batteries, J. Electrochem. Soc. 145 (10) (1998) 3647–3667.

[66] S. Albrecht, J. Kümpers, M. Kruft, S. Malcus, C. Vogler, M. Wahl, M. Wohlfahrt-Mehrens, Electrochemical and thermal behavior of aluminum- and magnesium-doped spherical lithium nickel cobalt mixed oxides Li1−x(Ni1−y−zCoyMz)O2 (M = Al, Mg), Journal of Power Sources 119-121 (2003) 178–183.

[67] S. Watanabe, M. Kinoshita, K. Nakura, Capacity fade of LiNi(1−x−y)CoxAlyO2 cathode for lithium-ion batteries during accelerated calendar and cycle life test. I. Comparison analysis between LiNi(1−x−y)CoxAlyO2 and LiCoO2 cathodes in cylindrical lithium-ion cells during long term storage test, Journal of Power Sources 247 (2014) 412–422.

[68] D. Abraham, R. Twesten, M. Balasubramanian, I. Petrov, J. McBreen, K. Amine, Surface changes on LiNi0.8Co0.2O2 particles during testing of high-power lithium-ion cells, Electrochemistry Communications 4 (8) (2002) 620–625.

[69] Y. Itou, Y. Ukyo, Performance of LiNiCoO2 materials for advanced lithium-ion batteries, Journal of Power Sources 146 (1-2) (2005) 39–44.

[70] S. Watanabe, M. Kinoshita, T. Hosokawa, K. Morigaki, K. Nakura, Capacity fading of LiAlyNi1−x−yCoxO2 cathode for lithium-ion batteries during accelerated calendar and cycle life tests (effect of depth of discharge in charge–discharge cycling on the suppression of the micro-crack generation of LiAlyNi1−x−yCoxO2 particle), Journal of Power Sources 260 (2014) 50–56.

[71] S. Watanabe, M. Kinoshita, K. Nakura, Comparison of the surface changes on cathode during long term storage testing of high energy density cylindrical lithium-ion cells, Journal of Power Sources 196 (16) (2011) 6906–6910.

[72] W. Prochazka, G. Pregartner, M. Cifrain, Design-of-Experiment and Statistical Modeling of a Large Scale Aging Experiment for Two Popular Lithium Ion Cell Chemistries, Journal of the Electrochemical Society 160 (8) (2013) A1039-A1051.

[73] S. Brown, N. Mellgren, M. Vynnycky, G. Lindbergh, Impedance as a Tool for Investigating Aging in Lithium-Ion Porous Electrodes, J. Electrochem. Soc. 155 (4) (2008) A320-A338.

[74] H. Zheng, J. Li, X. Song, G. Liu, V.S. Battaglia, A comprehensive understanding of electrode thickness effects on the electrochemical performances of Li-ion battery cathodes, Electrochimica Acta 71 (2012) 258–265.

[75] Y. Zhang, C.-Y. Wang, Cycle-Life Characterization of Automotive Lithium-Ion Batteries with LiNiO2 Cathode, J. Electrochem. Soc. 156 (7) (2009) A527-A535.
[76] D.P. Abraham, S.D. Poppen, A.N. Jansen, J. Liu, D.W. Dees, Application of a lithium–tin reference electrode to determine electrode contributions to impedance rise in high-power lithium-ion cells, Electrochimica Acta 49 (26) (2004) 4763–4775.
[77] I. Buchberger, S. Seidlmayer, A. Pokharel, M. Piana, J. Hattendorff, P. Kudejova, R. Gilles, H.A. Gasteiger, Aging Analysis of Graphite/LiNi 1/3 Mn 1/3 Co 1/3 O 2 Cells Using XRD, PGAA, and AC Impedance, J. Electrochem. Soc. 162 (14) (2015) A2737-A2746.
[78] D.R. Gallus, R. Schmitz, R. Wagner, B. Hoffmann, S. Nowak, I. Cekic-Laskovic, R.W. Schmitz, M. Winter, The influence of different conducting salts on the metal dissolution and capacity fading of NCM cathode material, Electrochimica Acta 134 (2014) 393–398.
[79] J.A. Gilbert, I.A. Shkrob, D.P. Abraham, Transition Metal Dissolution, Ion Migration, Electrocatalytic Reduction and Capacity Loss in Lithium-Ion Full Cells, J. Electrochem. Soc. 164 (2) (2017) A389-A399.
[80] A. Manthiram, J. Choi, W. Choi, Factors limiting the electrochemical performance of oxide cathodes, Solid State Ionics 177 (26-32) (2006) 2629–2634.
[81] L.-F. Wang, C.-C. Ou, K.A. Striebel, J.-S. Chen, Study of Mn Dissolution from LiMn2O4 Spinel Electrodes Using Rotating Ring-Disk Collection Experiments, Journal of the Electrochemical Society 150 (7) (2003) A905-A911.
[82] T. Joshi, K. Eom, G. Yushin, T.F. Fuller, Effects of Dissolved Transition Metals on the Electrochemical Performance and SEI Growth in Lithium-Ion Batteries, Journal of the Electrochemical Society 161 (12) (2014) A1915-A1921.
[83] N.P.W. Pieczonka, Z. Liu, P. Lu, K.L. Olson, J. Moote, B.R. Powell, J.-H. Kim, Understanding Transition-Metal Dissolution Behavior in LiNi 0.5 Mn 1.5 O 4 High-Voltage Spinel for Lithium Ion Batteries, J. Phys. Chem. C 117 (31) (2013) 15947–15957.
[84] D.P. Abraham, S. Kawauchi, D.W. Dees, Modeling the impedance versus voltage characteristics of LiNi0.8Co0.15Al0.05O2, Electrochimica Acta 53 (5) (2008) 2121–2129.
[85] K. Amine, C.H. Chen, J. Liu, M. Hammond, A. Jansen, D. Dees, I. Bloom, D. Vissers, G. Henriksen, Factors responsible for impedance rise in high power lithium ion batteries, Journal of Power Sources 97-98 (2001) 684–687.
[86] R. Kostecki, L. Norin, X. Song, F. McLarnon, Diagnostic Studies of Polyolefin Separators in High-Power Li-Ion Cells, J. Electrochem. Soc. 151 (4) (2004) A522-A526.
[87] K. Edström, T. Gustafsson, J.O. Thomas, The cathode–electrolyte interface in the Li-ion battery, Electrochimica Acta 50 (2-3) (2004) 397–403.
[88] K. Edström, T. Gustafsson, J. Thomas, The Cathode-Electrolyte Interface in a Li-ion Battery, in: P.B. Balbuena, Y. Wang (Eds.), Lithium-ion batteries: Solid-electrolyte interphase, Imperial College Press, London, 2004, pp. 337–364.
[89] D.P. Abraham, E.M. Reynolds, E. Sammann, A.N. Jansen, D.W. Dees, Aging characteristics of high-power lithium-ion cells with LiNi0.8Co0.15Al0.05O2 and Li4/3Ti5/3O4 electrodes, Electrochimica Acta 51 (3) (2005) 502–510.
[90] R.P. Day, J. Xia, R. Petibon, J. Rucska, H. Wang, A.T.B. Wright, J.R. Dahn, Differential Thermal Analysis of Li-Ion Cells as an Effective Probe of Liquid Electrolyte Evolution during Aging, J. Electrochem. Soc. 162 (14) (2015) A2577-A2581.

[91] L.O. Valøen, J.N. Reimers, Transport Properties of LiPF6-Based Li-Ion Battery Electrolytes, J. Electrochem. Soc. 152 (5) (2005) A882-A891.

[92] M.S. Ding, K. Xu, S.S. Zhang, K. Amine, G.L. Henriksen, T.R. Jow, Change of Conductivity with Salt Content, Solvent Composition, and Temperature for Electrolytes of LiPF6 in Ethylene Carbonate-Ethyl Methyl Carbonate, J. Electrochem. Soc. 148 (10) (2001) A1196-A1204.

[93] D.A. Stevens, R.Y. Ying, R. Fathi, J.N. Reimers, J.E. Harlow, J.R. Dahn, Using High Precision Coulometry Measurements to Compare the Degradation Mechanisms of NMC/LMO and NMC-Only Automotive Scale Pouch Cells, Journal of the Electrochemical Society 161 (9) (2014) A1364-A1370.

[94] D. Guyomard, J.M. Tarascon, Rechargeable Li[1+x]Mn[2]O[4]/Carbon Cells with a New Electrolyte Composition, J. Electrochem. Soc. 140 (11) (1993) 3071–3081.

[95] G. Pistoia, A. Antonini, R. Rosati, D. Zane, Storage characteristics of cathodes for Li-ion batteries, Electrochimica Acta 41 (17) (1996) 2683–2689.

[96] M. Broussely, P. Biensan, F. Bonhomme, P. Blanchard, S. Herreyre, K. Nechev, R.J. Staniewicz, Main aging mechanisms in Li ion batteries, Journal of Power Sources 146 (1-2) (2005) 90–96.

[97] A. Matasso, D. Wong, D. Wetz, F. Liu, Effects of High-Rate Cycling on the Bulk Internal Pressure Rise and Capacity Degradation of Commercial LiCoO2 Cells, Journal of the Electrochemical Society 162 (6) (2015) A885-A891.

[98] C.J. Weber, S. Geiger, S. Falusi, M. Roth, Material review of Li ion battery separators, in: Review on Electrochemical Storage Materials and Technology: Proceedings of the 1st International Freiberg Conference on Electrochemical Storage Materials, Freiberg, Germany, AIP Publishing LLC, 2014, pp. 66–81.

[99] Y. Merla, B. Wu, V. Yufit, N.P. Brandon, R.F. Martinez-Botas, G.J. Offer, Novel application of differential thermal voltammetry as an in-depth state-of-health diagnosis method for lithium-ion batteries, Journal of Power Sources 307 (2016) 308–319.

[100] B.P. Matadi, S. Geniès, A. Delaille, T. Waldmann, M. Kasper, M. Wohlfahrt-Mehrens, F. Aguesse, E. Bekaert, I. Jiménez-Gordon, L. Daniel, X. Fleury, M. Bardet, J.-F. Martin, Y. Bultel, Effects of Biphenyl Polymerization on Lithium Deposition in Commercial Graphite/NMC Lithium-Ion Pouch-Cells during Calendar Aging at High Temperature, J. Electrochem. Soc. 164 (6) (2017) A1089-A1097.

[101] C. Peabody, C.B. Arnold, The role of mechanically induced separator creep in lithium-ion battery capacity fade, Journal of Power Sources 196 (19) (2011) 8147–8153.

[102] J. Cannarella, C.B. Arnold, Ion transport restriction in mechanically strained separator membranes, Journal of Power Sources 226 (2013) 149–155.

[103] J. Cannarella, C.B. Arnold, The Effects of Defects on Localized Plating in Lithium-Ion Batteries, Journal of the Electrochemical Society 162 (7) (2015) A1365-A1373.

[104] T.C. Bach, S.F. Schuster, E. Fleder, J. Müller, M.J. Brand, H. Lorrmann, A. Jossen, G. Sextl, Nonlinear aging of cylindrical lithium-ion cells linked to heterogeneous compression, Journal of Energy Storage 5 (2016) 212–223.

[105] B. Stiaszny, J.C. Ziegler, E.E. Krauß, M. Zhang, J.P. Schmidt, E. Ivers-Tiffée, Electrochemical characterization and post-mortem analysis of aged LiMn2O4–NMC/graphite lithium ion batteries part II: Calendar aging, Journal of Power Sources 258 (2014) 61–75.

[106] T. Waldmann, S. Gorse, T. Samtleben, G. Schneider, V. Knoblauch, M. Wohlfahrt-Mehrens, A Mechanical Aging Mechanism in Lithium-Ion Batteries, Journal of the Electrochemical Society 161 (10) (2014) A1742-A1747.
[107] J. Cannarella, C.B. Arnold, Stress evolution and capacity fade in constrained lithium-ion pouch cells, Journal of Power Sources 245 (2014) 745–751.
[108] W.A. van Schalkwijk, B. Scrosati, Advances in lithium-ion batteries, Kluwer Academic/Plenum Publishers, New York, NY, 2002.
[109] E. Sarasketa-Zabala, I. Gandiaga, L.M. Rodriguez-Martinez, I. Villarreal, Calendar ageing analysis of a LiFePO4/graphite cell with dynamic model validations: Towards realistic lifetime predictions, Journal of Power Sources 272 (2014) 45–57.
[110] J. Wang, J. Purewal, P. Liu, J. Hicks-Garner, S. Soukazian, E. Sherman, A. Sorenson, L. Vu, H. Tataria, M.W. Verbrugge, Degradation of lithium ion batteries employing graphite negatives and nickel–cobalt–manganese oxide + spinel manganese oxide positives: Part 1, aging mechanisms and life estimation, Journal of Power Sources 269 (2014) 937–948.
[111] J. Schmalstieg, S. Käbitz, M. Ecker, D.U. Sauer, A holistic aging model for Li(NiMnCo)O2 based 18650 lithium-ion batteries, Journal of Power Sources 257 (2014) 325–334.
[112] C. Guenther, B. Schott, W. Hennings, P. Waldowski, M.A. Danzer, Model-based investigation of electric vehicle battery aging by means of vehicle-to-grid scenario simulations, Journal of Power Sources 239 (2013) 604–610.
[113] G. Hunt, USABC electric vehicle battery test procedures manual, Washington, DC, USA: United States Department of Energy, 1996.
[114] J. Neubauer, A. Pesaran, The ability of battery second use strategies to impact plug-in electric vehicle prices and serve utility energy storage applications, Journal of Power Sources 196 (23) (2011) 10351–10358.
[115] E. Wood, M. Alexander, T.H. Bradley, Investigation of battery end-of-life conditions for plug-in hybrid electric vehicles, Journal of Power Sources 196 (11) (2011) 5147–5154.
[116] R. Faria, P. Marques, R. Garcia, P. Moura, F. Freire, J. Delgado, A.T. de Almeida, Primary and secondary use of electric mobility batteries from a life cycle perspective, Journal of Power Sources 262 (2014) 169–177.
[117] C. Heymans, S.B. Walker, S.B. Young, M. Fowler, Economic analysis of second use electric vehicle batteries for residential energy storage and load-levelling, Energy Policy 71 (2014) 22–30.
[118] X. Han, M. Ouyang, L. Lu, J. Li, A comparative study of commercial lithium ion battery cycle life in electric vehicle: Capacity loss estimation, Journal of Power Sources 268 (2014) 658–669.
[119] Panasonic, Introduction of NCR18650PD, meeting presentation, 2012.
[120] P. Keil, S.F. Schuster, J. Wilhelm, J. Travi, A. Hauser, R.C. Karl, A. Jossen, Calendar Aging of Lithium-Ion Batteries, J. Electrochem. Soc. 163 (9) (2016) A1872-A1880.
[121] P. Keil, A. Jossen, Charging protocols for lithium-ion batteries and their impact on cycle life—An experimental study with different 18650 high-power cells, Journal of Energy Storage 6 (2016) 125–141.

[122] D. Doerffel, S.A. Sharkh, A critical review of using the Peukert equation for determining the remaining capacity of lead-acid and lithium-ion batteries, Journal of Power Sources 155 (2) (2006) 395–400.

[123] S. Paul, C. Diegelmann, H. Kabza, W. Tillmetz, Analysis of ageing inhomogeneities in lithium-ion battery systems, Journal of Power Sources 239 (2013) 642–650.

[124] S.F. Schuster, M.J. Brand, P. Berg, M. Gleissenberger, A. Jossen, Lithium-ion cell-to-cell variation during battery electric vehicle operation, Journal of Power Sources 297 (2015) 242–251.

[125] M. Dubarry, N. Vuillaume, B.Y. Liaw, From single cell model to battery pack simulation for Li-ion batteries, Journal of Power Sources 186 (2) (2009) 500–507.

[126] M.J. Brand, P.A. Schmidt, M.F. Zaeh, A. Jossen, Welding techniques for battery cells and resulting electrical contact resistances, Journal of Energy Storage 1 (2015) 7–14.

[127] J.R. Macdonald, Impedance spectroscopy, Ann Biomed Eng 20 (3) (1992) 289–305.

[128] E. Barsoukov, J.R. Macdonald, Impedance spectroscopy: Theory, experiment, and applications, Wiley-Interscience, a John Wiley & Sons, Inc., publication, Hoboken, New Jersey, 2005.

[129] N. Lohmann, P. Weßkamp, P. Haußmann, J. Melbert, T. Musch, Electrochemical impedance spectroscopy for lithium-ion cells: Test equipment and procedures for aging and fast characterization in time and frequency domain, Journal of Power Sources 273 (2015) 613–623.

[130] E. Karden, S. Buller, R.W. de Doncker, A method for measurement and interpretation of impedance spectra for industrial batteries, Journal of Power Sources 85 (1) (2000) 72–78.

[131] T. Osaka, D. Mukoyama, H. Nara, Review—Development of Diagnostic Process for Commercially Available Batteries, Especially Lithium Ion Battery, by Electrochemical Impedance Spectroscopy, J. Electrochem. Soc. 162 (14) (2015) A2529-A2537.

[132] J. Kowal, Spatially-resolved impedance of nonlinear inhomogeneous devices: using the example of lead-acid batteries, Shaker, Aachen, 2010.

[133] A. Jossen, Fundamentals of battery dynamics, Journal of Power Sources 154 (2) (2006) 530–538.

[134] M. Gaberscek, J. Moskon, B. Erjavec, R. Dominko, J. Jamnik, The Importance of Interphase Contacts in Li Ion Electrodes: The Meaning of the High-Frequency Impedance Arc, Electrochem. Solid-State Lett. 11 (10) (2008) A170-A174.

[135] A.-K. Hjelm, G. Lindbergh, Experimental and theoretical analysis of LiMn2O4 cathodes for use in rechargeable lithium batteries by electrochemical impedance spectroscopy (EIS), Electrochimica Acta 47 (11) (2002) 1747–1759.

[136] J. Illig, J.P. Schmidt, M. Weiss, A. Weber, E. Ivers-Tiffée, Understanding the impedance spectrum of 18650 LiFePO4-cells, Journal of Power Sources 239 (2013) 670–679.

[137] F.C. Laman, Inductive Impedance of a Spirally Wound Li⁄MoS2 Cell, J. Electrochem. Soc. 133 (12) (1986) 2441–2446.

[138] P.J. Osswald, S.V. Erhard, A. Noel, P. Keil, F.M. Kindermann, H. Hoster, A. Jossen, Current density distribution in cylindrical Li-Ion cells during impedance measurements, Journal of Power Sources 314 (2016) 93–101.

[139] M. Levi, K. Gamolsky, D. Aurbach, U. Heider, R. Oesten, On electrochemical impedance measurements of LixCo0.2Ni0.8O2 and LixNiO2 intercalation electrodes, Electrochimica Acta 45 (11) (2000) 1781–1789.
[140] J. Huang, Z. Li, J. Zhang, S. Song, Z. Lou, N. Wu, An Analytical Three-Scale Impedance Model for Porous Electrode with Agglomerates in Lithium-Ion Batteries, Journal of the Electrochemical Society 162 (4) (2015) A585-A595.
[141] C. Chen, J. Liu, K. Amine, Symmetric cell approach and impedance spectroscopy of high power lithium-ion batteries, Journal of Power Sources 96 (2) (2001) 321–328.
[142] T. Momma, T. Yokoshima, H. Nara, Y. Gima, T. Osaka, Distinction of impedance responses of Li-ion batteries for individual electrodes using symmetric cells, Electrochimica Acta 131 (2014) 195–201.
[143] R. Petibon, C.P. Aiken, N.N. Sinha, J.C. Burns, H. Ye, C.M. VanElzen, G. Jain, S. Trussler, J.R. Dahn, Study of Electrolyte Additives Using Electrochemical Impedance Spectroscopy on Symmetric Cells, Journal of the Electrochemical Society 160 (1) (2012) A117-A124.
[144] E. van Gheem, R. Pintelon, J. Vereecken, J. Schoukens, A. Hubin, P. Verboven, O. Blajiev, Electrochemical impedance spectroscopy in the presence of non-linear distortions and non-stationary behaviour, Electrochimica Acta 49 (26) (2004) 4753–4762.
[145] J.R. Macdonald, Impedance spectroscopy: Emphasizing solid materials and systems, Wiley, New York, 1987.
[146] Z.B. Stoynov, D.E. Vladikova, MEASUREMENT METHODS | Electrochemical: Impedance Spectroscopy, in: J. Garche (Ed.), Encyclopedia of electrochemical power sources, Elsevier, Amsterdam, 2009, pp. 632–642.
[147] M. Kiel, O. Bohlen, D.U. Sauer, Harmonic analysis for identification of nonlinearities in impedance spectroscopy, Electrochimica Acta 53 (25) (2008) 7367–7374.
[148] J. Kowal, A. Beleke, W. Heitkötter, G. Pilatowicz, H. Budde-Meiwes, D.U. Sauer, Improved parameter identification for current dependency from impedance spectroscopy, in: Advanced Battery Power Conference, Münster, 2014.
[149] J.P. Schmidt, S. Arnold, A. Loges, D. Werner, T. Wetzel, E. Ivers-Tiffée, Measurement of the internal cell temperature via impedance: Evaluation and application of a new method, Journal of Power Sources 243 (2013) 110–117.
[150] L. Raijmakers, D.L. Danilov, J. van Lammeren, M. Lammers, P. Notten, Sensorless battery temperature measurements based on electrochemical impedance spectroscopy, Journal of Power Sources 247 (2014) 539–544.
[151] W. Waag, S. Käbitz, D.U. Sauer, Experimental investigation of the lithium-ion battery impedance characteristic at various conditions and aging states and its influence on the application, Applied Energy 102 (2013) 885–897.
[152] A. Barai, G.H. Chouchelamane, Y. Guo, A. McGordon, P. Jennings, A study on the impact of lithium-ion cell relaxation on electrochemical impedance spectroscopy, Journal of Power Sources 280 (2015) 74–80.
[153] F.M. Kindermann, A. Noel, S.V. Erhard, A. Jossen, Long-term equalization effects in Li-ion batteries due to local state of charge inhomogeneities and their impact on impedance measurements, Electrochimica Acta 185 (2015) 107–116.

[154] S. Käbitz, J.B. Gerschler, M. Ecker, Y. Yurdagel, B. Emmermacher, D. André, T. Mitsch, D.U. Sauer, Cycle and calendar life study of a graphite|LiNi1/3Mn1/3Co1/3O2 Li-ion high energy system. Part A: Full cell characterization, Journal of Power Sources 239 (2013) 572–583.

[155] P. Röder, B. Stiaszny, J.C. Ziegler, N. Baba, P. Lagaly, H.-D. Wiemhöfer, The impact of calendar aging on the thermal stability of a LiMn2O4–Li(Ni1/3Mn1/3Co1/3)O2/graphite lithium-ion cell, Journal of Power Sources 268 (2014) 315–325.

[156] G. Piłatowicz, A. Marongiu, J. Drillkens, P. Sinhuber, D.U. Sauer, A critical overview of definitions and determination techniques of the internal resistance using lithium-ion, lead-acid, nickel metal-hydride batteries and electrochemical double-layer capacitors as examples, Journal of Power Sources 296 (2015) 365–376.

[157] M. Bauer, C. Guenther, M. Kasper, M. Petzl, M.A. Danzer, Discrimination of degradation processes in lithium-ion cells based on the sensitivity of aging indicators towards capacity loss, Journal of Power Sources 283 (2015) 494–504.

[158] B. Stiaszny, J.C. Ziegler, E.E. Krauß, J.P. Schmidt, E. Ivers-Tiffée, Electrochemical characterization and post-mortem analysis of aged LiMn2O4–Li(Ni0.5Mn0.3Co0.2)O2/graphite lithium ion batteries. Part I: Cycle aging, Journal of Power Sources 251 (2014) 439–450.

[159] H.M. Dahn, A.J. Smith, J.C. Burns, D.A. Stevens, J.R. Dahn, User-Friendly Differential Voltage Analysis Freeware for the Analysis of Degradation Mechanisms in Li-Ion Batteries, Journal of the Electrochemical Society 159 (9) (2012) A1405-A1409.

[160] K. Honkura, T. Horiba, Study of the deterioration mechanism of LiCoO2/graphite cells in charge/discharge cycles using the discharge curve analysis, Journal of Power Sources 264 (2014) 140–146.

[161] I. Bloom, L.K. Walker, J.K. Basco, D.P. Abraham, J.P. Christophersen, C.D. Ho, Differential voltage analyses of high-power lithium-ion cells. 4. Cells containing NMC, Journal of Power Sources 195 (3) (2010) 877–882.

[162] J. Wang, J. Purewal, P. Liu, J. Hicks-Garner, S. Soukazian, E. Sherman, A. Sorenson, L. Vu, H. Tataria, M.W. Verbrugge, Degradation of lithium ion batteries employing graphite negatives and nickel–cobalt–manganese oxide + spinel manganese oxide positives: Part 1, aging mechanisms and life estimation, Journal of Power Sources 269 (2014) 937–948.

[163] I. Bloom, A.N. Jansen, D.P. Abraham, J. Knuth, S.A. Jones, V.S. Battaglia, G.L. Henriksen, Differential voltage analyses of high-power, lithium-ion cells, Journal of Power Sources 139 (1-2) (2005) 295–303.

[164] M. Dubarry, V. Svoboda, R. Hwu, B. Yann Liaw, Incremental Capacity Analysis and Close-to-Equilibrium OCV Measurements to Quantify Capacity Fade in Commercial Rechargeable Lithium Batteries, Electrochem. Solid-State Lett. 9 (10) (2006) A454-A457.

[165] M. Dubarry, B.Y. Liaw, M.-S. Chen, S.-S. Chyan, K.-C. Han, W.-T. Sie, S.-H. Wu, Identifying battery aging mechanisms in large format Li ion cells, Journal of Power Sources 196 (7) (2011) 3420–3425.

[166] A. Eddahech, O. Briat, J.-M. Vinassa, Performance comparison of four lithium–ion battery technologies under calendar aging, Energy 84 (2015) 542–550.

[167] I. Bloom, J.P. Christophersen, D.P. Abraham, K.L. Gering, Differential voltage analyses of high-power lithium-ion cells, Journal of Power Sources 157 (1) (2006) 537–542.

[168] M. Safari, C. Delacourt, Aging of a Commercial Graphite/LiFePO4 Cell, J. Electrochem. Soc. 158 (10) (2011) A1123-A1135.
[169] X. Han, M. Ouyang, L. Lu, J. Li, Y. Zheng, Z. Li, A comparative study of commercial lithium ion battery cycle life in electrical vehicle: Aging mechanism identification, Journal of Power Sources 251 (2014) 38–54.
[170] M. Dubarry, B.Y. Liaw, Identify capacity fading mechanism in a commercial LiFePO4 cell, Journal of Power Sources 194 (1) (2009) 541–549.
[171] M. Ouyang, Z. Chu, L. Lu, J. Li, X. Han, X. Feng, G. Liu, Low temperature aging mechanism identification and lithium deposition in a large format lithium iron phosphate battery for different charge profiles, Journal of Power Sources 286 (2015) 309–320.
[172] I. Bloom, J. Christophersen, K. Gering, Differential voltage analyses of high-power lithium-ion cells, Journal of Power Sources 139 (1-2) (2005) 304–313.
[173] Y. Lee, B. Son, J. Choi, J.H. Kim, M.-H. Ryou, Y.M. Lee, Effect of back-side-coated electrodes on electrochemical performances of lithium-ion batteries, Journal of Power Sources 275 (2015) 712–719.
[174] M. Winter, J.O. Besenhard, M.E. Spahr, P. Novák, Insertion Electrode Materials for Rechargeable Lithium Batteries, Adv. Mater. 10 (10) (1998) 725–763.
[175] S.-I. Pyun, Y.-G. Ryu, Lithium transport through graphite electrodes that contain two stage phases, Journal of Power Sources 70 (1) (1998) 34–39.
[176] H. He, C. Huang, C.-W. Luo, J.-J. Liu, Z.-S. Chao, Dynamic study of Li intercalation into graphite by in situ high energy synchrotron XRD, Electrochimica Acta 92 (2013) 148–152.
[177] M. Hess, Kinetics and stage transitions of graphite for lithium-ion batteries, Zürich, ETH / PSI, 2013.
[178] P. Svens, R. Eriksson, J. Hansson, M. Behm, T. Gustafsson, G. Lindbergh, Analysis of aging of commercial composite metal oxide – Li4Ti5O12 battery cells, Journal of Power Sources 270 (2014) 131–141.
[179] W.-S. Yoon, K.Y. Chung, J. McBreen, X.-Q. Yang, A comparative study on structural changes of LiCo1/3Ni1/3Mn1/3O2 and LiNi0.8Co0.15Al0.05O2 during first charge using in situ XRD, Electrochemistry Communications 8 (8) (2006) 1257–1262.
[180] A.J. Smith, J.C. Burns, J.R. Dahn, A High Precision Study of the Coulombic Efficiency of Li-Ion Batteries, Electrochem. Solid-State Lett. 13 (12) (2010) A177-A179.
[181] S.R. Li, C.H. Chen, J. Camardese, J.R. Dahn, High Precision Coulometry Study of LiNi0.5Mn1.5O4/Li Coin Cells, Journal of the Electrochemical Society 160 (9) (2013) A1517-A1523.
[182] D.Y. Wang, J. Xia, L. Ma, K.J. Nelson, J.E. Harlow, D. Xiong, L.E. Downie, R. Petibon, J.C. Burns, A. Xiao, W.M. Lamanna, J.R. Dahn, A Systematic Study of Electrolyte Additives in Li[Ni1/3Mn1/3Co1/3]O2 (NMC)/Graphite Pouch Cells, Journal of the Electrochemical Society 161 (12) (2014) A1818-A1827.
[183] R.D. Deshpande, P. Ridgway, Y. Fu, W. Zhang, J. Cai, V. Battaglia, The Limited Effect of VC in Graphite/NMC Cells, Journal of the Electrochemical Society 162 (3) (2014) A330-A338.
[184] A.J. Smith, J.C. Burns, S. Trussler, J.R. Dahn, Precision Measurements of the Coulombic Efficiency of Lithium-Ion Batteries and of Electrode Materials for Lithium-Ion Batteries, J. Electrochem. Soc. 157 (2) (2010) A196-A202.

[185] T.M. Bond, J.C. Burns, D.A. Stevens, H.M. Dahn, J.R. Dahn, Improving Precision and Accuracy in Coulombic Efficiency Measurements of Li-Ion Batteries, Journal of the Electrochemical Society 160 (3) (2013) A521-A527.

[186] P. Keil, A. Jossen, Calendar Aging of NCA Lithium-Ion Batteries Investigated by Differential Voltage Analysis and Coulomb Tracking, J. Electrochem. Soc. 164 (1) (2016) A6066-A6074.

[187] R. Fu, S.-Y. Choe, V. Agubra, J. Fergus, Development of a physics-based degradation model for lithium ion polymer batteries considering side reactions, Journal of Power Sources 278 (2015) 506–521.

[188] N.N. Sinha, A.J. Smith, J.C. Burns, G. Jain, K.W. Eberman, E. Scott, J.P. Gardner, J.R. Dahn, The Use of Elevated Temperature Storage Experiments to Learn about Parasitic Reactions in Wound LiCoO2/Graphite Cells, J. Electrochem. Soc. 158 (11) (2011) A1194-A1201.

[189] D.Y. Wang, J.C. Burns, J.R. Dahn, A Systematic Study of the Concentration of Lithium Hexafluorophosphate (LiPF6) as a Salt for LiCoO2/Graphite Pouch Cells, Journal of the Electrochemical Society 161 (9) (2014) A1278-A1283.

[190] J. Kasnatscheew, M. Evertz, B. Streipert, R. Wagner, R. Klopsch, B. Vortmann, H. Hahn, S. Nowak, M. Amereller, A.-C. Gentschev, P. Lamp, M. Winter, The truth about the 1st cycle Coulombic efficiency of LiNi1/3Co1/3Mn1/3O2 (NCM) cathodes, Physical chemistry chemical physics PCCP 18 (5) (2016) 3956–3965.

[191] J.C. Burns, N.N. Sinha, D.J. Coyle, G. Jain, C.M. VanElzen, W.M. Lamanna, A. Xiao, E. Scott, J.P. Gardner, J.R. Dahn, The Impact of Varying the Concentration of Vinylene Carbonate Electrolyte Additive in Wound Li-Ion Cells, J. Electrochem. Soc. 159 (2) (2012) A85-A90.

[192] A.J. Smith, J.C. Burns, D. Xiong, J.R. Dahn, Interpreting High Precision Coulometry Results on Li-ion Cells, J. Electrochem. Soc. 158 (10) (2011) A1136-A1142.

[193] T. Waldmann, N. Ghanbari, M. Kasper, M. Wohlfahrt-Mehrens, Correlations between Electrochemical Data and Results from Post-Mortem Analysis of Aged Lithium-Ion Batteries, Journal of the Electrochemical Society 162 (8) (2015) A1500-A1505.

[194] J.-H. Kim, N.P. Pieczonka, Z. Li, Y. Wu, S. Harris, B.R. Powell, Understanding the capacity fading mechanism in LiNi0.5Mn1.5O4/graphite Li-ion batteries, Electrochimica Acta 90 (2013) 556–562.

[195] M. Metzger, B. Strehle, S. Solchenbach, H.A. Gasteiger, Origin of H 2 Evolution in LIBs: H 2 O Reduction vs. Electrolyte Oxidation, J. Electrochem. Soc. 163 (5) (2016) A798-A809.

[196] K. Nakura, Y. Ohsugi, M. Imazaki, K. Ariyoshi, T. Ohzuku, Extending Cycle Life of Lithium-Ion Batteries Consisting of Lithium Insertion Electrodes: Cycle Efficiency Versus Ah-Efficiency, J. Electrochem. Soc. 158 (12) (2011) A1243-A1249.

[197] B. Gyenes, D.A. Stevens, V.L. Chevrier, J.R. Dahn, Understanding Anomalous Behavior in Coulombic Efficiency Measurements on Li-Ion Batteries, Journal of the Electrochemical Society 162 (3) (2014) A278-A283.

[198] M. Lewerenz, J. Münnix, J. Schmalstieg, S. Käbitz, M. Knips, D.U. Sauer, Systematic aging of commercial LiFePO4|Graphite cylindrical cells including a theory explaining rise of capacity during aging, Journal of Power Sources 345 (2017) 254–263.

[199] G. Pasaoglu, D. Fiorello, A. Martino, G. Scarcella, A. Alemanno, C. Zubaryeva, C. Thiel, Driving and parking patterns of European car drivers: A mobility survey, Publications Office, Luxembourg, 2012.

[200] A.J. Smith, H.M. Dahn, J.C. Burns, J.R. Dahn, Long-Term Low-Rate Cycling of LiCoO2/Graphite Li-Ion Cells at 55°C, J. Electrochem. Soc. 159 (6) (2012) A705-A710.
[201] M. Ecker, N. Nieto, S. Käbitz, J. Schmalstieg, H. Blanke, A. Warnecke, D.U. Sauer, Calendar and cycle life study of Li(NiMnCo)O2-based 18650 lithium-ion batteries, Journal of Power Sources 248 (2014) 839–851.
[202] S. Grolleau, A. Delaille, H. Gualous, P. Gyan, R. Revel, J. Bernard, E. Redondo-Iglesias, J. Peter, Calendar aging of commercial graphite/LiFePO4 cell – Predicting capacity fade under time dependent storage conditions, Journal of Power Sources 255 (2014) 450–458.
[203] D. Li, D.L. Danilov, J. Xie, L. Raijmakers, L. Gao, Y. Yang, P.H. Notten, Degradation Mechanisms of C6/LiFePO4 Batteries: Experimental Analyses of Calendar Aging, Electrochimica Acta 190 (2016) 1124–1133.
[204] J. Belt, V. Utgikar, I. Bloom, Calendar and PHEV cycle life aging of high-energy, lithium-ion cells containing blended spinel and layered-oxide cathodes, Journal of Power Sources 196 (23) (2011) 10213–10221.
[205] I. Bloom, B. Cole, J. Sohn, S. Jones, E. Polzin, V. Battaglia, G. Henriksen, C. Motloch, R. Richardson, T. Unkelhaeuser, D. Ingersoll, H. Case, An accelerated calendar and cycle life study of Li-ion cells, Journal of Power Sources 101 (2) (2001) 238–247.
[206] S. Bourlot, P. Blanchard, S. Robert, Investigation of aging mechanisms of high power Li-ion cells used for hybrid electric vehicles, Journal of Power Sources 196 (16) (2011) 6841–6846.
[207] M. Kassem, J. Bernard, R. Revel, S. Pélissier, F. Duclaud, C. Delacourt, Calendar aging of a graphite/LiFePO4 cell, Journal of Power Sources 208 (2012) 296–305.
[208] M. Kassem, C. Delacourt, Postmortem analysis of calendar-aged graphite/LiFePO4 cells, Journal of Power Sources 235 (2013) 159–171.
[209] H. Zheng, L. Tan, L. Zhang, Q. Qu, Z. Wan, Y. Wang, M. Shen, H. Zheng, Correlation between lithium deposition on graphite electrode and the capacity loss for LiFePO4/graphite cells, Electrochimica Acta 173 (2015) 323–330.
[210] V. Pop, H.J. Bergveld, P.P.L. Regtien, Op het Veld, J. H. G., D. Danilov, P.H.L. Notten, Battery Aging and Its Influence on the Electromotive Force, J. Electrochem. Soc. 154 (8) (2007) A744-A750.
[211] M. Broussely, S. Herreyre, P. Biensan, P. Kasztejna, K. Nechev, R. Staniewicz, Aging mechanism in Li ion cells and calendar life predictions, Journal of Power Sources 97-98 (2001) 13–21.
[212] H.J. Ploehn, P. Ramadass, R.E. White, Solvent Diffusion Model for Aging of Lithium-Ion Battery Cells, J. Electrochem. Soc. 151 (3) (2004) A456.
[213] J.C. Burns, G. Jain, A.J. Smith, K.W. Eberman, E. Scott, J.P. Gardner, J.R. Dahn, Evaluation of Effects of Additives in Wound Li-Ion Cells Through High Precision Coulometry, J. Electrochem. Soc. 158 (3) (2011) A255-A261.
[214] F.-M. Chmielewski, A. Müller, E. Bruns, Climate changes and trends in phenology of fruit trees and field crops in Germany, 1961–2000, Agricultural and Forest Meteorology 121 (1-2) (2004) 69–78.
[215] S. Siebert, F. Ewert, Spatio-temporal patterns of phenological development in Germany in relation to temperature and day length, Agricultural and Forest Meteorology 152 (2012) 44–57.

[216] D.U. Sauer, BATTERIES | Charge–Discharge Curves, in: J. Garche (Ed.), Encyclopedia of electrochemical power sources, Elsevier, Amsterdam, 2009, pp. 443–451.

[217] S.S. Choi, H.S. Lim, Factors that affect cycle-life and possible degradation mechanisms of a Li-ion cell based on LiCoO2, Journal of Power Sources 111 (1) (2002) 130–136.

[218] Y.-F. Luo, Y.-H. Liu, S.-C. Wang, Search for an optimal multistage charging pattern for lithium-ion batteries using the Taguchi approach, in: TENCON 2009 - 2009 IEEE Region 10 Conference, Singapore, pp. 1–5.

[219] Y.-H. Liu, C.-H. Hsieh, Y.-F. Luo, Search for an Optimal Five-Step Charging Pattern for Li-Ion Batteries Using Consecutive Orthogonal Arrays, IEEE Trans. Energy Convers. 26 (2) (2011) 654–661.

[220] F. Savoye, P. Venet, M. Millet, J. Groot, Impact of Periodic Current Pulses on Li-Ion Battery Performance, IEEE Trans. Ind. Electron. 59 (9) (2012) 3481–3488.

[221] G. Pistoia, Battery operated devices and systems: From portable electronics to industrial products, Elsevier, Amsterdam, London, 2009.

[222] Linear Technologies, Datasheet LTC 4052-4.2: Lithium-ion Battery Pulse Charger with Overcurrent Protection, available at cds.linear.com/docs/en/datasheet/405242f.pdf (accessed on February 19, 2017).

[223] J. Li, E. Murphy, J. Winnick, P.A. Kohl, The effects of pulse charging on cycling characteristics of commercial lithium-ion batteries, Journal of Power Sources 102 (1-2) (2001) 302–309.

[224] B.K. Purushothaman, P.W. Morrison, U. Landau, Reducing Mass-Transport Limitations by Application of Special Pulsed Current Modes, J. Electrochem. Soc. 152 (4) (2005) J33-J39.

[225] P.d. Jongh, P. Notten, Effect of current pulses on lithium intercalation batteries, Solid State Ionics 148 (3-4) (2002) 259–268.

[226] H.Z.Z. Beh, G.A. Covic, J.T. Boys, Effects of pulse and DC charging on lithium iron phosphate (LiFePO4) batteries, in: 2013 IEEE Energy Conversion Congress and Exposition (ECCE), Denver, CO, USA, pp. 315–320.

[227] J. Fan, S. Tan, Studies on Charging Lithium-Ion Cells at Low Temperatures, J. Electrochem. Soc. 153 (6) (2006) A1081-A1092.

[228] P. Notten, J. Op het Veld, J. van Beek, Boostcharging Li-ion batteries: A challenging new charging concept, Journal of Power Sources 145 (1) (2005) 89–94.

[229] D. Anseán, M. González, J.C. Viera, V.M. García, C. Blanco, M. Valledor, Fast charging technique for high power lithium iron phosphate batteries: A cycle life analysis, Journal of Power Sources 239 (2013) 9–15.

[230] S.S. Zhang, The effect of the charging protocol on the cycle life of a Li-ion battery, Journal of Power Sources 161 (2) (2006) 1385–1391.

[231] Z. Guo, B.Y. Liaw, X. Qiu, L. Gao, C. Zhang, Optimal charging method for lithium ion batteries using a universal voltage protocol accommodating aging, Journal of Power Sources 274 (2015) 957–964.

[232] Marcello Torchio, Nicolas A. Wolff, Davide Martino Raimondo, Lalo Magni, Ulrike Krewer, Bhushan Gopaluni, Joel Paulson, Richard D. Braatz, American Control Conference (ACC), 2015: 1 - 3 July 2015, Chicago, IL, USA, IEEE, Piscataway, NJ, 2015.

[233] B. Suthar, P.W.C. Northrop, R.D. Braatz, V.R. Subramanian, Optimal Charging Profiles with Minimal Intercalation-Induced Stresses for Lithium-Ion Batteries Using Reformulated

Pseudo 2-Dimensional Models, Journal of the Electrochemical Society 161 (11) (2014) F3144-F3155.
[234] R. Methekar, V. Ramadesigan, R.D. Braatz, V.R. Subramanian, Optimum Charging Profile for Lithium-Ion Batteries to Maximize Energy Storage and Utilization, in: 216th ECS Meeting, Vienna, Austria, ECS, 2010, pp. 139–146.
[235] G. Sikha, P. Ramadass, B.S. Haran, R.E. White, B.N. Popov, Comparison of the capacity fade of Sony US 18650 cells charged with different protocols, Journal of Power Sources 122 (1) (2003) 67–76.
[236] R. Klein, N.A. Chaturvedi, J. Christensen, J. Ahmed, R. Findeisen, A. Kojic, Optimal Charging Strategies in Lithium-Ion Battery, in: 2011 American Control Conference, San Francisco, 2011, pp. 382–387.
[237] S. Tippmann, D. Walper, L. Balboa, B. Spier, W.G. Bessler, Low-temperature charging of lithium-ion cells part I: Electrochemical modeling and experimental investigation of degradation behavior, Journal of Power Sources 252 (2014) 305–316.
[238] J. Remmlinger, S. Tippmann, M. Buchholz, K. Dietmayer, Low-temperature charging of lithium-ion cells Part II: Model reduction and application, Journal of Power Sources 254 (2014) 268–276.
[239] B. Suthar, D. Sonawane, R.D. Braatz, V.R. Subramanian, Optimal Low Temperature Charging of Lithium-ion Batteries, IFAC-PapersOnLine 48 (8) (2015) 1216–1221.
[240] B. Suthar, V. Ramadesigan, S. De, R.D. Braatz, V.R. Subramanian, Optimal charging profiles for mechanically constrained lithium-ion batteries, Phys Chem Chem Phys 16 (1) (2014) 277–287.
[241] X. Hu, S. Li, H. Peng, F. Sun, Charging time and loss optimization for LiNMC and LiFePO4 batteries based on equivalent circuit models, Journal of Power Sources 239 (2013) 449–457.
[242] I. Abou Hamad, M.A. Novotny, D.O. Wipf, P.A. Rikvold, A new battery-charging method suggested by molecular dynamics simulations, Phys Chem Chem Phys 12 (11) (2010) 2740–2743.
[243] J.-W. Lee, Y.K. Anguchamy, B.N. Popov, Simulation of charge–discharge cycling of lithium-ion batteries under low-earth-orbit conditions, Journal of Power Sources 162 (2) (2006) 1395–1400.
[244] A. Hoke, A. Brissette, K. Smith, A. Pratt, D. Maksimovic, Accounting for Lithium-Ion Battery Degradation in Electric Vehicle Charging Optimization, IEEE J. Emerg. Sel. Topics Power Electron. 2 (3) (2014) 691–700.
[245] B. Nyland, Supercharging Tesla Model S 85 kWh to 100 %, available at https://www.youtube.com/watch?v=B3wOq6WbNoI (accessed on August 31, 2016).
[246] M. Ward, ChargeDataValuesGol2014-06-01.xlsx, available at https://drive.google.com/file/d/0Bx5_5custOL5Umt4djlDOU5UZ1k/edit?usp=sharing (accessed on August 31, 2016).
[247] L. Somerville, J. Bareño, S. Trask, P. Jennings, A. McGordon, C. Lyness, I. Bloom, The effect of charging rate on the graphite electrode of commercial lithium-ion cells: A post-mortem study, Journal of Power Sources 335 (2016) 189–196.
[248] P. Keil, A. Jossen, Aging of Lithium-Ion Batteries in Electric Vehicles: Impact of Regenerative Braking, Electric Vehicle Symposium (EVS28), Goyang, Korea, 2015.

[249] E. Sarasketa-Zabala, I. Gandiaga, E. Martinez-Laserna, L.M. Rodriguez-Martinez, I. Villarreal, Cycle ageing analysis of a LiFePO4/graphite cell with dynamic model validations: Towards realistic lifetime predictions, Journal of Power Sources 275 (2015) 573–587.

[250] J. Groot, M. Swierczynski, A.I. Stan, S.K. Kær, On the complex ageing characteristics of high-power LiFePO4/graphite battery cells cycled with high charge and discharge currents, Journal of Power Sources 286 (2015) 475–487.

[251] M.B. Camara, H. Gualous, F. Gustin, A. Berthon, B. Dakyo, DC/DC Converter Design for Supercapacitor and Battery Power Management in Hybrid Vehicle Applications—Polynomial Control Strategy, IEEE Trans. Ind. Electron. 57 (2) (2010) 587–597.

[252] M.-E. Choi, S.-W. Kim, S.-W. Seo, Energy Management Optimization in a Battery/Supercapacitor Hybrid Energy Storage System, IEEE Trans. Smart Grid 3 (1) (2012) 463–472.

[253] M.-E. Choi, J.-S. Lee, S.-W. Seo, Real-Time Optimization for Power Management Systems of a Battery/Supercapacitor Hybrid Energy Storage System in Electric Vehicles, IEEE Trans. Veh. Technol. 63 (8) (2014) 3600–3611.

[254] O.C. Onar, A. Khaligh, A Novel Integrated Magnetic Structure Based DC/DC Converter for Hybrid Battery/Ultracapacitor Energy Storage Systems, IEEE Trans. Smart Grid 3 (1) (2012) 296–307.

[255] J. Shen, S. Dusmez, A. Khaligh, Optimization of Sizing and Battery Cycle Life in Battery/Ultracapacitor Hybrid Energy Storage Systems for Electric Vehicle Applications, IEEE Trans. Ind. Inf. 10 (4) (2014) 2112–2121.

[256] K.L. Gering, S.V. Sazhin, D.K. Jamison, C.J. Michelbacher, B.Y. Liaw, M. Dubarry, M. Cugnet, Investigation of path dependence in commercial lithium-ion cells chosen for plug-in hybrid vehicle duty cycle protocols, Journal of Power Sources 196 (7) (2011) 3395–3403.

[257] S.B. Peterson, J. Apt, J.F. Whitacre, Lithium-ion battery cell degradation resulting from realistic vehicle and vehicle-to-grid utilization, Journal of Power Sources 195 (8) (2010) 2385–2392.

[258] K. Kleiner, P. Jakes, S. Scharner, V. Liebau, H. Ehrenberg, Changes of the balancing between anode and cathode due to fatigue in commercial lithium-ion cells, Journal of Power Sources 317 (2016) 25–34.

[259] J. Wang, P. Liu, J. Hicks-Garner, E. Sherman, S. Soukiazian, M. Verbrugge, H. Tataria, J. Musser, P. Finamore, Cycle-life model for graphite-LiFePO4 cells, Journal of Power Sources 196 (8) (2011) 3942–3948.

[260] T. Waldmann, M. Wilka, M. Kasper, M. Fleischhammer, M. Wohlfahrt-Mehrens, Temperature dependent ageing mechanisms in Lithium-ion batteries – A Post-Mortem study, Journal of Power Sources 262 (2014) 129–135.

[261] H. Neudorfer, A. Binder, N. Wicker, Analyse von unterschiedlichen Fahrzyklen für den Einsatz von Elektrofahrzeugen, Elektrotech. Inftech. 123 (7-8) (2006) 352–360.

[262] B. Heissing, M. Ersoy, Chassis handbook: Fundamentals, driving dynamics, components, mechatronics, perspectives, 1st ed., Vieweg+Teubner, Wiesbaden, 2010.

[263] M. Meywerk, Vehicle dynamics, Wiley, Chichester, West Sussex, 2015.

[264] dieselnet, Emission Test Cycles: Worldwide engine and vehicle test cycles, available at www.dieselnet.com/standards/cycles (accessed on January 6, 2017).

[265] C. Huang, S. Zhuang, F. Tu, Electrode/Electrolyte Interfacial Behaviors of LiCoO2/Mixed Graphite Li-Ion Cells during Operation and Storage, Journal of the Electrochemical Society 160 (2) (2012) A376-A382.
[266] J. Zhou, P. Notten, Studies on the degradation of Li-ion batteries by the use of microreference electrodes, Journal of Power Sources 177 (2) (2008) 553–560.
[267] G. Pistoia, Lithium-ion batteries: Advances and applications, Elsevier, Amsterdam, 2014.
[268] D. Kahneman, J.L. Knetsch, R.H. Thaler, Experimental Tests of the Endowment Effect and the Coase Theorem, Journal of Political Economy 98 (6) (1990) 1325–1348.
[269] C.K. Morewedge, C.E. Giblin, Explanations of the endowment effect: an integrative review, Trends in cognitive sciences 19 (6) (2015) 339–348.